A Versatile Seebeck Potential Measurement Device for Thermoelectric Thin Films, Powders and Pastes

DISSERTATION

zum Erlangen des akademischen Grades
doctor rerum naturalium
(Dr. rer. nat.)
im Fach Chemie

eingereicht an der
Mathematisch-Naturwissenschaftlichen Fakultät
der Humboldt-Universität zu Berlin
von

Dipl.-Chem. Kevin Oliver Roland Bethke

Präsidentin der Humboldt-Universität zu Berlin:
Prof. Dr.-Ing. Dr. Sabine Kunst

Dekan der Mathematisch-Naturwissenschaftlichen Fakultät:
Prof. Dr. Elmar Kulke

Gutachter:
1. Prof. Dr. Klaus Rademann
2. Prof. Dr. Hans-Joachim Freund
3. Prof. Dr. Jeyanthinath Mayandi

Tag der mündlichen Prüfung: 25.06.2020

Abstract

This thesis describes the development of a versatile, low-cost measurement instrument that can determine Seebeck coefficients for a multitude of samples such as thin films, powders, and pastes. Commercial instruments are relatively expensive and limited to one sample type. The developed device applied on several thermoelectric thin-film systems produced the same results as a standard commercial instrument. In addition, it was used to determine Seebeck coefficients for thermoelectric pastes and powders.

For thin-film materials, the developed device, in combination with other measuring methods such as grazing incidence X-ray fluorescence, atomic force microscopy, and photoelectron spectroscopy was used to establish relations between the thermoelectric properties and the material‘s structures. Based on these results, organic DMSO doped PEDOT:PSS multilayer films were developed with improved thermoelectric properties making them promising materials for flexible thermoelectric generators.

Furthermore, finite element method simulations on the thermal conductivity of thermoelectric materials were conducted in order to propose a manufacturing process for thin-film thermoelectrics, which can be carried out with already established methods in the mass production of thermoelectric generators.

Zusammenfassung

Die vorliegende Arbeit beschreibt die Entwicklung eines vielseitigen Messinstruments, um die für Thermoelektrika entscheidende Materialeigenschaft - den Seebeck-koeffizienten - zu ermitteln. Dieses Instrument ermöglicht es, mit einem einzigen Gerät unterschiedliche Probenarten zu messen, wofür in herkömmlichen Messverfahren mehrere Geräte notwendig sind. Um diese Vielseitigkeit aufzuzeigen, wurde das entwickelte Instrument an einer Vielzahl unterschiedlicher Proben von Dünnschichten, Pulvern und Pasten getestet.

Am Beispiel der Dünnschichtmaterialen wurden mit dem hier entwickelten Messgerät und anderen Messmethoden, wie zum Beispiel Röntgenfluoreszenz mit streifendem Einfallswinkel, Rasterkraftmikroskopie und Photoelektronenspektroskopie, Zusammenhänge zwischen den thermoelektrischen Eigenschaften und der Struktur der Materialien hergestellt. Der Seebeckkoeffizient der Kupferoxide wurde durch das Tempern in einer Sauertoffatmosphäre verbessert.

Bei organischen mehrschichtigen DMSO-dotierten PEDOT:PSS Filmen wurde überraschenderweise eine Verbesserung der thermoelektrischen Eigenschaften - vor allem der Leitfähigkeit - festgestellt. Für die Erhöhung der Leitfähigkeit im Vergleich zu einschichtigen Filmen wurden Mechanismen vorgeschlagen. Aufgrund der Minimierung des Widerstandes sind die PEDOT:PSS Filme vielversprechende Materialien für flexible thermoelektrische Generatoren.

Darüber hinaus wurden Finite-Elemente-Methode-Simulationen zur Wärmeleitfähigkeit von thermoelektrischen Materialien ausgeführt, um einen Herstellungsprozess für Dünnschicht-Thermoelektrika vorzuschlagen, der mittels bereits etablierter Methoden in der Massenproduktion von thermoelektrischen Generatoren durchgeführt werden kann.

Contents

1 Introduction and Motivation

Motivation for research in waste heat recovery The global demand for energy is rising steadily. The human hunger for energy will continue to grow for the foreseeable future.[1,2] Global warming and pollution due to anthropogenic sources are a huge threat to the future of our planet.[3,4] To limit CO_2 emissions, which are one of the main green house gases, the world has to become more carbon efficient.[4,5] The increase in carbon efficiency can be achieved by producing energy from renewable sources like wind, water, solar, and geo-thermal power. The renewable energy production is steadily gaining in the share of the global energy production.[1,6,7] Even though there have been significant advances in the reduction of CO_2 emissions per produced unit of energy, the rising demand for energy makes many countries struggle to reach their commitment.[8] Due to the need to cut greenhouse gas emissions, incentives have to be given by politicians, while scientists should find ways to increase the energy conversion efficiency. By increasing energy efficiency and by tapping into other renewable sources for energy production, the CO_2 greenhouse gas emissions can be decreased significantly.[9,10] Due to the urgency of the global warming problem most of the world leaders to agree on the reduction of greenhouse gas emissions, to the values below the emission levels of 1990.[7,10] The most important agreements are the Kyoto Protocol[7,10,11] or the Paris Climate Accord.[12] The Paris Climate Agreement is a commitment of all the signing countries to limit global warming to 1.5 °C.[4,12]

One possibility to achieve the goals of the Paris Climate Accord is to improve the efficiency of existing processes. A technology which is able to help improving the efficiency of all processes which produce heat is thermoelectrics. The thermoelectric effect was discovered by Thomas Johann Seebeck;[13] a detailed description of the effect can be found in section 2.2. Thermoelectric materials are energy converters, which can transform heat energy in temperature differences into electrical energy. Thermoelectric generators (TEGs) are solid state generators, which means they do not rely on any moving parts.[14,15] In addition, they are not only scalable from micro power generation in limited space applications to kilowatt power generation, but also completely noiseless, long term reliable and require low maintenance.[15] These generators are ideal to convert waste heat into electrical power. Besides, they are able to reverse the process and convert electrical energy directly into a temperature difference, by pumping heat from one side of the element to the other.[16] In this case, they are often called thermoelectric coolers (TECs) or Peltier elements. The many useful properties of thermoelectrics make them a worthwhile topic for research. In order to study thermoelectrics, measurement devices are necessary to investigate the properties of the thermoelectric materials. Currently, there are several commercial devices available, but they lack one or multiple properties, which are in high demand in research. Those requirements include the flexibility to measure multiple material types or to measure thin film materials with the chosen support, affordability, and ease of use. The challenges presented here led to the development of a custom built measurement device.

Availability of thermal waste energy Waste heat is found in most processes. Thermoelectric generators can tap into that potential and directly convert it into electricity. Automotive engines are good candidates for waste heat recovery. In diesel engines the hot gases can reach around 600 °C[17] and in petrol engines the temperatures of the hot gases can reach up to 700 °C.[18] Industrial power plants and factories can generate an enormous amount of thermal waste. For example, a combined cycle power plant with 500 MW needs around 50 MW of cooling.[19] Modern data centers have a huge problem with the thermal waste, since the power dissipation for processing units in data centers can reach 6,458–10,764 W/m^2.[20] Even though thermoelectricity is currently not capable of utilizing the heat from data centers due to the high cost and relatively low efficiency, waste heat from data centers is an excellent opportunity for the future of thermoelectric generators once they reach a ZT value of 3-4 or a price of around 5 $/W (for more information about the ZT value see page 18).[20] Electric engines also generate a considerable amount of heat, for example in a 150 kW motor about 7.5 kW of heat energy is dissipated by the stator and 3.5 kW by the rotor.[21]The applications are not limited to big scale power production. Small scale production is of particular interest in processes like human body waste heat recovery for wearable electronics.[22]

Economics of waste heat recovery A typical modern Panamax class[1] container ship is fitted with the main engine of over 30 MW.[23] Now even larger container ship sizes become common. Those post-panamax class ships have typical engine sizes of 54 MW.[24] For engines of this size the average fuel consumption is at approximately 190 g/kWh.[25] Assuming an efficiency

---

[1] The Panamax ship class is the largest ship size which is allowed through the Panama canal.

of 50 %[2], those engines produce between 15-27 MW of waste heat. A typical fuel consumption of a container ship is between 5.7 and 10.3 tons of fuel per hour. With a shipping route from Shanghai, China to Rotterdam, the Netherlands of 11,998 nautical miles (NM) (22,220.3 km) and a typical average speed of 24 knots (44.4 km/h),[26–28] it takes about 500 hours of travel or almost 21 days. This route is the typical China - Europe shipping route, for which each of the container ships consumes roughly 2,870 - 5,150 tons of oil. At a price of 517 \$/ton[3], each trip costs between 1,483,790 and 2,662,550 \$ in fuel alone. With these fuel costs, even a 1 % increase in fuel efficiency can save between roughly 14,800 and 26,600 \$ per trip. Medium size bulk carrier ships, which generate around 6.4 MW of waste heat energy have also a huge potential for thermoelectric energy recuperation.[29] Possible large financial savings are a strong motivation for the shipping industry to invest in new technologies, one of them could be thermoelectric generators.

Applications of thermoelectric generators There are countless possible applications for thermoelectric generators in the entire power scale from the nW range to the kW range.[30] Some of them are presented in fig. 1.1. In the nW range high resolution heat flux sensors,[31] in the μW range wristwatches[32,33] and pacemakers[34] and from 1 mW to 900 mW powering of remote wireless sensors[35] are possible applications. In the range starting at 1 W consumer electronics like smart phones,[36] wine coolers,[30] and cooling of sensitive electronics[37,38] are some of the possible uses. In the kW range large scale waste heat recovery in the transportation sector[15,39,40],

---

[2] https://www.wartsila.com/sustainability/environmental-responsibility/products-and-environmental-aspects/improving-efficiency, accessed at 23.07.2018

[3] Oil price at 18.07.2018 72.5 \$/barrel (0.14 tons) 517.86 \$/ton.

steel manufacuring,[41,42] and power plants[43,44] are applications with existing prototypes or even commercial products.

Prototypes for waste heat recovery systems have been developed for many applications like cars[39,40] or solar thermoelectric generators.[15] Bombardier filed a patent for diesel driven trains with thermoelectric waste heat recovery.[15] There is also potential for TEGs in micro-gas turbines as power co-generators.[44] Thermoelectric generators have been used for power generation in so called radioisotope thermoelectric generators (RTGs) for space exploration missions. These radioisotope thermoelectric generators range from the 50 mW to the kilowatt range.[45–47] Prime examples of those missions are Voyager[48], Cassini[49] and Curiosity.[15,47]

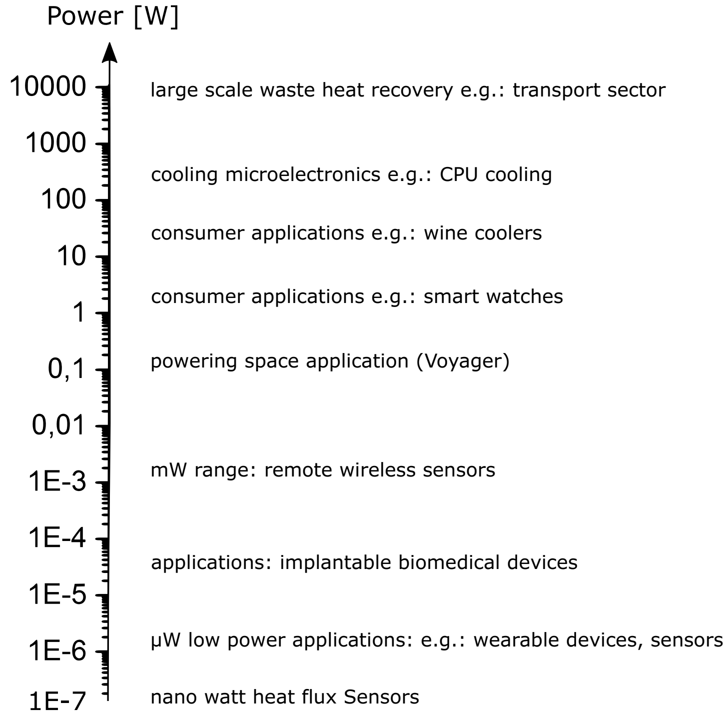

Figure 1.1 Possible applications for thermoelectrics ranging over eleven orders of magnitude.

Besides the use of primary energy production for remote power generation and deep space exploration, recuperation of thermal waste energy can boost energy conversion efficiency, which decreases the dependence on fossil fuel and thus reduces the emissions of CO_2 into the atmosphere.

Other applications of thermoelectric devices In addition to all the utilizations in the field of waste heat recovery and power generation, thermoelectric elements can be used as Peltier coolers.[50] Peltier coolers convert electrical energy into a temperature difference. There is a multitude of applications like polymerase chain reaction devices,[51] micro fluidic devices[51,52], valves without moving parts (which freeze the path to close it),[53] or precisely controllable coolers[54–56]. Thermoelectric devices can be employed as temperature sensors, the most widely employed of them is the k-type thermocouple.[57] In addition to all the different types of useful applications for TEGs and TECs, the world desperately needs improvements in energy efficiency where thermoelectrics might help, due to the enormous untapped potential of thermal waste energy. Furthermore, as shown above, with the exemplified calculation for container ships, there is a strong financial motivation for the development and investigation of thermoelectric generators. The numerous reasons mentioned above are the motivation for the research in the field of thermoelectric materials.

Motivation for this thesis Due to the lack of versatile measurement equipment in this field of thermoelectric materials, a major part of this work is focused on the development of a measurement device, which should be able to measure the Seebeck effect of multiple material systems. In contrast to most commercially available measurement setups, this device should be able to measure thin films on the substrate chosen by the experimenter.

One important goal for the development of the measurement setup is, that the device is easy to use. For many thin films it has been shown that the structure is highly dependent on the substrate.[58,59] The common method used by most commercial instruments involves the deposition of the thin film sample on a printed circuit board (PCB) which changes the sample significantly. In addition, this measurement device will be tested with various sample types like thin films, powders and pastes. The influence of the substrate on the thermal conductivity of a material carrier ensemble will be investigated in the section section 3.6 "Thermal Conductivity in Thin Films".

2 Theory

2.1 Electrical Conductivity in Solids

To investigate thermoelectric properties, a basic understanding of electrical conductivity in solids is necessary. Electrical conductivity describes the ability to let charge carriers pass through the body of the material. Charge carriers in solids are particles or quasi-particles which are free to move and carry a charge like electrons or holes. Electrical conductivity is measured in siemens. The inverse of the electrical conductivity is called the electrical resistance. In general, one divides materials into three types in the context of their electrical properties: insulators, semiconductors, and conductors. If the electrical conductivity is greater than $10^4\ \frac{S}{m}$, it is regarded a conductor. Anything in between of $10^{-8}\ \frac{S}{m}$ and $10^4\ \frac{S}{m}$ is called a semiconductor.[60,61] When two atoms form a molecule, their atomic orbitals combine and make a bonding orbital with low energy and an anti-bonding orbital with higher energy. The same principle holds when three or more atoms form a bond creating the same number of binding and anti-bonding orbitals (see fig. 2.1). The orbitals vary slightly in energy, and when many atoms are involved like in a solid macroscopic structure, it is not possible to distinguish between the individual orbitals. The energy difference becomes so small that they form non-discrete orbital energies. In this case, they are called energy

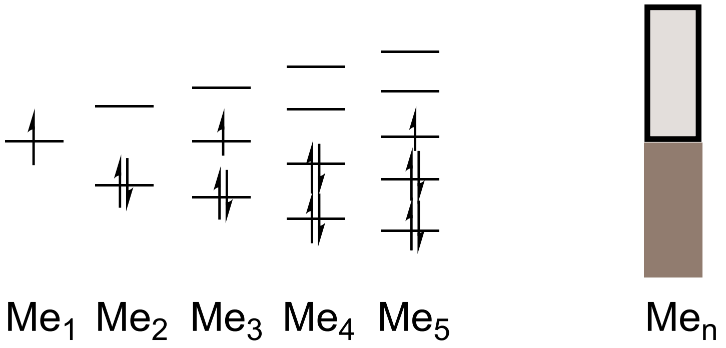

Figure 2.1 A combination of multiple metal atoms with a single s-electron (for example, Li) is shown. Each metal atom contributes one electron. With larger metal molecules, the distinction between the individual orbitals becomes smaller and smaller until they disappear entirely; at this point, they are considered energy bands. A band formed by occupied molecular orbitals is called a valence band, whereas a band formed by the unoccupied anti-binding orbitals is called a conduction band.

bands, where the binding orbitals form the valence band and energetically higher anti-bonding orbitals the conduction band.[61,62] The bandgap of the material can also characterize the difference between conductors, semiconductors, and insulators. If the bandgap is small enough for electrons to pass from the valence band to the conduction band by thermal excitation, the material is referred to as a semiconductor (fig. 2.2). In semiconductors, the electric conductivity can be achieved by the movement of electrons (n-type) or by the movement of electron holes (p-type). By doping the semiconductor with group V elements, the n-type conductivity is increased, while doping the semiconductor with group III elements, the p-type conductivity is increased.[61,62,64]

If the bandgap E_g of a material is greater than 4 eV, the material is considered an insulator. A material that has a bandgap between 4 and 1.5 eV is a semiconductor, which can be excited by visible light. Materials that have a bandgap between 1.5 and 0.1 eV are also semiconductors, but these semicon-

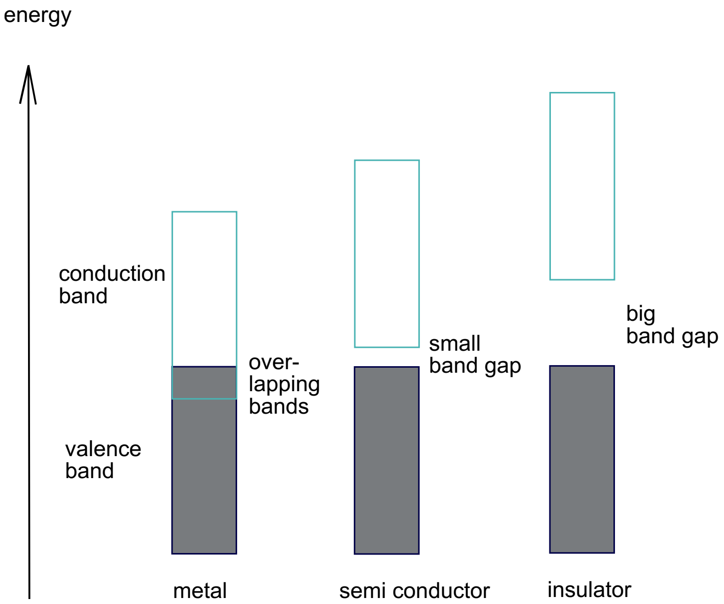

Figure 2.2 Schematic view of energy bands in metals where the conduction and valence band overlaps. For semiconductors that have a small bandgap, electrons can move from the valence band to the conduction band by, for example, thermal excitation. The right depiction shows an insulator where the bandgap is large, and thus, electrons can not move from the valence band to the conduction band.[63]

ductors can be excited thermally. Everything with a smaller bandgap than 0.1 eV or with overlapping bands is referred to as a conductor.[61] Another way to differentiate between semiconductors and conductors is the resistivity with changing temperatures. In conductors, the resistivity increases with increasing temperature. In contrast, in semiconductors, the resistivity decreases with increasing temperature.[65] Typical examples of conductors are metals like copper, silver, iron, and aluminum. The most common semiconductors are silicon (E_g = 1.09 eV[61]), gallium arsenide (E_g = 1.43 eV[61]), and germanium (E_g = 0.60 eV[61]). Some examples of insulators are diamonds (E_g = 5.2 eV[61]), most ceramics and glasses.

2.2 Seebeck Effect

2.2.1 Historical Overview

The Seebeck effect was named after Thomas Johann Seebeck, who discovered in 1821 that a closed loop of two dissimilar metals or metalloids affects the magnetic needle of a compass if a temperature difference is applied to that loop. He incorrectly concluded that it had to be a thermomagnetic effect.[13] His work was published in 1823. Due to his wrong conclusion that it was a thermomagnetic effect, he followed that line of thought and tried to explain the earth,s magnetic field due to the temperature difference between the poles and the equator. If he had known at the time that it was a thermoelectric effect and combined the first and last material in his list to a thermocouple, he could have created electricity with an efficiency of 3% in 1821, which was about the same efficiency that steam engines had at that time.[66]

Twelve years later, in 1834, Jean Charles Athanase Peltier passed currents through junctions of dissimilar metals and discovered a change in temperature.[67] Peltier did not find a link between his work and the earlier work of Seebeck. The correlation between the two effects was found 17 years later in 1851 by William Thomson (Lord Kelvin).[68] Not only did he find the link between the two discoveries, but he also predicted and later observed a third thermoelectric effect. The third thermoelectric effect causes conductors to change their thermal conductivity once a current passes through the conductor. The effect was named after him as the Thomson effect.[66,68] Gustav Magnus investigated several junctions of metals and found that the Seebeck potential does not correlate with the temperature distribution at the interface between the two metals.[69] This correlation is a strong indication that the Seebeck potential is a thermodynamic state function. This thermodynamic state function is the physical basis for a thermocouple used to measure temperature.[70]

Altenkirch developed a working theory of thermoelectricity in 1909 and 1911 and found, that for a good thermoelectric performance one needs a high Seebeck α coefficient and a high electrical conductivity σ with low thermal conductivity κ.[71,72] Interest began to rise after the Second World War when Telkes developed a generator in 1947 with an overall efficiency of around 5%.[66,73] With the development of a theory for thermoelectric semiconducting materials by Ioffe,[74] the development of modern Peltier elements, and thermoelectric generators got into motion. Ioffe introduced the figure of merit ZT by combining the three physical quantities Seebeck coefficient α, electrical conductivity σ, and thermal conductivity κ (see eq. (2.6)).[74,75] Julian H. Goldsmid has demonstrated that sub 0 °C cooling is possible with thermoelectric elements based on Bi_2Te_3. He achieved a 24 °C temperature difference with his bismuth telluride and bismuth experimental setup.[76] Besides, he was one of the first to apply quality factors for thermoelectric materials, like their high mobility and their high effective mass. With these quality factors, properly doped semiconductors could be manufactured, with excellent thermoelectric properties.[70] With the emergence of semiconductor thermoelectric materials and the increase in efficiency, first utilizations started to emerge in niche applications, where reliability is of utmost importance. Such areas of employment include for example coolers for optoelectronics and small refrigeration units or power generation in remote locations.[70,77] NASA started to use thermoelectric elements for power generation in deep-space exploration, particularly in missions going to Mars or beyond, where the light from the sun is not sufficient for significant power generation. As a heat source in their radioisotope thermoelectric generators (RTG), they utilize the radioactive decay of ^{238}Pu. The RTGs have been used in a variety of missions: Apollo, Cassini, Voyager, Pioneer, Viking, and Galileo.[70,78] Since thermoelectric generators have no moving parts, they are very reliable; the Voyager satellites operate for over 40 years (Voyager II: 20. August 1977[1] - 2018). The renewed interest in thermoelectrics can be attributed to Dresselhaus and Hicks who predicted in 1993 that low dimensional materials, especially nanomaterials, could drastically improve the figure of merit.[79–81] While some of the strategies to enhance thermoelectric materials proved to be ineffective, other strategies have lead researchers to develop new and sophisticated materials with improved thermoelectric properties.[82–85] In 2012, Cornett and Rabin showed that the power factor is more dependent on the modification of scattering rates than on the quantization of energy states.[86] An example of a more recent work has improved the thermal conductivity of PbSe by the introduction of vacancies to introduce dislocations in grains. These structural changes lowered the thermal conductivity significantly (to 0.4 $\mathrm{Wm^{-1}K^{-1}}$) and thus improved the figure of merit ZT (to 1.6 at 900 K).[87] The figure of merit is proportional to efficiency and is explained in the next section.

2.2.2 Theoretical Basics

To get a better understanding of thermoelectricity, we have to consider that the resistance is not only a ballistic process but also a diffusive process. For this purpose, the electron conductance function G(E) (see Eqn. 2.1)[88] for a resistor is defined as a function regarding the density of states D(E) and

---

[1] https://www.jpl.nasa.gov/missions/voyager-2/ access date: 06.02.2018

the time t(E) that an electron spends inside the resistor. The electric charge is denoted as q.

$$G(E) = \frac{q^2 D(E)}{2t(E)} \tag{2.1}$$

In this simplified concept an electron loses no energy through Joule heating inside the resistor but on the contacts of that resistor. Equation 2.1 shows that the conductance is proportional to the availability of states (D) and the ease with which electrons can flow through them (the inverse transfer time (1/t)).[88]

$$f_1 = \left(e^{\frac{E-\mu_1}{kT_1}} + 1\right)^{-1} \tag{2.2}$$

$$f_2 = \left(e^{\frac{E-\mu_2}{kT_2}} + 1\right)^{-1} \tag{2.3}$$

The difference in chemical potentials (μ) typically drives the difference in the Fermi functions. An example for this would be an electrochemical reaction. In the case of thermoelectricity, the difference in temperature (T_1 and T_2) causes the difference in the Fermi functions (f_1 and f_2 see eq. (2.2) and eq. (2.3)).[89] The approach is referred to as the Landauer approach and can be summarized as: Gradients in chemical potential (μ) change the local occupation, leading to diffusion of charge.[90] Since in n-type and p-type semiconductors, the density of states functions have opposing forms (see fig 2.3), the electron conductance G(E) increases with increasing energy for n-type semiconductors. Thus with n-type conductance states with E $>$ μ control the conductance. In contrast to n-type semiconductors in p-type semiconductors, the conductance G(E) decreases with increasing energy. Because of this, states with E $<$ μ are responsible for the conductance.[90] This means for p-type conductance the term $\frac{E-\mu}{kT}$ in eq. (2.2) will be almost 0 and the entire function f will be close to 1. Due to this, electrons flow

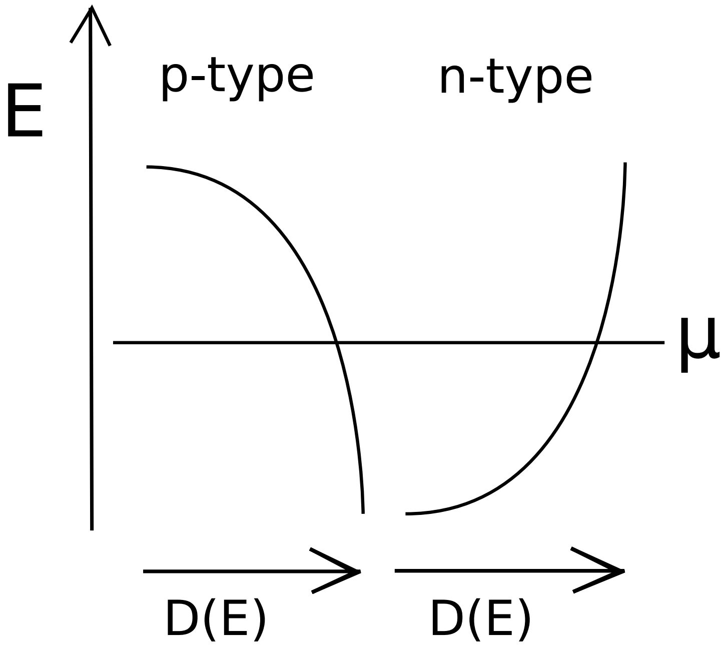

Figure 2.3 The graph schematically shows the density of states for p-type and n-type semiconductors and the corresponding energy. The chemical potential or fermi energy has been marked in the graphs.

from cold to hot inside a p-type channel, but from hot to cold in an n-type channel.[90]

The Seebeck potential refers to the potential which arises from a temperature difference under open circuit conditions. This voltage consists of three different parts (see eq. (2.4).[91]

$$\alpha = \alpha_\Phi + \alpha_d + \alpha_{Ph} \tag{2.4}$$

Where α is the Seebeck coefficient, α_Φ is the work function difference between the contact and the thermoelectric material. The term α_d is the diffusion current[91] and α_{Ph} the phonon term of (Eqn. 2.4) resulting from the charge drag created by phonons streaming from the hot part of the material to the cold part.[92] The phonon drag current is only relevant at low temperatures.[91,92] The term α_Φ might be relevant, but the influence on the total Seebeck coefficient is small. There are studies which contribute some of the improvement to the better phonon term of the Seebeck coefficient.[93] While α_Φ is discussed in relation to thermionic applications; the details are still under investigation.[91] Since α_d is, under normal circumstances, the dominating term,[91] α and α_d are considered equivalent for this work.

A simpler explanation compared to the Landauer approach for the Seebeck effect is that it is an effect of thermal diffusion. Charge carriers in a warmer region of a conductor have a higher average absolute velocity than those in the cooler areas of the conductor. This difference in velocity causes the electrons to flow to the colder regions of the metal. The thermodiffusion potential is in the first approximation directly proportional to the temperature difference (Eqn. 2.5).[94,95] In the equation 2.5 U_{Td} represents the Thermodiffusion potential and ΔT the temperature difference.

$$U_{Td} = \alpha \cdot \Delta T \tag{2.5}$$

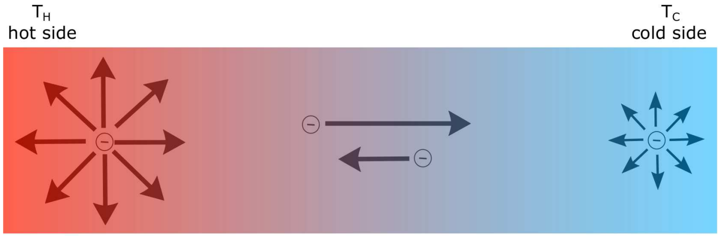

Figure 2.4 Schematic explanation of the Seebeck effect by thermal diffusion of charge carriers.

In this classical explanation charge carriers, electrons in n-type semiconductors or conductors and electron holes in p-type semiconductors, in the warmer region of the conducting material have a higher velocity than those in the colder area. An electron (or an electron-hole) which moves with high velocity from a hot region to a colder region cools down. The lower temperature of the charge carrier causes the movement in the opposite direction to be slower. This accumulation of charge carriers on one side is the cause of the resulting electric potential (see fig. 2.4).[94,96] Thus the material has to be a good electrical conductor to allow the electrons (or holes) to move with ease. Low thermal conductivity is an essential property of the material. The low thermal conductivity is necessary to keep the thermal gradient as high as possible. Ioffe combined the three material properties - the Seebeck coefficient, the electrical conductivity and the thermal conductivity - into the dimensionless figure of merit ZT (see eq. (2.6)). The figure of merit can be used to describe the efficiency of a thermoelectric material.[74,91]

$$ZT = \frac{\alpha^2 \cdot \sigma}{\kappa} \cdot T \tag{2.6}$$

In eq. (2.6) ZT is the figure of merit, α is the Seebeck coefficient, σ electrical conductivity, κ thermal conductivity and T the average temperature between the hot and cold end. The thermal conductivity is the sum of the lattice and the carrier thermal conductivity.[91,97] The maximum efficiency of a device η_{max} is dependent on the figure of merit ZT, this relation is described in eq. (2.7).[74] T_{Hot} refers to the temperature of the hot side of the generator and T_{Cold} to the cold side.

$$\eta_{\text{max}} = \frac{T_{\text{Hot}} - T_{\text{Cold}}}{T_{\text{Hot}}} \frac{\sqrt{1 + ZT} - 1}{\sqrt{1 + ZT} + \frac{T_{\text{Cold}}}{T_{\text{Hot}}}} \tag{2.7}$$

Thermoelectric materials can also be utilized to create temperature differences. In this case they are referred to as Peltier elements. The Peltier

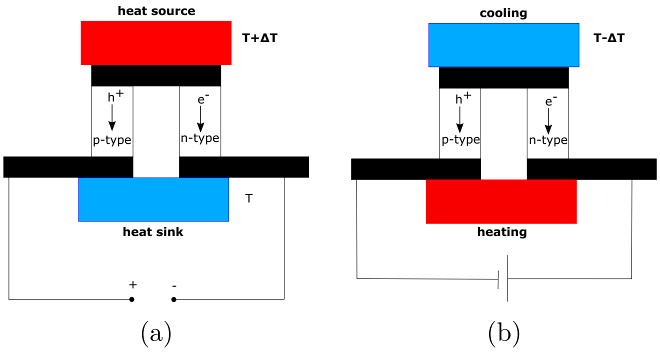

Figure 2.5 Schematic representation of a single thermoelectric junction. In (a), a thermoelectric generator is shown, which is placed between a heat source and a heat sink generating electric energy. In (b), a Peltier element is shown, which is connected to a DC power source, creating a temperature difference. The black bars are connectors between the p-type and n-type legs. Commercial devices contain a multitude of these junctions, typically 127 junctions for a medium-sized element.

effect is the opposing effect, where moving charge carriers also transport heat. The heat flow Q is proportional to the electrical current flow I, see eq. (2.8).[98]

$$Q = \Pi I \tag{2.8}$$

$$S = \Pi T \tag{2.9}$$

The Peltier and the Seebeck coefficient are related through the Kelvin relation, see eq. (2.9).[98] In eq. (2.9) T represents the absolute temperature, S the Seebeck coefficient and Π the Peltier coefficient.[98] In simple terms a current, which passes through a single junction of a Peltier cooler from the n-type to the p-type, causes the dominant charge carriers to move away from the junction. The moving charge carriers pump the heat from this junction away.[99] A schematic representation of a single junction for a thermoelectric generator and a Peltier element can be seen in fig. 2.5. For commercial devices these junctions are connected in series to create a thermoelectric or Peltier elements. Common elements like the 40 by 40 mm TEC1-12706 contain 127 of these junctions.

2.3 Atomic Force Microscopy

Atomic force microscopy AFM is a measurement technique, which uses the repulsion forces of atoms to map the surface of a sample material. Binning and Rohrer developed this technique in 1982.[100] With this technique, it is possible to plot the surface topography with a high resolution in the low nanometer scale. A fine tip facing the surface of the material is positioned at the end of a flat spring (called cantilever). The cantilever vibrates over the top of the surface of the sample and is scanning the entire measurement area in a line pattern. The repulsive forces between the tip and the sample surface can be registered by the changing vibration of the cantilever. The force varies according to the distance between atoms on the surface and the measurement tip on the cantilever. The vibration amplitude increases when the repulsive force gets stronger. A laser beam, which reflects of the other side of the cantilever and hits a sensor, for example, a photo-diode or a photo-diode array is used for recording the amplitude and frequency (see fig. 2.6).[101–103] With modern AFM it is even possible to rearrange atoms and molecules.[104]

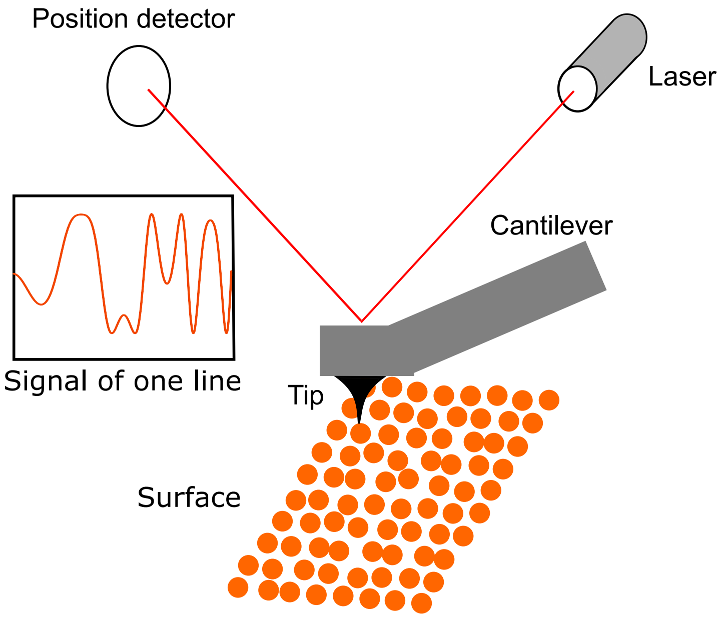

Figure 2.6 A schematic view of an atomic force microscope. The cantilever (gray) with the attached tip vibrates over the sample surface. The tip (black) is reflected by the atomic forces of the atoms (orange circles) on the surface of the sample. The change in amplitude is measured by a diode detector which is hit by a laser beam (red) reflected from the surface of the cantilever. The signal of each line is recorded and stitched into a 2d surface plot.

2.4 X-Ray Based Experiments

2.4.1 X-Ray Sources

X-rays were discovered by Wilhelm Conrad Röntgen in 1895. For the discovery of the X-rays he was awarded the first Nobel Prize in physics in 1901.[105,106] Today X-rays are an important tool in everyday analytics ranging from medicine to chemistry and material science. For the laboratory experiments with the Fischerscope XDV-SDD a Rh and a W X-ray tube were used. X-ray tubes provide a broad X-ray spectrum called bremsstrahlung.[107,108] Bremsstrahlung is created when the impulse of an electron is changed, which results in an emission of electromagnetic radiation. The change of the impulse in X-ray tubes is caused by the impact of the electrons into the solid anode. The anode is often water-cooled and is usually made of a pure metal like copper, tungsten or rhodium.[105,109] The continuous X-ray spectrum emitted from such an X-ray tube also contains the characteristic emission lines of the anode material like K_α and K_β. Due to these emission lines a copper X-ray tube can interfere in the detection of copper. A sketch of an X-ray tube is shown in fig. 2.7.

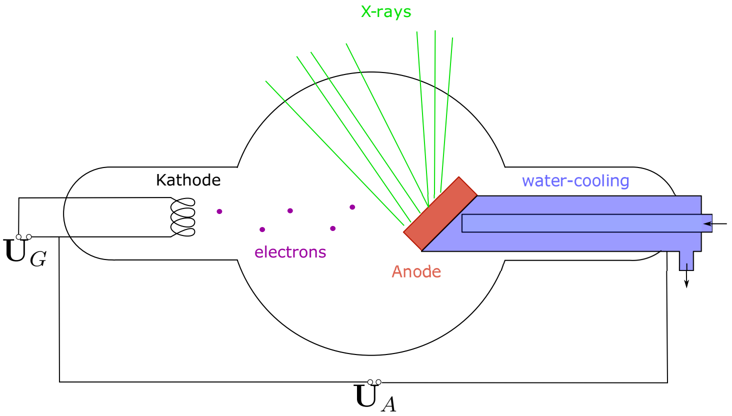

Figure 2.7 A sketch of an X-ray tube. U_G is the voltage applied to the cathode in order to make it glow and emit electrons. U_A is the high voltage, which accelerates the electron. This voltage usually ranges from ten to 100 kV. When the electrons hit the anode, their change in impulse causes the emission of X-rays. The anode is water-cooled. The entire tube is made of glass and contains a vacuum.

For the near edge X-ray adsorption fine structure (NEXAFS) and grazing incidence X-ray fluorescence (GIXRF) experiments the monochromatic X-rays of the BESSY II synchrotron have been used. The electron storage ring has a diameter of 240 m and a magnetic field of 7 T. The electrons have an energy of 1.7 GeV.[110] During normal operation, the BESSY II synchrotron storage ring has an electron current of 200 mA.[111] The 200 mA of electron current can provide a photon flux between $6 \cdot 10^9$ photons/s at 1.7 keV and $6 \cdot 10^{11}$ photons/s at 400 eV.[112,113] Light provided by a synchrotron is highly brilliant.[114,115] The brilliance of X-ray light combines several aspects which determine the quality of the light. The quality depends on the number of photons emitted per second, the beam collimation, the source area and the energy distribution of the X-ray light. The beam collimation is a measure for how much the beam spreads out and is usually given in milliradians in horizontal and vertical direction. The source area is important because it determines the focusability and thus the imaging resolution. The convention for the energy distribution is defined as a fixed relative energy bandwidth (BW). This bandwidth has been set to 0.1%.[116] All these parameters have been combined into one formula for the brilliance, see eq. (2.10).

$$brilliance = \frac{photons/second}{(mrad)^2(mm^2 sourcearea)(0.1\% BW)} \tag{2.10}$$

To summarize, the brilliance determines how many photons of given direction and wavelength can be focused onto a spot in a unit of time.

For experiments with soft X-rays between 78 eV to 1870 eV[113,117] at the BESSY II the PTB beamline with the plane-grating monochromator (PGM) has been used. For experiments with intermediate X-rays between 1.75 and 10.5 keV,[118,119] the PTB beamline with the four-crystal monochromator has been used. This beamline is called KMC[2] beamline. Experiments in the hard X-ray region between 6 and 80 keV[120,121] have been performed at the BAM beamline, with either a double layer or a double crystal monochromator.

These three beamlines are described later in detail (see page 77). In this section the general setup of such a beamline at a synchrotron is described.

A synchrotron consists of a booster, where the electrons or other charged particles are accelerated to relativistic speeds. The magnetic field in the

---

[2] Kristall Monochromator

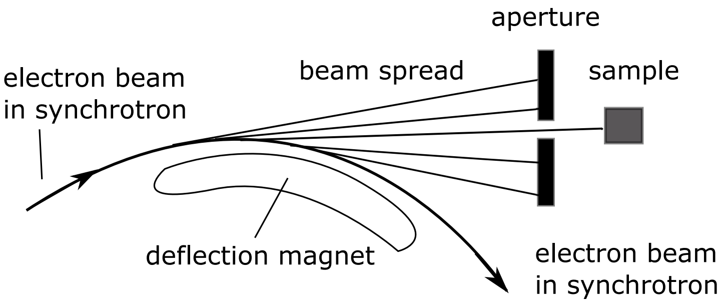

Figure 2.8 Horizontal beam spread of synchrotron radiation while passing a deflection magnet.

booster ring is increased synchronously to reach these speeds. This synchronous increase of the magnetic field is the origin of the name Synchrotron. Once the charged particles reach the desired speed (close to the speed of light), they are injected into the outer storage ring, where they are kept at a quasi-circular path.[122]

Since electric charged particles which are accelerated or subjected to a force generate electromagnetic radiation,[122] there are various ways to generate radiation from the fast moving charged particles, for example by changing their path with a magnetic field. The electrons from the synchrotron are deflected with magnets to keep them in a quasi circular path. The deflection in the curves is the place where synchrotron radiation is emitted.[123] These deflection magnets give a broad horizontal spread of the synchrotron radiation see fig. 2.8.[124] Only a small amount of synchrotron radiation deflected by the deflection magnet can be used, due to the wide horizontal spread. The unused radiation has to be blocked by an aperture. The deflection magnets are now mostly used in traditional or older synchrotron facilities. Today most synchrotron radiation sources use so-called insertion devices which do not influence the optics of the synchrotron. Due to the non-changing optical properties insertion devices can be inserted later

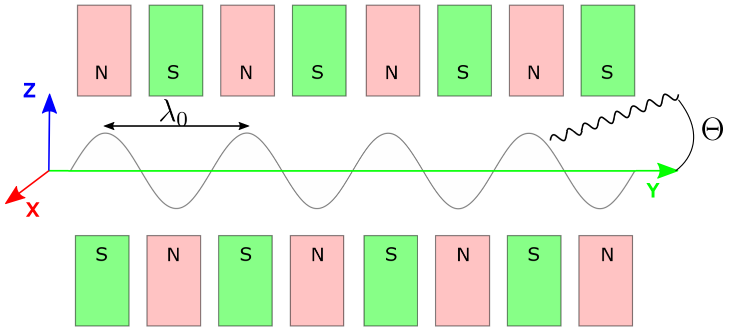

Figure 2.9 A sketch of an undulator that causes the electron beam in an electron accelerator to oscillate. Through the oscillation at high-velocity electromagnetic radiation is emitted.

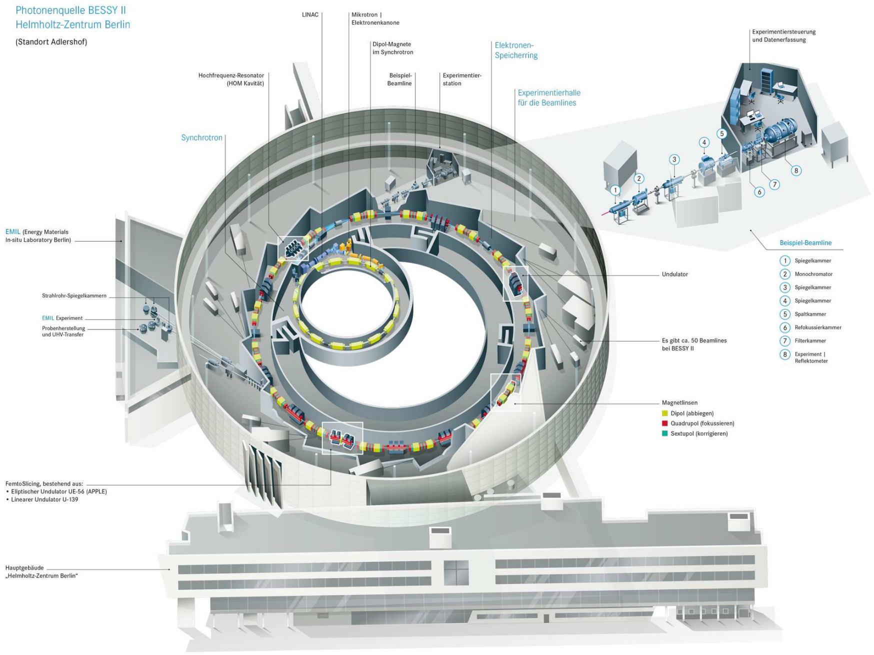

Figure 2.10 Schematic overview of the synchrotron BESSY II. Image obtained with permission from Helmholtz-Zentrum Berlin.[3]

into the synchrotron.[123] A common insertion device is a so-called undulator

---

[3] Helmholtz-Zentrum Berlin made by Ela Strickert, `https://www.helmholtz-berlin.de/quellen/bessy/wie-funktioniert-bessy_de.html`, access date: 16.04.2019.

or wiggler. In an undulator an alternating magnetic dipole field forces the electrons to oscillate while passing the undulator in a sinusoidal motion.[123] At high electron speeds this oscillation causes the electrons to emit electromagnetic radiation. A sketch of an undulator is depicted in fig. 2.9. A general overview of the BESSY II Synchrotron is depicted in fig. 2.10

2.4.2 X-Ray Fluorescence

In X-ray spectroscopy electrons of atoms are excited by X-rays. The incoming X-rays excite inner shell electrons. The created electron vacancy is filled by electrons falling from higher shells. When electrons fall from a higher energy state (higher shell) to a lower energy state (lower shell), they lose energy. The loss of energy happens by the emission of a photon (see fig. 2.11). These emitted photons are called fluorescence photons. The fluorescence lines, which are detected after inner-shell electrons have been ionized are characteristic for the element they were emitted from and can thus be used for the identification of elements.[125,126]

2.4.3 Angle Dependence of X-Ray Measurements

In an X-ray measurement, the incident X-ray beam of an X-ray source always has the same absorption length in any given material. By varying the angle of the incident beam, it is possible to achieve different penetration depths, due to the constant absorption length. The penetration depth is defined as the distance from the surface to the deepest point of the incident X-ray beam perpendicular to the surface. A schematic explanation for this is depicted in fig. 2.12.

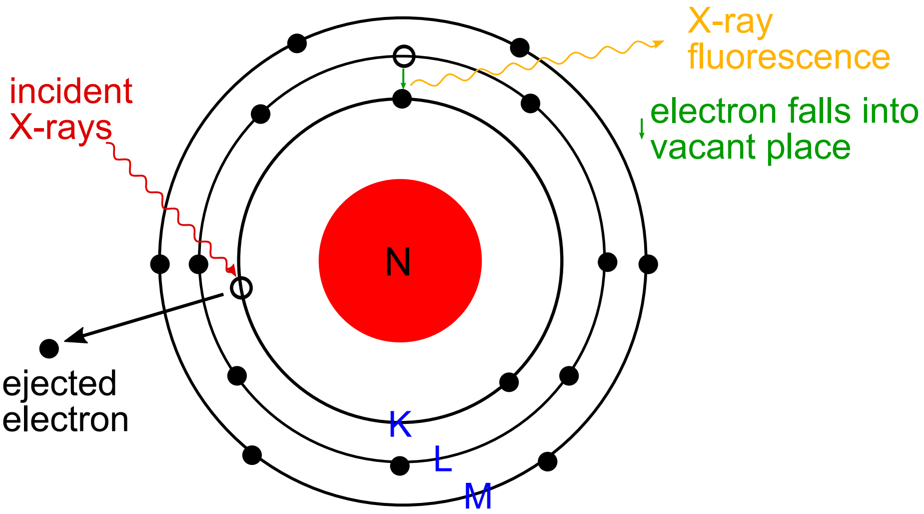

Figure 2.11 Schematic view of an atom with orbiting electrons excited by X-rays and emitting fluorescence photons. Incident X-rays eject an electron from an inner electron shell. The created electron vacancy is filled by an outer shell electron. The difference in energy between the outer and inner shell orbit is emitted as a fluorescence photon. Shells are marked by convention with the letters K, L and M corresponding to their principal quantum numbers 1, 2 and 3.

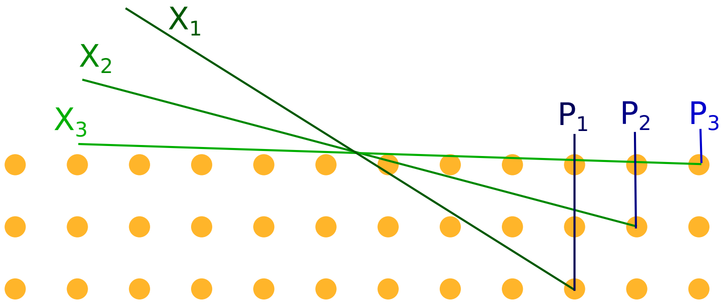

Figure 2.12 A schematic view of the X-ray beams at different angles and their penetration depth. The X-rays are marked in different shades of green (X_1 - X_3). The penetration depth is depicted in different shades of blue (P_1 - P_3).

These angle dependent measurements are well suited to use for depth dependent analyses of the composition. The techniques which work close to the angle of total reflection are called grazing incidence X-ray fluorescence (GIXRF) and grazing emission X-ray fluorescence(GEXRF).[125,127]

2.4.4 Near Edge X-Ray Adsorption Fine Structure

Near edge X-ray adsorption fine structure (NEXAFS) is a synchrotron radiation based technique, which analysis the transitions of electrons from the K-shell to higher energy states like molecular orbitals of bonds within the molecule or with neighbors like the surface atoms of a substrate.[122] The K-shell is the core shell of an atom (see fig. 2.11). The technique has been developed in the 1980 with the goal to investigate single atoms bonded to a surface.[122] The technique was intended mainly for light atoms like carbon, nitrogen, oxygen and fluorine.[122,128] Since the 1980s, the technique has been applied to many materials, heavier atoms, and molecules.[122]

2.4.5 X-Ray Photo Emission Spectroscopy

X-ray photo emission spectroscopy (XPS), sometimes called photoelectron spectroscopy (PES), is a well established and powerful measurement technique for solid surfaces, bulk material interfaces, and gases, in ultra high vacuum chambers.[129,130] With XPS it is possible to determine the elemental composition, the oxidation state of elements, and the electronic structure of the sample in the surface region. The XPS analysis procedure works by focusing monochromatic high energy photons onto the sample surface. These incident photons have an energy of hν and cause the emission of photoelectrons emitted from every element on the sample surface. With this method, core and valence electrons emitted to the vacuum level can be detected. The penetration depth of the photons depends on their energy. For metals, the usual penetration depth of X-rays is 1-10 μm. The photoelectrons which are emitted from the sample can scatter, recombine, be trapped, excite other sample atoms or be absorbed. This loss of photoelectrons emitted from the bulk is one of the strength of XPS, because it makes the technique surface sensitive. The escape depth is typically only in the region of 1 to 2 nm and is related to the inelastic mean free path (IMFP) of the electron.[130–132]

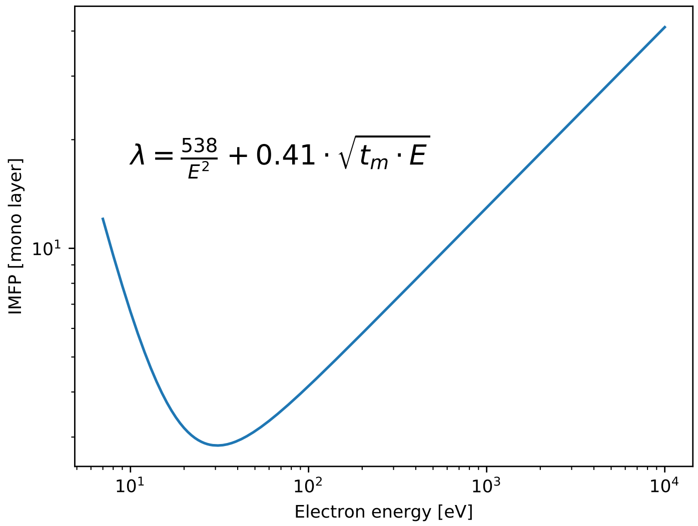

Figure 2.13 Inelastic mean free path in monolayers for electrons against the electron energy. Equation taken from Seah and Dench[133].

The IMFP of the electron is plotted schematically in fig. 2.13. The function for the graph (fig. 2.13) was determined by M. P. Seah and W. A. Dench.[133] A schematic representation of an XPS measurement can be found in fig. 2.14.

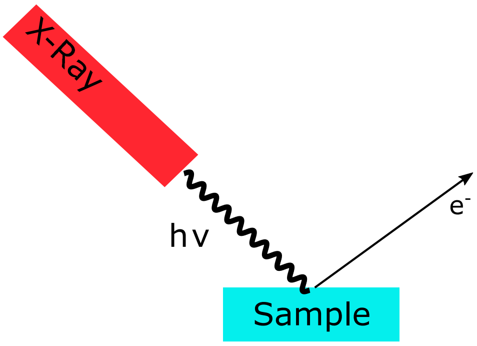

Figure 2.14 A schematic view of an XPS experiment. Incident X-rays cause core and valence electrons to be emitted.

2.4.6 Powder X-Ray Diffraction

Powder X-ray diffraction (XRD) was invented over 100 years ago independently in Germany by Paul Scherrer and Peter W. Debye[134] in the University of Göttingen and in the United States by Albert W. Hull[135] at the General Electric Company. Since then it has become one of the most widely used methods in science and technology to characterize materials.[136,137]

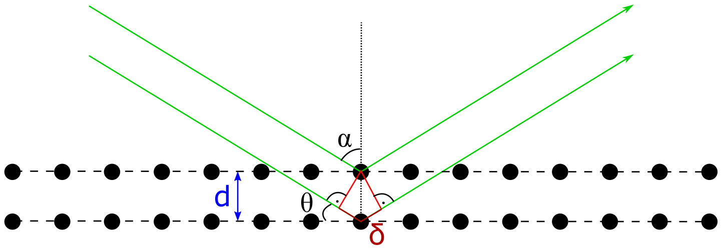

Figure 2.15 Schematic view of constructive interference during X-ray diffraction. The green lines represent the incoming and refracted X-rays. The blue distance d is the distance between lattice planes. δ is the difference in the length of the upper and lower X-ray beam represented in dark red. α is the incidence angle and θ, which is $90° - \alpha$ is called the Bragg angle.

In X-ray diffractometry X-rays are directed onto the sample. The intensity of the diffracted X-rays is measured. When X-rays hit a substance the electrons of the atoms of the material are excited and vibrate. These electrons emit electromagnetic radiation of the same frequency as the exciting radiation. When the X-rays interact with the lattice, the X-rays are diffracted in discrete directions. Constructive interference between X-rays happens if the difference in travel between two X-rays (δ see fig. 2.15) is an integer multiple of the wavelength. Due to destructive interferences of scattered X-rays the others are eliminated. This constructive interference is described by the equation $2\delta = n\lambda$. Where n is the order of diffraction and λ the wavelength of the X-rays. With the definition of the sine and the geometry from fig. 2.15 the following equation can be obtained: δ = 2d sin(θ). By putting the last equation for delta in the first equation, the equation for the maximum intensity of positive interference is obtained (eq. (2.11)). This equation is called the Bragg equation,[138] where n is the order of diffraction, λ is the wave length, d is the distance between atomic layers and θ is the incident angle of primary X-rays.

$$n\lambda = 2d\sin(\theta) \tag{2.11}$$

Monochromatic X-rays can only be reflected from a crystal in one defined angle (see. eq. (2.11)). This angle is called the diffraction angle. These X-ray diffraction lines are like fingerprints for the substances. By comparing those diffraction patterns with other diffraction patterns of known substances (which are stored in databases) it is possible to identify crystalline samples unambiguously. Since amorphous substances do not give clear reflexes but diffuse scattering, it is possible to identify whether a substance is amorphous or crystalline, with this technique.[138] In powdered samples the crystals are arranged in a random pattern. The right orientation of some crystals is thus obvious, due to the large number of crystallites. Observing a powdered sample with a volume of 1 mm^3, and the average particle size is 10 μm, this sample would have about 1 million crystals. In such a sample only 100-200 crystals would have the right orientation for X-ray diffractometry. This small number of aligned crystals causes a large standard deviation. The standard deviation caused by the orientation statistic of the crystals can be greatly reduced (more than halved) by rotating the sample.[139] For the measurement of thin films the incident angle can be reduced, thus increasing the volume of the thin film, which is analyzed. This technique is often called grazing incidence X-ray diffraction. In summary X-ray diffraction is a versatile technique which is widely used to identify solid sample powders with the help of diffraction databases. In addition the technique is able to provide information about thin inorganic films if the incidence angle is decreased.

2.5 Sputter Coating

Sputter coating or sputter deposition is a process that is considered a physical vapor deposition (PVD) technique. The first record of the sputtering process is from 1852 by W. R. Grove.[140] It can be utilized for small scale lab experiments and scaled up to industrial large-area production. Sputter coating is used on an industrial scale, for example, for solar selective coatings in photovoltaics or transparent heat-regulating coatings for energy cost-reducing windows.[141,142] Other applications for thin films deposited by sputter coating are low friction coatings and wear-resistant coatings. With thin films deposited by sputter coating, it is possible to improve the corrosion resistance and to coat materials with films with specially designed

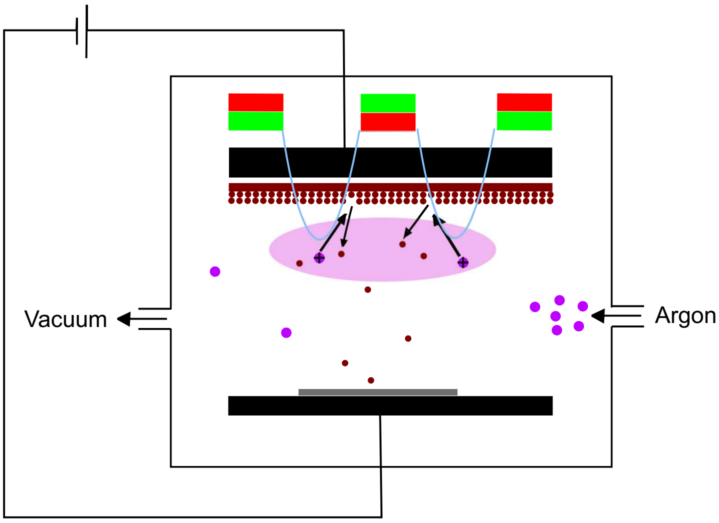

Figure 2.16 A schematic view of a magnetron sputter coater, while the device is switched on. The two magnets (red/ green) - one ring-shaped and a disc-shaped - pull the argon ions (violet with a plus sign) along the magnetic field lines (light blue) towards the surface of a metal target (brown). Through the bombardment of the metal, metal atoms are separated from the surface and move across the vacuum chamber. The metal atoms eventually condense, on surfaces adjacent to the target, like the sample (gray) or the vacuum chamber walls. The argon plasma is depicted with a light violet color. The plasma ignites with an applied DC voltage of -500 V.

optical and electrical properties.[143] Occasionally, even a combination of the properties is created through the sputtering process like the transparent and conductive indium tin oxide. In the conventional sputtering process, a metal target located at the cathode of a glow discharge plasma generator is bombarded by plasma ions inside a vacuum container. Ions knock out atoms from the surface of the target, which are now able to move through the vacuum chamber and condense onto a surface in the proximity. With this conventional technique, the deposition rate of the target material onto the sample surface is low. With the help of a static magnetic field below the cathode, it is possible to constrain, concentrate, and shape the plasma next to the target. This process is now called a magnetron sputter coating process and has higher deposition rates. Two permanent magnets usually generate the magnetic field. A ring-shaped magnet is used for the outer pole, and a permanent disc magnet is used for the other pole in the center hole of the ring magnet (see fig. 2.16). The higher plasma density and the proximity of the plasma increase the chance of high energetic ions hitting the target, which is the reason for the higher deposition rates of the target atoms onto the sample surface.[143,144]

3 Results and Discussion

3.1 Development of a Computer Controlled Seebeck Measurement Device

Devices to measure Seebeck coefficients are commercially available, but have several drawbacks. First of all, they are very specific to a material class like bulk materials or thin films. Secondly, most of the available thin film devices work by depositing the thin film on a commercial sample holder, which is typically a printed circuit board (PCB). The holder of a thin film thermoelectric material has a great influence on the thermal conductivity of the final device, which has been proven by FEM simulations in section 3.6.[145] Such a setup is not the ideal way to measure real samples. Thirdly, there are no known measurement devices which can measure thin films powders and pastes, without special sample preparation. For powders, the standard procedure is to compact them with techniques like spark sintering or hot pressing. Typically these measurement instruments sell for around 50 000 - 100 000 € and are specific to one type of sample.

For all the mentioned reasons, a first proof of principle prototype to measure Seebeck coefficients has been developed in our group which can measure Seebeck coefficients independently from the used sample holder. The only requirements for thin films is that the sample holder has to be flat and electrically insulating to prevent a short-circuit.

At the beginning of this thesis, a prototype has been developed, which was complicated to use for untrained graduate and postgraduate students. The prototype has been improved from a proof of principle device, which required several days of training and in-depth knowledge of the working mechanism of the measurement device, to a device, which could be handled by undergraduate students with a short 5 to 10 minute introduction. Besides the usability, several significant improvements to the instrument have been made: First of all, the reliability has been improved. Secondly, the algorithm which is responsible for the temperature stability has been changed completely, which provides stable temperatures with an accuracy of up to ±0.0625 °C at 40 °C (see fig. 3.1), which is the practical limit of the used temperature sensor at 12-bit resolution. Thirdly, the usability has been improved from the original console based program, which required commands which had to be memorized to a graphical user interface with real time graphs displaying the data and automatic saving of measurement data. The data is saved with a unique name containing the date time and the sample name provided by the user. This program has been used in practical lab courses for students with as little as 10 minutes of introduction to the entire device. A schematic view of the measurement setup can be found in fig. 3.2. The usability was tested by a survey which all the students participating in the lab course had to take (see section 3.1.7 on page 48). The complete code of the graphical user interface can be found in the appendix listing 7.4 on page 194.

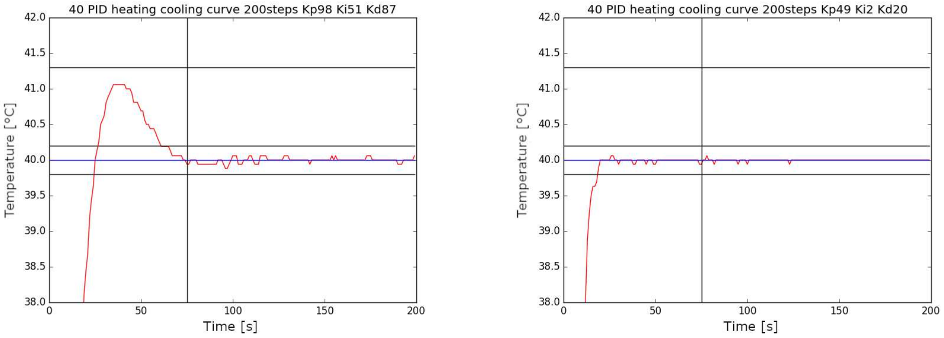

(a) (b)

Figure 3.1 In figure (a) and (b) one tuned heating curve for the PID controller in the measurement is shown. The red line shows the measured temperature, the blue horizontal line the set point. The black lines are visual guides to quickly identify curves, which fulfill the requirements. The horizontal lines from top to bottom represent the maximal acceptable overshoot (1.3 °C), maximum acceptable oscillation around set point (±0.2 °C). The vertical black line represents the acceptable time for reaching the set point. Fig. (a) shows one of the best results for the air-cooled version of the measurement device. Fig. (b) shows one of the best results for the water-cooled version of the measurement device.

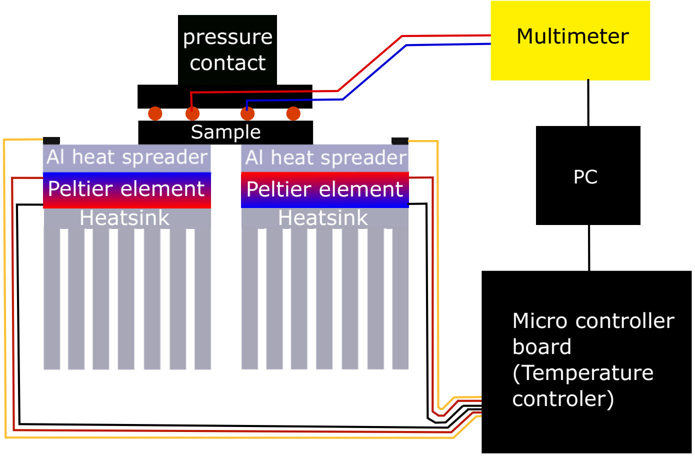

Figure 3.2 A schematic overview of the measurement setup, which consists of two Peltier elements, two temperature sensors, and a Fluke 283 multimeter.

3.1.1 Working Principle

The measurement device consists of many parts divided into hardware, software, and firmware. In order to give a general overview of the working principle, the parts are briefly introduced, and their function is described. Each digital device based on a microcontroller has a low-level control software, which is directly on the microcontroller, this software is called firmware. This measurement device consists of a Fluke 283 multimeter which has a firmware provided by the manufacturer. This firmware is responsible for the measurements, the display, and the communication with the computer. The temperature controller is based on an ATmega328P microcontroller. On the flash memory of this controller is the firmware, which controls and records the temperature and communicates with the PC. A personal computer (PC) is running the software for the setup. This software consists of two drivers and the main software. For both of the hardware devices, matching drivers have been written. These drivers are responsible for sending and receiving commands from the firmware over the USB port. The communication between driver and firmware is done via serial communication. The main software combines all the received data and provides a graphical user interface for more comfortable use. A schematic overview can be found in fig. 3.3.

3.1.2 Fluke 289 Driver

The Fluke 289 multimeter has been bought and was not modified. This multimeter can communicate with the computer over the universal serial bus (USB). The driver for the multimeter has been programmed in the

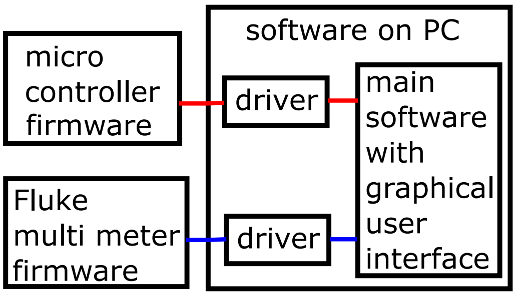

Figure 3.3 A schematic overview of the different parts of the measurement setup is shown. The red lines symbolize data communication between the temperature controller via the driver to the main software. The blue lines symbolize the communication between the Fluke 283 multimeter via the driver to the main software.

programming language python. The complete source code can be found in listing 7.2 in the appendix on page 182.

This driver has been tested with two different Fluke 289 multimeters, the program contains the serial numbers of those two multimeters and recognizes them automatically. Once the serial connection is established (listing 7.2 lines 9-36), the driver can send the command to return a reading from the multimeter and returns that in an appropriate format (listing 7.2 lines 44-64) to another program using this driver. The driver closes the serial communication once the driver object is released, allowing other programs to communicate with the Fluke (listing 7.2 lines 37-42). The last lines of this driver are solely for testing purposes: if the driver is executed on its own, the program connects to the Fluke multimeter and returns 20 readings (listing 7.2 lines 66-71). In lines 1-3 of the program, the necessary libraries are included.

3.1.3 Firmware and Hardware

A program running on a microcontroller itself is called firmware. The electronics used in this setup have a number of different purposes. The five most important are:

1. Control the power provided to two Peltier elements
2. Switch the current direction for the Peltier elements
3. Read at least two temperature sensors
4. Control the temperature of each of the Peltier elements
5. Communicate with a PC running a measurement program with the corresponding driver

One of the most popular 8-bit low-cost microcontrollers is the Atmel ATmega328P. This microcontroller has sufficient input/output(IO) capabilities. Besides, it can communicate over serial communication and can provide six PWM signals, which are explained later. The Arduino Uno microcontroller development board provides the fundamental circuit to run such a microcontroller with power regulation, quartz oscillator, and a chip to make easy access over USB possible. This development board also gives easy access to all the IO pins of the microcontroller. Since this board is readily available, open-source, and can be bought commercially for less than 10 €, the Arduino Uno has been chosen as the basis for this project. In fig. 3.4 a schematic view of the Arduino Uno development board with the used connections is depicted. Controlling the power to a Peltier element can be done by using a metal-oxide-semiconductor field-effect transistor MOSFET. This field-effect transistor can be switched quickly. By varying the time, such

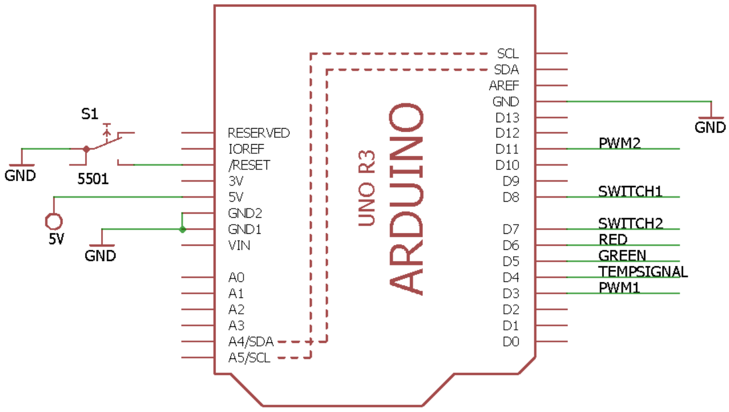

Figure 3.4 Atmel ATmega328P on arduino development board and the connections to hardware on the Peltier Temperature Control Shield. All connections and the switch are on the shield. The image was created with Eagle 7.5.0 Light.

a MOSFET is switched on and off resulting in a floating average, which corresponds to an analog regulation. This is called pulse width modulation (PWM). Switching the current direction for the Peltier elements can be done by using two bistable relays in front of the outlets for the Peltier elements. The electronic schematic is presented in fig. 3.5. The temperature

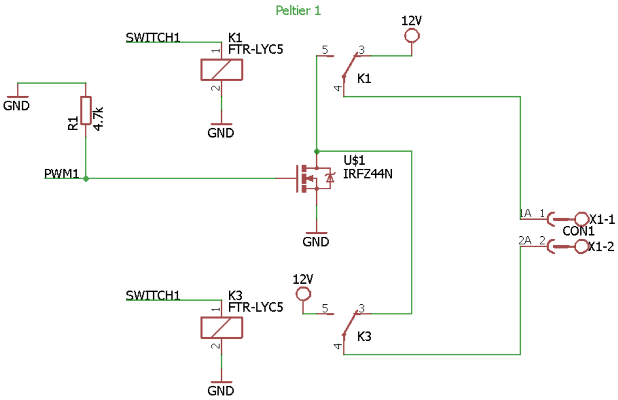

Figure 3.5 Schematic of the control circuit for the first Peltier element, terminated at screw terminals. The image was created with Eagle 7.5.0 Light.

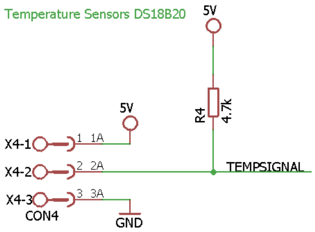

Figure 3.6 Schematic for connecting one or more Maxim Integrated Products, Inc. DS18B20 temperature sensors to an Atmel microcontroller. The image was created with Eagle 7.5.0 Light.

sensors used for this device are the MAXIM DS18B20 since they are very precise with a programmable resolution from 9 bits (0.5 °C at one measurement every 93.75 ms) to 12 bits (0.0625 °C at one measurement every 750 ms). Thus, the frequency of measurements can be traded for temperature resolution. The DS18B20 have three main advantages which make them suitable for this application: Firstly, the temperature sensors have good accuracy (±0.5 °C). Secondly, they are easy to read with an ATMEL microcontroller. Thirdly, the DS18B20 have a suitable temperature range from -10 °C to 85 °C.[146] By preselecting the sensors before integrating them into the device, the mismatch in their accuracy can be minimized. The sensors have been connected to the microcontroller like depicted in fig. 3.6. The complete schematic of the created Peltier Temperature Control Shield can be found in fig. 7.1 in the appendix on page 209. Besides, in the appendix on page 210 in table 7.1 the bill of materials used for the construction of one measurement device can be found. To control the temperature with a closed-loop, one needs to be able to change the power provided to the heater or cooler, read the temperature of it, and adjust the power output accordingly. The most straightforward type of controller is a proportional controller. In a proportional controller, the output is changed proportionally to the deviation from the desired value. This type of controller has one significant drawback since if the error is zero, the output is also zero. Thus a good proportional controller can never reach and maintain the desired value. By adding an integral controller to the proportional controller, the set-point can be reached. The integral controller changes its output according to the time and distance from the desired value. The combination of a proportional and an integral controller is called a PI controller. PI controller can reach and maintain the desired value. PI controllers tend to take a long time to reach a set value, and they tend to overshoot and oscillate around that value for quite some time. By adding a derivative controller, the response time can be lowered. Besides, the added derivative controller minimizes the problem of overshooting the target. These controllers are called PID controllers. The output of each of the three parts of the controller has to be tuned for each application. The tuning is done by one constant for each of the parts of the PID. The constants are named K_p, K_i, and K_d. During this work, over 1400 tuning curves have been recorded, and the best results have been used for the measurement device. A brief description of the tuning can be found later in this chapter on page 45. The communication between the microcontroller and the PC is done through the USB port via serial communication. The firmware has been programmed in the programming language C. A schematic overview of the different parts of the firmware can be found in fig. 3.7.

3.1.4 Serial Communication

The firmware has to communicate with the software on the PC over a serial communication line, which is implemented via USB (see fig. 3.7). The microcontroller sends and receives data, and the computer sends and receives

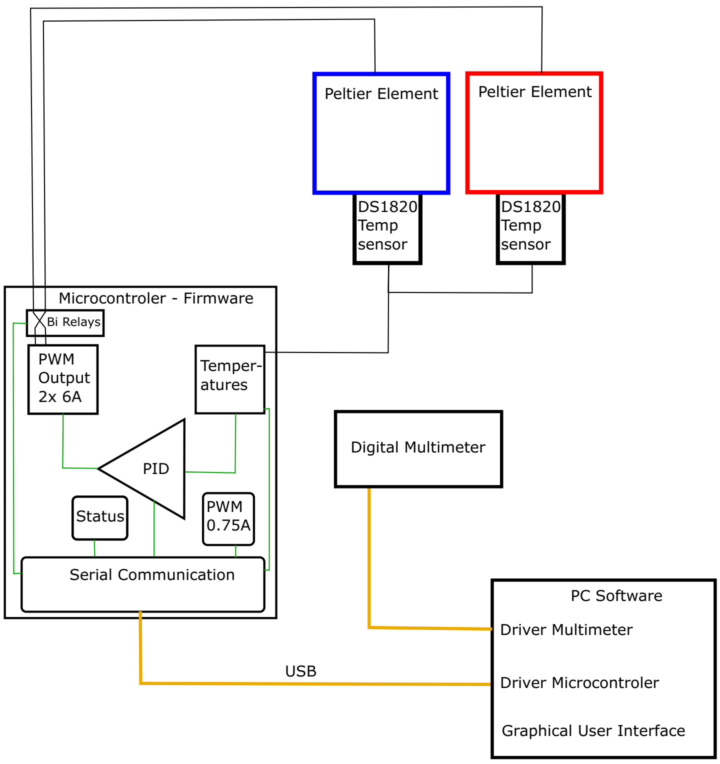

Figure 3.7 Schematic overview of the microcontroller firmware installed on the Atmel ATmega328P. This firmware reads the temperature of two or more Maxim DS18B20 temperature sensors. It has three PWMs to control the current of two Peltier elements and a fan or waterpump, and a PID controller to control the temperatures of the Peltier elements. It communicates the with the PC over USB with a serial communication protocoll.

data as well. Multiple problems arise from this type of communication. First of all, data might get lost since a device either listens or sends data. Since the communication is relatively slow compared to the clock speed of the microcontroller or the computer CPU, the program might be several steps ahead before it receives an instruction or is finished sending data. There are two basic approaches to this problem. In the first approach, each device can send data as soon as it is available, and the other device listens all the time. With this event-driven approach, there is an enormous potential for communication collisions and collisions between the running program and the instructions sent. In the second strategy, one of the devices is listening for instructions and responds to the instruction. A simple example of this call and response approach is the following example: The microcontroller reads the temperature all the time, but only sends the current value once it is requested to send it. With this reduced amount of data sent over the slow serial communication, the load on the bottleneck of the serial communication is drastically reduced. Because of the problem of collisions with the first approach, the second approach has been chosen.

The reduced load on the bottleneck of the serial communication is critical because of the enormous difference in speed. The microcontroller operates at 16 MHz and thus can process 16 million instructions per second. Typical serial communication speeds are between 9600 bps and 112500 bps; bps stands for bits per second. Any character like a letter or a symbol is coded with an 8-bit code. Thus between 1200 - 14062 characters can be sent per second, which is approximately 2 - 3 orders of magnitude slower than the processing speed of the microcontroller. To further decrease the load instructions are sent as single letters plus parameters. During tests of the measurement device, there were quite a few problems with incomplete serial messages. Because of this problem, it was decided to standardize the messages. Each message starts with a unique character (‘ <,) and ends with a unique character (‘ >,). This way, only complete instructions are handled, which eliminated all of the communication errors.

3.1.5 Tuning of the PID Controller

Each PID controller consists of three parts: the proportional, the integral, and the derivative controller. Their constants set the influence of each part on the total controller. k_P is the constant for the proportional part, k_I the constant for the integral control part, and k_D is the constant for the derivative part. These values have to be determined for each application of a PID controller. There are several ways to get some starting values for the constants. The most prominent is the Ziegler-Nichols method.[147] In this method, a proportional controller is changed until it oscillates. From this oscillating curve, the period of the oscillation is determined. This period is called the ultimate period (P_U). The gain used to get the oscillation is called the ultimate gain (K_U). With these values, initial guesses for k_P, k_I, and k_D can be made. For k_P the initial guess is $K_U/1.7$, k_I is $P_U/2$, and k_D is $P_U/8$. There are other methods like the Cohen-Coon method, which can provide initial guesses. From these initial values, the PID constants have to be tuned manually. The results the constants have on the system are summarized in table 3.1.

Table 3.1 Influence of k_P, k_I, and k_D on the response of the controlled system.[148]

Parameter	Rise time	Overshoot	Settling time	Steady-state error	Stability
k_P	Decrease	Increase	Minor	Decrease	Degrade
k_i	Decrease	Increase	Increase	Eliminate	Degrade
k_D	Minor	Decrease	Decrease	No effect	Improve

From the initial guess provided by the Ziegler-Nichols method, the constants were systematically changed around those starting values. As a setpoint for the tests, 40 °C was chosen. The initial goals of ± 0.2 °C temperature variation, a maximum overshoot of 1.3 °C, and a maximum settling time of 75 s were defined, to determine when the PID is good. By testing over 1000 parameter combinations for the air- and the water-cooled setups, the goals were reached, and even better results were obtained. The response curves for the best PID constants for the air- and water-cooled setup are shown in fig. 3.6 on page 42. A few selected response curves recorded during the tuning process are shown in fig. 7.4 in the appendix on page 223.

3.1.6 Comparison Between a Commercially Available Measurement Device and the Developed Device.

A sample of TiO_2 doped with 5 % Nb with a thickness of 77 nm has been measured six times, to test the developed Seebeck measurement device. The OUT e.V. prepared the TiO_2 sample. The annealing was done in a vacuum IR furnace at 450 °C for 5 min. The same sample has also been measured with a commercially available device for comparison of the results. After compensating for the fact that the developed device measures against copper, which has a Seebeck coefficient of 2 μV/K[149] at the measurement temperature, the error was estimated by the error of the DS18B20 temperature sensors, the error of the Fluke multimeter and the statistical deviation between measurements, this results in an error of ± 6%. This error should only be seen as an estimate for the error of the device since there are sources for additional contribution to the error, which are neglected. These neglected sources are, for example, the position of the temperature sensors and the thermal contacts. The position of the temperature sensors would be ideally directly on the sample. Since this would potentially damage the sample and the temperature difference between the sample and the surface of the high thermal mass of the aluminum heat spreader would be small, this difference can be neglected in a first approximation after thermal stability has been reached. After adding the 2 μVK^{-1} of the copper contacts to the measured

Seebeck coefficient, the resulting measurement gives a Seebeck coefficient of -68 ± 4 μVK^{-1}.

The same sample has been measured with a commercial Netzsch SBA458 Nemesis (an image of the device is presented in fig. 7.19 in the appendix on page 237). The instrument has been chosen because it was one of the few which does not require thin films to be prepared on a special PCB. This selection was made to make the results more comparable. The commercial measurement setup gave a value of 65 ± 2 μVK^{-1}, so the results from the commercial setup and the low-cost setup match. In an international round robin test of top laboratories the results differed by 5% and 9% in Seebeck measurements.[150] Other measurement devices used in literature show uncertainties between 5.5% and 13%.[151–153] Considering the results from the round-robin tests and the other published uncertainties, the results shown here have an excellent match.

3.1.7 Usability of the Seebeck Potential Measurement Device

The ease of use was one of the priorities during the development process of the software for the Seebeck measurement device. During one of the lab courses of advanced physical chemistry, students with a bachelor‘ s degree in chemistry had to use the device to measure the Seebeck coefficient of multiple samples. At the end of the lab course, all students were required to fill out a survey. In the survey, they were asked to rate the usability of the device and its software. The students were asked if they agree with ten statements. With the numbers 1 to 10, where ten means "I agree completely" and one means, "I do not agree at all". Each student was given a short introduction, which consisted of a demonstration measurement with

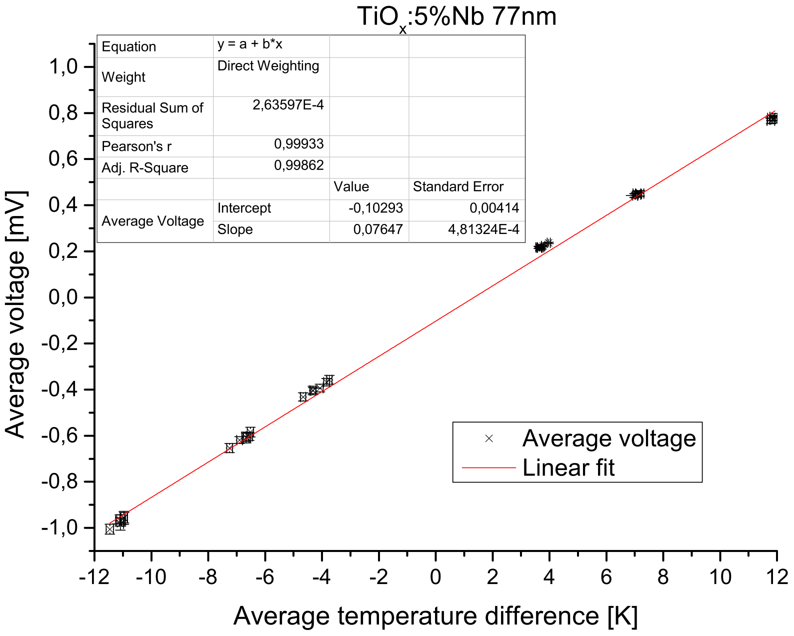

Figure 3.8 Seebeck measurement for sample T975a ((TiOx) with 5 % Nb doping 77 nm tempered in IR vacuum furnace at 450 °C for 300 s). The measurement has been performed six times. Each measurement point is an average of 20 measurement values.

instructions. After the introduction, they were supposed to do nine measurements by themselves and could ask for help at any time. As a tool for the survey, the free online service www.umfrageonline.com was used. There were 21 participants in this survey. In general, the 21 students, who used the device with its software, agreed on all statements with almost total agreement values (see fig. 3.9). Some of the students gave constructive criticism about what could be improved in order to make the program even easier to use. The main suggestion was to add an additional clue to when a measurement is finished. An audio signal was implemented as an additional clue to signalize the end of each measurement. The complete code of the graphical user interface can be found in the appendix listing 7.4 on page

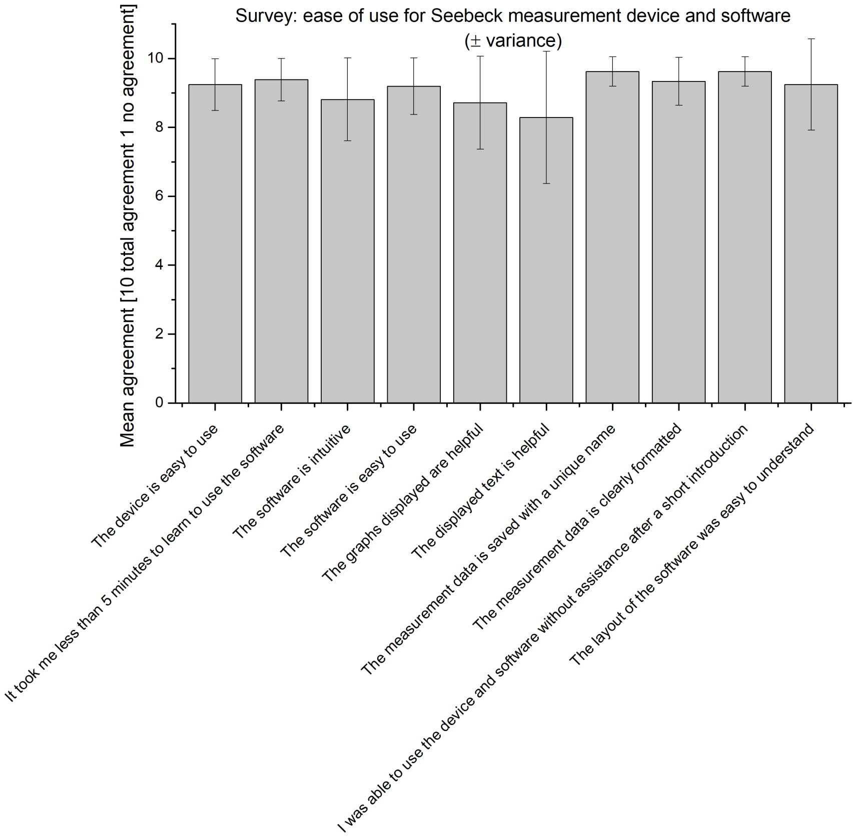

Figure 3.9 Statements about the usability of the Seebeck measurement device rated by students who used the device in 2018 during the advanced physical chemistry lab course. Ten means a complete agreement while one means they do not agree at all. These averaged results are based on the 21 participants in the lab course.

194. Additional information on the survey and the comments can be found in the appendix in section 7.1.7 on page 211.

3.1.8 Summary

During this thesis, a measurement device has been developed, which has been running stable and reliable in routine laboratory use for more than three years. The current iterations of this device are employed in our laboratory in Germany (three devices), and a research group employs two devices at the Madurai Kamaraj University in India. These devices were brought to the Indian group through a DAAD-DST collaboration program (grant number: DST/INT/FRG/DAAD/P-29/2017). The software was improved to be run by undergraduate students with minimal prior instructions. The results from the survey in section 3.1.7 show that the students had no problem to operate and understand the device and software. The results from comparing measurements with a commercial device in section 3.1.6 show that this setup can produce measurements that are in agreement with those produced by commercial measurement setups. The device has several advantages compared to the commercially available devices:

1. Ability to work with chosen substrates
2. Ability to measure thin films, powders and pastes
3. Complete control over software, firmware and hardware
4. Low price
5. Ease of use

3.2 Properties of Thin Film Thermoelectrics

In this section, the key features and the performance of the measurement setup, which was described in the previous section, will be used. For most of the measurements, thin film samples were chosen. Those samples are characterized in depth by multiple analytical methods. In addition, other possible sample systems will be measured. In the end, a theoretical discussion about thermal conductivity in thin films is presented in section "FEM Simulations of Thermal Conductivity in Thin Films" on page 109. The results are supported by finite element method (FEM) simulations.

3.2.1 Synthesis of Copper Oxide Thermoelectric Films

In this section, the primary sample system and its synthesis are described. In addition, the sample shape is calculated theoretically and measured. Lastly, the adherence of the thin film to the substrate is tested, which is essential for sample handling. As the main sample system copper oxides were chosen, since they have a high Seebeck coefficient, are relatively easy to prepare, and are stable under ambient conditions.

The sputtering process was used to copper, copper oxides, doped copper, and doped copper oxide films. A Cressington 108 Auto sputter coater has been used to produce all films. As a substrate soda-lime silicate glass slides (Menzel Glass) have been chosen for most samples. Some selected samples have been prepared on silicon(111) wafers pieces. The glass carriers were thoroughly cleaned for 20 min in Piranha Solution (3 parts of H_2SO_4 to 1 part of H_2O_2 by volume). Prior to the sample preparation with a new target, the target has been cleaned. The cleaning was done by sputtering for a duration of 100 s on waste substrates. As processing gas for sputtering pure metals, Alphagaz TM 1 Ar from Air Liquide has been used. The argon contains less than 3.0 ppm H_2O, less than 2.0 ppm O_2 and less than 0.5 ppm Hydrocarbons (C_nH_m). For the direct sputtering of copper oxides, CARGAL 4 (8 ± 0.8 O_2, the remaining percentage being argon) has been used as a processing gas. Aluminum masks have been used, which expose a 14 by 14 mm square with rounded corners in the center of the glass slide, to ensure the reproducibility of the sample geometry. After the preparation of the sample, gold contacts have been sputtered onto the sample. For this purpose, a second mask has been used, which exposes two rectangles 10 mm apart from each other for the deposition of gold contacts. The preparation procedure is summarized in fig. 3.10. The technical drawings of the masks can be found in the appendix on page 221 , see fig. 7.2.

To improve the electrical conductivity of the copper oxide samples, copper has been co-sputtered with various other metals. For the experiments, copper targets have been drilled with an even distribution of holes with 1 mm diameter. The drilling was performed by a computer numeric controlled (CNC) gantry mill. The holes expose between 2.5% and 10% of the total area of the target. The exposed area has been calculated using the area of the target and the area of the drilled holes. In fig. 3.11 an example of the hole pattern is shown. In fig. 7.3 in the appendix on page 222 all drill patterns are presented. For the sputtering, the special copper target has been stacked with the target used for doping. The target stack was inserted into the sputter coater. Fig. 3.12 shows a sketch of the procedure. For the experiments performed in this work, the copper was co-sputtered with gold, gold/palladium(80/20), silver, and silicon.

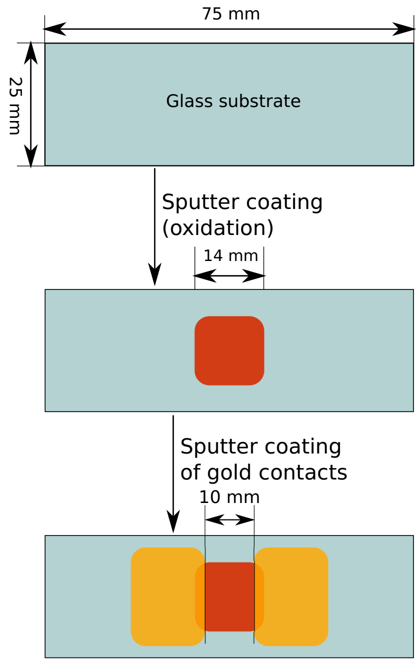

Figure 3.10 Preparation method for thin film copper oxide samples. The glass slide is coated with either copper or copper oxides through sputter coating or reactive sputter coating with the help of an aluminum mask. Then, the sample is oxidized or tempered. Following the tempering process, gold contacts are coated on the sample with the help of a second aluminum mask. The contacts overlap 2 mm with the sample and are 10 mm apart.

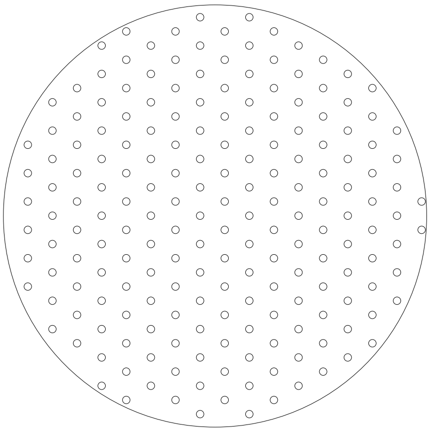

Figure 3.11 Drill pattern of copper target exposing 6.25% of a second target in a stack.

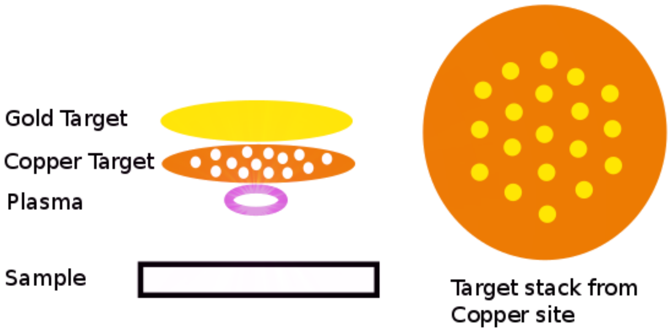

Figure 3.12 Schematic representation of the doping procedure used. A copper target is drilled with an even distribution of 1 mm holes, according to the desired amount of dopant. A stack of the drilled target and the dopant target are co-sputtered.

3.2.2 Adhesion Tests of Copper Oxide Thin Films

The good adherence of the copper films has been proven by the scotch test (DIN EN ISO 2409) in a previous work.[145] It was found in this work that copper oxides adhere to the glass similarly to copper or even better. The tests were done according to DIN EN ISO 2409:2013.[154] Six parallel cuts into the thin copper oxide films were made with a 1 mm spacing. Additionally, six parallel cuts were made perpendicular to the first cuts. The cuts have been made on a computer numeric controlled (CNC) gantry milling machine with a carbide drag engraver to ensure repeatability. The angle of the tungsten carbide engraving bit is 60 degrees. The force of the engraver applied onto the sample was measured, by moving the engraver on top of a scale and moving the engraver the same distance down as on the sample.[1] The engraver was pushed down with a force of 20.5 N. The g-code[2] for the engraving is provided in the appendix on page 214. The film was

---

[1] The engraver is fixed in a holder, which has a magnetic "spring". The force the engraver applies to the surface increases, after touching, when the holder is lowered.

[2] CNC machines are controlled with a programming language called g-code.

brushed with a soft brush diagonally to the cuts, four times in each diagonal direction. A piece of adhesive tape (Tesa brand) was pressed firmly on the cuts. It was removed in one quick pull approximately with a 60 degrees angle.

A sample image of one of the tests is shown in fig. 3.13 with optical microscopy and secondary electron microscopy. The films were scored by the tungsten carbide engraving bit as expected. The copper oxide thin films show no visible delamination. Most of the samples show a lot of glue residue. If the samples are cleaned with ethanol, most of the glue can be scrubbed off with a gentle brush. In the appendix, a sample is shown before and after washing (see fig. 7.5 on page 224). A close-up electron microscopy image (fig. 7.6) can be found in the appendix on page 224. Even in the close-up, no edges of the squares were damaged during the test. Thus, the samples have the highest adhesion level (ISO GT0).

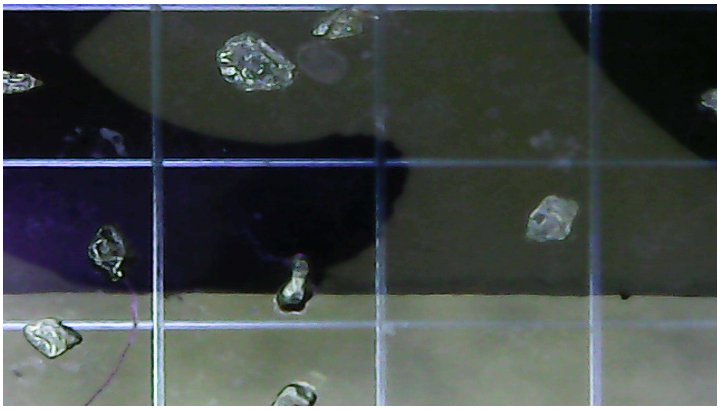

(a)

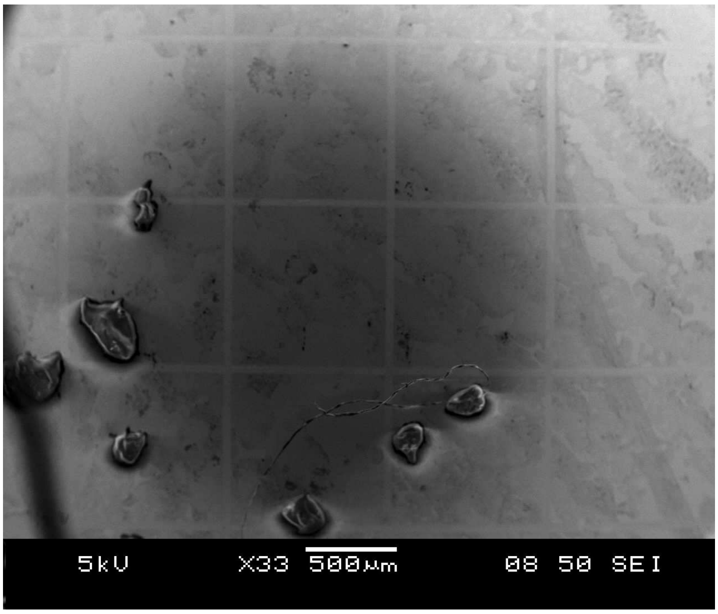

(b)

Figure 3.13 One of the samples tested for the adhesion with the procedure specified in DIN EN ISO 2409:2013. The straight lines in the film were scored with a tungsten carbide engraver on a CNC gantry machine. Images of sample 203a recorded via (a) optical microscopy and (b) secondary electron microscopy. Fig (a) shows an image of sample 203a taken with an optical microscope. Both images show no visible damage to the squares.

3.2.3 Thickness and Shape of Copper Oxide Thin Films

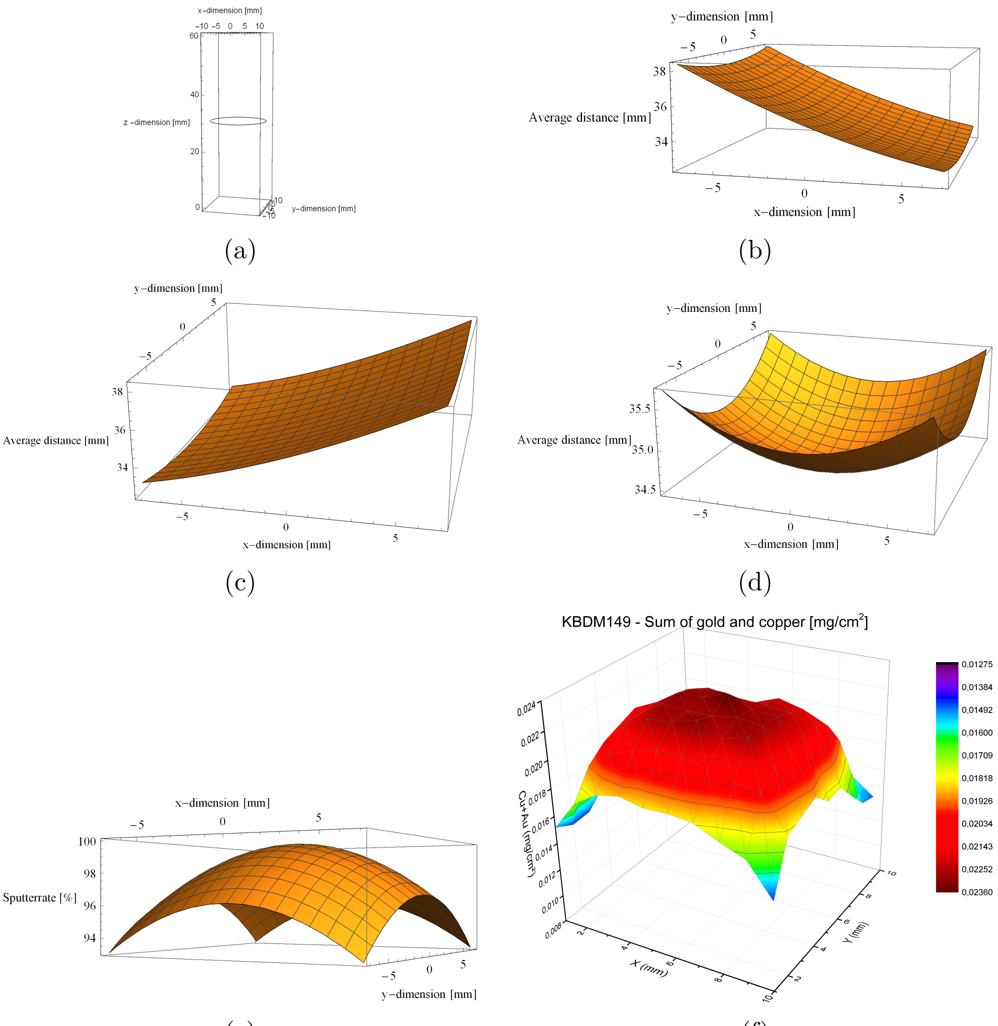

(a) (b) (c) (d) (e) (f)

Figure 3.14 Intersection of plasma torus and sputter target (Circle (r=10 mm)) with 30 mm distance from sample (a). Plotted distance from source to sample (b). Plotted distance after rotation of sample by 180 degrees to the source (c). Average time-dependent distance between spots on the sample to the sputter source (d). Predicted relative film thickness of sputtered film (e). In (f) a 3d plot of the mass per unit area measured with a Fischerscope X-ray XDV-SDD XRF spectrometer is shown. The prediction and measurement is in good agreement. The drop in mass at the edge of the sample can be explained by the mask. The XRF measurements are presented in section 3.2.5.

The sputtering process has been modeled in Mathematica, to predict the homogeneity of the film thickness. For this purpose, the assumption that the amount of deposited metal is solely determined by the distance from the location of the sample to the source has been made. The plasma created by the magnetron sputter-coater has the shape of a torus, with an approximate mean diameter of 10 mm. This plasma is located directly below the metal target. Thus, the source of the metal atoms which are knocked out of the metal surface can be approximated by a ring (see figure 3.14 (a)). The sample is located 30 mm below the source and 14 mm off-center. The off-center location is necessary because the mask is made for the preparation of two samples (see fig. 7.2 on page 221). In figure 3.14 (b) the distance between each point on the sample and each point on the ring is plotted. The sample is turned around its center by 180 degrees after half of the sputtering time, to reduce the gradient on the sample. Figure 3.14 (c) depicts the average distance of each point after turning, which is the mirror image of figure 3.14 (b).

By adding those two distance plots and dividing by 2, one gets a plot of the average time-dependent distance (see figure 3.14 (d)). The spot with the lowest average time-dependent distance to the source is the middle point. By calculating the distance between the center point and each point on the sample and normalizing the average distance between the sample and the source, a sputter pattern can be predicted (see figure 3.14 (e)). The complete calculation of the plots shown here can be found in the appendix on page 216. In figure 3.14 (f), a plot of the cumulative mass per unit area of gold and copper is shown. This plot has been measured with a Fischerscope XDV-SDD X-ray fluorescence spectrometer. Details of the measurements can be found in section 3.2.5. The prediction and the measurement are in good

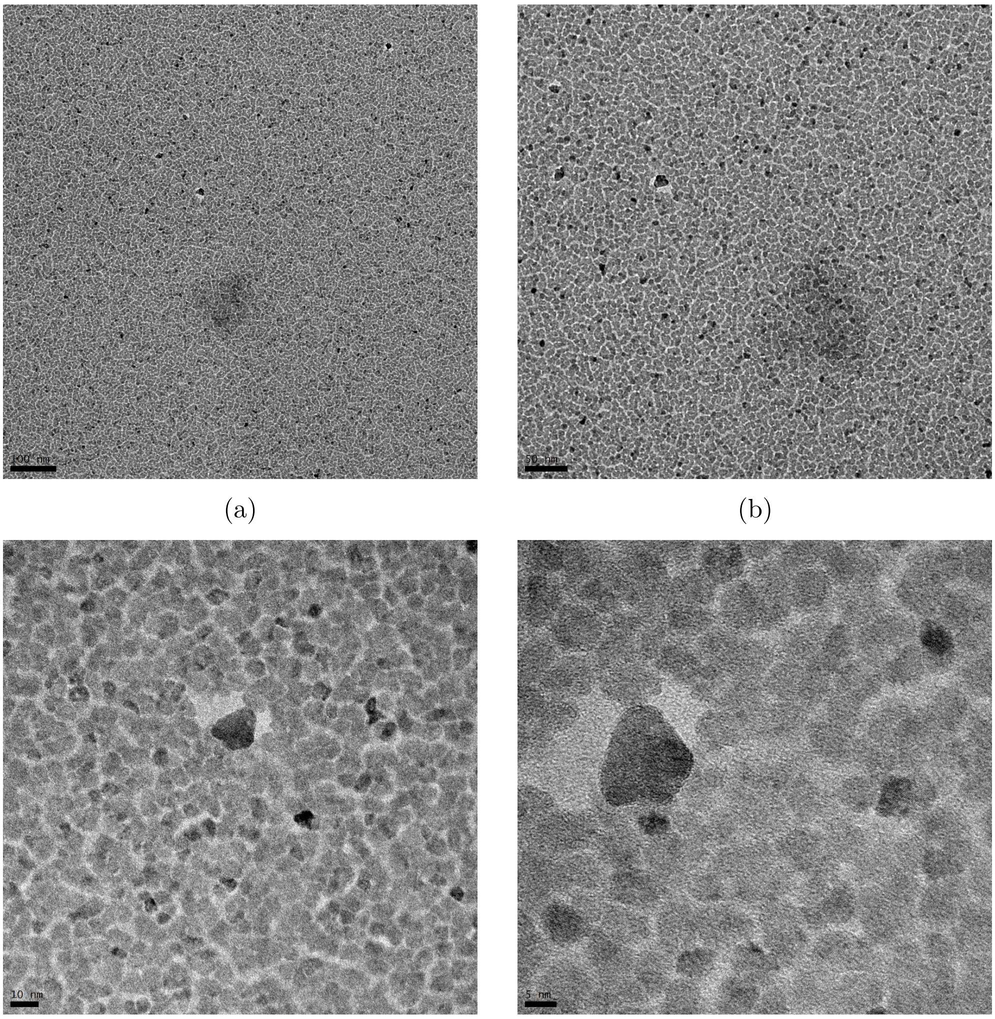

(a) (b) (c) (d)

Figure 3.15 TEM images of Cu sputtered for 10 s on a Ni grid in different magnifications. The copper grows in islands of roughly 5-8 nm.

agreement. The deviation at the edge of the sample from the prediction can be explained mask‘s thickness. The mask blocks some of the possible paths at the sample‘s edge for the metal atoms during the sputtering process.

Copper has been sputtered on a Ni TEM grid for 10 s and was analyzed by transmission electron microscopy in different magnifications, as shown in fig. 3.15, to visualize how the copper film starts to grow. The TEM images show that the copper starts with the formation of small islands of 5-8 nm.

In summary, in this section, it has been shown that thin copper oxide films can be made by sputtering with various doping materials. This co-sputtering was achieved by using a single target sputter-coater. The reproducibility and homogeneity have been improved by the used masks and the rotation of the sample. The shape of the sample film has been predicted, which matches XRF measurements. The growth of the films starts with many tiny particles in island structures. The films are mechanically stable, as shown by the DIN EN ISO 2409 tests.

3.2.4 Annealing Atmosphere Studies

This section is part of a publication, currently in the submission process. The working title of this publication is "The effect of post-deposition annealing conditions on structural and thermoelectric properties of sputtered Cu films". Systematic studies for copper oxide thin films have been performed in order to investigate the influence of different annealing conditions on the final thin film. During those studies, copper oxides were prepared by sputtering copper in an argon atmosphere and annealing in air, nitrogen, and oxygen. For the annealing in nitrogen, a mixture of argon and oxygen (Cargal 4 from Air Liquide), containing 8% O_2 was used during the sputtering process. The partial pressure during the sputtering process was kept at 0.1 mbar. The investigated materials are later denoted as CuO:Air for copper oxide annealed in air, CuO:N for copper oxide annealed in nitrogen, and CuO:O for copper oxide annealed in oxygen. All samples were annealed at 300 °C for 300 s. The samples varied in their resistance and Seebeck coefficients. The results from the measurements and preparation conditions can be found in table 3.2.

Table 3.2 Seebeck and resistances of copper oxides with different annealing conditions.

sample	sputter time [s]	sputter current [mA]	sputter gas	annealing gas	Seebeck [μV/K]	resist-ance [MΩ]
CuO:Air	2x45	40	Ar	Air	175±8	6.4
CuO:N	2x45	40	Ar + 8% O_2	N_2	184±5	4.9
CuO:O	2x45	40	Ar	O_2	204±1	0.2

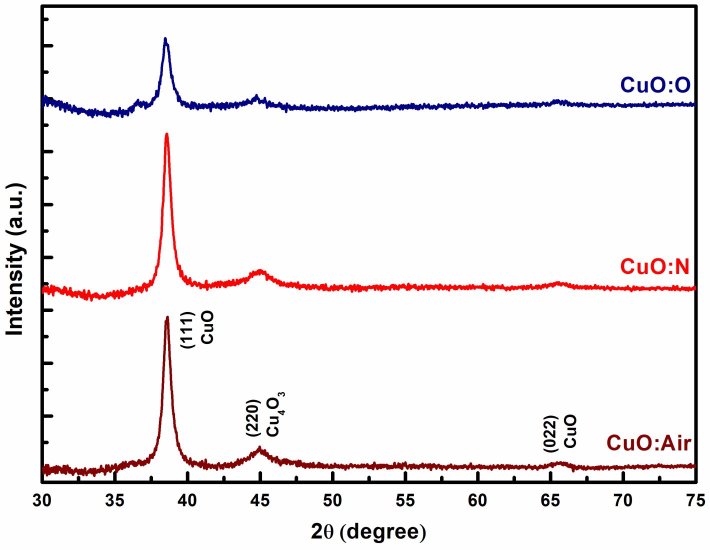

Figure 3.16 X-ray diffraction profiles of three samples oxidized in different gas atmospheres: Air(CuO:Air), N_2 (CuO:N) and O_2 CuO:O.

The samples have been analyzed with X-ray diffraction (XRD). The XRD profiles in fig. 3.16 show that all samples contain a mixed copper(I/II) oxide, which is sometimes identified in the literature as Cu_4O_3 and called paramelaconite.[155,156] This phase, which is sometimes identified as paramelaconite is described to have a stoichiometry of $Cu^{II}{}_2Cu^{I}{}_2O_3^{-II}$).[157,158] In addition, all samples contain CuO and Cu_2O.

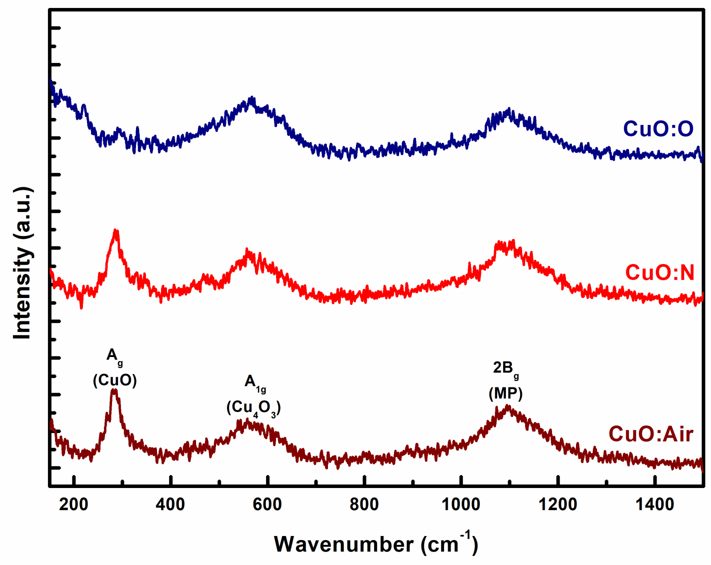

Figure 3.17 Raman spectra of three samples oxidized in different gas atmospheres: Air (CuO: Air), N_2 (CuO:N) and O_2 (CuO:O).

The Raman spectrum confirms the presence of the mixed copper (I/II) oxide. (see fig. 3.17). Since Raman spectroscopy is very sensitive to the surface, the mixed oxide should be located in the regions in or close to the surface layer of the thin film.

The amount of the mixed copper oxide decreases from the air-annealed sample to the nitrogen-annealed sample and is lowest in the sample annealed in oxygen. The oxygen-annealed sample also has the lowest reflection intensity, which indicates a smaller grain size. These samples indicate that there might be a correlation between the higher Seebeck coefficient and the lower amount of the mixed copper oxide. Regarding the Seebeck coefficient, the samples compare rather favorably with commonly used thermoelectric materials like BiTe,[159] PbTe,[160] and $CuAlO_2$.[161] Also, the high Seebeck coefficients found for the thin-film copper oxides are comparable to values reported for bulk materials.[162–164]

For the undoped samples, the thickness of the samples has been determined by SEM cross-section with the back-scattered electron signal. Fig. 3.18 (a) shows the SEM cross-section of the CuO:O. The film cannot be identified due to the smooth surface. Due to the different density of the glass and copper oxide the film can be identified by the back-scattered electron (BE) signal (see fig. 3.18 (b)). The observed thickness by BE is approximately 60-70 nm, which is close to the detection limit of the system. Thus the thickness has to be determined with a different method.

Table 3.3 Material properties of the samples. The d-spacing and mean crystallite size of the copper oxide thin films are obtained from the (111) peak of the XRD analysis. Cu and O quantification and the film thickness are calculated from EDS spectra measured at 3 keV.

Sample	D-spacing [Å]	Cu [at. %]	O [at. %]	Crystallite size [nm]	Thickness [nm]
CuO: Air	2.2327	53.10 ± 0.31	46.90 ± 0.39	119	49 ± 2
CuO: N	2.337	51.94 ± 0.33	48.06 ± 0.45	129	44 ± 4
CuO: O	2.3314	61.20 ± 0.46	37.80 ± 0.42	135	72 ± 3

The Strategem software has determined the thickness of each sample. The software bases its calculation on the XPP[3] model proposed by Pouchou et al.[165,166] The method calculates the thickness by analyzing K-ratios from

---

[3] exponential model of Pouchou and Pichoir with matrix correction

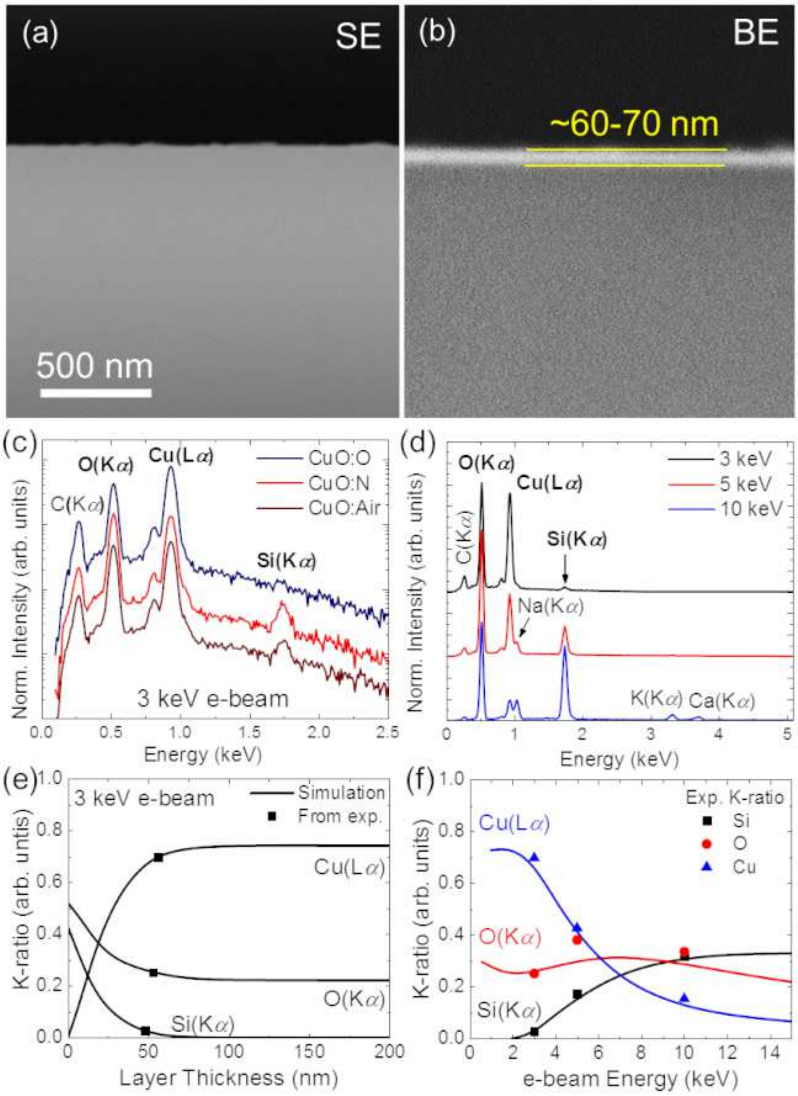

Figure 3.18 Fig (a) and (b) show cross-sectional SEM images of CuO:O sample using (a) secondary electron, and (b) back-scattered electron signal. In figure (c) EDS spectra for all samples measured at 3 keV are presented. In (d) EDS spectra measured at 3, 5 and 10 keV for CuO:N sample are shown. Figure (e) shows the calculated K-ratio. In (f) the simulated K-ratios are presented as a function of the electron beam energy.

energy-dispersive X-ray spectroscopy (EDS) spectra, which have been measured at 3, 5, and 10 keV. For the calculation, constant densities for the CuO film and the SiO_2 substrate have been assumed. For the copper oxide films, the composition listed in table 3.3 has been used. The EDS spectra, which were used to obtain the compositions, are shown in fig. 3.18 (c). Fig. 3.18 (d) shows the EDS spectra (normalized with respect to the total intensity) for CuO:N measured at 3, 5, and 10 keV. In these spectra, the peak intensities of the $O(K_\alpha)$, $Cu(L_\alpha)$, and $Si(K_\alpha)$ vary as a function of the e-beam energy, and thus the K-ratio changes. Fig. 3.18 (e) shows the calculated K-ratio as a function of the film thickness for a 3 keV e-beam. The dark squares represent the intersection of the calculated curves and the experimental K-ratio. In fig. 3.18 (f), the simulated K-ratios are presented as a function of the electron beam energy. The estimated film thicknesses show good agreement with the experimental values measured. With the corresponding procedure the film thicknesses of the other samples have been estimated. The results are summarized in table 3.3.

In summary, in this section, copper oxide thin films have been prepared by oxidation of sputtered metallic Cu films. The influence of post-deposition annealing of the samples in nitrogen, oxygen, and air has been studied. All investigated samples are mixed copper oxides that contain phases of CuO, mixed Cu(I)/Cu(II) oxides, and Cu_2O. The samples show a p-type character. Trends between the thermoelectric properties (Seebeck coefficient and electrical resistance) and the crystallite size of the copper oxide could be observed. Thus with fewer grain boundaries, the in-plane charge transport is better. The annealing in an oxygen atmosphere results in the lowest overall oxygen concentration in the copper oxides. The copper oxide sample annealed in oxygen exhibits a high Seebeck coefficient of 204 μVK^{-1} and electrical conductivity of 50 Sm^{-1}. By doping, these results could likely be further improved.

3.2.5 X-Ray Fluorescence

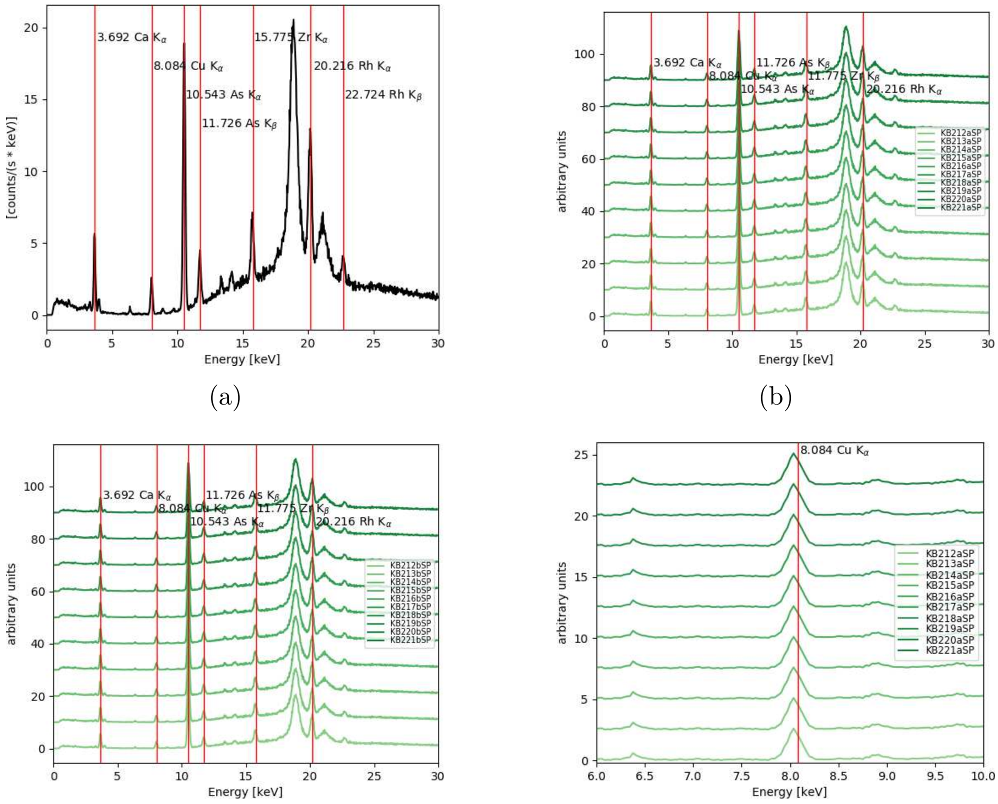

(a) (b)

(c) (d)

Figure 3.19 In this figure, a selection of the XRF spectra measured with the Fischerscope X-ray XDV-SDD is shown. These spectra are the basis for the calculation of mass deposition done by the Fischer software. All measurements have been performed with a rhodium X-ray tube. In fig. (a) an example of a full spectrum is shown. Here, the bremsstrahlung of the Rh K_α and K_β lines from the X-ray tube can be seen. Besides, several lines associated with glass are visible. The most intense peaks include Zr K_α, Ca K_α and As K_α and K_β. The Cu K_α signal is visible at 8.084 keV. In fig. (b), one spectrum of each "a sample" is shown. In fig. (c), one spectrum from each "b sample" is shown. Fig. (d), is a zoom of the "a samples" Cu region of the spectrum.

A variety of samples have been measured with the Fischerscope X-ray XDV-SDD (Helmut Fischer GmbH) X-ray fluorescence spectrometer. With this spectrometer, it is possible to measure multiple spots on a sample surface to get a 2D mapping of the measured elements. Some pure copper samples have been prepared with different sputter times to get a mass deposition and thickness from the used cumulative sputter times. For pure copper films, single-point measurements in the middle of each sample have been performed with 36 measurements for 100 s.

In fig. 3.19, a selection of the recorded XRF spectra measured with the Fischerscope XDV-SDD X-ray fluorescence spectrometer is shown. These spectra are the basis for the calculation of the mass deposition done by the Fischer software. These results are presented in figs. 3.21 to 3.23 later in this section. All measurements have been performed with a rhodium X-ray tube. In fig. 3.19 (a), an example of a full spectrum is shown. Here we can see the bremsstrahlung together with the Rh K_α and K_β lines from the X-ray tube. Besides, several lines associated with soda-lime silicate glass are visible, which is used as the substrate. The most intense peaks include Zr K_α, Ca K_α, As K_α, and K_β. Arsenic is commonly used in optical glasses for refinement purposes (fining agent: arsenic oxide) to remove the gas bubbles.[167] Zirconium (IV) fluoride is used as a base for heavy metal halide glasses,[167] in soda-lime silicate glasses ZrO_2 can be used to decrease the coefficient of thermal expansion.[168] The Cu K_α signal is visible at 8.084 keV. In fig. 3.19 (b) from each "a sample"[4] one spectrum is shown. In fig. 3.19 (c), one spectrum from each "b sample" is shown. Fig. 3.19 (d) is a zoom of the Cu region of the spectrum from the "a samples".

---

[4] During the preparation of the sputtered thin films two samples are sputtered at the same time side by side the left samples are marked as "a sample" the right as "b sample"

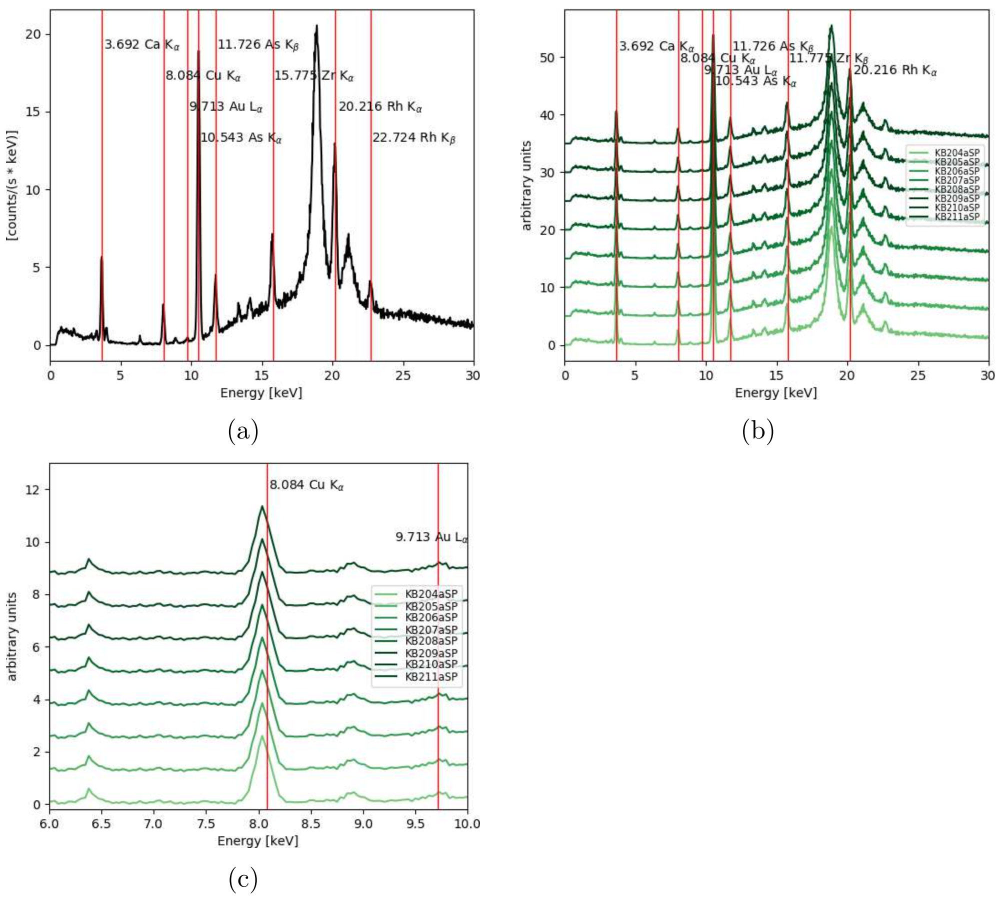

(a)

(b)

(c)

Figure 3.20 In fig (a), a representative XRF spectrum of a gold-doped copper oxide sample is shown. Besides the Au and Cu signals, the Rh Bremsstrahlung, Rh peaks and signals from the glass support can be observed in the spectrum. In fig (b), some of the measured spectra of gold-doped copper oxides are shown. In fig (c), the zoomed in Cu and Au region of the spectra is shown.

In fig. 3.20, a selection of representative XRF spectra of gold-doped copper oxide films is shown. Additional spectra of the pure Cu samples (fig. 7.7) and spectra of samples containing gold (fig. 7.8) can be found in the appendix on page 225.

In fig. 3.21 the mass deposition and the calculated film thickness is displayed. The results from fig. 3.21 (a) are used as an estimate of the film

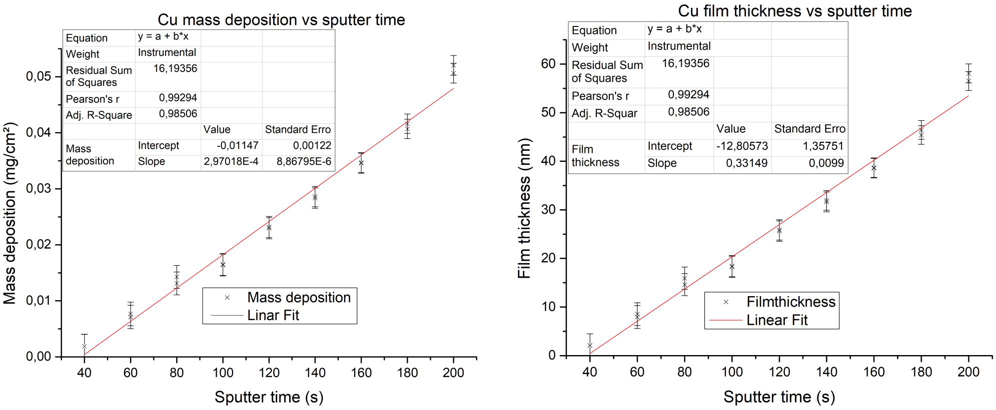

(a) (b)

Figure 3.21 Fig (a) shows XRF measurements of mass deposition for pure copper samples with sputter times between 2 x 20 s and 2 x 100 s. Between the first and the second sputter period each sample has been turned around its center by 180°. All displayed points are averages of 36 measurements with 100 s integration time. For each sputter period two samples have been prepared and measured. From the mass deposition results film thicknesses were calculated using the density of bulk copper (8960 mg/cm^3 [169]), which is represented in the figure (b).

thickness shown in fig. 3.21 (b). This estimation is due to the fact that the density of the sputtered thin film copper samples is unknown. To get values for the thickness the density of bulk Cu - 8960 mg/cm^3 [169] - was used. For the thinner samples the measurement error is higher due to the smaller signal coming from the sample. From the measurements an approximate mass deposition per time can be calculated which is 2.9 x 10^{-4} mg/cm^2 per second of sputter time, which corresponds to 0.33 nm/s.

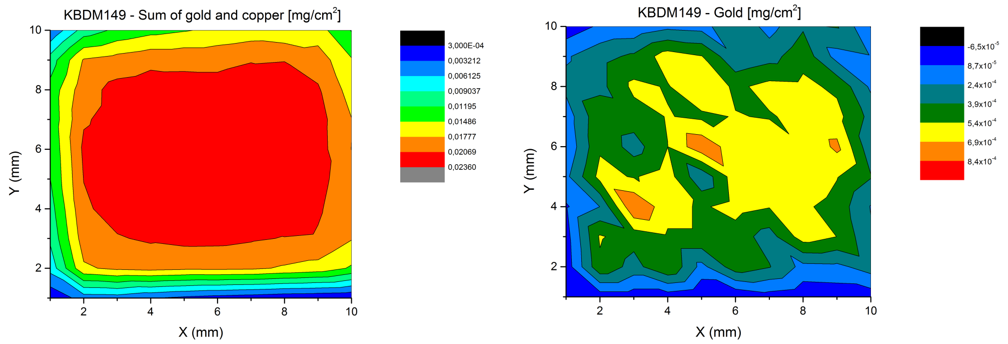

(a) (b)

Figure 3.22 XRF measurement results for sample(KBDM149A), which was sputtered two times for 40 s with a Cu target exposing 2.5% Au. The substrate for this sample was an silicon (111) wafer. The sample was tempered for 360 s at 300 °C. In (a) a contour plot of the sum of the Cu and Au mass per unit area is shown. In (b) a contour plot of the Au distribution is shown. Most of the samples' area shows a gold distribution between $3.8 \cdot 10^{-4}$ and $6.8 \cdot 10^{-4}$ mg/cm^2. The deviations at the edge can be explained by the thickness of the sample and the lower overall mass deposition.

Fig. 3.22 (a) shows the cumulative mass deposition of Cu and Au on the sample surface. The sample is relatively flat in the center with steeply falling edges. In fig. 3.22 (b) the distribution of the Au used for doping is shown. In fig. 3.23 the relative percentage of Au is shown over the sample area. The average percentage of Au is 1.9% (by mass) with a standard deviation of 1.1%. Since the film thickness drops steeply at the edge and the film thickness gets in the region of the limit of detection, the border of this measurement should be regarded with caution. This is especially visible in the lower left corner with an improbable high gold concentration.

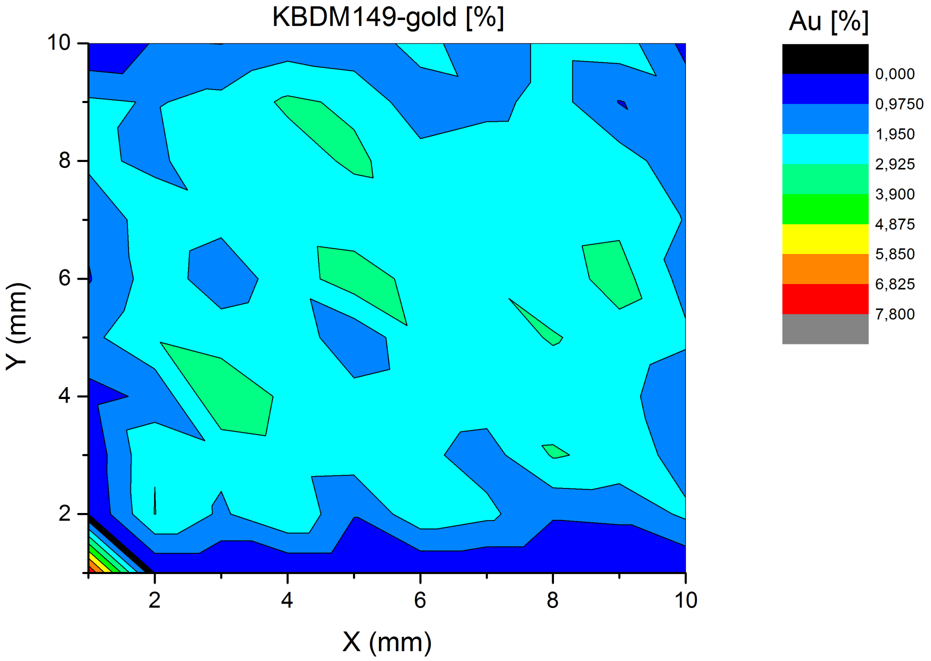

Figure 3.23 XRF mapping of Au in mass percent over the sample area. The average Au percentage over the entire sample is 1.9 % with a standard deviation of 1.1. The center region of the sample is more homogeneous than the edges.

In summary, in this section, the deposition rate of the sputter coater has been determined to be 2.9 x 10^{-4} mg/cm^2 per second of sputter time (0.33 nm/s at a density of 8960 mg/cm^3). It has been shown that the gold distribution with the used sputter technique of drilled copper targets stacked with a gold target produces a largely homogeneous Au distribution in the center of the sample.

3.2.6 Near Edge X-Ray Adsorption Fine Structure of Copper Oxide Thin Films

To analyze the oxidation state of the copper oxide thin films parallel to the surface with increasing depth, angle-dependent near-edge X-ray absorption fine structure (NEXAFS) measurements at the BESSY II plane-grating monochromator (PGM) beamline have been performed. This beamline is operated by the *Physikalisch Technische Bundesanstalt* (PTB). It provides monochromatic X-rays with energies between 78 and 1870 eV. Typically the BESSY synchrotron storage ring has an electron current of 200 mA and provides a photon flux of $6 \cdot 10^9$ photons/s at 1.7 keV to $6 \cdot 10^{11}$ photons/s at 400 eV. The focused spot size of the X-rays is adjustable with the help of apertures.[170] Further details about the used GIXRF-NEXAFS setup can be found in the Ph.D. thesis of B. Pollakowski.[117] Additional information about the plane-grating monochromator can be found in a research article by M. Krumrey.[118]

For all investigated samples, a spot in the center has been measured at shallow angles. Changing the incidence angle adjusts the penetration depth of the X-rays (see angle dependence of X-ray measurements on page 26). The adjustable penetration depth gives the opportunity to get information in a non-destructive manner. The used samples were prepared on silicon wafers. The wafers were chosen as a substrate due to their low surface roughness and their purity. In addition, the oxygen content in a glass substrate would cause interference when measuring the oxygen content of the sample. As a reference sample, pellets (disc shape with 10 mm diameter and approximately 3 mm height) of KBr (per analysis) containing 20 % of CuO(per analysis) or Cu_2O(per analysis) have been produced with a pressure of 1248 MN/m^2 (10 tons/78.54 mm^2). These pellets have been measured to obtain reference

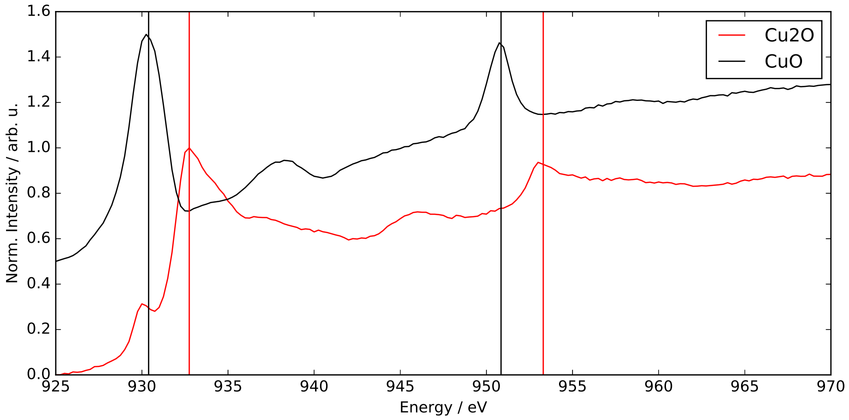

Figure 3.24 NEXAFS spectra show the reference spectra for Cu(I) and Cu(II) oxide, with characteristic peaks at 932.75 eV and 953.30 eV for $Cu^{I}_{2}O$ and at 930.39 eV and 950.85 eV for $Cu^{II}O$. The measured reference samples were pressed from the corresponding copper oxide powder and KBr.

spectra for the two main copper oxides. The measured reference spectra are depicted in fig. 3.24.

Besides the two reference samples, copper oxide thin films have been measured. The two untempered samples contain mainly Cu^{I} (see fig. 3.25 (a) and (b)) while the tempered sample in fig. 3.25 (c) shows a clear increase in Cu^{II}. With an increasing angle, the small peak at 930.39 eV loses intensity. This decrease in intensity is especially true for the tempered sample, where the peak at 932.75 eV increases at the same time. This increase in intensity is a clear indication that there is a gradient in the sample with Cu^{II} mainly in the upper parts, and with increasing depth, the content of $Cu^{I}_{2}O$ also increases. The NEXAFS measurements show that the average oxidation state of the copper oxide decreases with increasing depth for the tempered sample (KBDM0149A). Thus, the oxygen content of the sample decreases with the depth of the measurement. Together with the XRD data and Raman results, these measurements indicate that the sample has a mixed copper

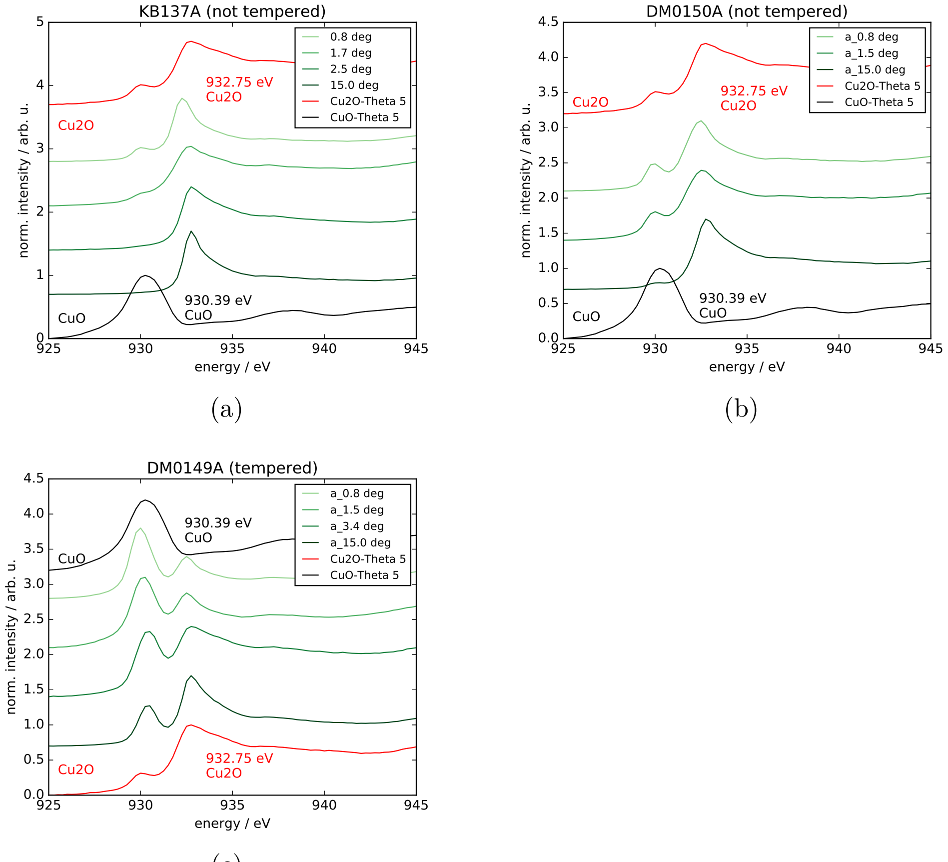

(a)

(b)

(c)

Figure 3.25 NEXAFS spectra showing the untempered copper oxide thin films (a) and (b) which are mainly comprised of $\mathrm{Cu^{I}}$ species and the tempered thin film copper oxide (c) which has mainly $\mathrm{Cu^{II}}$ at the surface. With decreasing depth the ratio between $\mathrm{Cu^{II}}$ and $\mathrm{Cu^{I}}$ changes in favor of the $\mathrm{Cu^{I}}$ species.

(I/II) layer at the top and a Cu_2O layer at the bottom. In between, the ratio of Cu(II) to Cu(I) oxide diminishes from the top to the bottom of the sample (see fig. 3.26). Measurements on different Cu(0/I/II) compounds have been performed by Grioni[171] et al. The spectra measured for $\mathrm{Cu^{I}}_2\mathrm{O}$ and $\mathrm{Cu^{II}O}$ (fig. 3.25) bear a close resemblance to those measured by Grioni et al. The raw NEXAFS spectra are not corrected for self-absorption, which does

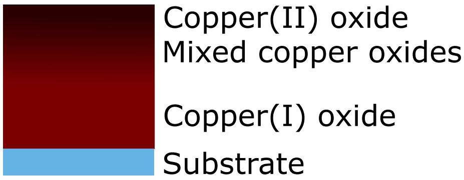

Figure 3.26 Schematic view of the copper oxide depth profile. The top layer is mostly oxidized to copper(II) oxide (black), in the intermediary region is a layer of decreasing oxygen content (depicted black to red) and the bottom layer is oxidized to copper(I) oxide (red).

not influence the general statements concluded from the graphs. However, in the appendix on page 231, the graphs are shown again with the Cu-L_α signal divided by the O-K signal (see fig. 7.13). These normalized spectra should compensate for most of the effects due to self-absorption.

In this section, it was shown by angle-dependent NEXAFS measurements, that the composition of the sample is changing laterally. At the surface of the sample, the Cu(II) content, and thus the oxygen content is higher. With increasing depth, the Cu(I) species becomes more abundant, and thus the oxygen content is lower.

3.2.7 Grazing Incidence X-Ray Fluorescence of Copper Oxide Thin Films

The measurements and evaluation discussed here were performed by J. Baumann with the help of B. Pollakowski. The interpretation of the results was done in cooperation with J.B. and B.P. Since this work is a significant part of the Ph.D. thesis of J. Baumann[113] this section will only summarize the parts relevant to the supplied sample system.

For a number of samples, studies have been performed at the BESSY II Synchrotron, using X-ray fluorescence with shallow incident angles. This technique is called grazing incidence X-ray fluorescence (GIXRF); it allows nondestructive measurements in the subsurface region of the sample. For these experiments copper and copper oxides doped with gold were prepared on silicon wafer pieces. Most of the experiments were conducted in the soft X-ray range in order to excite the fluorescence of the O-K and Cu-L_α efficiently. In the soft X-ray region, the photon energy is high enough to excite the O-K fluorescence. Some measurements were performed in the hard X-ray region. The hard X-rays have enough energy to excite the Au-L and Cu-K fluorescence. Due to the need for different energy regions, the experiments have been performed at three different beamlines at the BESSY II synchrotron. The measurements with soft X-rays has been done at the *Physikalisch-Technische Bundesanstalt* (PTB) beamline. The measurements in the hard X-ray region have been performed at the BAM beamline.

The plane grating monochromator (PGM)[113,172] beamline operated by the PTB, provides monochromatic X-rays from the undulator U49 in the energy range between 78 eV to 1870 eV. During normal operation, the BESSY II synchrotron storage ring has an electron current of 200 mA. The 200 mA of electron current can provide a photon flux between $6 \cdot 10^9$ photons/s at 1.7 keV and $6 \cdot 10^{11}$ photons/s at 400 eV.[112,113] The smallest possible focus of the beam in the region where the sample is placed has a spot size of 40 μm by 40 μm in the horizontal-vertical direction. A more detailed description of this PGM beamline can be found in the Ph.D. thesis of J.B.[113] and the Ph.D. thesis of B.P.[117]. The PGM beamline gives access to soft X-rays.

The KMC beamline uses a four-crystal monochromator to access the radiation in the intermediate energy region. This monochromator is installed after the dipole magnet D71. The monochromatic X-rays from this beamline have an energy between 1.75 and 10.5 keV. The photon flux is about 10^{10} photons per second during normal operation.[118,119]

For the hard X-ray range the BAM beamline, which is operated by the *Bundesanstalt für Materialforschung* (BAM) is used. This beamline is equipped with 7 T superconducting wavelength shifter (7T-WLS-1). The energy of the produced photons can be adjusted between 4 keV and 100 keV.[173] The beamline is either equipped with a double multilayer monochromator (DMM) or a double crystal monochromator (DCM).[173] The wholly automated DMM monochromatizes the X-ray light if a high photon flux is needed. If the energy resolution is instead prioritized, the DCM can be used to get the monochromatic X-ray light.[120,121,173] Through the adjustable focus, the photon flux density of the X-ray light can reach $5.7 \cdot 10^{10}$ photons $(s \cdot mm^2)^{-1}$ at 7 keV.[113,121]

The experiments are conducted in an ultra-high vacuum (UHV) chamber containing a nine-axis manipulator, which allows the sample to be positioned with six degrees of freedom (6-DOF).[174] The three additional axes are not used for the sample but photodiode location. The positioning of the photodiodes allows additional experiments like X-ray reflectometry, for example.[113,174] A schematic representation of the UHV measurement chamber is presented in fig. 3.27. Baumann explains further details about the measurement setup and data acquisition.[113]

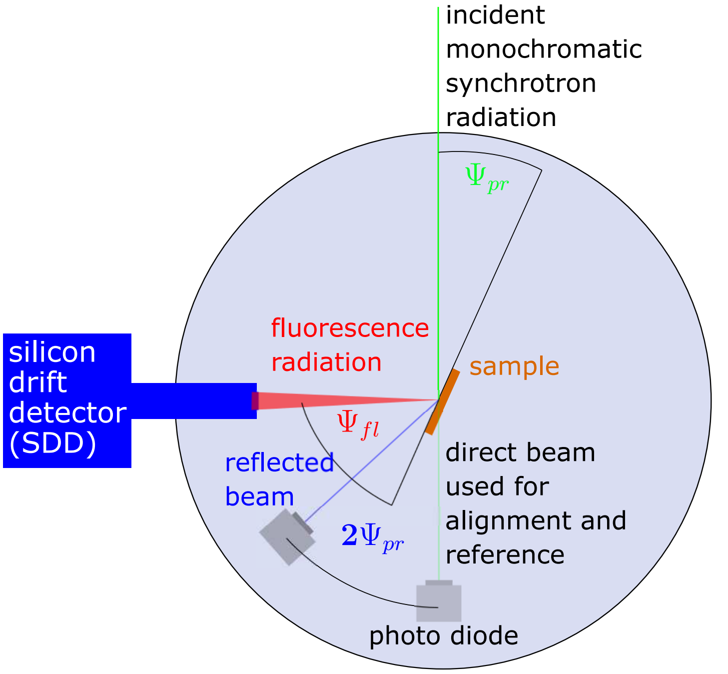

Figure 3.27 Schematic representation of the utilized GIXRF measurement setup. The ultra high vacuum chamber contains a six degrees of freedom sample holder (three translational and three rotational). In addition, the detectors can be moved as well.

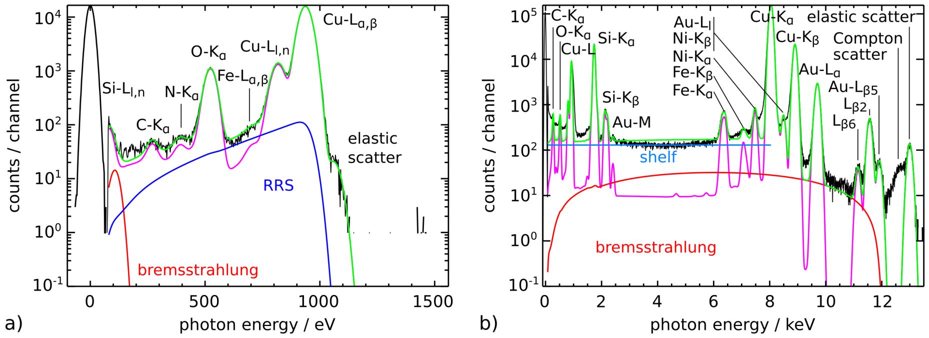

Figure 3.28 Recorded energy-dispersive fluorescence spectra. Figure a) shows the spectrum of sample KBDM149A, excited with 1060 eV at the PGM beamline. Figure b) shows the same sample at 13 keV at the BAMline. The incidence angle shown here is 0.05°. Deconvolution is performed with physical background models and detector response functions. This image was published by J. Baumann.[113]

In figure 3.28 two sample energy-dispersive fluorescence spectra are shown at excitation energies of 1060 eV (a) and at 13 keV (b). Details about the deconvolution, fitting and integration can be found in the Ph.D. thesis of J. Baumann.[113] During the GIXRF measurements, the atomic ratio between Cu and Au was determined at the BAMline beamline with both 13 keV and 17 keV. Besides, the total copper mass deposited was measured at 10 keV at the KMC beamline. With the measured values, the total deposited amount of gold was calculated. The results are summarized in table 3.4.

Table 3.4 In this table, the quantification results of the relative atomic fractions for gold and copper atoms are summarized. The measurements were performed on the samples KBDM0150A (untempered) and KBDM0149A (tempered), which were identically prepared, except for the tempering of sample KBDM0149A. The measurements for the relative atomic fractions were conducted at the BAMline (BAM). The measurements for the absolute mass deposition of Cu were performed at the KMC beamline (KMC). The absolute mass deposited for the gold was calculated from the relative atomic fractions. The results presented in the table were taken from J. Baumann.[113]

relative atomic fraction	energy [keV] (beamline)	KBDM0150A	KBDM0149A
C^{at}_{Au}/C^{at}_{Cu}	13 keV (BAM)	1.04% ± 0.12%	0.99% ± 0.11%
C^{at}_{Au}/C^{at}_{Cu}	17 keV (BAM)	1.07% ± 0.12%	0.98% ± 0.11%
absolute mass deposition	energy [keV] (beamline)	KBDM0150A $[\mathrm{ng} \cdot \mathrm{cm}^{-2}]$	KBDM0149A $[\mathrm{ng} \cdot \mathrm{cm}^{-2}]$
m_{Au}		580 ± 80	560 ± 80
m_{Cu}	10 keV (KMC)	18900 ± 1400	18500 ± 1300

The samples KBDM0149A and KBDM0150A were prepared by sputter coating with a 2.5% perforated copper target with a gold target on top for 2 x 40 s. KBDM0149A was tempered for 360 s at 300 °C. The results show, as expected that the gold content is identical. The amount of gold is lower than the perforation, which makes sense since the plasma ions have to pass through the 1 mm holes in the copper target. To path through the hole near the edge of the copper target, some angles are blocked from the 0.2 mm thick copper target. The same reasoning applies when the Au atoms need to pass through the 1 mm holes, some of them condense onto the copper. Those Au atoms on the copper will be sputtered again shortly after they condense, but it reduces the rate at which the Au atoms are sputtered. Similar to the traffic at an intersection during rush hour, where cars stop at a red light before they can move again.

The overall quantification was repeated at the PGM beamline with an excitation energy of 1060 eV to quantify Au, Cu, and O in the sample system. The results are summarized in table 3.5. The results from the quantification show that there is carbon contamination present in both samples. AFM images show that this contamination is due to particles of irregular size and shape on top of the sample surface (see fig. 3.29).

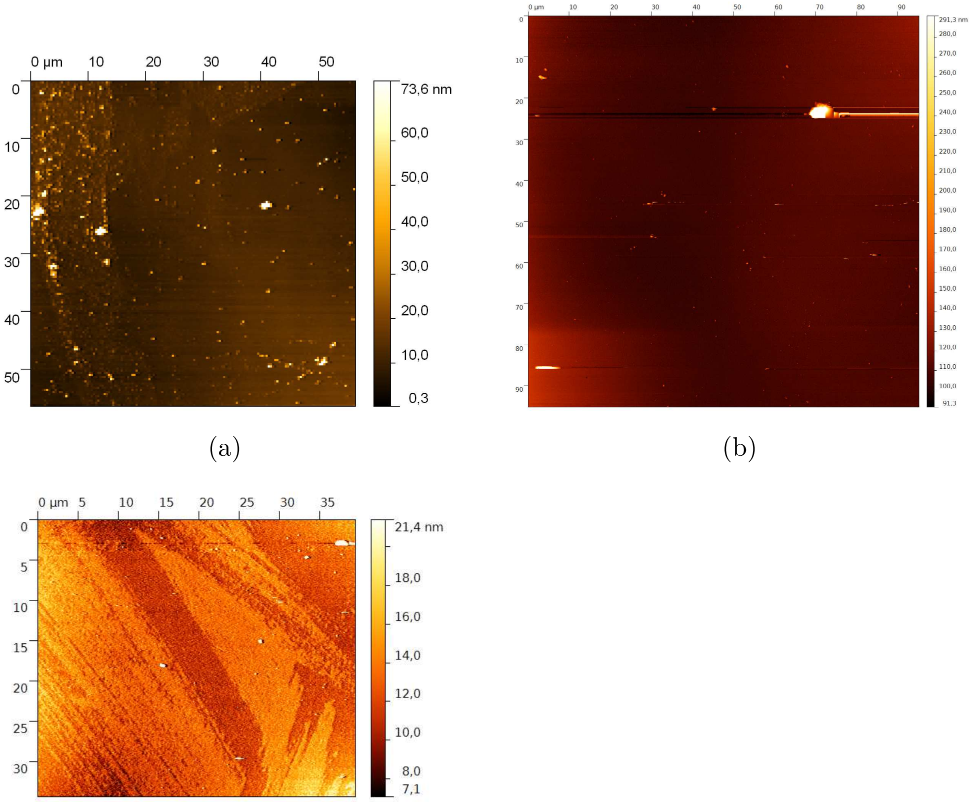

(a) (b)

(c)

Figure 3.29 AFM images taken with the Nanosurf Mobile S atomic force microscope. In (a) one of the Si wafers used to prepare the samples for the GIXRF is measured. It shows particles on top of the surface which are most likely one of the source of the carbon contamination. In (b) and (c), a sample prepared like KBDM0150A is shown in two different magnifications. The surface roughness over the entire measurement area of (c) is Ra: 1.6 nm Rms: 2.5 nm.

Since in this experiment all the parameters of the measurement like incoming photons, detector response functions, and angles are known it is possible to assume a model of the sample, add all the parameters to it and compare the theoretical fit to the measurement. J. Baumann simulated these fits for both samples.[113]

Table 3.5 Quantification results for the Au, Cu and O content of the samples KBDM0150A and KBDM0149A at the PGM beamline. The measurements were performed at 1060 eV. The results presented in the table were published by J. Baumann.[113]

	KBDM0150A	KBDM0149A
$\hat{m}_C$ [ng·cm^{-2}]	1600 ± 200	970 ± 120
$\hat{m}_{Au}$ [ng·cm^{-2}]	600 ± 170	560 ± 160
$\hat{m}_{Cu}$ [ng·cm^{-2}]	18000 ± 5000	18000 ± 5000
$\hat{m}_O$ [ng·cm^{-2}]	3800 ± 800	4300 ± 900
C^{at}_{Au} [at %]	0.57 ± 0.17	0.51 ± 0.15
C^{at}_{Cu} [at %]	50 ± 20	50 ± 20
C^{at}_{O} [at %]	45 ± 9	48 ± 10

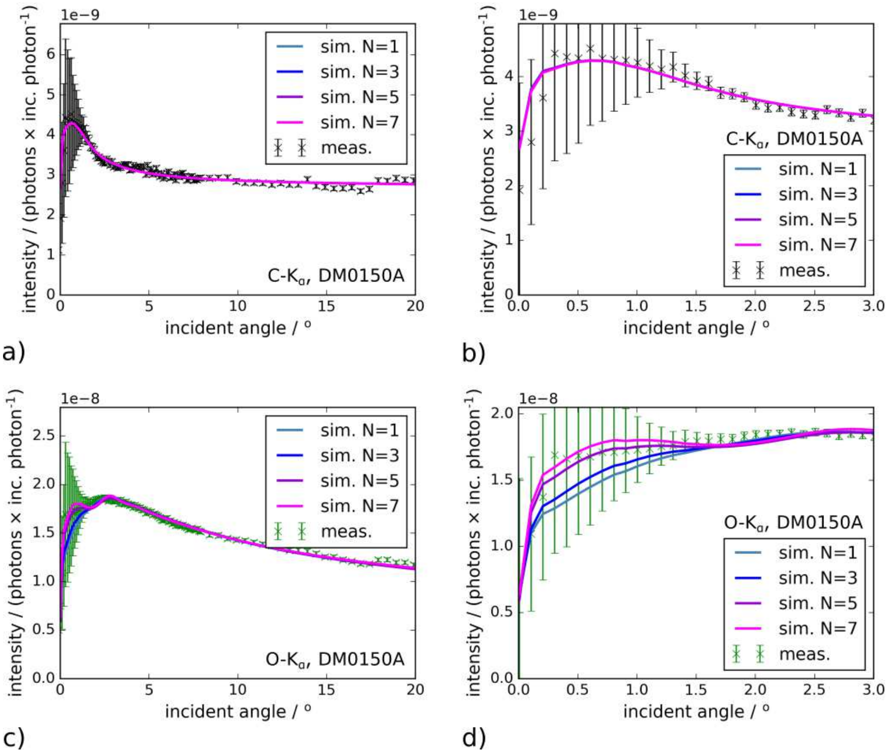

Figure 3.30 Measured GIXRF data of sample KBDM0150A and fitting profiles for carbon in a) and a zoomed view in b). In c) the data for the oxygen is presented and in d) a close up view is shown. The measurement has been performed with photons at 1060 eV. The fits were modelled with an N-layer model with carbon content. This image was published by J. Baumann.[113]

Due to the well-known experimental parameters, theoretical models can be assumed. With the well-known parameters spectra can be calculated out of the different contributions which emit electromagnetic radiation in the measured energy range. These contributions, for example, consist of bremsstrahlung and resonant Raman scattering of the substrate, which is in this case silicon. In fig. 3.28 those background contributions are presented in red and blue. The X-ray fluorescence signals from the expected elements (Cu-L, Cu-Ll, O-K and Si-Ll) in this figure are marked pink. There are also smaller contributions from carbon and nitrogen visible in this spectrum.

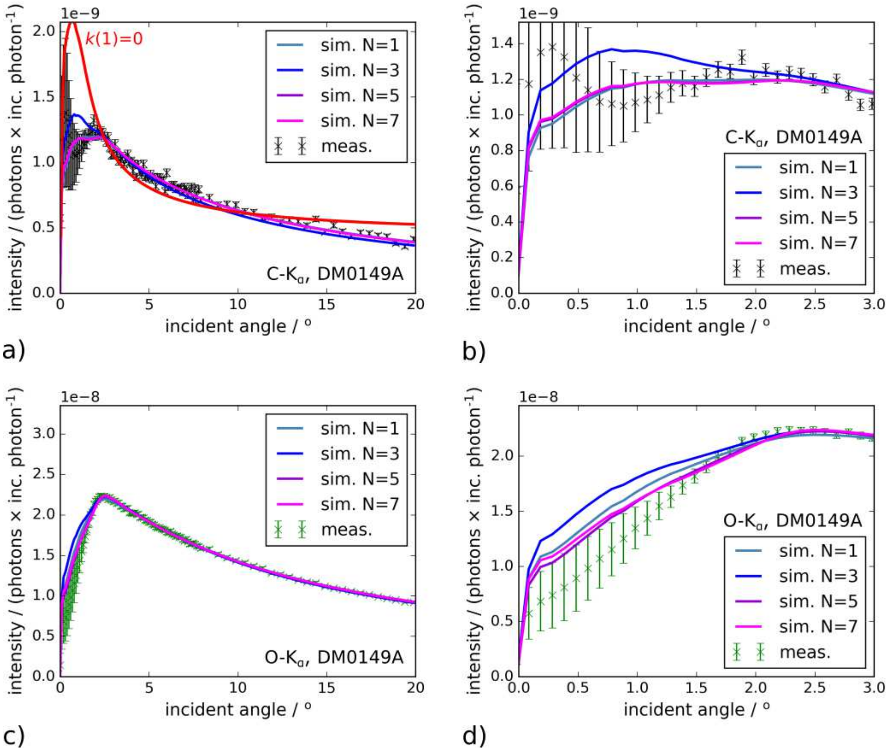

Figure 3.31 Measured GIXRF data of sample KBDM0149A and fitting profiles for carbon in a) and a zoomed view in b). In c) the data for the oxygen is presented and in d) a close-up view is shown. The red curve in a) is a fit for N=1, where carbon is only on top of the surface. The measurement has been performed with photons at 1060 eV. The fits were modeled with an N-layer model with carbon content. This image was published by J. Baumann.[113]

The fit calculated by model systems has to contain carbon and oxygen-rich particles at the surface. These particles, which were probably introduced by not handling the samples in a clean room, have been seen in AFM images as well (see figure 3.29). They have been simplified in the model as a thin homogenous film on top of the sample. Due to the change in the area the incident beam hits when the angle is changed, this model of the homogenous film is just an approximation. At angles above 20°, the C-K fluorescence is much lower than expected from the model. This lower fluorescence signal is a strong indication, that the smaller footprint of the incident photons does not hit the carbon-containing particle anymore. The fitted measurements are shown in fig. 3.30. For the tempered sample (KBDM0149A), the carbon GIXRF profiles can be fitted if some part of the carbon signal is modeled inside the copper oxide film. The measurement and corresponding fits are presented in fig. 3.31. The fitting functions were calculated according to the sketch presented in fig. 3.32. The model used for the sample KBDM0150A was applied to the sample KBDM0149A (see in fig. 3.31 (a) red line). In this model, the carbon species are always overestimated by the fit. To achieve a better agreement with the measurement results especially at high angles, the carbon was also modeled throughout the entire copper oxide film.[113] Some of the particles which are most likely the carbon-containing species, are visible in the AFM image in fig. 3.29 as bright white spots on the relatively flat surface.

In conclusion, the GIXRF profiles give a destruction-free insight into the buried subsurface region of the thin film sample. The model with the best fit to the measurement shows a complex multilayer system of copper oxides. Both samples had carbon-containing particles on top of the surface. The particles were introduced due to the handling in non-clean-room conditions.

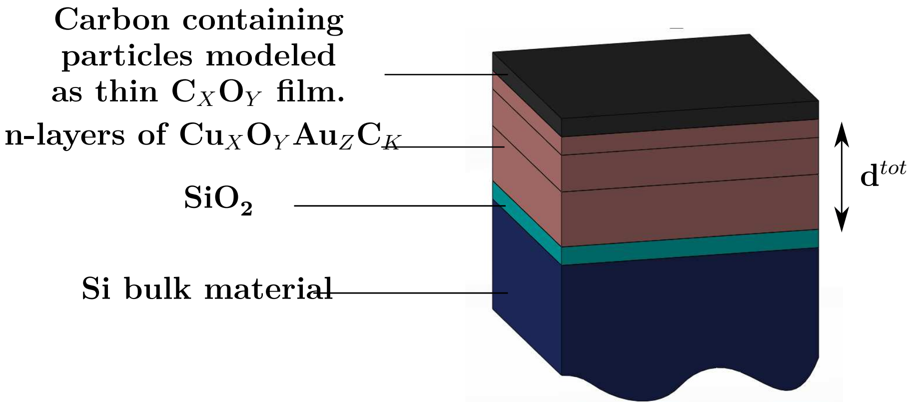

Figure 3.32 A sketch of the n-layer model with carbon containing particles on top, which are modeled as a thin film. For the tempered sample carbon containing species are also present in the gold doped copper oxide layers ($K > 0$). Underneath the sample is a thin SiO_2 film followed by bulk Si.

For the tempered sample, it was shown, that a small amount of carbon was introduced to the copper oxide below the sample surface. Nevertheless the measurements give an indication that the oxygen content decreases from the surface towards the bottom of the film.

3.2.8 X-ray Photoelectron Spectroscopy

X-ray Photoelectron Spectroscopy measurements have been performed on specially prepared samples. Each sample carrier was coated with a thin gold film of 10 nm (30 s of sputtering) to prevent a buildup of charge during the measurement. On top of the Au-film, a gold-doped copper oxide sample was prepared by co-sputtering copper and gold. The gold-doped copper films were thermally oxidized at 300 °C for 300 s. All XPS measurements were performed with a Jeol JPS-0930 XPS system. For surveys, a dwell time of 50 ms, and for detailed scans of the elemental region, 100 ms of dwell time were chosen. As an excitation line, Al K_α (1487 eV) was used. The spectra have been recorded with 10 eV pass energy. Each spectrum was scanned five times. For all samples, one XPS measurement just of the surface was performed first. One of the samples was chosen for depth profiling, with three additional measurements. Measurements 2-4 were done after removing the surface layer by sputtering for 25 s before each consecutive measurement.

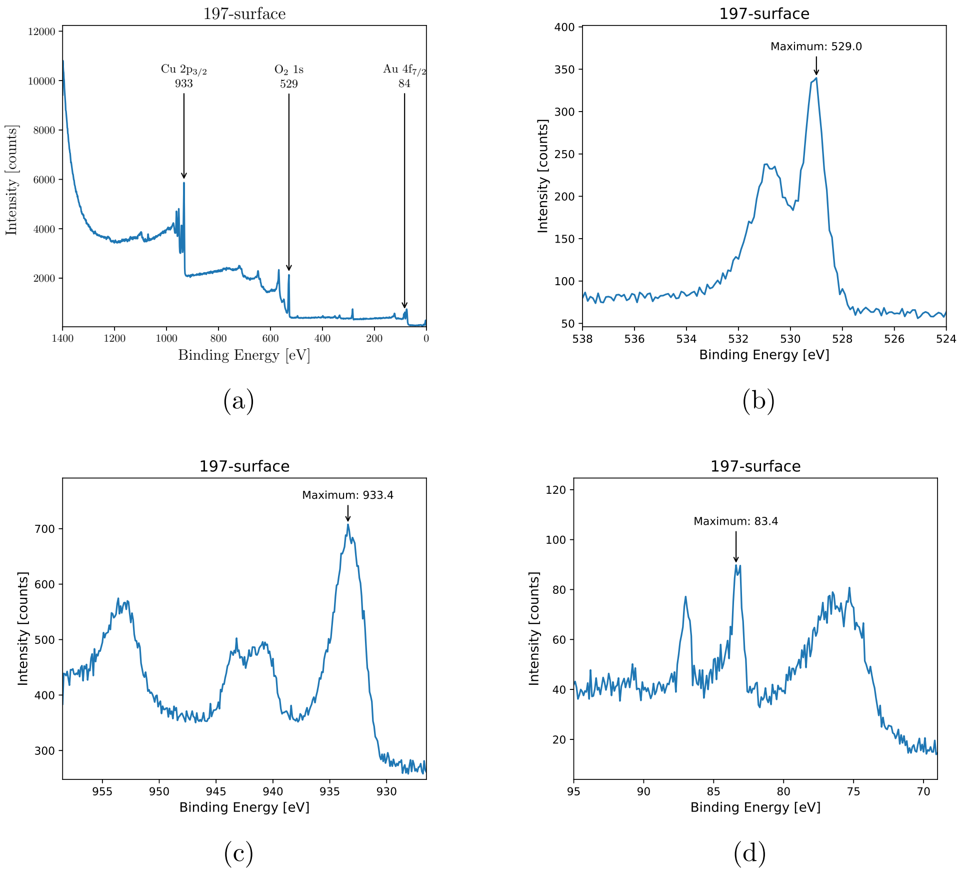

(a) (b)

(c) (d)

Figure 3.33 XPS spectra of sample 197a: A thin film of gold (30 s Au sputtering) was sputtered on the carrier surface to prevent charge buildup. On top of the gold film, copper was sputtered for 2 x 30 s. The copper targets were drilled and expose an area of 7.5 % of the gold target on top. The sample was thermally oxidized at 300 °C for 300 s. Figure (a) is a complete survey of the surface. In (b) the oxygen content of the sample surface is depicted. In (c) the binding energies of copper species are presented. In (d) the binding energies of gold are shown.

Fig. 3.33 clearly shows the presence of gold, copper and oxygen. The Cu region in fig. 3.33 (c) shows that there are Cu(I) and Cu(II) species present.[175–177] The binding energies of Cu(0), Cu(I) and Cu(II) are close together. Metallic Cu^0 has a binding energy of 932.64 eV.[177,178] The binding energy in Cu_2O is 932.43 eV,[177,178] and that of CuO is 933.57 eV.[177,178] In fig. 3.33 (c) the maximum counts are at 933.4 eV[141,177] which is close to the binding energy of CuO. Since the distribution is not perfectly Gaussian and the maximum is shifted from the literature value towards the Cu_2O species, it is safe to assume that both Cu(I) and Cu(II) species are present.

The copper region of the XPS spectra shows that after the top layer of the sample is removed the maximum shifts away from the Cu(II) and in the area of Cu(I). The maximum intensity positions are a bit lower than the expected 932.4 eV, with 932.1 eV (fig. 3.34 (b)) 931.9 eV (fig. 3.34 (c)) and 931.8 eV (fig. 3.34 (d)). Other researchers observed the binding energy of 931.8 eV as Cu 2p core level peaks in thin cleaved Cu foil.[179]

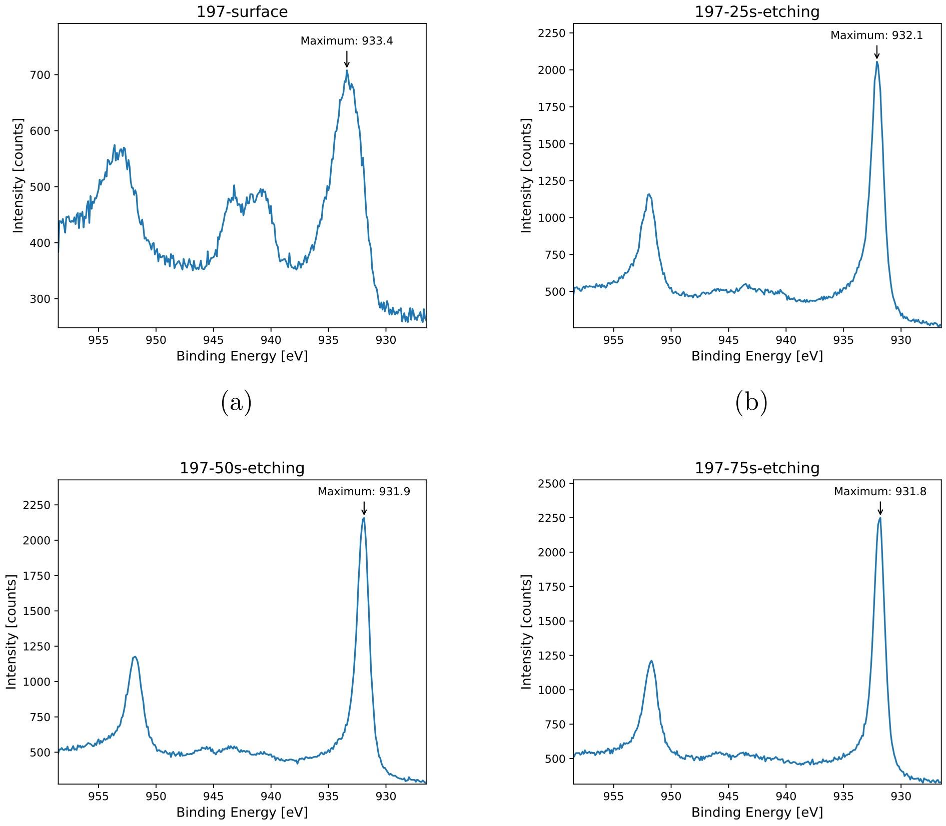

(a) (b) (c) (d)

Figure 3.34 XPS spectra of the Cu binding energy region for sample 197a: Subfigure (a) shows the binding energies of copper at the sample surface. The shift of the binding energy is an indication that Cu(I) and Cu(II) are present. In (b) the same region is depicted after 25 s of sputtering. In (c) the surface layer of the sample was removed again by an additional sputtering of 25 s. In (d) the total sputtering time was 75 s.

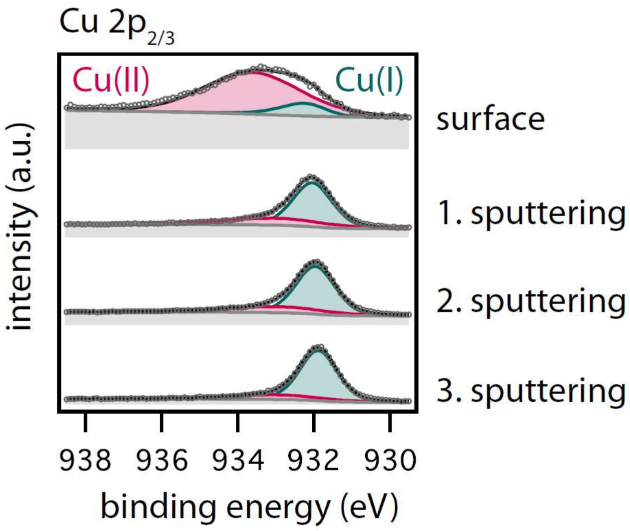

Figure 3.35 The graph displays the measured XPS values in the range of 939 to 929 eV with fitting curves for Cu(I) and Cu(II). The fitting function parameters were taken from the NIST Database.[180] The surface shows a large percentage of Cu(II). Underneath the surface, the main oxidation state of the Cu is one. The Cu(II) species decreases with the depth in the sample.

In fig. 3.35, the measurements in the Cu region between 939 to 929 eV have been fitted. For the fitting curve parameters values are taken from the NIST XPS Database,[180] as described by Biesinger et al.[178] (see table 3.6 on page 91). The fitted measurements show clearly that the surface of the sample consists mainly of Cu(II). After the top layer is removed, through sputtering the main component in the subsurface region of the sample is Cu(I) with a small part of Cu(II). With increasing depth in the subsurface region of the sample, the concentration of Cu(II) decreases further.

The XPS measurements of Au (see fig. 3.36) show no significant shift in the position of the peak. The intensity increases however from the surface to the subsurface regions. In the deepest measured part of the sample the intensity doubles again. This intensity change is visualized more clearly in fig. 3.37. The scans in the oxygen region change in counts. The complete

Table 3.6 Fitting parameters for Cu species in XPS measurements. The values are taken from Biesinger et al.[178] and NIST XPS Database[180].

Compound	Cu $2p_{3/2}$ (eV)	Std. Dev. (±eV)	FWHM (eV), 10 eV pass energy	FWHM (eV), 20 eV pass energy	Modified Auger par. (eV)	Std. Dev. (±eV)
Cu^{I}_2O	932.18	0.12	0.88	0.98	1849.17	0.03
$Cu^{II}O$	933.76	0.11	3.00	3.00	1851.33	0.05

surveys for the sample can be found in the appendix on page 227 - 229. In the two surveys (fig. 7.12a and b) all mayor peaks are described, they can be found in the appendix on page 230.

In fig. 3.37, the counts at the maximum of the Cu binding energy and the Au binding energy have been plotted against the cumulative sputter etching time. For both graphs, there is a generally increasing trend from the surface to buried subsurface regions. The subsurface regions were made accessible by removing the surface with plasma etching inside of the UHV system. For the Au (fig. 3.37 (a)), the 75 s of etching results in a sharp increase of the measured counts. To explain this, one has to assume that the Au atoms are mobile during the tempering process. There are two possible ways the trend can be explained. The first explanation is that the Au atoms move in all directions during the tempering step. Since there is a thin 100 % Au layer under the sample, statistically more Au atoms move from the bottom towards the surface than from the upper layer towards the bottom. Since there is a region of 0% Au (air) on top of the sample, it also explains that the surface region has less gold content. The second explanation is best suited to describe the sharp increase in the gold content from the third to the fourth measurement, which could be caused due to the very thin sample film, which is left after 75 s of Ar sputtering. Thus parts of the gold could

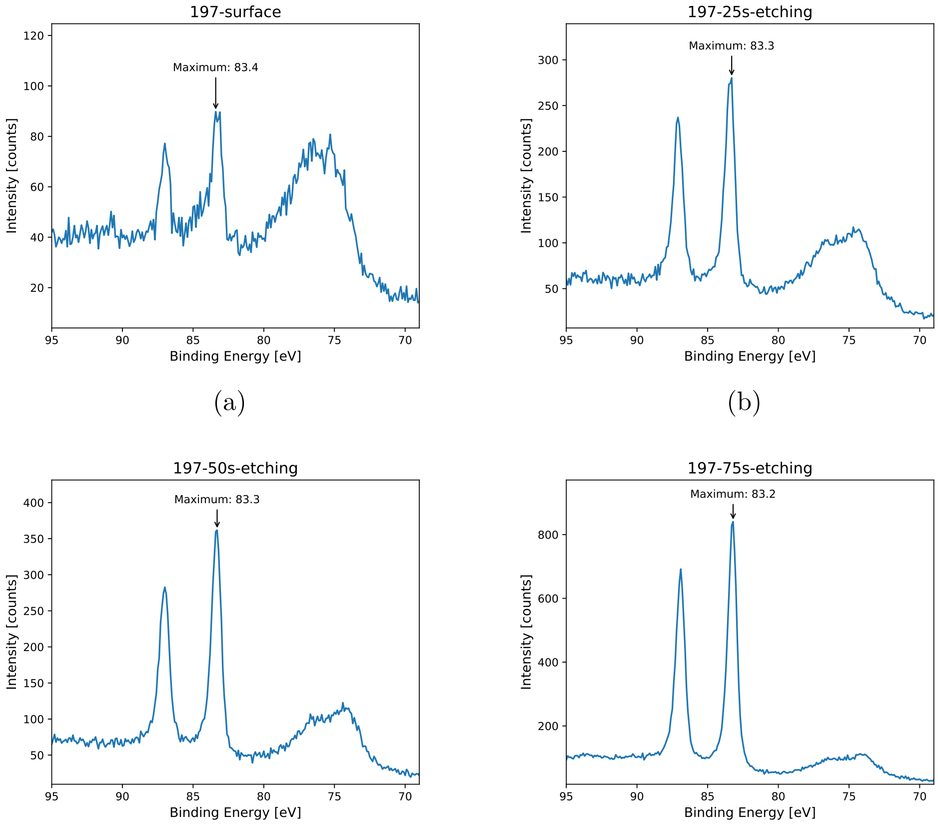

(a) (b)

(c) (d)

Figure 3.36 XPS spectra of the Au binding energy region for sample 197a: In (a) the binding energies of gold is depicted, at the sample surface. In (b) the same region is depicted after 25 s of sputtering. In (c) the surface layer of the sample was removed again by an additional sputtering of 25 s. In (d) the total sputtering time was 75 s.

already be partly exposed, or the remaining film is so thin that part of the signal comes from the gold layer underneath the thin film.

For Cu, the sharp increase in counts from the surface to the etched measurements in fig. 3.37 (b) can be explained by the higher oxygen content at the surface. These measurements confirm the depth profile suggested in fig. 3.26 on page 76. The conclusions drawn from the XPS measurements

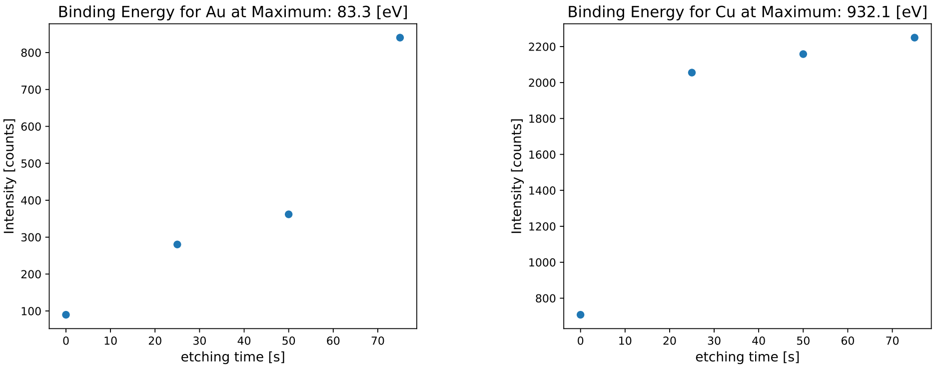

(a) (b)

Figure 3.37 The graphs display the maximum counts of the XPS spectra at their respective maxima vs. cumulative etching time. In (a) the change of the Au counts at the maximum are shown. The maximum counts rise slightly from the surface to the 50 s of etching time, for the 75 s, there is a significant increase in counts. This last increase could be due to the gold layer underneath the sample. In (b) the change of the Cu adsorption is shown. The higher amount of oxygen at the surface is an explanation for the low Cu counts.

correspond to the conclusions drawn from the NEXAFS measurements under different incidence angles. Moreover, these results are fully consistent with GIXRF data.

3.3 Thermoelectric Properties of Organic Thin Films

In this section the investigation into organic thin film thermoelectrics is summarized. The organic thin films have been prepared from solution by spin-coating them onto a carrier material. The measurements have been performed with the developed Seebeck measurement device. The organic thin films made from PEDOT:PSS and PANI have high conductivities with Seebeck coefficients slightly lower than the inorganic thin films.

3.3.1 Thin Organic PEDOT:PSS Films

The preparation and measurements were part of publications in "Advanced Electronic Materials"[181] and "ACS Applied Materials & Interfaces"[182], the relevant parts for this work are summarized in this chapter. PEDOT:PSS (poly (3,4-ethylenedioxythiophene): poly (styrenesulfonate)) samples have been prepared by making 20 g of an aqueous solution of PEDOT:PSS (Orgacon DRY, a product manufactured by Agfa-Gevaert, the product was purchased from Sigma-Aldrich) with a concentration of 10 g per liter. The PEDOT:PSS was dissolved at room temperature by stirring it for 48 h. Samples made from this solution are later abbreviated with PP. A similar solution to the 1 wt % solution described above, with an added 5 vol% of dimethyl sulfoxide (DMSO) was prepared. Samples made from this solution are later abbreviated with PP5D. The solutions were coated on a glass substrate of 25 mm by 25 mm. The glass substrates were treated with piranha solution (volume ratio: 7:3 H_2SO_4(97%) : H_2O_2(30%)) for 20 min in order to remove any organic residues and to make the surface hydrophilic. For each layer, two drops of the polymeric solution were spread on the substrate and then spread at 500 RPM with a spin coater (Chemat Technology KW-4A Spin-Coater) for 15 s. The excess solution was removed with the second speed of the spin coater for 60 s. This second speed was varied between 1000 and 3000 rpm. After each spin-coating of a layer, the samples were dried for 300 s at 403 K. The number of tested layers was varied between 1 and 5. For each sample, two contact stripes were applied using a mask. The stripes are 17 mm apart. The stripes were made with Ferro GmbH silver

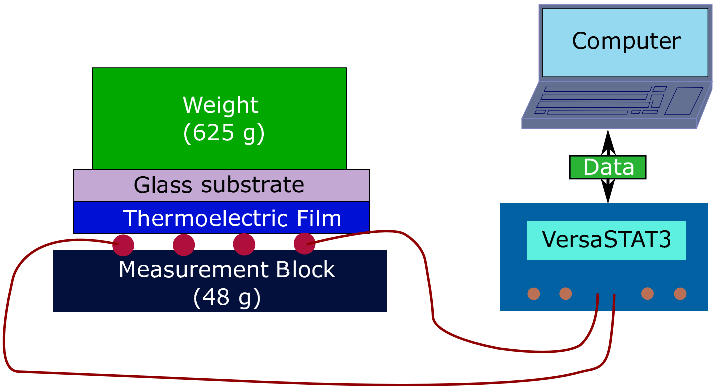

Figure 3.38 Schematic of the measurement setup used to determine the electrical conductivity of thin film samples. The measurements are conducted using the quasi-4-point method.

paste. The film thickness of the samples has been measured with AFM. The details of the AFM measurements have been reported in the publication.[182]

For the PEDOT:PSS samples, the electrical resistance was measured with a quasi-4-point configuration. Fig. 3.38 illustrates the measurement setup. The sample to be measured is located over a POM block containing four copper wires which are embedded parallel and milled to have the same height. The VersaSTAT3 electrode pairs connect to the outer wires serving both as a current source and voltage sensors. The electrode block is held down by a 625 g weight to apply even pressure. In the measurement software (VersaStudio 2.44.4), the chrono potentiometric sequence was chosen. The chrono potentiometric sequence keeps the current constant and measures the voltage once every second for a measurement period of 30 s. As an example of the obtained results, the measurement in fig. 3.39 is shown.

The average electrical resistivity was calculated with eq. (3.1) and the uncertainty of the result with eq. (3.2). The average height of the sample

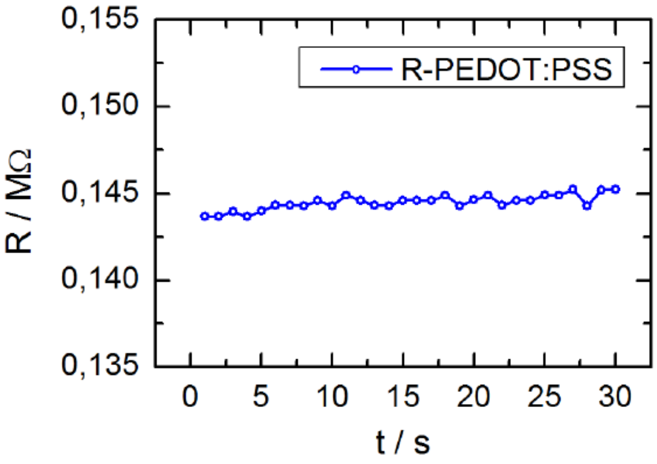

Figure 3.39 Room temperature measurement of resistance for a PEDOT:PSS thin film. The image shows the raw measurement data. This image has been published in "Advanced Electronic Materials".[181] Permission to reproduce kindly granted by Wiley.

($\overline{h}$) and the corresponding uncertainty (e_h) of the thin film samples were calculated using the same equations with n=3.

$$\overline{R} = \frac{\sum_{i=1}^{n} R_i}{n} \tag{3.1}$$

$$e_R = \sqrt{\frac{\sum_{i=1}^{n}(R_i - \overline{R})^2}{n-1}} \tag{3.2}$$

The width of the samples (w) for the PEDOT:PSS films is 25 mm. With this information, the average conductivity was calculated using eq. (3.3) and the uncertainty with eq. (3.4). The error of the width of the sample was neglected.

$$\overline{\sigma}_{tf} = \frac{1}{\overline{h} \cdot \overline{R} \cdot w} \tag{3.3}$$

$$\%e_{\sigma_{tf}} = \sqrt{\%e_h^2 + \%e_R^2} \tag{3.4}$$

The Seebeck coefficient has been measured for all the samples using a similar setup to the one described in fig. 3.2. In fig. 3.40, the thermoelectric properties of the single-layer PEDOT:PSS samples are summarized. The spin-coating velocity (v2) has a negligible effect on the thermoelectric properties but influences the film thickness significantly at v2 =1000 rpm the film thickness is 168 ± 38 nm. At v2 = 3000 rpm, the film thickness decreases to 66 ± 22 nm. The electrical conductivity (σ) decreases only slightly from a maximum of 0.53 ± 0.12 S cm^{-1} to a minimum of 0.39 ± 0.07 S cm^{-1}. The DMSO doped samples (PP5D) show similar results to the PP samples. The change in thickness descends steeper from 202 ± 83 to 60 ± 17 nm. For the electrical conductivity, the PP5D samples vary between the maximum of 140 ± 58 S cm^{-1} and a minimum of 98 ± 29 S cm^{-1}. This variation is

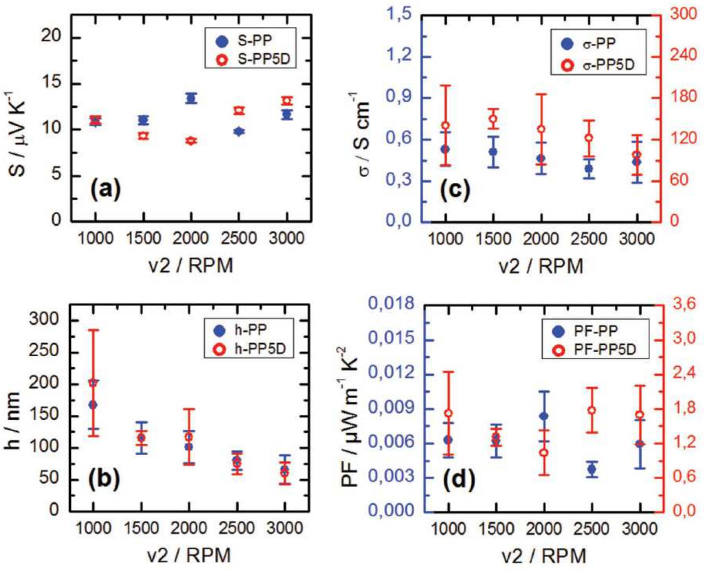

Figure 3.40 Thermoelectric properties of single layer PEDOT:PSS samples. The blue results are made from PP solution, the red from PP5D. a) shows the Seebeck coefficient, b) the film thickness, c) the electrical conductivity and d) the power factor. All values are displayed against the rotation per minute during preparation. This image has been published in "Advanced Electronic Materials".[181] Permission to reproduce kindly granted by Wiley.

similar to the typical experimental uncertainty and is comparable to other results in the literature.[83,150,183] Thus, the primary influence on the power factor is the Seebeck coefficient, which fluctuates around 11.5 μVK^{-1} as shown in fig. 3.40a) and d). The results obtained for the Seebeck coefficient are consistent with the work by Crispin et al.,[184] which also used PEDOT:PSS from Agfa-Gevaert as a starting material.

The results for the multilayer samples are summarized in fig. 3.41, where the situation is different. The thickness of the films is rising as expected, with increasing numbers of coated layers. For the PP samples, the thickness starts at 101 ± 25 nm for a single layer and increases up to 445 ± 52nm for five layers (see fig. 3.41 b)). The electrical conductivity increases faster than the layer thickness resulting in a total enhancement of a factor of 4.5 from a single layer with an electrical conductivity of 0.46 ± 0.11 S cm^{-1} to the 2.10 ± 0.26 S cm^{-1} for the five-layer samples. These results are surprising since literature reports values of less than 1 S cm^{-1} for pristine PEDOT:PSS films.[184,185] For the samples with different numbers of layers, the Seebeck coefficient stays in a narrow range between 9 and 13 μVK^{-1} (see fig. 3.41 a). This improvement of the conductivity with a relatively constant Seebeck coefficient results in an increase of the power factor by approximately 3.4 times from 8.3 ± 2.2 to 28.3 ± 3.6 nW m^{-1} K^{-2} (fig. 3.41d). For the PP5D samples, the conductivity is higher by two orders of magnitude, but there seems to be a plateau at approximately 200 S cm^{-1}, which is reached with just three layers (fig. 3.41b). The higher conductivity leads to an increase of the power factor up to a value of 2.11 ± 0.22 μWm^{-1}K^{-2}. This is an enhancement of 1.9 times compared to the single-layer sample. The shown enhancements surpass the improvements usually reached by conventional

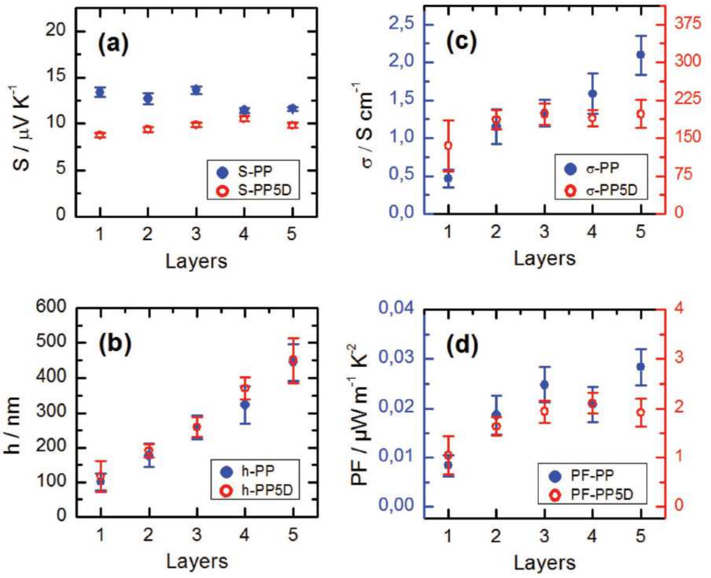

Figure 3.41 Thermoelectric properties of multilayer PEDOT:PSS samples. The blue results are made from PP solution, the red from PP5D. a) shows the Seebeck coefficient, b) the film thickness, c) the electrical conductivity and d) the power factor. All values are displayed against the number of layers coated onto the substrate. This image has been published in "Advanced Electronic Materials".[181] Permission to reproduce kindly granted by Wiley.

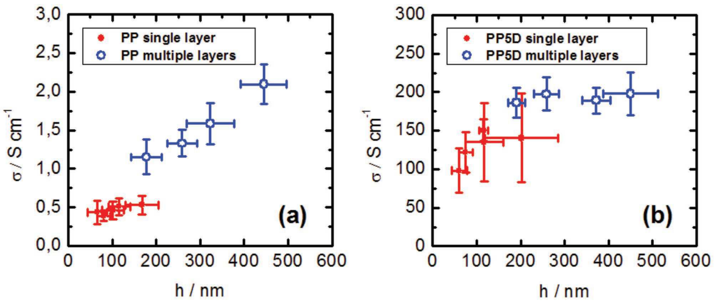

Figure 3.42 Conductivity and film thickness comparison of the single (red) and multilayer (blue) samples. In a) the PP samples are shown, in b) the PP5D samples. This image has been published in "Advanced Electronic Materials".[181] Permission to reproduce kindly granted by Wiley.

surface treatment. The typical treatment for PEDOT:PSS samples is the removal of excess PSS chains by washing with polar solvents.

The correlation between the sample preparation, electrical conductivity, and film thickness are illustrated in fig. 3.42. In general, the electrical conductivity σ increases with film thickness h. In addition, there is a significant increase in σ between single and multilayer samples. There are two proposed mechanisms for this increased conductivity, which are discussed in detail in our publication.[181] The first possible mechanism: partial solvation of the polar PSS chains leads to inner surfaces with increased conductivity. In the case of the second possible mechanism, smaller grains or even single chains are included in the structure, which increases the number of contacts between the grains.

In summary, the conductive polymer PEDOT:PSS has been coated onto a carrier material. The samples have been prepared purely from aqueous solution and doped with 5% DMSO. The doped samples show increased conductivity. By multiple coating of PEDOT:PSS layers, a significant improvement of the electrical conductivity was observed. Since the increase in conductivity is higher than expected by ordinary methods, two possible mechanisms were suggested to explain the improvement. The enhancement is probably caused by a combination of the reorganization of conjugated polymer chains and percolation between grains.

3.3.2 Thin Organic Alternating PEDOT:PSS and PANI Films

In this section, thin films of the conductive polymers PEDOT:PSS and PANI (polyaniline) have been deposited on a glass substrate by spin coating. The work was published in "ACS Applied Materials & Interfaces."[182]

Table 3.7 Details about the purchased chemicals. The displayed information is publicly available at the manufacturer or vendor website. The information in this table has been published in the supporting information of the "ACS Applied Materials & Interfaces" publication by V. Andrei et al.[182]

Substance	Other names	Vendor	Specifications
PEDOT:PSS	Orgacon™ DRY	Sigma Aldrich (Agfa-Gevaert)	dry re-dispersible pellets sheet resistance: 200-450 Ω/sq melting point > 300 °C Virtually 100% absorption from 900-2000 nm No absorption maximum from 400-800 nm Visual Light Transmission: ~85%
PANI	Emeraldine base	Sigma Aldrich	Molecular weight ≈ 50000 $\lambda_{max} = 330$ nm soluble in: m-cresol, DMAC, DMF, DMSO, NMP
DMSO	Dimethyl sulfoxide ROTIPURAN®	ROTH	≥99.8 %, p.a. M = 78.13 g/mol; $\rho \approx 1.1$ g/mL Flp 87 °C; Kp ≈ 189 °C

This section is a summary of the publication. A stock solution of PEDOT:PSS has been prepared by dissolving 200 mg of PEDOT:PSS from Sigma-Aldrich/Agfa-Gevaert in 19.8 mL of deionized water. The dissolving was done with stirring at room temperature for 48 h. The stock solution of PANI was prepared at room temperature by stirring 33 mg of PANI in 3.0 mL of dimethyl sulfoxide (DMSO) for 48 h. The saturated solution contained undissolved PANI. Therefore the liquid part was decanted to obtain the stock PANI solution. Details of the used chemicals can be found in table 3.7.

With the stock solutions, multilayered films have been spin-coated on a 25 by 25 mm square glass slide using a Chemat Technology KW- 4A spin coater. The glass carriers were cleaned for 20 min in piranha solution (3 parts of H_2SO_4 to 1 part of H_2O_2 by volume). Due to the difference in polarity of the two polymers, they are interacting with each other. The interaction is the reason for the low wetting ability of the solution onto a previous film. The solutions were manually spread onto the already deposited films to increase the homogeneity. The spin coater was set to spin in two steps: first at 500 rpm for 15 seconds to spread the solution and then at 2000 rpm for 60 s. The deposition of multilayers was done in two different procedures: In the "dry" procedure, the films were annealed in an oven at 403 K for 5 min after each deposition of a polymer solution.

In contrast, in the "wet" procedure, the annealing step was omitted, and the next film was spin-coated onto the moist layer underneath. With the "wet" procedure, the alternating polymer solutions were directly coated onto each other. The annealing was only performed after the last deposition. For both procedures, the final dry multilayer films were coated with two silver paste stripes, to provide proper electrical contact areas.

The properties relevant to thermoelectrics were measured at room temperature. The Seebeck coefficient was investigated with the measurement setup for thin films. Fig. 3.2 on page 37 gives a schematic representation of the measurement setup employed. The measurements were performed in steps of 10 K. For the electrical resistance a VersaSTAT3 programmable current source was used to measure in a quasi-four-point configuration. Quasi-four-point means that probe and current source are connected at the sample, eliminating the resistance of the wire.

For the non-doped PANI Seebeck values of 12 μVK^{-1} were observed. The 12 μVK^{-1} corresponds to the values between 2–17 μVK^{-1} as found from many different research groups for PANI.[186–191] The Seebeck coefficient of such sample systems has been enhanced by several groups for example by adding tellurium nanorods,[192,193] carbon nanotubes[193–195] or by tuning the charge doping of the polymer chains.[186,196,197]

3.4 Thermoelectric Powders

During this work, Al-doped ZnO powders have been analyzed for their thermoelectric properties. The samples have been prepared by our partners from the Madurai Kamaraj University.

The Al-doped ZnO powder was prepared by dissolving 9.1 g (41.5 mmol) of zinc acetate dihydrate and 0.8 g (5 wt.% of the solution, 2.1 mmol) aluminum nitrate nonahydrate in 250 ml of double-distilled water. To this solution, 250 ml NaOH solution (0.8 mol/l) was added dropwise under vigorous stirring over a time period of 30 min. The reaction was performed at room temperature. The suppliers and the purity of the used chemicals are listed in table 3.8. A white gelatinous precipitate was obtained. This precipitate was heated at 80 °C for 5 hours. After centrifuging the precipitate, the product was washed three times with bi-distilled water and ethanol to remove the remaining sodium salts. The obtained samples were annealed at temperatures between 600 °C and 1200 °C for two hours.

Table 3.8 Used chemicals for the synthesis of aluminum-doped zinc oxide with suppliers and purity.

Substance	Vendor	Purity
$Zn(COOH)_2 \cdot 2\,H_2O$	Merck	97%
$Al(NO_3)_3 \cdot 9\,H_2O$	Merck	98%
NaOH	Merck	99%

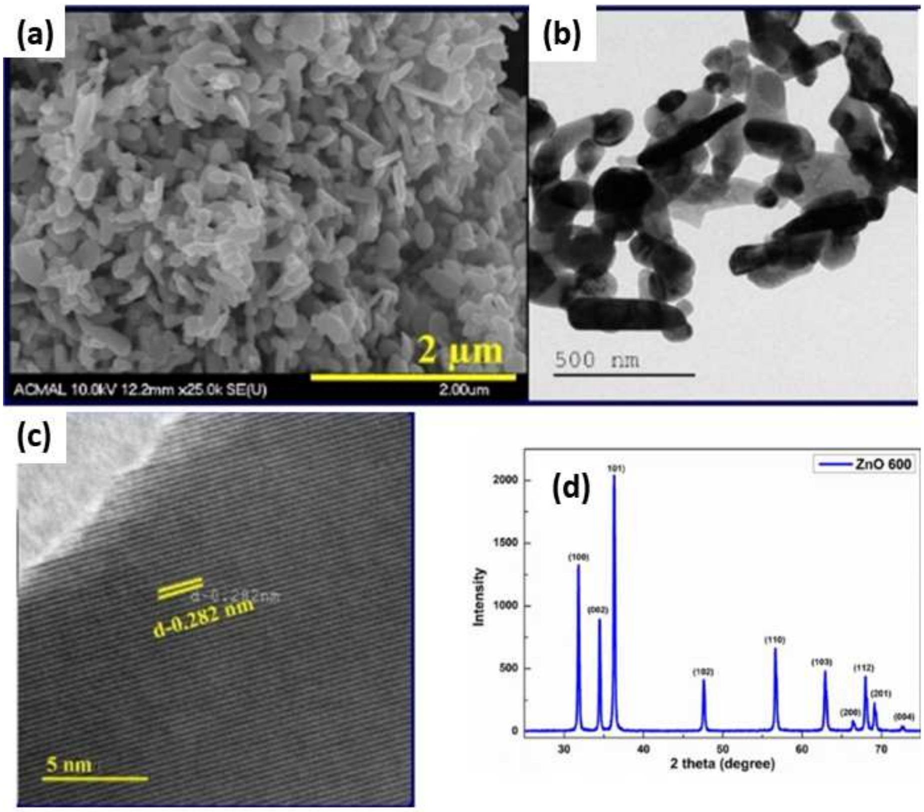

Figure 3.43 Characterisation of the ZnO samples at 600 °C: (a) SEM micrograph, (b) HRTEM image, (c) corresponding fringe pattern, (d) powder XRD.

In fig. 3.43 the characterization of the ZnO powder annealed at 600 °C is summarized. The SEM and HRTEM in fig. 3.43 (a) and (b) show pebble-like nanoparticles of irregular shape, with sizes between 50-500 nm. The particles reveal a good crystallinity, as seen from the HRTEM fringe pattern fig. 3.43 (c), and the sharp powder XRD peaks fig. 3.43 (d). The samples were annealed at temperatures between 600 °C and 1200 °C, to investigate the influence of the grain size, shape, and connectivity on the electronic properties. As observed from the SEM images in fig. 3.44, the increase in temperature leads to a growth in the particle size from the initial 50-500 nm to up to 10 μm. The growth in size corresponds to a change in morphology, from the poorly connected particles, via face-sharing grains, to sintered macro-particles with well-defined grain boundaries. The change in the particle shape and size significantly influences the conductivity. The increase in conductivity is due to the charges being easily transmitted over larger grains instead of hopping between a multitude of individual smaller particles.

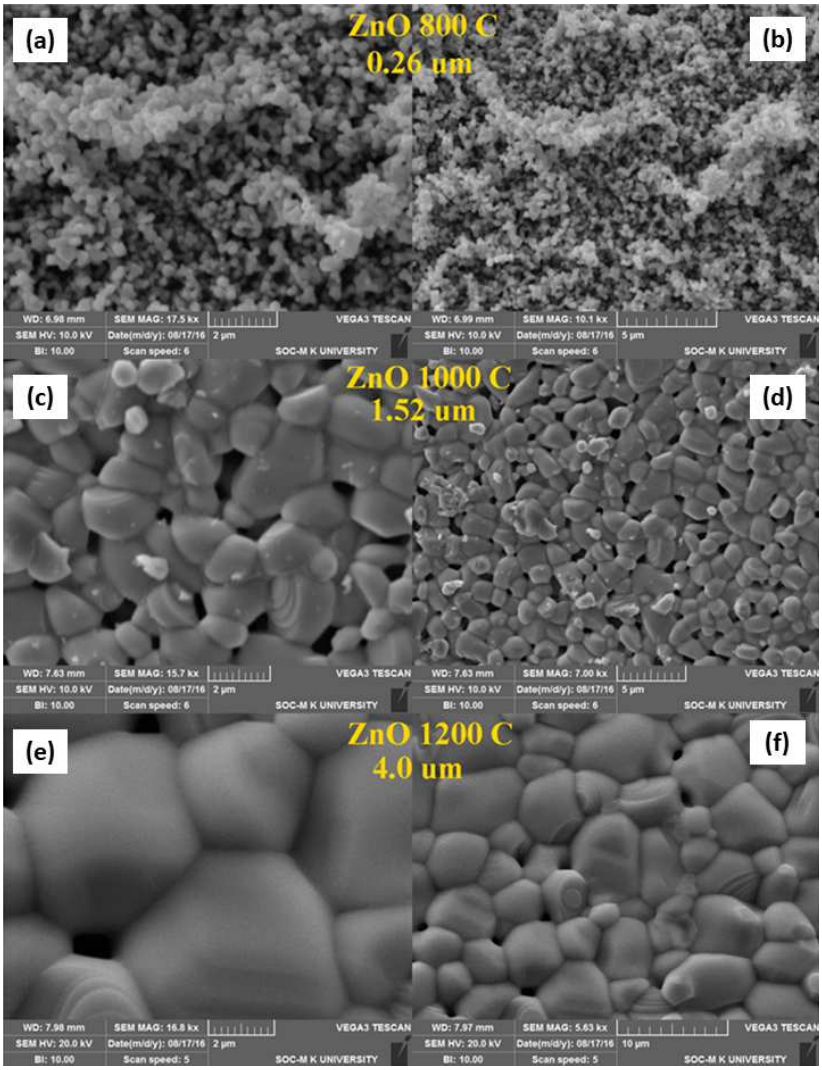

Figure 3.44 In these SEM images ZnO powders annealed at 800 °C (a) and (b), 1000 °C (c) and (d) and at 1200 °C (e) and (f) are shown. The particle size increases with increasing annealing temperature and the number of grain boundaries decreases.

The measurement results for the thermoelectric potential are presented in fig. 3.45. The aluminum-doped samples annealed below 1200 °C show significant noise and non-linear behavior. Thus, it was not possible to interpret the measurement results. The Al-doped ZnO sample annealed at 1200 °C shows a linear behavior with little noise in the measurement. The noise, for the sample annealed below 1200 °C, during the measurement, is most likely caused by the low conductivity of the samples. Due to its improved percolation, the thermoelectric potential of the aluminum-doped sample of ZnO annealed at 1200 °C follows the expected linear behavior with the temperature, corresponding to an average Seebeck coefficient of 7.3 μVK^{-1}.

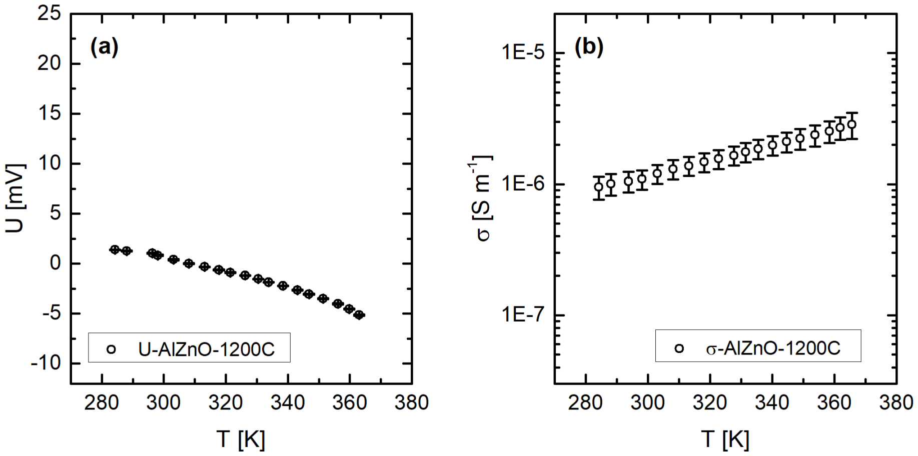

Figure 3.45 Thermovoltages and conductivity of Al doped ZnO powder annealed at 1200 °C.

To summarize, the samples show comparable behavior to other ZnO samples reported in the literature,[198] but their thermoelectric values are well below the ones reported for sintered or nanowire samples.[163] Nevertheless, the measurements show that it is possible to use the modified measurement device for powdered samples if the overall powder has a sufficiently high conductivity. For the Al-doped ZnO powders, the conductivity has been increased by higher temperatures during the tempering process.

3.5 Thermoelectric Pastes

With a modified measurement setup, powders and pastes made from thermoelectric materials have been measured. The modified setup contains a ring-shaped Teflon cell with the sample between two copper contacts. The Peltier elements are arranged above and below the measurement cell. A schematic representation of the setup is shown in fig. 3.46.

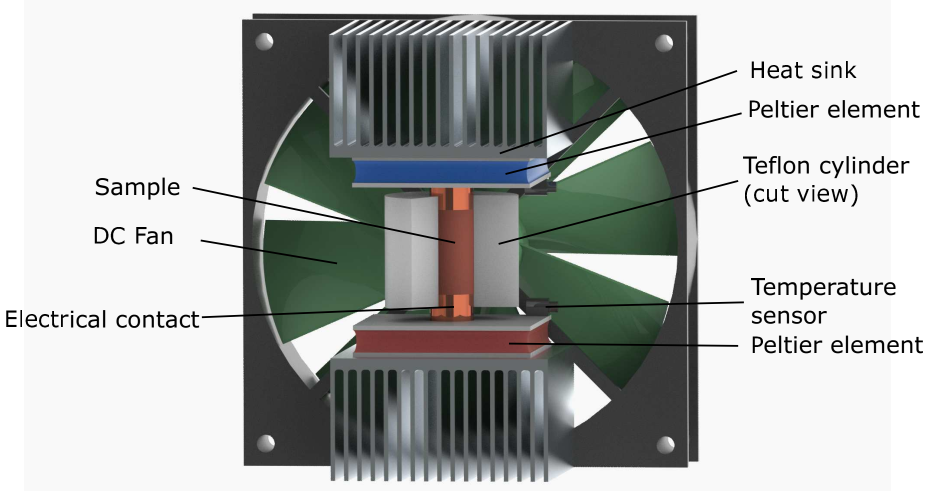

Figure 3.46 Schematic rendering of the measurement setup used to measure powder and paste-like samples. The Teflon cylinder used to contain the samples is shown in a cut view to show the inside. To prepare for the measurement, the bottom copper contact is put in the Teflon cell, the sample is filled on top of the contact and compacted with the second copper contact.

The samples investigated in the publications by Andrei et al.[164,199] were measured with the setup described in fig. 3.46, in addition to measurements with one heat source and a water-based cold reference. The measured samples were prepared from copper(I) oxide (Cu_2O, powder <5 μm). To improve the electrical properties graphite powder (< 20 μm) in various ratios was added. The samples were compacted in the Teflon cell between the copper cylinders, with a manual vise, thus maintaining the original properties of the powders. For the paste-like samples the premixed powders were mixed with polychlorotrifluoroethene (PCTFE, Kels-F90 from ROTH). The samples have been prepared with a mass ratio of 7 : 1 (molar ratio of powder : CTFEmonomer $\approx$ 5.7). The molar mass ratio is calculated as an example for the Cu_2O:graphite = 65:35 sample in eq. (3.5).

$$m_{PCTFE} : m_{Cu_2O} : m_{graphite} = 1 : 7 \cdot \left(\frac{65}{35} \cdot \frac{12.01}{143.09}\right) \tag{3.5}$$

Table 3.9 Seebeck coefficients of the copper oxide mixtures, as powders and as pastes with PCTFE.

Sample	S_{Powder} (μV/K)	S_{Paste} (μV/K)
Cu_2O	656±5	539±4
Fe_2O_3,Cu_2O	698±5	606±5
CuO,Cu_2O	690±4	530±4
TiO_2,Cu_2O	729±4	465±5

Besides the pure Cu_2O powder and paste sample, several mixed samples have been prepared. First powder mixed samples have been prepared; those were used to prepare the pastes like described earlier. The Powder samples were always mixtures of nine parts by weight of Cu_2O with 1 part by weight of a transition metal oxide. With the PCTFE samples, Seebeck coefficients of up to 656 ± 5 μVK^{-1} have been measured.[199] For pure powder samples with small amounts of transition metal doping values of up to 729 ± 4 μVK^{-1} were observed. The Seebeck coefficients of all the samples are summarized in table 3.9.

In this section and the previous sections, it has been shown that the measurement setup is capable of measurements for organic and inorganic thin films. Besides, the analysis of powders and pastes is possible with slight modifications of the setup. For the measurements of powders, the high resistivity is the limiting factor of what can be measured.

3.6 FEM Simulations of Thermal Conductivity in Thin Films

This chapter has been published in large parts in plosOne.[145] For many materials, which can be considered for thermoelectric applications, the thermal conductivity is high which results in a low ZT value (see eq. (2.6) on page 18) and thus a low efficiency. By lowering the thermal conductivity κ, the performance is improved. The higher efficiency for a lowered κ can be explained in a simple way. A higher κ means a faster heat transfer through a thermoelectric material, which results in a reduced temperature difference between the two ends. Since the magnitude of the generated voltage is directly proportional to the extent of the temperature difference, the performance also dwindles.[66,83,200,201]

In this chapter, a theoretical consideration on supported materials, especially thin films, will be conducted and backed up by FEM analysis. The hypothesis which shall be checked is that in thin films the effective thermal conductivity of the entire ensemble is mainly dependent on the supporting material. In fig. 3.47, both possible types of thermal resistance (parallel and in series) for a system consisting of two dissimilar materials are illustrated. Depending on the direction of the heat flow $\dot{Q}$, the thermal resistance is either in parallel, in series, or a combination of both.

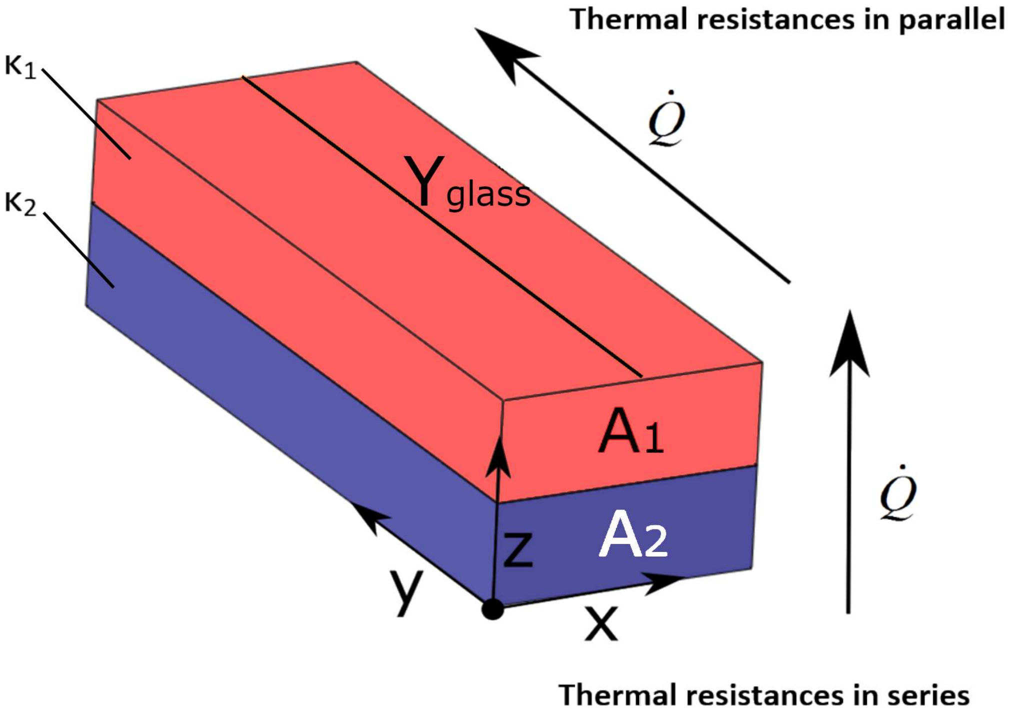

Figure 3.47 This model illustrates the different possible types of heat transfer. Two materials shown in red and blue contact each other. If the heat flow $\dot{Q}$ is along the Z-axis, their thermal resistance is in series, while the heat flow along the Y-axis has to overcome the thermal resistance in parallel. y_{glass} represents the length of the layers, A is their heated area and κ the thermal conductivity. The red upper layer, which will also be referred to as the active or thermoelectric layer, is indicated by index 1, while supporting material colored in blue has the index 2.

κ_i represents the thermal conductivity of each of the materials. The symbol A_i represents the area of the thermoelectric material (index i = 1), and the support material (index i = 2). y_{Glass} is the length of the materials. In this thought experiment, the thermal conductivity of the supporting material κ_2 is lower than the thermal conductivity of the thermoelectric material κ_1. In the case of parallel thermal conduction, both layers are heated through the surfaces A_1 and A_2, whereas in the FEM simulations only one of the two areas is heated at a time. This similar 1D case can be used to verify the qualitative conclusions drawn from the FEM simulations, as discussed later in this chapter. The definition of the thermal resistance R is given in eq. (3.6). Similar to electric resistance, the thermal resistance is inversely proportional to the thermal conductivity κ.

$$R = F\frac{y_{Glass}}{A \cdot \kappa} \tag{3.6}$$

In analogy to electrical circuits, the effective thermal conductivity κ_{eff} of this model system can be calculated as follows:

$$\frac{1}{R_{eff}} = \frac{1}{R_1} + \frac{1}{R_2} \tag{3.7}$$

$$\frac{(A_1 + A_2) \cdot \kappa_{eff}}{y_{Glass}} = \frac{A_1 \cdot \kappa_1}{y_{Glass}} + \frac{A_2 \cdot \kappa_2}{y_{Glass}} \tag{3.8}$$

$$(A_1 + A_2) \cdot \kappa_{eff} = A_1 \cdot \kappa_1 + A_2 \cdot \kappa_2 \tag{3.9}$$

$$\kappa_{eff} = \frac{A_1 \cdot \kappa_1 + A_2 \cdot \kappa_2}{A_1 + A_2} \tag{3.10}$$

For parallel resistors the inverse resistance values are added to find the inverse effective resistance (eq. (3.7)). By inserting eq. (3.6) into eq. (3.7), eq. (3.8) is obtained. From eq. (3.8) y_{Glass} can be eliminated which results in eq. (3.9). Finally eq. (3.9) is divided by (A_1+A_2) this results in eq. (3.10) for the effective thermal conductivity. If the area A_1 of the thermoelectric material is much smaller than the area of the substrate A_2, and if the same is true for the products of A_i and k_i ($A_1 \cdot \kappa_1 << A_2 \cdot \kappa_2$), the following eq. (3.11) holds.

$$\kappa_{eff} \approx \frac{A_2 \cdot \kappa_2}{A_2} \Leftrightarrow \kappa_{eff} \approx \kappa_2 \qquad (3.11)$$

These equations lead to the conclusion that a decreased thickness of the thermoelectric layer leads to a reduction of the effective thermal conductivity κ_{eff}. This reduction can go down to the value of the substrate material κ_2.

If the areas of the two materials A_1 and A_2 are the same size ($A_1 = A_2$) and if the thermal conductivity of the active materials is higher than the thermal conductivity of the supporting material ($\kappa_1 > \kappa_2$), one gets eq. (3.12) from eq. (3.10).

$$\kappa_{eff} \approx \frac{A_2 \cdot (\kappa_1 + \kappa_2)}{2 \cdot A_2} \Leftrightarrow \kappa_{eff} \approx \frac{\kappa_2 + \kappa_1}{2} \qquad (3.12)$$

Even in this case, the effective thermal conductivity of the ensemble is smaller than κ_1.

All simulations done in this chapter are performed using the software Comsol Multiphysics 4.4. In the study, thin films of three sample materials with thermoelectric properties (Cu, Cu_2O, and PbTe) are modeled on a glass microscope slide as supporting material. Glass microscope slides have been chosen as supporting material because it is a cheap, convenient and widely available material for laboratory samples. For the glass type Pyrex glass was chosen due to its availability and defined properties. Three essential parameters for the simulations, the thermal conductivity (κ), the heat capacity at constant pressure (C_P) and the density (ρ) of the mentioned substances are presented in table 3.10, along with their thermoelectric properties.[202,203]

Table 3.10 In this table several relevant material parameters of copper, copper(I) oxide and lead telluride at 293 K are summarized. This table has been reproduced from the manuscript published in PlosONE.[145]

Sample	S [μV K^{-1}]	σ [S m^{-1}]	κ [W m^{-1} K^{-1}]	PF [μW m^{-1} K^{-2}]
Cu	1.83 ^{a}	$5.99{\cdot}10^7$ ^{b}	397 ^{b}	201
Cu_2O	1100 ^{c}	$2.24{\cdot}10^{-3}$ ^{c}	6.28 ^{c}	$2.71{\cdot}10^{-3}$
PbTe	187 ^{d}	$6.10{\cdot}10^4$ ^{d}	1.46 ^{d}	2132
Sample	ZT [-]	C_P [J kg^{-1} K^{-1}]	ρ [kg m^{-3}]	
Cu	$1.48{\cdot}10^{-4}$	383 ^{b}	8940 ^{b}	
Cu_2O	$1.26{\cdot}10^{-7}$	436 ^{b}	6000 ^{b}	
PbTe	0.43	151 ^{d}	8160 ^{d}	

a - Value at 300 K, taken from Cusack and Kendall.[202]
b - Data obtained using the fitted functions in the Comsol Multiphysics database (see table 7.3 in the Appendix on page 238).
c - Data taken from the works of Vogt.[203] σ is given at 298 K and κ at 273 K.
d - Given values in the Comsol Multiphysics database.
The parameters are needed to describe the materials thermoelectric properties and to simulate the heat transfer. The power factors (PF) and the figures of merit (ZT) are calculated at 293 K from the given S, σ and κ values.

The values given in table 3.10 are at a temperature of 293 K, unless stated otherwise. The thermal conductivity κ and C_P of glass are plotted in fig. 3.48 in the temperature range between 270 and 400 K. The functions used to plot those curves, were obtained from the Comsol Multiphysics database and are shown in table 7.3 in the Appendix on page 238. The thermal conductivity has a significant change in this temperature interval, and it increases from 1.05 to 1.25 Wm^{-1}K^{-1}. Also the thermal capacity undergoes a substantial change. The thermal capacity increases from 700 to 900 J kg^{-1}K^{-1} (see fig. 3.48). For the density of glass, the change is minimal in that temperature range from 2227 to 2231 kg m^{-3}. The simulated glass was modeled to the size of a standard microscope slide (25.4 mm x 76.2 mm x 1.0 mm). Thick layers are modeled as rectangular solids with identical dimensions as the supporting material. For thin layers, the thickness was changed to 100 nm, while the other dimensions are identical to the substrate. For all the graphs obtained from this simulation, the temperature is displayed as a function of the distance in the y direction from the origin in the middle of the glass. The y-direction is marked in fig. 3.47 and in fig. 3.49.

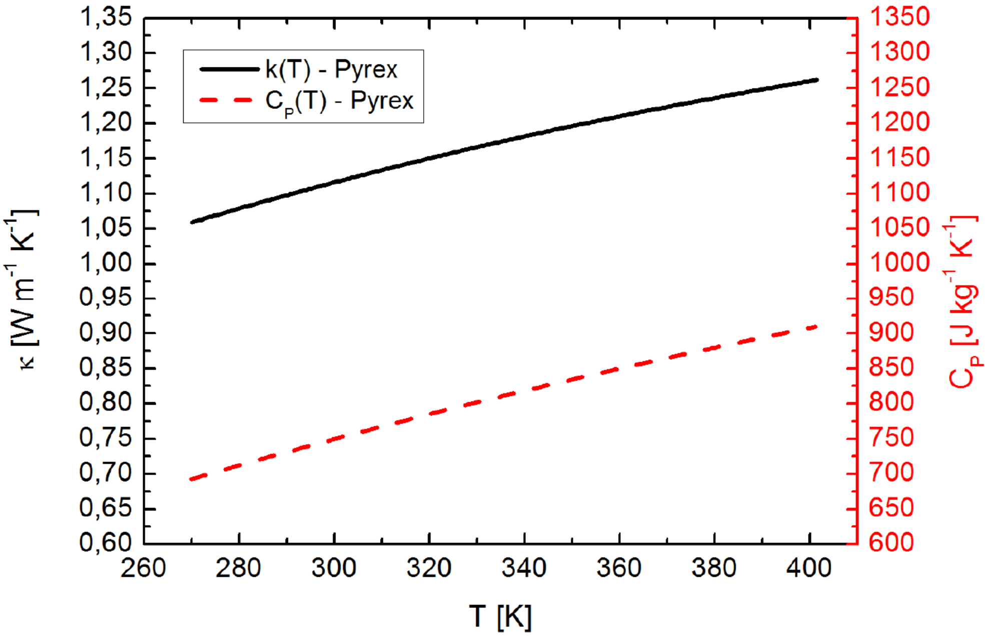

Figure 3.48 The thermal conductivity (κ) of Pyrex glass is depicted in black, the heat capacity at constant pressure (C_p) of Pyrex glass is represented in red. The Data displayed was obtained by fitting the functions in the Comsol Multiphysics database (see table 7.3 in the Appendix on page 238). This image is reproduced from Bethke et al.[145]

For the FEM simulations performed in Comsol Multiphisics eq. (3.13) was used to calculate the heat transfer in solids. In eq. (3.13) ρ represents the density, C_P is the heat capacity at constant pressure, T is the absolute temperature, v the velocity field, κ the thermal conductivity and Q the heat source.

$$\rho C_P \frac{\partial T}{\partial t} + \rho C_P v \cdot \nabla T = \nabla \cdot (\kappa \nabla T) + Q \tag{3.13}$$

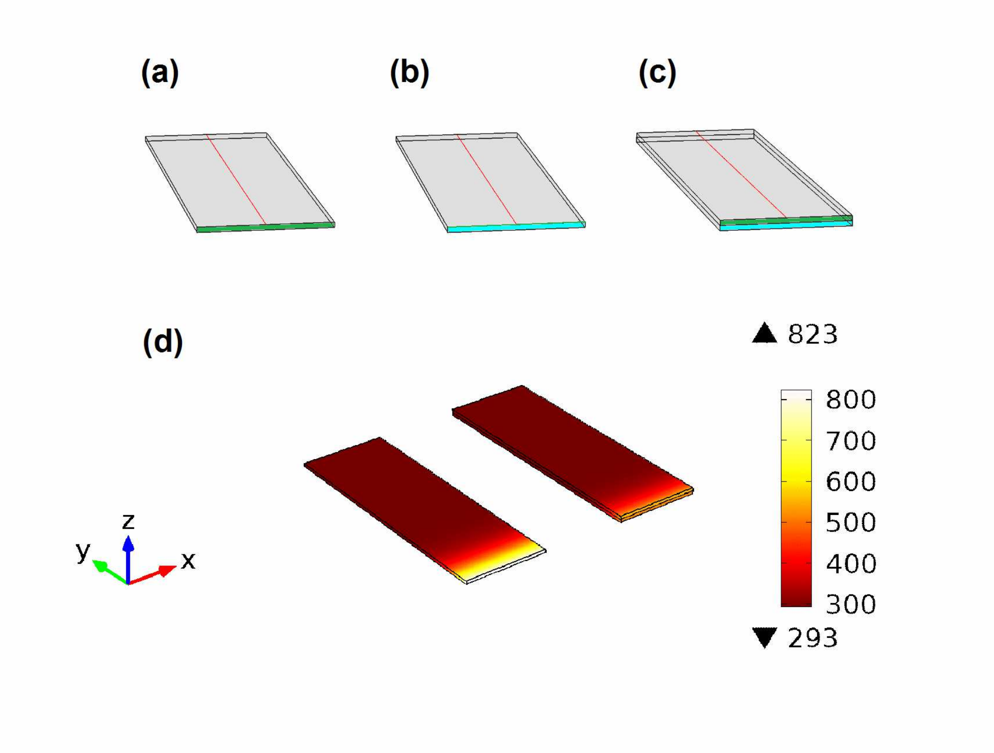

Figure 3.49 Figure (a)-(c) each show a wireframe model of a simulated sample with red cut lines at which the temperature is measured. Figure (a) shows a free standing thick film. Figure (b) shows a thin film supported on Pyrex glass and figure (c) a thick film supported on Pyrex glass. The heating contact interface is represented either by the green area (for the thermoelectric layer) or the blue area (for the Pyrex glass); the gray surfaces are thermally isolated from the outside for this simulation. Figure (d) is a visualization of the temperature distribution in a 1 mm thick PbTe layer on the left and for the same layer supported on a Pyrex substrate on the right side. For this simulation a heat flux of $10^5\,\mathrm{W\,m^{-2}}$ is applied to the front face of each PbTe film. The temperature distribution is illustrated after 40 seconds of heating. This image is reproduced from Bethke et al.[145]

Table 3.11 In this table, the mesh parameters used for the FEM simulations are presented.

sample type	mesh type	max element size [m]	min element size [m]	element growth rate
bulk	tetrahedron	$4.19\cdot10^{-3}$	$3.0\cdot10^{-4}$	1.4
thin film	swept	$4.19\cdot10^{-3}$	$3.0\cdot10^{-4}$	1.4
sample type	curvature factor	resolution at narrow regions	relative repair distance [m]	
bulk	0.4	0.7	$1\cdot10^{-8}$	
thin film	0.4	0.7	$1\cdot10^{-8}$	

The parameters for the mesh creation are found in table 3.11. The mesh is visualized in fig. 7.14 in the appendix on page 232. Another approximation in this simulation of classical heat diffusion is the absence of interfacial thermal resistance and size effects. Those effects can influence the thermal conduction of nanometer scale films. However, those effects only fortify the conclusion drawn from the simulation, because they lower the thermal conductivity of thin films even further.[204,205] These effects and their influence will be explained in more detail later in this section. In addition, the interfacial thermal resistance is highly dependent on experimental conditions and cannot be evaluated precisely by well-known physical models due to the acoustic and diffusive mismatch. Because of the problematic evaluation, its influence can only be discussed qualitatively.[206,207]

The performed time-dependent simulations are done from 0 to 40 seconds. The results were calculated in steps of 0.1 s. During the entire simulation all sides except the heated surfaces depicted as blue or green areas in fig. 3.49 (a) - (c) are thermally isolated. Thus, the simulated system resembles, in general, the earlier discussed thermal resistance in parallel. For performed experiments, the body temperature at the start was defined as 293 K. There were two types of heating done in the simulation, by maintaining a constant temperature of 393 K at the heated face, or by setting a constant heat flux q_0 of 10^5 Wm^{-2}. The first set of experiments resembles a more practical application like heating through an industrial waste heat exchanger. The second set of simulations gives a measure of the thermodynamic device efficiency and is more of theoretical interest.

In fig. 3.49 (d) the temperature distribution is visualized as an example. In this case, the image visualizes a free-standing and a supported lead telluride film on a glass microscope slide, after it was heated for 40 seconds at the front face with a heat flux of 10^5 Wm^{-2}. In table 3.12 an overview of all performed simulations is given with the relevant parameters like thickness, material and type of heating.

Table 3.12 In this table, an overview of the conducted simulation experiments and their corresponding figures is given. This table has been published in a very similar form.[145]

Figure	Heated surface	Heat source	Thermo-electric material	Thickness	Carrier
3.50(a)	Pyrex	$T_0 = 373\,\mathrm{K}$	Cu	100 nm	Pyrex
3.50(a)	Pyrex	$T_0 = 373\,\mathrm{K}$	Cu	1 mm	Pyrex
3.50(b)	Pyrex	$T_0 = 373\,\mathrm{K}$	Cu_2O	100 nm	Pyrex
3.50(b)	Pyrex	$T_0 = 373\,\mathrm{K}$	Cu_2O	1 mm	Pyrex
3.50(c)	Pyrex	$T_0 = 373\,\mathrm{K}$	PbTe	100 nm	Pyrex
3.50(c)	Pyrex	$T_0 = 373\,\mathrm{K}$	PbTe	1 mm	Pyrex
3.50(d)	Pyrex	$q_0 = 10^5\,\mathrm{W\,m^{-2}}$	Cu	100 nm	Pyrex
3.50(d)	Pyrex	$q_0 = 10^5\,\mathrm{W\,m^{-2}}$	Cu	1 mm	Pyrex
3.50(e)	Pyrex	$q_0 = 10^5\,\mathrm{W\,m^{-2}}$	Cu_2O	100 nm	Pyrex
3.50(e)	Pyrex	$q_0 = 10^5\,\mathrm{W\,m^{-2}}$	Cu_2O	1 mm	Pyrex
3.50(f)	Pyrex	$q_0 = 10^5\,\mathrm{W\,m^{-2}}$	PbTe	100 nm	Pyrex
3.50(f)	Pyrex	$q_0 = 10^5\,\mathrm{W\,m^{-2}}$	PbTe	1 mm	Pyrex
3.52(a)	thin layer	$T_0 = 373\,\mathrm{K}$	Cu	1 mm	-
3.52(a)	thin layer	$T_0 = 373\,\mathrm{K}$	Cu	1 mm	Pyrex
3.52(b)	thin layer	$T_0 = 373\,\mathrm{K}$	Cu_2O	1 mm	-
3.52(b)	thin layer	$T_0 = 373\,\mathrm{K}$	Cu_2O	1 mm	Pyrex
3.52(c)	thin layer	$T_0 = 373\,\mathrm{K}$	PbTe	1 mm	-
3.52(c)	thin layer	$T_0 = 373\,\mathrm{K}$	PbTe	1 mm	Pyrex
3.52(d)	thin layer	$q_0 = 10^5\,\mathrm{W\,m^{-2}}$	Cu	1 mm	-
3.52(d)	thin layer	$q_0 = 10^5\,\mathrm{W\,m^{-2}}$	Cu	1 mm	Pyrex
3.52(e)	thin layer	$q_0 = 10^5\,\mathrm{W\,m^{-2}}$	Cu_2O	1 mm	-
3.52(e)	thin layer	$q_0 = 10^5\,\mathrm{W\,m^{-2}}$	Cu_2O	1 mm	Pyrex
3.52(f)	thin layer	$q_0 = 10^5\,\mathrm{W\,m^{-2}}$	PbTe	1 mm	-
3.52(f)	thin layer	$q_0 = 10^5\,\mathrm{W\,m^{-2}}$	PbTe	1 mm	Pyrex

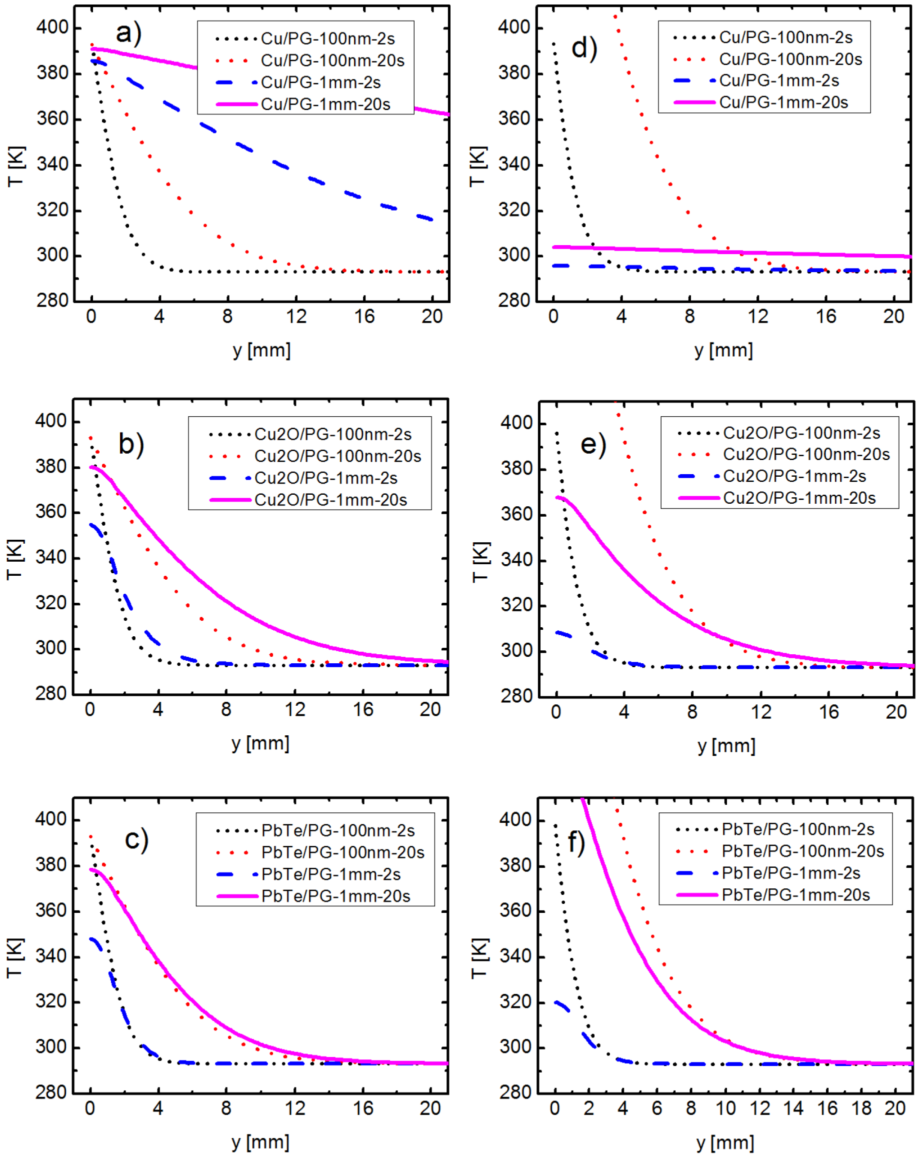

Figure 3.50 Simulation results of samples heated at the glass face. 1 mm thick films and 100 nm thick films which are supported on a Pyrex glass slide are compared by their temperature distribution along the y-axis. The temperature is kept constant at 393 K at the front face of the glass object slide for: (a) Cu, (b) Cu_2O, (c) PbTe. The heat flux of 10^5 Wm^{-2} is applied constantly at the front face of the Pyrex glass for: (d) Cu, (e) Cu_2O, (f) PbTe. This image is reproduced from Bethke et al.[145]

The thermal capacity at constant pressure C_P and the thermal conductivity of the samples play a vital role in the samples‘ thermal conductivity as mentioned earlier in this section. Two other material properties have a major influence on the heat transfer: the existence or absence of a supporting substrate and the thickness of the sample. All the tested variances of parameters are summarized in table 3.12. Those simulations are visualized in fig. 3.50 and fig. 3.52. In those simulations, the changes in the temperature distribution along the y-axis of several thin layers are investigated. The temperature distributions illustrate the effective thermal conductivity of the samples. The y-axis is only plotted from 0 to 20 mm and the temperature from 280 to 410 K. This cropped presentation was chosen in order to allow a better comparison of the simulation experiments. The full range plots (fig. 7.15 and fig. 7.16) can be found in the appendix on page 233 and page 234.

Even though the simulation studies were performed over a time interval of 40 s, only two arbitrary times, 2 and 20 s were chosen to be represented here. This selection was made to improve the clarity of the results and remove redundant results. The two times were chosen, because they differ significantly, which makes the observations easier. The chosen temperature profiles do not influence the validity of the deduced conclusions. Thus the same conclusions could have been drawn from any of the other pair of curves. This can be verified by observing fig. 3.49 on page 115 (d). This figure gives a graphical representation of the temperature distribution after 40 s of heating. fig. 7.17 in the Appendix on page 235, gives an example of the temperature curves in a PbTe layer from 0 to 40 s in 1 s intervals. Other than the gradually increasing temperature curves, no difference is observable.

3.6.1 Comparison between Thin Films and Thick Layers Supported on a Glass Slide

For the comparison between the 100 nm thin films and 1 mm thick layers, only the front face of the supporting Pyrex glass is heated (colored in a light blue in fig. 3.49 (b) and 3.49 (c)). The outer surfaces of the thermoelectric layer or film remain completely isolated, like all other outer surfaces. Due to this starting condition, the temperature is lower at the outer edge of the thermoelectric film (y = 0 mm in fig. 3.50(a) to fig. 3.50(c)). The time-dependent temperature distribution is visualized in fig. 3.51.

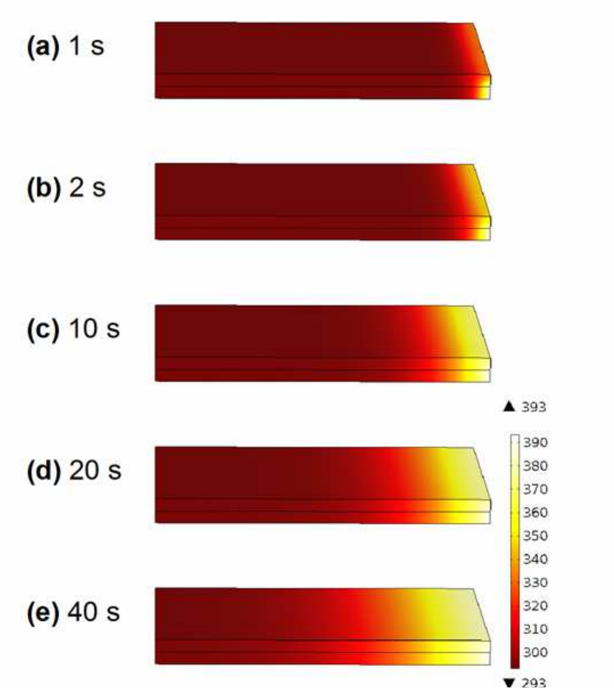

Figure 3.51 Time dependent temperature profiles for a Pyrex glass supported PbTe layer. The angle of observation highlights the direction of the main temperature gradient. The xz-face of the supporting material (facing right in this figure) is heated with a constant temperature of 393 K. This image is reproduced from Bethke et al.[145]

Figures 3.50(a)-(c) showcase the simulation results with a constant temperature of 392 K at one end. In the case of the simulation experiment with a 1 mm thick copper layer (fig. 3.50(a)), the effect of the thermal conductivity on the heat transfer is most apparent, when it is compared to the Cu_2O (fig. 3.50(b)) or PbTe (fig. 3.50(c)). The last two samples reach a temperature of 293 K at y = 20 mm after 20 s. While the copper layer achieves a value of 363 K at the same time and y = 20 mm. For the 100 nm thin films the temperature profiles are very similar for all three materials (fig. 3.50(a)-(c) dotted red and black curves). This similarity is caused by the small mass of the thin films, when compared to the supporting material. The curves resemble the curve of the supporting glass, which is shown in fig. 7.18 on page 236 in the appendix. This similarity between the curves of the thin films and the supporting material leads to the conclusion that the thermal transfer properties are mainly dependent on the supporting material. This dependance matches the results from the 1D model of thermal resistances in parallel, if the effective thermal conductivity is close to the thermal conductivity of the supporting material (earlier in this chapter on page 112). The smaller effective thermal conductivity causes the supported material to have a steeper thermal gradient, which makes it possible to make the film carrier ensemble shorter in order to achieve the same gradient.

In fig. 3.50(d) to (f), a second approach to this case is illustrated. In this *in silico* experiment, the same front surface is heated by a constant heat flux of 10^5 $\mathrm{Wm^{-2}}$. This constant heat flux causes a different temperature distribution in the sample. The heated surface is 25.4 mm by 1 mm, which has an area of $25.4 \cdot 10^{-6}$ $\mathrm{m^2}$, which results in an applied heating power of 2.54 W. Like in the previously described experiment with the constant temperature heating the thin film plays an insignificant role in the heat

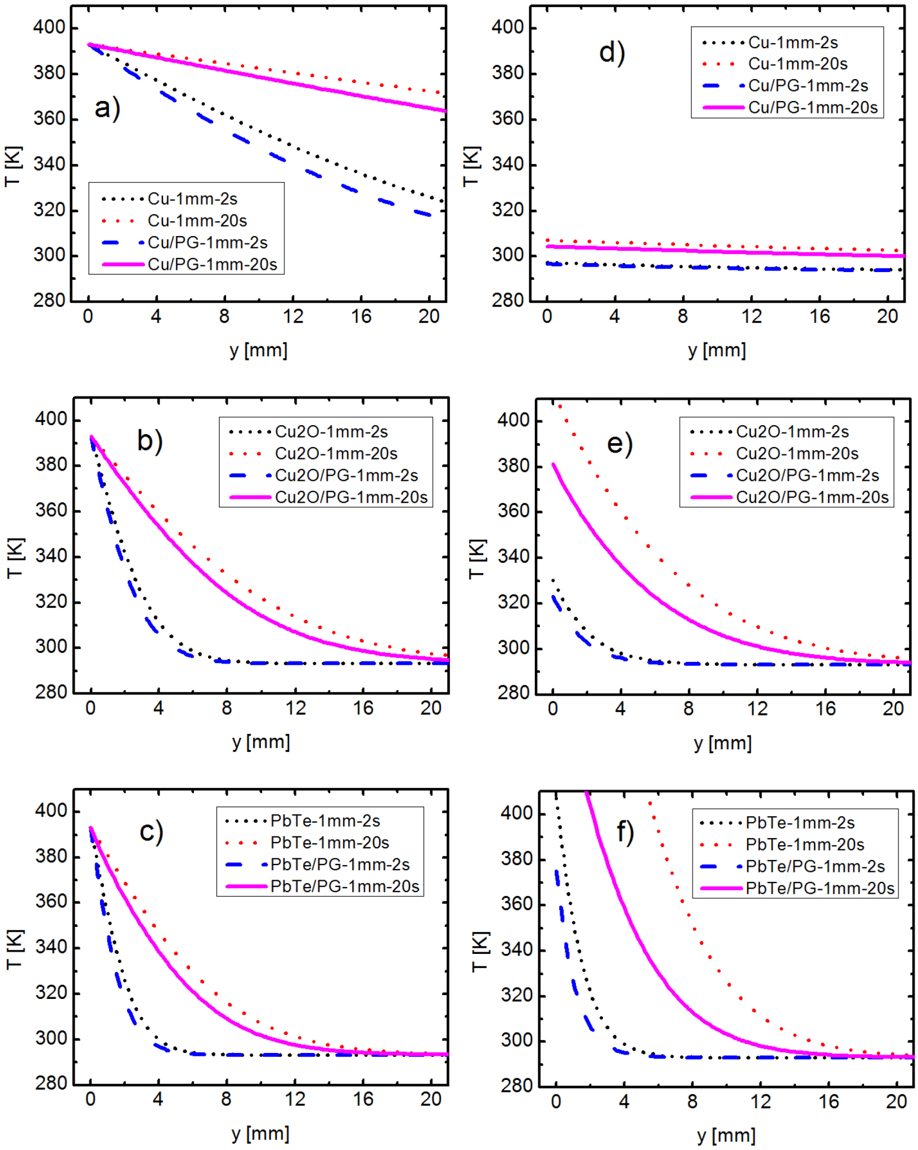

Figure 3.52 Simulation results of samples heated at the thermoelectric layer front face. Here, 1 mm thick films with and without supported on a Pyrex glass slide are compared by their temperature distribution along the y-axis. The temperature is kept constant at 393 K at the front face of the thermoelectric layer for: (a) Cu, (b) Cu_2O, (c) PbTe. The heat flux of 10^5 Wm^{-2} is applied constantly at the front face of the thermoelectric layer for: (d) Cu, (e) Cu_2O, (f) PbTe. This image is reproduced from Bethke et al.[145]

transfer of the ensemble. The low thermal conductivity of the glass leads to more localized heating. The temperature increases to a value of up to 595 K at y = 0 mm for the PbTe (see fig. 7.15 (f) in the Appendix on page 233).

In the cases where 1 mm thick films are simulated, the thermal properties are fundamentally important. The resulting temperature gradient from the heating is lower when compared to the 100 nm thin films. Due to the same constant heating power of 2.54 W and the higher mass of the sample, the lower thermal gradient has to be the logical result. The high thermal conductivity of especially copper conducts the heat along the sample body. The high conductivity and the higher thermal mass are responsible for the drastically lower thermal gradient. After 20 s of heating the thick copper sample, there is a temperature difference between the two ends of the sample of only 9 K, which gives the apparent result that a thick copper sample is entirely unsuitable for thermoelectric applications, where a high temperature difference needs to be maintained. In contrast, the 1 mm supported PbTe film, can produce the highest temperature difference, given the heat flux of 2.54 W. The supported 1 mm PbTe film can reach a temperature difference of 142 K, but the ensemble cools over the shortest distance (approximatly 17 mm) down to 293 K.

3.6.2 Comparison of a Free Standing Thick Layer with Thick Layer on a Microscope Slide

The previous simulations demonstrated that for thin films, the thermal conductivity is almost entirely dictated by the properties of the supporting material. In this section, 1 mm thick layers are investigated to illustrate the differences in their temperature profiles. The layers are modeled according to the wireframe in fig. 3.49. One set of simulations was done with the unsupported free-standing 1 mm thick layers (fig. 3.49 (a)). The other set was done with the layers supported on glass (fig. 3.49 (c)). For these simulation experiments, only the active layer (highlighted in green in fig. 3.49) is heated, while the front surface of the supporting Pyrex glass (blue) remains thermally isolated.

Due to the change in the starting conditions of the simulation, the maximum temperature achieved in fig. 3.52 differs for all sample materials (Cu fig. 3.52 (a), Cu_2O (b), and PbTe (c)). The temperature at y = 0 mm is kept at 392 K. This time the vertical temperature gradient is created across the substrate, which keeps the results from the previous discussion still valid. Due to the high thermal conductivity of copper, the starting temperature of 293 K is raised over the entire length of the sample (326 K at y = 76.2 mm after 20 s, see fig. 7.16 in the appendix on page 234). Lead telluride is a slightly better thermal insulator than Cu_2O. For all samples, a reduction of the effective thermal conductivity can be observed when they are supported. This reduction in thermal conductivity matches the results from the similar 1D case, as discussed at the beginning of the chapter.

In fig. 3.52(d), 3.52(e), and 3.52(f) the distribution of the temperature along the y - axis for thick films is shown with a constant heat flux of 10^5 Wm^{-2}. The different temperature profiles for the copper can again be explained by the high thermal conductivity, which is the cause of the quick distribution throughout the entire sample. This explanation is also valid for the supported film since the heat transport through the metal is vastly faster than through the Pyrex glass. The temperature difference between y = 0 mm and y = 76.2 mm is approximately 9 K for the supported and unsupported layer. Thus, the influence of the supporting glass is trifling for the thick copper sample. The results shown in fig. 3.50(d) and fig. 3.52(d) expose the limitations of the analytical 1D approach, which cannot describe the heat transport in thick supported samples accurately. The PbTe is again the superior material since it can produce the highest temperature difference of 369 K at a distance of approximately 22 mm.

The free-standing and the supported materials have minute distinctions (see fig. 3.52(b)- fig. 3.52(d)). The small magnitude of the distinctions is due to the thickness and thus the higher mass of the sample. The sample is heated directly through its front surface at y = 0 mm. Since for all the sample materials, the thermal conductivity is higher than the thermal conductivity of the substrate, the heat diffuses mainly through the material rather than the supporting glass. The heat exchange between the active material and the support is somewhat limited. This is the cause for the smaller influence of the supporting material, especially when the temperature difference between sample and support is low. This is most obvious in fig. 3.52(d). Almost the entire heat is conducted through the bulk copper layer.

In contrast to thinner films, the heat transfer directly through the film is rather difficult, while the exchange with the supporting material is significant. The importance of the heat exchange for thin films can be explained by the propagation of phonons, which is more challenging in thinner materials when their thickness is below their mean free path. The boundary scattering is highly dependent on the supporting material. This boundary scattering increases for thin films. When the coating thickness of the thermoelectric film decreases, the difference between the free-standing and the supported material increases. This difference becomes evident by comparing fig. 3.50 with fig. 3.52, and is further confirmed by the 1D approach at the beginning of this section. In this 1D approach, a lower effective thermal conductivity was expected with resistances in parallel.

Another observation about the heat transfer must be mentioned. It can be seen looking at the graphs of the heat distribution of the free active material in fig. 3.52(d)-(f) that with a lower κ, the maximum temperature gradients are increased, but they are also higher than the ones in the supported materials. The higher thermal mass can explain this decreased temperature for the supported materials. Another explanation is from a thermodynamic point of view: the heat flow across the support generates entropy, but it does not generate work. This increases the irreversibility of the device even more, which diminishes the theoretically achievable efficiency. Consequently, thick supported thermoelectric materials are not desirable in the case of constant heat flux. In the case of constant heat flux, the highest possible temperature difference is desired.

3.6.3 Other Influences on the Thermoelectric Efficiency in Thin Supported Films

This FEA approach is a simplification of the reality. FEA analysis makes it possible to draw a general conclusion based on the classical heat diffusion model, about how the thickness of the film, the substrate and the composition influence the heat transfer. These conclusions can be drawn without the complications which can arise from thermal resistance of nanometer thin films, which can differ from the bulk material. This part is dedicated to the differences between the model and the reality.

There are two main factors which have to be considered in real life nanometer-scale heat transfer. The size effects influence the effective thermal conductivity in nanometer-scale thin films, which is best described by a ballistic-diffusive heat transfer.[204,205,208] Another significant effect is the thermal contact resistance which is also called thermal boundary resistance or interfacial thermal resistance. The thermal contact resistance influences the heat transmission between the glass substrate and the sample film.[206] The influence of these effects on the results will be described qualitatively. The discussion on a quantitative more theoretical approach would go beyond the scope of this work; these effects are discussed in detail in several publications on the subject.[204,205,208–214]

At the nanometer scale size effects can be separated into two major parts. The first one is lateral phonon-boundary scattering, which reduces the heat flux. The second effect is ballistic heat transport, which applies to samples where the mean free path of the heat carrier is higher or comparable to the film thickness.[204,205,208] Both of these cases lead to a reduction of the thin films‘ κ. This lower thermal conductivity of the thin film further reduces the effective thermal conductivity.[205] The ballistic heat transport must be taken under special consideration, since it can cause temperature jumps at the contact boundaries with heat sources. This effect may reduce the actual temperature gradient.[205] Besides, electrons, which are present along with phonons, can affect the temperature gradient in conductive materials, like the thick copper layer. Even though these effects might have an additional effect on the simulation of the 100 nm thin samples, the effects do not affect the validity of the general conclusions. The size-effects, for example, are expected to have a smaller impact at the micrometer scale since the mean free path of the heat carrier is considerably shorter than the thickness of the film. This is visualized in fig. 3.53. In this figure, the dependence between the effective thermal conductivity κ_{eff} and the thickness of the copper film is shown. The graph was plotted using the 1D model of thermal

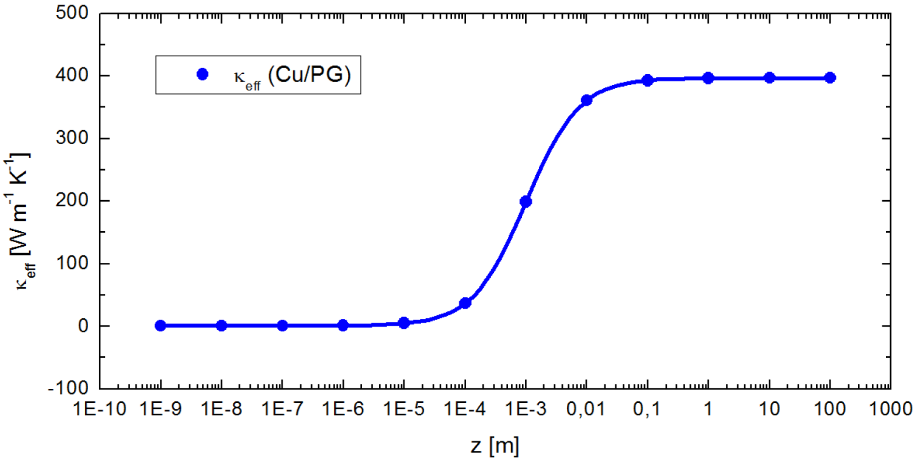

Figure 3.53 Theoretical influence of the thickness of a copper film supported on a 1 mm glass. The points in this graph are calculated with eq. (3.10). This image is reproduced from Bethke et al.[145]

resistances in parallel, see eq. (3.10) on page 111. κ_{eff} drops significantly after its thickness is below 1 mm and approaches the thermal conductivity of glass (roughly 1.1 $\mathrm{Wm^{-1}K^{-1}}$ at 298 K), once the thickness of the support is 100 times thicker than the copper film (at 10 μm). At thicknesses below 10 μm the influence of the support on the effective thermal conductivity is only changing marginally.

Table 3.13 In this table, an overview of the mean free path of phonons in some materials is given.

Compound	mean free path [nm]
Si (bulk)	40 - 300[205,214–216]
PbTe	$<$ 100[217,218]
pristine graphene	300 - 1100[219]
graphene 0.1% defects	200 - 700[219]
graphene 0.5% defects	40 - 200[219]

The examples given in table 3.13 for the mean free path of phonons show that for many samples the mean free path of the phonons is well below

10 μm. In the case that the mean free path is below 10 μm, the heat transport is mainly diffusive, which can be described by the classical model.

The temperature gradient along the y-axis of the sample can be influenced by interfacial thermal resistance. It becomes particularly relevant if just the support is heated, which indirectly heats the thermoelectric film. This contact resistance was mostly studied for helium to solid interfaces, at very low temperatures between 0.1 to 1 K. It also is known as Kapitza resistance.[209] The main two models for the Kapitza resistance are the acoustic and diffusive mismatch. Even though the Kapitza resistance has traditionally only been used in temperatures below the Debye temperature, it has also been applied to explain solid-solid interfaces.[206,220] The diffusive model is the more suitable model at higher temperatures.

Nevertheless, the acoustic and diffusive mismatch model have both failed to describe interfacial thermal resistance above 30 K. At higher temperatures, the theoretical values from those models are about one order of magnitude below the experimental ones. Various research groups have found this mismatch between the theoretical and the experimental values. They attribute the differences to the high dependency of the sample preparation, the surface treatment and the purity of the sample.[206] Even though the effect plays a role, the magnitude cannot be accurately quantified since the results depend highly on the conditions of the experiment. The boundary resistance can be significantly diminished by having homogenous surfaces. Thus, the surfaces of the support and thermoelectric layer are considered to be perfect, without any defects. The purpose of the definition of a perfect surface is to neglect the acoustic and diffusive mismatch in the entire simulations. This should enhance the generality of the results and seems to be a reasonable approximation.

3.6.4 Design of a Supported Thin Film Thermoelectric Device

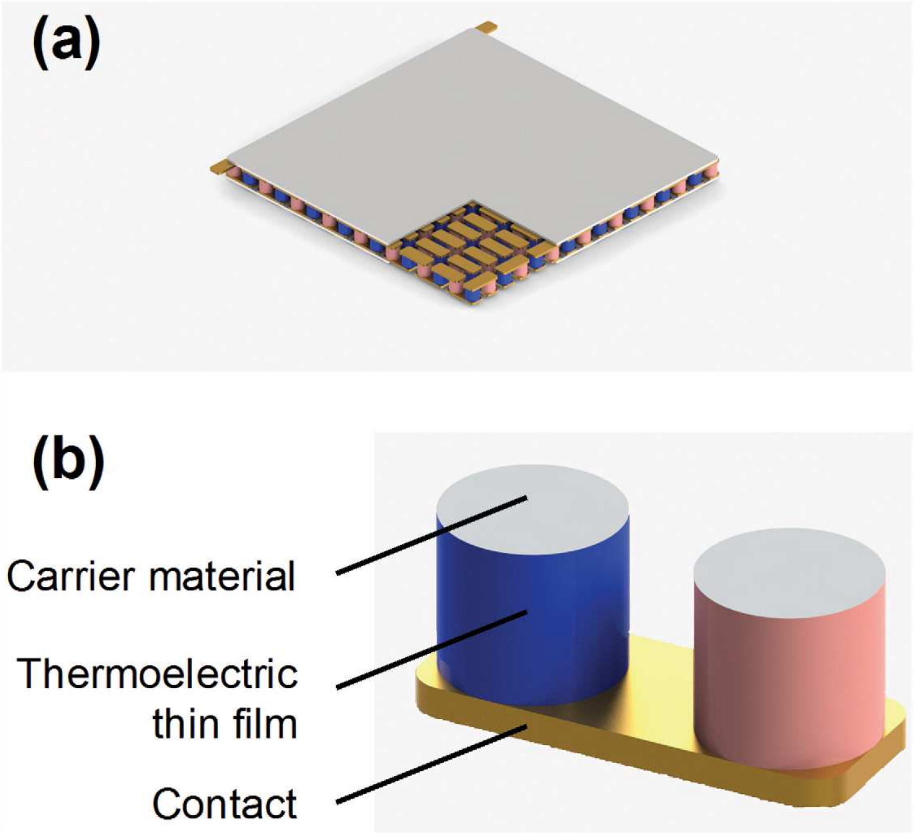

Figure 3.54 Rendering of a proposed thin film thermoelectric device. Subfigure (a) shows a rendered model of a propsed thermoelectric device, which is based on thin film technology. In one corner, a square of the ceramic heatspreader has been cut out to reveal the thermoelectric legs underneath. Subfigure (b) shows a pair of thermoelectric legs in more detail. The substrate is colored in gray, the p-type thermoelectric thin film is colored in blue, the n-type thin film in red, the metallic contact is represented in gold. The supporting material, which has a low κ is made from coated cylinders which are cut to the required size. This image is reproduced from Bethke et al.[145]

The simulation results clearly showed that there is an advantage for thin films, particularly supported ones in the effective thermal conductivity. By applying the results of the simple planar layers above, to more complex systems, it should be possible to predict their thermoelectric behavior. For the construction of a thin film thermoelectric device, the use of a low κ substrate is favorable, to increase the temperature difference along the leg. By using thin films on a substrate, the cost is reduced since less of the typically more expensive active material is used. With steeper thermal gradients the thickness of the entire thermoelectric generator can be decreased which again decreases the cost due to the reduction in material consumption.

Here, it is vital to illustrate the difference between device performance and thermodynamic efficiency in practical applications. Often the two are used interchangeably, which has been discussed in length in the literature.[221] As shown in fig. 3.52(d)-(f), the thermodynamic efficiency is reduced for supported thin films due to the reduction of the temperature difference at a constant heat flux. While in most applications like radiators and industrial heat exchangers, a constant temperature is maintained. Those systems act as thermostats. Since, in this case, the focus should be put on the length needed to cool the leg instead of the energy required to preserve the temperature. In those cases, the use of thin supported films is favorable and leads to overall better device performance.

The general knowledge deduced from the simulations can be applied to suggest how an actual thin-film device can be constructed. In fig. 3.54, a model of such a thermoelectric generator is shown. In this proposed model-thermoelectric p- and n-type legs are cylinders. Those cylinders consist of a low κ support material, which is coated with a nanometer-scale thin film of the p- or n-type thermoelectric material. These cylinders can be easily produced on a large scale by using the corresponding support material in long rod form, spinning it while it is coated with the appropriate thin-film

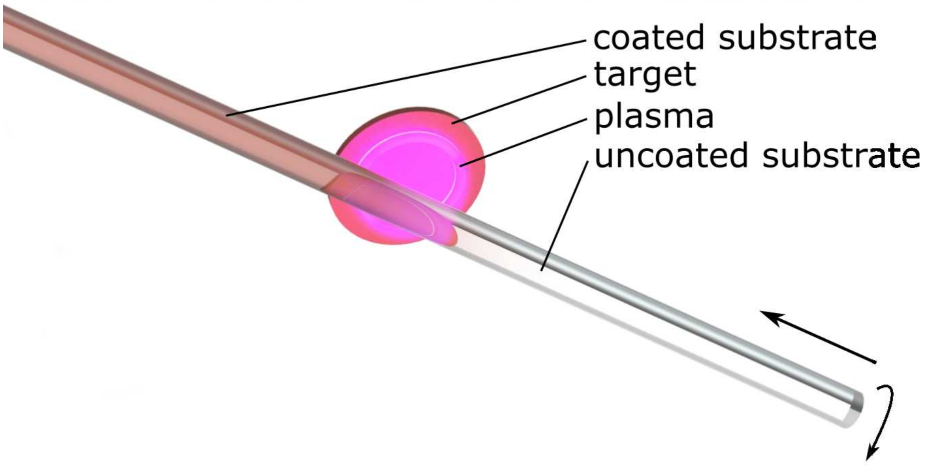

Figure 3.55 Rendering of the proposed production of supported thin film thermoelectric legs. A substrate rod is turned while a linear motion along the axis of the rod is performed. These simultaneous motions are performed in a thin film deposition process like sputter coating. The coated rod will be sliced to the appropriate size of each leg. The final product will be assembled with the pick and place process commonly used in thermoelectric device manufacturing.

technique. This is sketched in fig. 3.55. These rods can be sliced into the desired length for the thermoelectric generator. The cylinders obtained from that process can be used in traditional production techniques for bulk material thermoelectric devices like pick and place machines. The legs consisting mainly of the support material, would give the device high mechanical stability. This high stability would give such a device an advantage over nano-structured arrays,[222–225] like the ones using silicon nanowires,[226–229], which are difficult to produce and could pose problems when mechanical stress is applied.

In addition, such thermoelectric legs would have thermal resistances that closely resemble the thermal resistances in the parallel case. This case of thermal resistance is especially true if the support and thermoelectric film are simultaneously heated. With such a device, the effective thermal conductivity can be easily lowered to the value of the substrate since the mass of the film is negligible when compared to the material of the support. As shown in fig. 3.50(a)-(c), there should not be any significant radial temperature gradient in such a thermoelectric leg.

In this section, it has been shown by two different methods, that thin-film thermoelectrics benefit from the support by the lowering of the effective κ_{eff}. This beneficial influence is especially true in a constant temperature application. This lower κ_{eff} not only improves existing materials, but it opens up the opportunity for other materials which were previously dismissed due to their high κ. The simulations have been performed on three different materials: copper, copper(I) oxide, and lead telluride. With the chosen materials, conductive substances were chosen with properties ranging from metallic to semi-conductive behavior. With these simple sample systems, it was possible to draw the general conclusion that thin-film thermoelectrics can be enhanced by reducing the thickness of the thin films or by a low κ support material. For supported thin-film devices, production techniques have been proposed, which are scalable for large scale production. In addition to the scalability, those techniques can be integrated into commonly utilized production lines.

4 Summary and Conclusion

In this work, a device to measure thermoelectric Seebeck coefficients of thin films, powders, and pastes has been developed. Commercial instruments can only measure thin films or bulk materials and require preparing the thin film on specially printed circuit boards. The newly developed device uses a different approach than commercial instruments in order to characterize thin films, powders, and pastes as well as to measure the sample on any electrical isolating support. The setup of the device comprises two movable heating and cooling stages below the sample, whereby the voltage measurement is implemented via a pressure contact from above.

For several different thin films, the Seebeck effect was measured with the developed instrument and compared with a commercial setup, whereby the results from the two different instruments are in agreement. The developed low-cost Seebeck measurement device was also optimized for usability, making it possible for an untrained operator to perform measurements after a short 5-minute introduction.

Furthermore, the novel instrument was used to determine structure/property relations for a broad range of thermoelectric thin films, powders, and pastes without special sample preparations for the measurements.

The studies of thin films comprise copper oxide, doped copper oxide, titanium dioxide, and organic films (PANI, Pedot:PSS).

The lateral structure of the copper oxide confirmed a gradient distribution of the oxygen content from the surface of the copper oxide sample to the bottom. Both techniques suggest that the oxygen-rich CuO_2 species are only present in a thin surface region, pure CuO in the bottom region, and mixed copper oxides in between. Based on observations of the very thin surface layers of CuO_2, it is very likely that the oxygen-rich copper species play a negligible role in the overall thermoelectric properties of the samples. The inorganic copper oxide films showed high Seebeck values of up to 204 μVK^{-1}. The high Seebeck coefficient makes it a promising candidate for temperature sensing applications.

Single-layer PEDOT:PSS films showed good conductivities for thermoelectric materials, which are in agreement with values reported in the literature. Also, the Seebeck coefficients of the single-layer films are in agreement with literature values. By preparing multilayer films of DMSO doped PEDOT:PSS, a significant increase in the electrical conductivity was observed. This increase in electrical conductivity had no significant influence on the Seebeck coefficient of the material and resulted in a higher power factor. Two possible mechanisms were proposed to explain this increase in electrical conductivity. Either the partial solvation of PSS chains leads to inner surfaces with high conductivity or smaller grains, or even single chains are included in the structure, which raises the number of contacts between the grains. The enhancements surpass the improvements usually reached by conventional surface treatment. The organic multilayers, with their increased conductivities, make them promising candidates for flexible thermoelectric devices.

The high resistance values of powders due to grain boundaries, is the limiting factor for their use as thermoelectric devices. However, samples with paste-like properties and sufficiently high conductivities did not show the problems of a low signal-to-noise ratio observed for pure powders and are therefore promising candidates for flexible thermoelectric devices, especially in sensor applications. Such a stable thermoelectric paste was prepared by mixing composite thermoelectric materials like copper oxide with polychlorotrifluoroethene.

In order to investigate the influence of the supporting material on the entire thermoelectric leg, simulations for thin-film thermoelectric materials with the finite element method have been performed. The simulations reveal that the support can improve the effective thermal conductivity substantially. Based on those results, a preparation procedure of supported thin-film thermoelectric generators for commercial applications has been proposed whereby all synthetic steps can be conducted with established mass manufacturing processes.

The measurement device shows potential for commercial applications due to its low price, usability, and versatility. So far, it is already used by our partners at the Madurai Kamaraj University. There is still room for improvement; for example, the temperature sensor could be integrated into the pressure contact stamp.

The organic thin films have the potential to be utilized in wearable electronics for low-scale power production, especially if they are coated onto flexible supports. Potentially, fibers could be coated with the materials and woven into fabrics for small-scale power generators or to sense local body temperatures to find inflammations to extend the range of applications into the medical field.

5 Bibliography

[1] R. Saidur, M. R. Islam, N. A. Rahim, K. H. Solangi, *Renewable and Sustainable Energy Reviews* **2010**, *14*(7), 1744–1762, DOI 10.1016/j.rser.2010.03.007.

[2] A. Mirchi, S. Hadian, K. Madani, O. M. Rouhani, A. M. Rouhani, *Energies* **2012**, *5*(12), 2626–2651, DOI 10.3390/en5082626.

[3] K. V. Kumar, K. Preuss, M.-M. Titirici, F. Rodríguez-Reinoso, *Chemical reviews* **2017**, *117*(3), 1796–1825, DOI 10.1021/acs.chemrev.6b00505.

[4] P. Goodwin, A. Katavouta, V. M. Roussenov, G. L. Foster, E. J. Rohling, R. G. Williams, *Nature Geoscience* **2018**, *11*(2), 102–107, DOI 10.1038/s41561-017-0054-8.

[5] S. Brown, C. Kruger, S. Subler, *Journal of environmental quality* **2008**, *37*(4), 1396–1410, DOI 10.2134/jeq2007.0453.

[6] K. H. Solangi, M. R. Islam, R. Saidur, N. A. Rahim, H. Fayaz, *Renewable and Sustainable Energy Reviews* **2011**, *15*(4), 2149–2163, DOI 10.1016/j.rser.2011.01.007.

[7] M. Pacesila, S. G. Burcea, S. E. Colesca, *Renewable and Sustainable Energy Reviews* **2016**, *56*, 156–170, DOI 10.1016/j.rser.2015.10.152.

[8] T. J. Hammons, *International Journal of Electrical Power & Energy Systems* **2006**, *28*(8), 548–564, DOI 10.1016/j.ijepes.2006.04.001.

[9] A. Hepbasli, *Renewable and Sustainable Energy Reviews* **2008**, *12*(3), 593–661, DOI 10.1016/j.rser.2006.10.001.

[10] I. M. de Alegría, A. Basañez, P. D. de Basurto, A. Fernández-Sainz, *Renewable and Sustainable Energy Reviews* **2016**, *59*, 858–867, DOI 10.1016/j.rser.2015.12.208.

[11] D. P. van Vuuren, M. G. J. den Elzen, P. L. Lucas, B. Eickhout, B. J. Strengers, B. van Ruijven, S. Wonink, R. van Houdt, *Climatic Change* **2007**, *81*(2), 119–159, DOI 10.1007/s10584-006-9172-9.

[12] R. Clémençon, *The Journal of Environment & Development* **2016**, *25*(1), 3–24, DOI 10.1177/1070496516631362.

[13] T. J. Seebeck, *Physikalische und Medizinische Abhandlungene der königlichen Akademie der Wissenschaften* **1823**, 265–373.

[14] Y. Zhang, X. Wang, M. Cleary, L. Schoensee, N. Kempf, J. Richardson, *Applied Thermal Engineering* **2016**, *96*, 83–87, DOI 10.1016/j.applthermaleng.2015.11.064.

[15] D. Champier, *Energy Conversion and Management* **2017**, *140*, 167–181, DOI 10.1016/j.enconman.2017.02.070.

[16] L. E. Bell, *Science* **2008**, *321*(5895), 1457–1461, DOI 10.1126/science.1158899.

[17] C.-C. Weng, M.-J. Huang, *International Journal of Thermal Sciences* **2013**, *71*, 302–309, DOI 10.1016/j.ijthermalsci.2013.04.008.

[18] L. Zhang, X. Mao, Y. Chen, J. Zhong, J. Wang, M. Zhao, M. Gong, *Journal of Rare Earths* **2007**, *25*(4), 512–514, DOI 10.1016/S1002-0721(07)60466-9.

[19] V. Gadhamshetty, V. G. Gude, N. Nirmalakhandan, *Energy* **2014**, *66*, 938–949, DOI 10.1016/j.energy.2014.01.046.

[20] K. Ebrahimi, G. F. Jones, A. S. Fleischer, *Renewable and Sustainable Energy Reviews* **2014**, *31*, 622–638, DOI 10.1016/j.rser.2013.12.007.

[21] M. Groll, H. Krahling, W. D. Munzel, *Journal of Energy* **1978**, *2*(6), 363–367, DOI 10.2514/3.62387.

[22] T. Park, C. Park, B. Kim, H. Shin, E. Kim, *Energy & Environmental Science* **2013**, *6*(3), 788, DOI 10.1039/c3ee23729j.

[23] E. L. Yuksek, P. Mirmobin, in *Volume 2: Photovoltaics; Renewable-Non-Renewable Hybrid Power System; Smart Grid, Micro-Grid Concepts; Energy Storage; Solar Chemistry; Solar Heating and Cooling; Sustainable Cities and Communities, Transportation; Symposium on Integrated/Sustainable Building Equipment and Systems; Thermofluid Analysis of Energy Systems Including Exergy and Thermoeconomics; Wind Energy Systems and Technologies*, ASME, V002T12A002, DOI 10.1115/ES2015-49226.

[24] S. M. Murphy, H. Agrawal, A. Sorooshian, L. T. Padró, H. Gates, S. Hersey, W. A. Welch, H. Jung, J. W. Miller, D. R. Cocker, A. Nenes, H. H. Jonsson, R. C. Flagan, J. H. Seinfeld, *Environ. Sci. Technol.* **2009**, *43*(13), 4626–4640, DOI 10.1021/es802413j.

[25] Wärtsilä, Wärtsilä 32 Product Guide.

[26] Y. Du, Q. Meng, Y. Wang, *Transportation Research Record: Journal of the Transportation Research Board* **2015**, *2477*, 68–75, DOI 10.3141/2477-08.

[27] P. Yun, L. I. Xiangda, W. Wenyuan, L. Ke, L. I. Chuan, *Ocean Engineering* **2018**, *163*, 288–298, DOI 10.1016/j.oceaneng.2018.05.054.

[28] I. Senjanović, N. Vladimir, M. Tomić, N. Hadžić, Š. Malenica, *Ships and Offshore Structures* **2014**, *9*(2), 199–217, DOI 10.1080/17445302.2012.762728.

[29] N. R. Kristiansen, H. K. Nielsen, *Journal of Electronic Materials* **2010**, *39*(9), 1746–1749, DOI 10.1007/s11664-010-1189-1.

[30] P. Pichanusakorn, P. Bandaru, *Materials Science and Engineering: R: Reports* **2010**, *67*(2-4), 19–63, DOI 10.1016/j.mser.2009.10.001.

[31] S.-K. Nam, S.-K. Lee, *International Journal of Precision Engineering and Manufacturing* **2014**, *15*(11), 2391–2396, DOI 10.1007/s12541-014-0605-5.

[32] M. Kishi, H. Nemoto, T. Hamao, M. Yamamoto, S. Sudou, M. Mandai, S. Yamamoto, in *Eighteenth International Conference on Thermoelectrics. Proceedings, ICT,99 (Cat. No.99TH8407)*, (Herausgegeben von IEEE), IEEE, 301–307, DOI 10.1109/ICT.1999.843389.

[33] X. Yu, D. Xu, Y. Liu, H. Zhou, Y. Wang, X. Gao, F. Feng, Y. Wang, T. Li, *International Journal of Electrical Power & Energy Systems* **2015**, *67*, 417–422, DOI 10.1016/j.ijepes.2014.12.039.

[34] M. Ashraf, N. Masoumi, *IEEE Trans. VLSI Syst.* **2016**, *24*(1), 26–37, DOI 10.1109/TVLSI.2015.2391442.

[35] J. Leicht, P. Heilmann, T. Hehn, X. Li, D. Maurath, C. Moranz, M. Thewes, G. Scholl, Y. Manoli, *Journal of Physics: Conference Series* **2013**, *476*, 012022, DOI 10.1088/1742-6596/476/1/012022.

[36] C. C. Lim, H. H. Al-Kayiem, C. Y. Sing, *MATEC Web of Conferences* **2014**, *13*, 02028, DOI 10.1051/matecconf/20141302028.

[37] C. Li, D. Jiao, J. Jia, F. Guo, J. Wang, *IEEE Transactions on Industry Applications* **2014**, *50*(6), 3995–4005, DOI 10.1109/TIA.2014.2319576.

[38] A. Martinez, D. Astrain, P. Aranguren, *Energy* **2016**, *112*, 1–7, DOI 10.1016/j.energy.2016.06.007.

[39] F. Frobenius, G. Gaiser, U. Rusche, B. Weller, *Journal of Electronic Materials* **2016**, *45*(3), 1433–1440, DOI 10.1007/s11664-015-4059-z.

[40] B. Orr, A. Akbarzadeh, M. Mochizuki, R. Singh, *Applied Thermal Engineering* **2016**, *101*, 490–495, DOI 10.1016/j.applthermaleng.2015.10.081.

[41] B. Lu, X. Meng, M. Zhu, R. O. Suzuki, *Journal of Elec Materi* **2018**, *47*(6), 3238–3247, DOI 10.1007/s11664-018-6073-4.

[42] T. Kuroki, K. Kabeya, K. Makino, T. Kajihara, H. Kaibe, H. Hachiuma, H. Matsuno, A. Fujibayashi, *Journal of Electronic Materials* **2014**, *43*(6), 2405–2410, DOI 10.1007/s11664-014-3094-5.

[43] L. Liu, *New Journal of Physics* **2014**, *16*(12), 123019, DOI 10.1088/1367-2630/16/12/123019.

[44] A. Miozzo, S. Boldrini, A. Ferrario, M. Fabrizio, *Journal of Nanoscience and Nanotechnology* **2017**, *17*(3), 1601–1607, DOI 10.1166/jnn.2017.13734.

[45] D. Freis, J. F. Vigier, K. Popa, T. Wiss, J.-C. Griveau, E. D‘ Agata, J. Somers, *E3S Web of Conferences* **2017**, *16*, 05001, DOI 10.1051/e3sconf/20171605001.

[46] D. Woerner, *Journal of Electronic Materials* **2016**, *45*(3), 1278–1283, DOI 10.1007/s11664-015-3998-8.

[47] T. C. Holgate, R. Bennett, T. Hammel, T. Caillat, S. Keyser, B. Sievers, *Journal of Electronic Materials* **2015**, *44*(6), 1814–1821, DOI 10.1007/s11664-014-3564-9.

[48] D. M. Rowe, *Applied Energy* **1991**, *40*(4), 241–271, DOI 10.1016/0306-2619(91)90020-X.

[49] P. S. Cooper, *Astroparticle Physics* **2009**, *31*(4), 267–269, DOI 10.1016/j.astropartphys.2009.02.005.

[50] W. Li, J. Peng, W. Xiao, H. Wang, J. Zeng, J. Xie, Q. Huang, K. Mao, L. Zhang, *Applied Thermal Engineering* **2017**, *118*, 742–747, DOI 10.1016/j.applthermaleng.2017.03.022.

[51] S. H. Lee, J. Song, B. Cho, S. Hong, O. Hoxha, T. Kang, D. Kim, L. P. Lee, *Biosensors & bioelectronics* **2019**, *126*, 725–733, DOI 10.1016/j.bios.2018.10.005.

[52] S. Julich, M. Riedel, M. Kielpinski, M. Urban, R. Kretschmer, S. Wagner, W. Fritzsche, T. Henkel, R. Möller, S. Werres, *Biosensors & bioelectronics* **2011**, *26*(10), 4070–4075, DOI 10.1016/j.bios.2011.03.035.

[53] J. A. DuVall, D. Le Roux, A.-C. Tsuei, B. L. Thompson, C. Birch, J. Li, D. A. Nelson, D. L. Mills, M. M. Ewing, R. S. McLaren, D. R. Storts, B. E. Root, J. P. Landers, *Analytical Methods* **2016**, *8*(40), 7331–7340, DOI 10.1039/c6ay01984f.

[54] L. L. Josephson, W. J. Galush, E. M. Furst, *Biomicrofluidics* **2016**, *10*(4), 043503, DOI 10.1063/1.4953863.

[55] C. J. McKinney, M. W. Nader, *Applied Radiation and Isotopes* **2001**, *54*(1), 97–100, DOI 10.1016/S0969-8043(00)00189-5.

[56] A. Ihring, E. Kessler, U. Dillner, U. Schinkel, M. Kunze, S. Billat, *Journal of Microelectromechanical Systems* **2015**, *24*(4), 990–996, DOI 10.1109/JMEMS.2014.2367103.

[57] A. Patel, S. K. Pandey, *Instrumentation Science & Technology* **2017**, *45*(4), 366–381, DOI 10.1080/10739149.2016.1262396.

[58] H. Uemura, T. Kawaguchi, T. Ohno, M. Tabuchi, T. Ujihara, Y. Takeda, H. Ikuta, *Solid State Communications* **2012**, *152*(8), 735–739, DOI 10.1016/j.ssc.2012.01.037.

[59] M. Azmi Abdul Hamid, M. Abu Bakar, A. Jalar, R. Shamsudin, *Current Nanoscience* **2012**, *8*(1), 50–54, DOI 10.2174/157341371120801050.

[60] (Hrsg.: O. G. Palanna), *Engineering chemistry*, Tata MrGraw-Hill, New Delhi, Kap. Conductivity in Solids, **2009**, 391–413.

[61] (Hrsg.: N. Wiberg, E. Wiberg, A. F. Holleman), *Lehrbuch der anorganischen Chemie*, 102 Aufl., de Gruyter, Berlin, Kap. Einige Grundlagen der Festkörperchemie, **2007**, 1420–1425.

[62] (Hrsg.: Rudolf Huebener), *Leiter, Halbleiter, Supraleiter - Eine Einführung in die Festkörperphysik: Für Physiker, Ingenieure und Naturwissenschaftler*, Springer Spektrum, Kap. Elektrischer Leiter oder Isolator, **2013**, 45–52.

[63] Kevin Bethke, Diplomarbeit, Humboldt-Universität zu Berlin, Berlin, **2014**.

[64] S. Hunklinger, *Festkörperphysik*, Oldenbourg Wissensch.Vlg, **2011**.

[65] M. R. Stoker, *Anaesthesia & Intensive Care Medicine* **2009**, *10*(1), 62–64, DOI 10.1016/j.mpaic.2008.11.013.

[66] (Hrsg.: D.M. Rowe), *CRC Handbook of Thermoelectrics*, CRC Press, Kap. Introduction, **1995**, 1–6.

[67] J. C. A. Peltier, *Annales de Chimie et de Physique* **1834**, *Tome 56*, 371–386.

[68] W. Thomson, *Proceedings of the Royal Society of Edinburgh* **1851**, *3*, 91–98.

[69] G. Magnus, *Poggendorf,s Annalen der Physik* **1851**, *83*(8), 469–504.

[70] (Hrsg.: C. Goupil), *Continuum theory and modeling of thermoelectric elements*, Wiley-VCH Verlag GmbH & Co. KGaA, Weinheim, Kap. Thermodynamics and Thermoelectricity, **2016**, 1–73.

[71] E. Altenkirch, *Physikalische Zeitschrift* **1909**, *10*(16), 560–568.

[72] E. Altenkirch, *Physikalische Zeitschrift* **1911**, *12*, 920–924.

[73] M. Telkes, *Journal of Applied Physics* **1947**, *18*(12), 1116–1127, DOI 10.1063/1.1697593.

[74] A. F. Ioffe, *Semiconductor Thermoelements and Thermoelectric Cooling*, Infosearch Ltd., **1957**.

[75] D. Nemir, J. Beck, *Journal of Electronic Materials* **2010**, *39*(9), 1897–1901, DOI 10.1007/s11664-009-1060-4.

[76] H. J. Goldsmid, R. W. Douglas, *Br. J. Appl. Phys.* **1954**, *5*(11), 386–390, DOI 10.1088/0508-3443/5/11/303.

[77] (Hrsg.: C. Vining, D. M. Rowe, J. Stockholm, K. R. Rao), *Thermoelectrics handbook: Macro to nano*, Taylor & Francis, Boca Raton, Fla., Kap. Appendix I: History of the International Thermoelectric Society, **2005**, AI1–AI8, DOI 10.1201/9781420038903.

[78] F. de Winter, G. Stapfer, E. Medina, *IEEE Aerospace and Electronic Systems Magazine* **2000**, *15*(4), 5–12, DOI 10.1109/62.839628.

[79] L. D. Hicks, M. S. Dresselhaus, *Physical Review B* **1993**, *47*(19), 12727–12731, DOI 10.1103/PhysRevB.47.12727.

[80] L. D. Hicks, M. S. Dresselhaus, *Physical Review B* **1993**, *47*(24), 16631–16634, DOI 10.1103/PhysRevB.47.16631.

[81] P. J. Taroni, I. Hoces, N. Stingelin, M. Heeney, E. Bilotti, *Israel Journal of Chemistry* **2014**, *54*(5-6), 534–552, DOI 10.1002/ijch.201400037.

[82] M. S. Dresselhaus, G. Chen, M. Y. Tang, R. G. Yang, H. Lee, D. Z. Wang, Z. F. Ren, J.-P. Fleurial, P. Gogna, *Advanced Materials* **2007**, *19*(8), 1043–1053, DOI 10.1002/adma.200600527.

[83] G. J. Snyder, E. S. Toberer, *Nature materials* **2008**, *7*(2), 105–114, DOI 10.1038/nmat2090.

[84] M. G. Kanatzidis, *Chemistry of Materials* **2010**, *22*(3), 648–659, DOI 10.1021/cm902195j.

[85] J. E. Cornett, O. Rabin, *Applied Physics Letters* **2011**, *98*(18), 182104, DOI 10.1063/1.3585659.

[86] J. E. Cornett, O. Rabin, *Appl. Phys. Lett.* **2012**, *100*(24), 242106, DOI 10.1063/1.4729381.

[87] Z. Chen, B. Ge, W. Li, S. Lin, J. Shen, Y. Chang, R. Hanus, G. J. Snyder, Y. Pei, *Nature communications* **2017**, *8*, 13828, DOI 10.1038/ncomms13828.

[88] (Hrsg.: S. Datta), *Lessons from nanoelectronics- A new perspective on transport*, second edition Aufl., World Scientific, New Jersey and London and Singapore and Beijing and Shanghai and Hong Kong and Taipei Chennai and Tokyo, Bd. vol. 5 von *Lessons from nanoscience*, Kap. The Elastic Resistor, **2017**, 31–41.

[89] (Hrsg.: S. Datta), *Lessons from nanoelectronics- A new perspective on transport*, second edition Aufl., World Scientific, New Jersey and London and Singapore and Beijing and Shanghai and Hong Kong and Taipei Chennai and Tokyo, Bd. vol. 5 von *Lessons from nanoscience*, Kap. Why Electrons Flow, **2017**, 24.

[90] (Hrsg.: S. Datta), *Lessons from nanoelectronics- A new perspective on transport*, second edition Aufl., World Scientific, New Jersey and London and Singapore and Beijing and Shanghai and Hong Kong and Taipei Chennai and Tokyo, Bd. vol. 5 von *Lessons from nanoscience*, Kap. Thermoelectricity, **2017**, 171–186.

[91] P. Pichanusakorn, P. Bandaru, *Materials Science and Engineering R* **2010**, *67*, 19–63.

[92] C. Herring, *Physical Review* **1954**, *96*(5), 1163–1187, DOI 10.1103/PhysRev.96.1163.

[93] A. I. Boukai, Y. Bunimovich, J. Tahir-Kheli, J.-K. Yu, W. A. Goddard, J. R. Heath, *Nature* **2008**, *451*(7175), 168–171, DOI 10.1038/nature06458.

[94] R. Pelster, R. Pieper, I. Hüttl, *Phy. Did.* **2005**, *1*(4), 10–22.

[95] C. Wood, *Reports on Progress in Physics* **1988**, *51*(4), 459–539, DOI 10.1088/0034-4885/51/4/001.

[96] G. D. Mahan, *APL Materials* **2016**, *4*(10), 104806, DOI 10.1063/1.4954055.

[97] H. Julian Goldsmid, *Introduction to Thermoelectricity*, Springer, **2010**, DOI 10.1007/978-3-642-00716-3.

[98] G. Chen, M. S. Dresselhaus, G. Dresselhaus, J.-P. Fleurial, T. Caillat, *International Materials Reviews* **2003**, *48*(1), 45–66, DOI 10.1179/095066003225010182.

[99] DiSalvo, *Science* **1999**, *285*(5428), 703–706, DOI 10.1126/science.285.5428.703.

[100] G. Binnig, H. Rohrer, C. Gerber, E. Weibel, *Physical Review Letters* **1982**, *49*(1), 57–61, DOI 10.1103/PhysRevLett.49.57.

[101] D. Rugar, P. Hansma, *Phys. Today* **1990**, *43*(10), 23–30, DOI 10.1063/1.881238.

[102] F. J. Giessibl, *Science* **2000**, *289*(5478), 422–425, DOI 10.1126/science.289.5478.422.

[103] (Hrsg.: S. N. Magonov, M.-H. Whangbo), *Surface Analysis with STM and AFM*, Wiley-VCH Verlag GmbH, Weinheim, Germany, Kap. Introduction, **1995**, 1–8, DOI 10.1002/9783527615117.

[104] N. Pavliček, L. Gross, *Nature Reviews Chemistry* **2017**, *1*(1), 0005, DOI 10.1038/s41570-016-0005.

[105] R. F. Mould, *Phys. Med. Biol.* **1995**, *40*(11), 1741–1787, DOI 10.1088/0031-9155/40/11/001.

[106] (Hrsg.: W. C. Röntgen), *Ueber eine neue Art von Strahlen*, 2. Aufl., Stahel, Würzburg, Kap. Ueber eine neue Art von Strahlen, **1896**, 1–12.

[107] R. Behling, F. Grüner, *Nucl. Instrum. Methods Phys. Res. A* **2018**, *878*, 50–57, DOI 10.1016/j.nima.2017.05.034.

[108] J. Trincavelli, G. Castellano, *Spectrochimica Acta Part B: Atomic Spectroscopy* **2008**, *63*(1), 1–8, DOI 10.1016/j.sab.2007.11.009.

[109] J. M. Boone, T. R. Fewell, R. J. Jennings, *Medical physics* **1997**, *24*(12), 1863–1874, DOI 10.1118/1.598100.

[110] U. Mueller, N. Darowski, M. R. Fuchs, R. Förster, M. Hellmig, K. S. Paithankar, S. Pühringer, M. Steffien, G. Zocher, M. S. Weiss, *Journal of synchrotron radiation* **2012**, *19*(Pt 3), 442–449, DOI 10.1107/S0909049512006395.

[111] B. Beckhoff, R. Fliegauf, M. Kolbe, M. Müller, J. Weser, G. Ulm, *Anal. Chem.* **2007**, *79*(20), 7873–7882, DOI 10.1021/ac071236p.

[112] C. Streeck, S. Brunken, M. Gerlach, C. Herzog, P. Hönicke, C. A. Kaufmann, J. Lubeck, B. Pollakowski, R. Unterumsberger, A. Weber, B. Beckhoff, B. Kanngießer, H.-W. Schock, R. Mainz, *Applied Physics Letters* **2013**, *103*(11), 113904, DOI 10.1063/1.4821267.

[113] J. Baumann, Advanced X-ray analytical methods for the characterization of buried interfaces with relevance for energy conversion devices, DOI 10.14279/depositonce-6581.

[114] W. Xu, Y. Liu, A. Marcelli, P. P. Shang, W. S. Liu, *Materials Today Physics* **2018**, *6*, 68–82, DOI 10.1016/j.mtphys.2018.09.002.

[115] J.-D. Grunwaldt, C. G. Schroer, *Chemical Society reviews* **2010**, *39*(12), 4741–4753, DOI 10.1039/c0cs00036a.

[116] (Hrsg.: J. Als-Nielsen, Des McMorrow), *Elements of modern X-ray physics*, Wiley, New York, NY, Kap. Sources, **2001**, 42–43.

[117] B. Pollakowski, Dissertation, Technische Universität Berlin, Berlin, **20.12.2011**, DOI 10.14279/depositonce-3061.

[118] M. Krumrey, *Journal of synchrotron radiation* **1998**, *5*(Pt 1), 6–9, DOI 10.1107/S0909049597011825.

[119] M. Krumrey, G. Ulm, *Nuclear Instruments and Methods in Physics Research Section A: Accelerators, Spectrometers, Detectors and Associated Equipment* **2001**, *467-468*, 1175–1178, DOI 10.1016/S0168-9002(01)00598-8.

[120] W. Görner, M. P. Hentschel, B. R. Müller, H. Riesemeier, M. Krumrey, G. Ulm, W. Diete, U. Klein, R. Frahm, *Nuclear Instruments and Methods in Physics Research Section A: Accelerators, Spectrometers, Detectors and Associated Equipment* **2001**, *467-468*, 703–706, DOI 10.1016/S0168-9002(01)00466-1.

[121] A. Rack, S. Zabler, B. R. Müller, H. Riesemeier, G. Weidemann, A. Lange, J. Goebbels, M. Hentschel, W. Görner, *Nuclear Instruments and Methods in Physics Research Section A: Accelerators, Spectrometers, Detectors and Associated Equipment* **2008**, *586*(2), 327–344, DOI 10.1016/j.nima.2007.11.020.

[122] G. Hähner, *Chemical Society reviews* **2006**, *35*(12), 1244–1255, DOI 10.1039/b509853j.

[123] U. Schindler, Ein supraleitender Undulator mit elektrisch umschaltbarer Helizität, DOI 10.5445/IR/270058615.

[124] K. Wille, *Physik der Teilchenbeschleuniger und Synchrotronstrahlungsquellen*, 2., überarbeitete und erweiterte auflage Aufl., Teubner-Studienbücher Physik, Springer Fachmedien GmbH, Wiesbaden, **1996**.

[125] B. Beckhoff, *J. Anal. At. Spectrom.* **2008**, *23*(6), 845, DOI 10.1039/b718355k.

[126] D. Weiß, H. Brandl, *Chemie in unserer Zeit* **2013**, *47*(1), 50–54, DOI 10.1002/ciuz.201300586.

[127] Y. Kayser, P. Hönicke, D. Banaś, J.-C. Dousse, J. Hoszowska, P. Jagodziński, A. Kubala-Kukuś, S. H. Nowak, M. Pajek, *Journal of Analytical Atomic Spectrometry* **2015**, *30*(5), 1086–1099, DOI 10.1039/c4ja00461b.

[128] G. Ertl, R. Gomer, D. L. Mills, H. K. V. Lotsch, J. Stöhr, *NEXAFS Spectroscopy*, Bd. 25, Springer Berlin Heidelberg, Berlin, Heidelberg, **1992**, DOI 10.1007/978-3-662-02853-7.

[129] M. A. Brown, M. Faubel, B. Winter, *Annual Reports Section "C" (Physical Chemistry)* **2009**, *105*, 174, DOI 10.1039/B803023P.

[130] D. D. Sarma, P. K. Santra, S. Mukherjee, A. Nag, *Chem. Mater.* **2013**, *25*(8), 1222–1232, DOI 10.1021/cm303567d.

[131] J. F. Watts, J. Wolstenholme, *An Introduction to Surface Analysis by XPS and AES*, John Wiley & Sons, Ltd, Chichester, UK, **2003**, DOI 10.1002/0470867930.

[132] T. Fransson, Y. Harada, N. Kosugi, N. A. Besley, B. Winter, J. J. Rehr, L. G. M. Pettersson, A. Nilsson, *Chemical reviews* **2016**, *116*(13), 7551–7569, DOI 10.1021/acs.chemrev.5b00672.

[133] M. P. Seah, W. A. Dench, *Surface and Interface Analysis* **1979**, *1*(1), 2–11, DOI 10.1002/sia.740010103.

[134] Debye, P., Scherrer, P., *Nachrichten von der Gesellschaft der Wissenschaften zu Göttingen, Mathematisch-Physikalische Klasse* **1916**, 1–15.

[135] A. W. Hull., *Physical Review* **1917**, *10*(6), 661–696, DOI 10.1103/PhysRev.10.661.

[136] J. M. Delgado, *Powder Diffraction* **2017**, *32*(01), 2–9, DOI 10.1017/S0885715616000750.

[137] K. D. M. Harris, M. Tremayne, B. M. Kariuki, *Angewandte Chemie International Edition* **2001**, *40*(9), 1626–1651, DOI 10.1002/1521-3773(20010504)40:9{\%}3C1626::AID-ANIE16260{\%}3E3.0.CO;2-7.

[138] (Hrsg.: G. Schwedt), *Analytische Chemie*, Wiley-VCH, Kap. Spezielle Methoden und Anwendungsgebiete, **2008**, 504–507.

[139] (Hrsg.: G. Schwedt), *Analytische Chemie*, Wiley-VCH, Kap. Strukturanalyse und Beugungsmethoden, **2008**, 508.

[140] W. R. Grove, *Phil. Trans. R. Soc. Lon.* **1852**, *142*, 87–101, DOI 10.1098/rstl.1852.0008.

[141] N. Selvakumar, H. C. Barshilia, *Solar Energy Materials and Solar Cells* **2012**, *98*, 1–23, DOI 10.1016/j.solmat.2011.10.028.

[142] G. K. Dalapati, A. K. Kushwaha, M. Sharma, V. Suresh, S. Shannigrahi, S. Zhuk, S. Masudy-Panah, *Progress in Materials Science* **2018**, *95*, 42–131, DOI 10.1016/j.pmatsci.2018.02.007.

[143] P. Kelly, R. Arnell, *Vacuum* **2000**, *56*(3), 159–172, DOI 10.1016/S0042-207X(99)00189-X.

[144] J. E. Greene, *J. Vac. Sci. Technol. A* **2017**, *35*(5), 05C204, DOI 10.1116/1.4998940.

[145] K. Bethke, V. Andrei, K. Rademann, *PloS one* **2016**, *11*(3), e0151708, DOI 10.1371/journal.pone.0151708.

[146] I. Maxim Integrated Products, DS18B20.

[147] J. G. Ziegler, N. B. Nicols, *TRANSACTIONS OF THE A.S.M.E.* **1942**, *64*, 759–765.

[148] K. H. Ang, G. Chong, Y. Li, *IEEE Trans. Contr. Syst. Technol.* **2005**, *13*(4), 559–576, DOI 10.1109/TCST.2005.847331.

[149] R. B. Roberts, *Measurement* **1986**, *4*(3), 101–103, DOI 10.1016/0263-2241(86)90016-3.

[150] E. Alleno, D. Bérardan, C. Byl, C. Candolfi, R. Daou, R. Decourt, E. Guilmeau, S. Hébert, J. Hejtmanek, B. Lenoir, P. Masschelein, V. Ohorodnichuk, M. Pollet, S. Populoh, D. Ravot, O. Rouleau, M. Soulier, *Rev. Sci. Instrum.* **2015**, *86*(1), 011301, DOI 10.1063/1.4905250.

[151] J. Martin, G. S. Nolas, *The Review of scientific instruments* **2016**, *87*(1), 015105, DOI 10.1063/1.4939555.

[152] H. Wang, W. D. Porter, H. Böttner, J. König, L. Chen, S. Bai, T. M. Tritt, A. Mayolet, J. Senawiratne, C. Smith, F. Harris, P. Gilbert, J. W. Sharp, J. Lo, H. Kleinke, L. Kiss, *Journal of Electronic Materials* **2013**, *42*(4), 654–664, DOI 10.1007/s11664-012-2396-8.

[153] J. Mackey, F. Dynys, A. Sehirlioglu, *The Review of scientific instruments* **2014**, *85*(8), 085119, DOI 10.1063/1.4893652.

[154] DIN 2409, Beschichtungsstoffe - Gitterschnittprüfung, **2013**.

[155] P. Morgan, D. E. Partin, B. L. Chamberland, M. O‘ Keeffe, *Journal of Solid State Chemistry* **1996**, *121*(1), 33–37, DOI 10.1006/jssc.1996.0005.

[156] L. Debbichi, M. C. Marco de Lucas, J. F. Pierson, P. Krüger, *The Journal of Physical Chemistry C* **2012**, *116*(18), 10232–10237, DOI 10.1021/jp303096m.

[157] D. S. Murali, S. Aryasomayajula, *Applied Physics A* **2018**, *124*(3), 336, DOI 10.1007/s00339-018-1666-6.

[158] Y. Wang, J. Ghanbaja, S. Bruyère, F. Soldera, D. Horwat, F. Mücklich, J. F. Pierson, *Scientific reports* **2017**, *7*(1), 11122, DOI 10.1038/s41598-017-10540-6.

[159] Y. Zhang, C. L. Hapenciuc, E. E. Castillo, T. Borca-Tasciuc, R. J. Mehta, C. Karthik, G. Ramanath, *Applied Physics Letters* **2010**, *96*(6), 062107, DOI 10.1063/1.3300826.

[160] K. Kishimoto, M. Tsukamoto, T. Koyanagi, *Applied Physics Letters* **2002**, *92*(9), 5331–5339, DOI 10.1063/1.1512964.

[161] H. Kawazoe, M. Yasukawa, H. Hyodo, M. Kurita, H. Yanagi, H. Hosono, *Nature* **1997**, *389*(6654), 939–942, DOI 10.1038/40087.

[162] V. Andrei, K. Bethke, K. Rademann, *Energy Environ. Sci.* **2016**, *9*(5), 1528–1532, DOI 10.1039/C6EE00247A.

[163] S. Walia, S. Balendhran, H. Nili, S. Zhuiykov, G. Rosengarten, Q. H. Wang, M. Bhaskaran, S. Sriram, M. S. Strano, K. Kalantar-zadeh, *Progress in Materials Science* **2013**, *58*(8), 1443–1489, DOI 10.1016/j.pmatsci.2013.06.003.

[164] V. Andrei, K. Bethke, K. Rademann, *Appl. Phys. Lett.* **2014**, *105*(23), 233902, DOI 10.1063/1.4903832.

[165] J.-L. Pouchou, *Analytica Chimica Acta* **1993**, *283*(1), 81–97, DOI 10.1016/0003-2670(93)85212-3.

[166] A. T. Marshall, *Journal of microscopy* **2017**, *266*(3), 231–238, DOI 10.1111/jmi.12531.

[167] (Hrsg.: J. E. Shelby), *Introduction to Glass Science and Technology*, Royal Society of Chemistry, Kap. Glass melting, **2007**, 26–50, DOI 10.1039/9781847551160-00026.

[168] E. Meechoowas, S. Suriyoporn, U. Pantulap, K. Tapasa, *Key Engineering Materials* **2017**, *751*, 374–378, DOI 10.4028/www.scientific.net/KEM.751.374.

[169] (Hrsg.: R. C. Weast), *CRC handbook of chemistry and physics*, 58. ed., 2nd pr Aufl., CRC Press, Cleveland, Ohio, Kap. The Elements, Selected handbook series, **1978**, B–17.

[170] B. Beckhoff, R. Fliegauf, G. Ulm, J. Weser, G. Pepponi, C. Streli, P. Wobrauschek, T. Ehmann, L. Fabry, S. Pahlke, B. Kanngießer, W. Malzer, *Solid State Phenomena* **2003**, *92*, 165–170, DOI 10.4028/www.scientific.net/SSP.92.165.

[171] Grioni, Goedkoop, Schoorl, F. M. de Groot, Fuggle, Schäfers, Koch, Rossi, Esteva, Karnatak, *Phys. Rev. B* **1989**, *39*(3), 1541–1545.

[172] F. Senf, U. Flechsig, F. Eggenstein, W. Gudat, R. Klein, H. Rabus, G. Ulm, *Journal of synchrotron radiation* **1998**, *5*(Pt 3), 780–782, DOI 10.1107/S0909049597020323.

[173] A. Kulow, S. Witte, S. Beyer, A. Guilherme Buzanich, M. Radtke, U. Reinholz, H. Riesemeier, C. Streli, *Journal of Analytical Atomic Spectrometry* **2019**, *34*(1), 239–246, DOI 10.1039/c8ja00313k.

[174] J. Lubeck, B. Beckhoff, R. Fliegauf, I. Holfelder, P. Hönicke, M. Müller, B. Pollakowski, F. Reinhardt, J. Weser, *The Review of scientific instruments* **2013**, *84*(4), 045106, DOI 10.1063/1.4798299.

[175] D. Barreca, A. Gasparotto, E. Tondello, *Surface Science Spectra* **2007**, *14*(1), 41–51, DOI 10.1116/11.20080701.

[176] S. Poulston, P. M. Parlett, P. Stone, M. Bowker, *Surf. Interface Anal.* **1996**, *24*(12), 811–820, DOI 10.1002/(SICI)1096-9918(199611)24:12{\textless}811::AID-SIA191{\textgreater}3.0.CO;2-Z.

[177] Y. Sakai, S. Ninomiya, K. Hiraoka, *Surface and Interface Analysis* **2012**, *44*(8), 938–941, DOI 10.1002/sia.4843.

[178] M. C. Biesinger, L. W. Lau, A. R. Gerson, R. S. Smart, *Applied Surface Science* **2010**, *257*(3), 887–898, DOI 10.1016/j.apsusc.2010.07.086.

[179] J.-Y. Park, Y.-S. Jung, J. Cho, W.-K. Choi, *Applied Surface Science* **2006**, *252*(16), 5877–5891, DOI 10.1016/j.apsusc.2005.08.019.

[180] C. Powell, X-ray Photoelectron Spectroscopy Database XPS,Version 4.1, NIST Standard Reference Database 20, DOI 10.18434/T4T88K.

[181] V. Andrei, K. Bethke, F. Madzharova, S. Beeg, A. Knop-Gericke, J. Kneipp, K. Rademann, *Adv. Electron. Mater.* **2017**, *3*(2), 1600473, DOI 10.1002/aelm.201600473.

[182] V. Andrei, K. Bethke, F. Madzharova, A. C. Bronneberg, J. Kneipp, K. Rademann, *ACS Appl. Mater. Interfaces* **2017**, *9*(38), 33308–33316, DOI 10.1021/acsami.7b10106.

[183] K. A. Borup, J. de Boor, H. Wang, F. Drymiotis, F. Gascoin, X. Shi, L. Chen, M. I. Fedorov, E. Müller, B. B. Iversen, G. J. Snyder, *Energy & Environmental Science* **2015**, *8*(2), 423–435, DOI 10.1039/C4EE01320D.

[184] O. Bubnova, Z. U. Khan, H. Wang, S. Braun, D. R. Evans, M. Fabretto, P. Hojati-Talemi, D. Dagnelund, J.-B. Arlin, Y. H. Geerts, S. Desbief, D. W. Breiby, J. W. Andreasen, R. Lazzaroni, W. M. Chen, I. Zozoulenko, M. Fahlman, P. J. Murphy, M. Berggren, X. Crispin, *Nature materials* **2014**, *13*(6), 662, DOI 10.1038/nmat3981.

[185] H. Shi, C. Liu, Q. Jiang, J. Xu, *Advanced Electronic Materials* **2015**, *1*(4), 1500017, DOI 10.1002/aelm.201500017.

[186] Q. Zhang, Y. Sun, W. Xu, D. Zhu, *Advanced Materials* **2014**, *26*(40), 6829–6851, DOI 10.1002/adma.201305371.

[187] X. Y. Wang, C. Y. Liu, L. Miao, J. Gao, Y. Chen, *Journal of Electronic Materials* **2016**, *45*(3), 1813–1820, DOI 10.1007/s11664-015-4231-5.

[188] Q. Wang, Q. Yao, J. Chang, L. Chen, *Journal of Materials Chemistry* **2012**, *22*(34), 17612, DOI 10.1039/c2jm32750c.

[189] J. Liu, H.-Q. Yu, *Journal of Electronic Materials* **2014**, *43*(4), 1181–1187, DOI 10.1007/s11664-013-2958-4.

[190] L. Wang, Q. Yao, H. Bi, F. Huang, Q. Wang, L. Chen, *Journal of Materials Chemistry A* **2015**, *3*(13), 7086–7092, DOI 10.1039/C4TA06422D.

[191] Y. Wang, S. M. Zhang, Y. Deng, *Journal of Materials Chemistry A* **2016**, *4*(9), 3554–3559, DOI 10.1039/C6TA01140C.

[192] S. K. Yee, N. E. Coates, A. Majumdar, J. J. Urban, R. A. Segalman, *Physical chemistry chemical physics : PCCP* **2013**, *15*(11), 4024–4032, DOI 10.1039/c3cp44558e.

[193] B. T. McGrail, A. Sehirlioglu, E. Pentzer, *Angewandte Chemie (International ed. in English)* **2015**, *54*(6), 1710–1723, DOI 10.1002/anie.201408431.

[194] C. Cho, B. Stevens, J.-H. Hsu, R. Bureau, D. A. Hagen, O. Regev, C. Yu, J. C. Grunlan, *Advanced Materials* **2015**, *27*(19), 2996–3001, DOI 10.1002/adma.201405738.

[195] C. Cho, K. L. Wallace, P. Tzeng, J.-H. Hsu, C. Yu, J. C. Grunlan, *Advanced Energy Materials* **2016**, *6*(7), 1502168, DOI 10.1002/aenm.201502168.

[196] A. J. Heeger, *The Journal of Physical Chemistry B* **2001**, *105*(36), 8475–8491, DOI 10.1021/jp011611w.

[197] O. Bubnova, M. Berggren, X. Crispin, *Journal of the American Chemical Society* **2012**, *134*(40), 16456–16459, DOI 10.1021/ja305188r.

[198] Z. Lu, J. Zhou, A. Wang, N. Wang, X. Yang, *Journal of Materials Chemistry* **2011**, *21*(12), 4161, DOI 10.1039/c0jm03299a.

[199] V. Andrei, K. Bethke, K. Rademann, *Phys. Chem. Chem. Phys.* **2016**, *18*(16), 10700–10707, DOI 10.1039/c5cp06828b.

[200] J. R. Sootsman, D. Y. Chung, M. G. Kanatzidis, *Angewandte Chemie (International ed. in English)* **2009**, *48*(46), 8616–8639, DOI 10.1002/anie.200900598.

[201] D. Music, F. H.-U. Basse, L. Han, Devender, T. Borca-Tasciuc, J. J. Gengler, A. A. Voevodin, G. Ramanath, J. M. Schneider, *Applied Physics Letters* **2014**, *104*(5), 053903, DOI 10.1063/1.4864078.

[202] N. Cusack, P. Kendall, *Proceedings of the Physical Society* **1958**, *72*(5), 898–901, DOI 10.1088/0370-1328/72/5/429.

[203] W. Vogt, *Annalen der Physik* **1930**, *399*(2), 183–204, DOI 10.1002/andp.19303990204.

[204] R. B. Wilson, D. G. Cahill, *Nature communications* **2014**, *5*, 5075, DOI 10.1038/ncomms6075.

[205] Y.-C. Hua, B.-Y. Cao, *International Journal of Thermal Sciences* **2016**, *101*, 126–132, DOI 10.1016/j.ijthermalsci.2015.10.037.

[206] E. T. Swartz, R. O. Pohl, *Reviews of Modern Physics* **1989**, *61*(3), 605–668, DOI 10.1103/RevModPhys.61.605.

[207] C.-W. Nan, R. Birringer, D. R. Clarke, H. Gleiter, *Journal of Applied Physics* **1997**, *81*(10), 6692–6699, DOI 10.1063/1.365209.

[208] H.-L. Li, Y.-C. Hua, B.-Y. Cao, *International Journal of Heat and Mass Transfer* **2018**, *127*, 1014–1022, DOI 10.1016/j.ijheatmasstransfer.2018.06.080.

[209] G. L. POLLACK, *Reviews of Modern Physics* **1969**, *41*(1), 48–81, DOI 10.1103/RevModPhys.41.48.

[210] G. Chen, *Physical Review B* **1998**, *57*(23), 14958–14973, DOI 10.1103/PhysRevB.57.14958.

[211] R. S. Prasher, P. E. Phelan, *Phys. Rev. B* **2001**, *123*(1), 105, DOI 10.1115/1.1338138.

[212] E. S. Landry, A. J. H. McGaughey, *Physical Review B* **2009**, *80*(16), 334, DOI 10.1103/PhysRevB.80.165304.

[213] M. D. Losego, M. E. Grady, N. R. Sottos, D. G. Cahill, P. V. Braun, *Nature materials* **2012**, *11*(6), 502–506, DOI 10.1038/nmat3303.

[214] Y. Dong, B.-Y. Cao, Z.-Y. Guo, *Physica E: Low-dimensional Systems and Nanostructures* **2014**, *56*, 256–262, DOI 10.1016/j.physe.2013.10.006.

[215] Y.-C. Hua, B.-Y. Cao, *International Journal of Heat and Mass Transfer* **2014**, *78*, 755–759, DOI 10.1016/j.ijheatmasstransfer.2014.07.037.

[216] K. T. Regner, D. P. Sellan, Z. Su, C. H. Amon, A. J. H. McGaughey, J. A. Malen, *Nature communications* **2013**, *4*, 1640, DOI 10.1038/ncomms2630.

[217] B. Qiu, H. Bao, G. Zhang, Y. Wu, X. Ruan, *Computational Materials Science* **2012**, *53*(1), 278–285, DOI 10.1016/j.commatsci.2011.08.016.

[218] K. Biswas, J. He, I. D. Blum, C.-I. Wu, T. P. Hogan, D. N. Seidman, V. P. Dravid, M. G. Kanatzidis, *Nature* **2012**, *489*(7416), 414–418, DOI 10.1038/nature11439.

[219] S. Hu, J. Chen, N. Yang, B. Li, *Carbon* **2017**, *116*, 139–144, DOI 10.1016/j.carbon.2017.01.089.

[220] L. D. Bellis, P. E. Phelan, R. S. Prasher, *Journal of Thermophysics and Heat Transfer* **2000**, *14*(2), 144–150, DOI 10.2514/2.6525.

[221] Y. Apertet, H. Ouerdane, C. Goupil, P. Lecoeur, *J. Appl. Phys.* **2014**, *116*(14), 144901, DOI 10.1063/1.4897350.

[222] R. Mitdank, M. Handwerg, C. Steinweg, W. Töllner, M. Daub, K. Nielsch, S. F. Fischer, *Journal of Applied Physics* **2012**, *111*(10), 104320, DOI 10.1063/1.4721896.

[223] T. E. Huber, R. Scott, S. Johnson, T. Brower, J. H. Belk, J. H. Hunt, *Applied Physics Letters* **2013**, *103*(4), 041114, DOI 10.1063/1.4816621.

[224] Z. Wang, D. Kojda, N. Peranio, M. Kroener, R. Mitdank, W. Toellner, K. Nielsch, S. F. Fischer, S. Gutsch, M. Zacharias, O. Eibl, P. Woias, *Nanotechnology* **2015**, *26*(12), 125707, DOI 10.1088/0957-4484/26/12/125707.

[225] B. Endrődi, G. F. Samu, D. Fejes, Z. Németh, E. Horváth, A. Pisoni, P. K. Matus, K. Hernádi, C. Visy, L. Forró, C. Janáky, *Journal of Polymer Science Part B: Polymer Physics* **2015**, *53*(21), 1507–1518, DOI 10.1002/polb.23782.

[226] G. Yuan, R. Mitdank, A. Mogilatenko, S. F. Fischer, *The Journal of Physical Chemistry C* **2012**, *116*(25), 13767–13773, DOI 10.1021/jp212427g.

[227] B. Xu, K. Fobelets, *Journal of Applied Physics* **2014**, *115*(21), 214306, DOI 10.1063/1.4881781.

[228] J. Choi, K. Cho, S. Kim, *Advanced Energy Materials* **2017**, *7*(7), 1602138, DOI 10.1002/aenm.201602138.

[229] J. Maire, R. Anufriev, T. Hori, J. Shiomi, S. Volz, M. Nomura, *Scientific reports* **2018**, *8*(1), 4452, DOI 10.1038/s41598-018-22509-0.

6 Acknowledgement

This doctoral thesis success was only possible due to numerous collaborations. I want to thank all the researchers from many different disciplines for their excellent work and their great and helpful attitude. All of the people involved in this thesis have my deepest gratitude for the contribution, which made this thesis a success.

First of all, I want to thank my supervisor Prof. Dr. Klaus Rademann. I want to thank him for the opportunity to write my doctoral thesis in his research group. I am very thankful for his great spirit and interest in my work. In particular, I like to thank him for all the contacts he provided, which led to great collaborations and the challenges he gave me in teaching and research, which offered me the opportunity to grow.

I like to thank my second supervisor Prof. Dr. Freund from the Max-Planck Institute, for all the time he took reviewing my doctoral thesis. I would like to express my gratitude to Prof. Dr. Reinhard Stößer, who sadly passed away during the time of this thesis. I enjoyed the work and talks with him and to express my deepest condolences to his family and friends. I like to thank Prof. Dr. Birgit Kanngießer from Technical University Berlin, for the helpful discussions and the opportunity to measure X-Ray Fluorescence at her group.

I am most grateful to Dr. Burkhard Beckhoff and Dr. Beatrix Pollakowski from *Physikalisch-Technische Bundesanstalt* for the chance to use modern synchrotron grazing incidence X-Ray fluorescence at the PTB beam line at BESSY.

I am most thankful to M.Sc. Virgil Andrei for his continued support, great spirit, and his devotion to science. I like to express my deepest gratitude to Dr. Jonas Baumann for his support and the long-lasting collaboration, the helpful discussions, and the insight into physics. I am very thankful to Dr. Dany Kojda for the Seebeck and Hall measurements he performed for me. Another valued colleague I like to thank M.Sc. Nicolas Zorn Morales for the X-ray Photoelectron Spectroscopy measurements he performed for me. I like to thank Ph.D. G. Cristian Vásquez and Prof. Dr. Terje G. Finstad from the University of Oslo for the measurements, the performed SEM cross-sections with back-scattered electron measurements, and the analysis of k-ratios. I like to express my gratitude to Christoph Erdmann for his help with TEM and SEM measurements.

I am very thankful to Prof. Jeyanthinath Mayandi from Madurai Kamaraj University, India, for his dedication to science, his great spirit, and the fruitful collaboration. I like to thank Ph. D. Abinaya Chandrasekaran, for her positive attitude and the fruitful partnership with India.

I like to express my thanks to Dipl. Chem. Daniel Muschke for his hard work during his diploma thesis and his cheerful attitude. I like to thank all Bachelor students, where I had the privilege to supervise and support their thesis: M.Sc. Virgil Andrei, M.Sc. Tassilo Waniek, M.Sc. Marcel Roß, M.Sc. Christian Dictus, M.Sc. Tobias Grosser, M.Sc. Kim Greis, M.Sc. Julius Stückrath, M.Sc. Tjark Ingber, B.Sc. Eric Pasche and Mete-Sungur Dal-

gic. Each of them did outstanding work, and their great spirit made it a delight to work with them.

I like to express my gratitude to all members of the group from Prof. Dr. Rademann for the excellent working environment and support. In particular, I want to thank Dr. Robert Wendt and Dr. Christian Schaumberg for the help with AFM and fixing the ESEM, M.Sc. Alexander Birnbaum, for his help with UV-Vis. I like to thank Dr. Jörg Polte for the helpful discussions. I am very thankful for the countless hours M. A. Marie Mohrmann spent with me reviewing applications for grants and helping me with University formalities. I like to thank Dipl.-Chem. Paul Saftien for his help with supervising students in the physical-chemical lab courses.

I am very grateful to the Max-Planck Society and their International Max-Planck Research School for the scholarship they provided for me and all the great seminars. My thanks go to the DAAD for the opportunity they gave me to build up the collaboration with the Madurai Kamaraj University in India. I like to thank the *Humboldt-Universität zu Berlin* for the great travel program, which made the start of the collaboration with India possible.

I like to thank M.Sc. Richard Reisig for the great and helpful discussions, the insights he gave me into engineering and his great attitude and support. I am very grateful to Dipl. Chem. Dennis Dietz for the great friendship we have and his continued support. I am very grateful to M.Sc. Niels Kramer, Dipl.-Finw. (FH) LL. M. Melanie Kramer and Dipl.-Finw. (FH) Jana Hübner for the great friendship. I like to thank Dirk Behrends for his friendship and joyous attitude. I like to thank my brothers for their ongoing support. In particular, I want to express my gratitude to B.Sc. Patrick Bethke, for the helpful debate about the theoretical mathematical part of this thesis.

I like to thank my parents, family, and friends for their continued support during my studies and my doctoral thesis. I am particularly very grateful to my father, Dr. Rudolf Mathias, who sadly passed away, for sparking my interest in science. I like to thank my mother, Martina Bethke, for all the support she provided. I would also like to thank Peter Möck for his continued support.

7 Appendix

7.1 Seebeck Measurement Device

7.1.1 Firmware of Atmel Microcontroler

```
//author: KOR
// working callresponse code including PID
// beta 0.31415 watercooled
// increased serial speed (baudrate 115200)
#include <OneWire.h>
#include <DallasTemperature.h>
#include <PID_v1.h>
#include "helper.c"
//global variables
int inByte = 0;                                   // incoming serial ↩
    byte
int pwmpeltier1 = 3;                             //The N-Channel MOSFET ↩
    is on digital pin 3
int pwmpeltier2 = 11;                            //The N-Channel MOSFET ↩
    is on digital pin 11
int dirpeltier1 = 8;
int dirpeltier2 = 7;
int fan = 9;
int green = 5;
int red = 6;
int dirstate = LOW;
int power = 0;                                    //Power level fro 0 to↩
     99%
```

```
int peltier_level = map(power, 0, 99, 0, 255);  //This is a value from 0 to 255 that actually controls the MOSFET
int lx = 0;                                     //LED status
int fanstat=0;
//-------------------------------------------- One Wire Tempsensors Setup------------------------------------------------
// Data wire is plugged into pin 4 on the Arduino
#define ONE_WIRE_BUS 4

// Setup a oneWire instance to communicate with any OneWire devices
// (not just Maxim/Dallas temperature ICs)
OneWire oneWire(ONE_WIRE_BUS);

// Pass our oneWire reference to Dallas Temperature.
DallasTemperature sensors(&oneWire);
DeviceAddress tmp_address;
int numberOfDevices;
//---------------------------------------end One Wire Tempsensors Setup------------------------------------------------
//-------------------------------------------------------- PID Setup---------------------------------------------------------------
//Define Variables we'll be connecting to
double Setpoint1, Input1, Output1, Setpoint2, Input2, Output2;
//Define the aggressive and conservative Tuning Parameters
double Kp1=39, Ki1=0.9, Kd1=43;
double Kp2=4, Ki2=0.2, Kd2=1;
byte PIDon=0;

//Specify the links and initial tuning parameters
PID myPIDh(&Input1, &Output1, &Setpoint1, Kp1, Ki1, Kd1, DIRECT);
PID myPIDc(&Input2, &Output2, &Setpoint2, Kp2, Ki2, Kd2, REVERSE);
//-----------------------------------------------------------end PID Setup---------------------------------------------------------------
//setup is the first function which is called.
void setup()
{
  // start serial port at 115200 bps:
  Serial.begin(115200);
  while (!Serial) {
    ; // wait for serial port to connect. Needed for Leonardo only
  }
```

```
  pinMode(fan, OUTPUT);
  digitalWrite(fan, fanstat);
  establishContact();  // send a byte to establish contact until receiver responds
  sensors.begin();
  delay(1000);
  numberOfDevices = sensors.getDeviceCount();
  Serial.print("Found ");
  Serial.print(numberOfDevices);
  Serial.println(" sensors. Starting now...");

  //setup peltier
  pinMode(dirpeltier1, OUTPUT);
  pinMode(dirpeltier2, OUTPUT);
  digitalWrite(dirpeltier1, dirstate);
  digitalWrite(dirpeltier2, dirstate);
  setPwmFrequency(11, 1024);

  //----------setup PID----------
  //flush temperature sensor buffer
  for(int i=0;i<=3;i++)
  {
    float t1,t2;
    getTemp(t1,t2);
  }
  //declaring Setpoints to be initial values
  float t1,t2;
  getTemp(t1,t2);
  Input1=t1;
  Input2=t2;
  Setpoint1=t1;
  Setpoint2=t2;
  //Initializing values
  //PID stays off for now
  //---------- end setup PID----------
}

void mainfkt(int mini, int maxi)
{
  if (Serial.peek() == 'r')
  {
```

```
    char y = Serial.read();
    //Serial.write(y);Serial.println(" Reads data from sensors.");
    SendTemperature();
  }
  else if (Serial.peek() == 's')
    {
    char y = Serial.read();
    int t=power;
    power=readint(mini,maxi);
    if (t!=power){
        setpowerlevel();
      }
    }
   else if (Serial.peek() == 'c')
   {
     char y = Serial.read();
     changedir(power);
   }
    else if (Serial.peek() == 'f')
   {
     char y = Serial.read();
     fanstat=readint(0,1);
     Serial.println("changing fanstat");
     if (fanstat==1)
     {
      digitalWrite(fan, HIGH);
     }
     else
     {
      digitalWrite(fan, LOW);
     }
   }
   else if  (Serial.peek() == 'n')
   {
     char y = Serial.read();
     //Serial.print(y);Serial.print(" Number of found sensors: ");
     numberOfDevices = sensors.getDeviceCount();
     Serial.println(numberOfDevices);
   }
   else if (Serial.peek() == 'p')
   {
```

```
      char y = Serial.read();
      Serial.print(y);Serial.println(" starting PIDs!");
      myPIDh.SetMode(AUTOMATIC);
      myPIDc.SetMode(AUTOMATIC);
      PIDon=1;
    }
    else if (Serial.peek() == 'a')
    {
      char y = Serial.read();
      Serial.print(y);Serial.println(" starting PID hot side!");
      myPIDh.SetMode(AUTOMATIC);
      PIDon=1;
    }
    else if (Serial.peek() == 'b')
    {
      char y = Serial.read();
      Serial.print(y);Serial.println(" starting PID cold side!");
      myPIDc.SetMode(AUTOMATIC);
      PIDon=1;
    }
    else if (Serial.peek() == 'k')
    {
      char y = Serial.read();
      Kp1=readdouble(0.0,500.0);
      Ki1=readdouble(0.0,500.0);
      Kd1=readdouble(0.0,500.0);
      SendHotKs();
    }
    else if (Serial.peek() == 'j')
    {
      char y = Serial.read();
      Kp2=readdouble(0.0,500.0);
      Ki2=readdouble(0.0,500.0);
      Kd2=readdouble(0.0,500.0);
      SendColdKs();
    }
    else if (Serial.peek() == 't')
    {
      //get Setpoint for hot side
      char y = Serial.read();
      Setpoint1=readdouble(22,80);
```

```
    SendHotKs();
  }
  else if (Serial.peek() == 'u')
  {
    //get Setpoint for cold side
    char y = Serial.read();
    Setpoint2=readdouble(10,22);
    SendColdKs();
  }
  else if (Serial.peek() == 'o')
  {
    // turn off both peltiers
    char y = Serial.read();
    Setpoint1=25;
    myPIDh.SetMode(MANUAL);
    myPIDc.SetMode(MANUAL);
    PIDon=0;
    Output1=0;
    Output2=0;
    analogWrite(pwmpeltier1, Output1);
    analogWrite(pwmpeltier2, Output2);
    Serial.println("PID off");
  }
  else if (Serial.peek() == 'd')
  {
    // turn off PID hot side //? =e
    char y = Serial.read();
    Setpoint1=25;
    myPIDh.SetMode(MANUAL);
    PIDon=0;
    Output1=0;
    analogWrite(pwmpeltier1, Output1);
    Serial.println("hot side PID off");
  }
  else if (Serial.peek() == 'e')
  {
    // turn off PID hot side //? =d
    char y = Serial.read();
    Setpoint1=25;
    myPIDc.SetMode(MANUAL);
    PIDon=0;
```

```
    Output1=0;
    analogWrite(pwmpeltier2, Output1);
    Serial.println("hot side PID off");
  }
  else if (Serial.peek() == 'g')
  {
    //get data for hot side
    char y = Serial.read();
    Serial.print("In.: ");Serial.print(Input1);Serial.print(" SP: ");↩
        Serial.print(Setpoint1);Serial.print(" Out: ");Serial.print(↩
        Output1);Serial.print(" Kp: ");Serial.print(Kp1);
    Serial.print(" Ki: ");Serial.print(Ki1);Serial.print(" Kd: ");↩
        Serial.print(Kd1);Serial.print(" PIDon: ");Serial.println(↩
        PIDon);
  }
  else if (Serial.peek() == 'i')
  {
    //get data for cold side
    char y = Serial.read();
    Serial.print("In.: ");Serial.print(Input2);Serial.print(" SP: ");↩
        Serial.print(Setpoint2);Serial.print(" Out.: ");Serial.print(↩
        Output2);Serial.print(" Kp: ");Serial.print(Kp2);
    Serial.print(" Ki: ");Serial.print(Ki2);Serial.print(" Kd: ");↩
        Serial.print(Kd2);Serial.print(" PIDon: ");Serial.println(↩
        PIDon);
  }
  else if (Serial.peek() == 'l')
  {
   //change led status 0 off 1 red 2 green 3 both
    char y = Serial.read();

    lx=readint(0,4);
    if (lx==0){
     digitalWrite(red, 0);
     digitalWrite(green, 0);
    }
    else if (lx==1){
     digitalWrite(red, 1);
     digitalWrite(green, 0);
    }
    else if (lx==2){
```

```
     digitalWrite(red, 0);
     digitalWrite(green, 1);
    }
    else {
     digitalWrite(red, 1);
     digitalWrite(green, 1);
    }
  }
  else if (Serial.peek() == 'h')
  {
    char y = Serial.read();
    Serial.println(" Help: known commands:\n");
    Serial.print(" a turn on pid hot side\n");
    Serial.print(" b turn on pid cold side\n");
    Serial.print(" c change current direction keep power levels\n");
    Serial.print(" d turn off pid hot side\n");
    Serial.print(" e turn off pid cold side\n");
    Serial.print(" f (int 0-1) switch fan on or off\n");
    Serial.print(" g get data relevant for PID hot side\n");
    Serial.print(" h help\n");
    Serial.print(" i get data relevant for PID cold side\n");
    Serial.print(" j (int)(int)(int) change kp ki and kd for PID (cold side)\n");
    Serial.print(" k (int)(int)(int) change kp ki and kd for PID (hot side)\n");
    Serial.print(" l (int 0-3) turn leds on of 0 off 1 red 2 green 3 both\n");
    Serial.print(" n number of sensors\n");
    Serial.print(" o turn PIDs off\n");
    Serial.print(" p start PIDs\n");
    Serial.print(" s(int) set powerlevels to (int)\n");
    Serial.print(" t (double) set setpoint for PID (hot side) to (double) range (22-80)\n");
    Serial.print(" u (double) set setpoint for PID (cold side) to (double) range (10 - 22)\n");
  }
  else{
    char y = Serial.read();
    Serial.print(y);Serial.println(" Not recognized command");
  }
}
```

```

void SendHotKs() {
  char buffer[25];
  String sKp1=ftoa(buffer, Kp1, 2);
  String sKi1=ftoa(buffer, Ki1, 2);
  String sKd1=ftoa(buffer, Kd1, 2);
  Serial.println("Kp1: "+sKp1+" Ki1: "+sKi1+" Kd1: "+sKd1);
}
void SendColdKs() {
  char buffer[25];
  String sKp2=ftoa(buffer, Kp2, 2);
  String sKi2=ftoa(buffer, Ki2, 2);
  String sKd2=ftoa(buffer, Kd2, 2);
  Serial.println("Kp2: "+sKp2+" Ki2: "+sKi2+" Kd2: "+sKd2);
}
void loop()
{
  // if we get a valid byte, read analog ins:
  if (Serial.available() > 0) {
    // get incoming byte:

    //Serial.println("Serial Available");
    mainfkt(0,100);

  }
  else if (PIDon==1) {
    //do PID Stuff
    float t1,t2;
    getTemp(t1,t2);
    if (dirstate==LOW)
    {
      Input1 = t1;
      Input2 = t2;
    }
    else
    {
      //changed direction: switch input values
      Input1 = t2;
      Input2 = t1;
    }
    myPIDh.SetTunings(Kp1, Ki1, Kd1);
```

```
    myPIDh.Compute();
    myPIDc.SetTunings(Kp2, Ki2, Kd2);
    myPIDc.Compute();
    //Serial.print("Input: ");Serial.print(Input1);Serial.print("Setpoint: ");Serial.print(Setpoint1);Serial.print("Output: ");Serial.println(Output1);
    if (dirstate==LOW)
    {
      analogWrite(pwmpeltier1, Output1); // Peltier1 set to PID Output
      analogWrite(pwmpeltier2, Output2); // Peltier2 set to PID Output
    }
    else
    {
      //changed direction: switch pwmpeltiers to corresponding Outputs
      analogWrite(pwmpeltier1, Output2); // Peltier1 set to PID Output
      analogWrite(pwmpeltier2, Output1); // Peltier2 set to PID Output
    }
  }
}

void changedir(int power){
  // takes the current power level switches relays to change
  // current direction for peltiers. switches the PWM signal off
  // during switching process
  if (dirstate== LOW) dirstate=HIGH;
  else dirstate=LOW;
  //switch off pwm
  peltier_level = map(0, 0, 99, 0, 255);
  analogWrite(pwmpeltier1, peltier_level); //Write this new value out to the port
  analogWrite(pwmpeltier2, peltier_level);
  Serial.println("Off ");
  delay(100);
  //change direction
  digitalWrite(dirpeltier1, dirstate);
  digitalWrite(dirpeltier2, dirstate);
  delay(100);
  //switch pwm back on to prevois level
  peltier_level = map(power, 0, 99, 0, 255);
  analogWrite(pwmpeltier1, peltier_level); //Write this new value out to the port
```

```
  analogWrite(pwmpeltier2, peltier_level);
  Serial.println("On ");
}

double readdouble(double mini, double maxi)
{
    double x = Serial.parseFloat();
    if (x< mini || x>maxi){
      if (x< mini){
        x=mini;
      }
      else{
        x=maxi;
      }
     }
     return(x);
}

int readint(int mini, int maxi)
{
  float in=Serial.parseFloat();
    int x =(int)in;
    if (x< mini || x>maxi){
      if (x< mini){
        x=mini;
      }
      else{
        x=maxi;
      }
     }
     return(x);
}

void setpowerlevel()
{
  if(power > 100) power = 100;
  if(power < 0) power = 0;
  peltier_level = map(power, 0, 100, 0, 255);
  Serial.print("Power=");
  Serial.print(power);
  Serial.print(" PLevel=");
```

```
  Serial.println(peltier_level);
  analogWrite(pwmpeltier1, peltier_level); //Write this new value out to the port
  analogWrite(pwmpeltier2, peltier_level); //Write this new value out to the port
}

void getTemp(float &t1, float &t2)
{
  float t[numberOfDevices];
  sensors.requestTemperatures(); // Send the command to get temperatures
  for(int i=0;i<numberOfDevices; i++) // parse through all temperature sensors
  {
    t[i]=sensors.getTempCByIndex(i);

    if (t[i]==-127)
    {
      delay(50);
      i-=1; //read again after 50ms
    }
  }
  t2=t[0];
  t1=t[1];
}

void SendTemperature()
{
  float t1,t2;
  getTemp(t1,t2);
  char buffer[25];
  String T1=ftoa(buffer, t1, 2);
  String T2=ftoa(buffer, t2, 2);
  Serial.println("Sensor 1: "+T1+" Sensor 2: "+T2);
}

void establishContact() {
  while (Serial.available() <= 0) {
    Serial.print('A');   // send a capital A
    delay(300);
```

```
  }
}

void setPwmFrequency(int pin, int divisor) {
  //change the PWM frequency
  byte mode;
  if(pin == 5 || pin == 6 || pin == 9 || pin == 10) {
    switch(divisor) {
      case 1: mode = 0x01; break;
      case 8: mode = 0x02; break;
      case 64: mode = 0x03; break;
      case 256: mode = 0x04; break;
      case 1024: mode = 0x05; break;
      default: return;
    }
    if(pin == 5 || pin == 6) {
      TCCR0B = TCCR0B & 0b11111000 | mode;
    } else {
      TCCR1B = TCCR1B & 0b11111000 | mode;
    }
  } else if(pin == 3 || pin == 11) {
    switch(divisor) {
      case 1: mode = 0x01; break;
      case 8: mode = 0x02; break;
      case 32: mode = 0x03; break;
      case 64: mode = 0x04; break;
      case 128: mode = 0x05; break;
      case 256: mode = 0x06; break;
      case 1024: mode = 0x7; break;
      default: return;
    }
    TCCR2B = TCCR2B & 0b11111000 | mode;
  }
}
```

Listing 7.1 Firmware installed on the Atmel ATmega328P Microcontroller for Peltier temperature controller. Description can be found in section section 3.1.3 on page 40.

7.1.2 Driver for Fluke Multimeter

```
import serial, struct, sys, time
import serial.tools.list_ports
from time import gmtime, strftime
__author__ = 'KOR'
__version__ = 0.1

class Fluke:
    """Class for Fluke 289 Multimeter"""
    def __init__(self):
        try:
            #setup serial communications
            ports = list(serial.tools.list_ports.comports())
            portnumber = 0
            for p in ports:
                print p
                if ("USB Serial Port" in p[1] and "A9009BFBA" in p[2])↩
                     or ("USB Serial Port" in p[1] and "AI02M6UCA" in ↩
                    p[2]):
                    print "This is a Fluke!"
                    portnumber = int(p[0][3:]) - 1
                    print portnumber
                print portnumber
            self.fluke = serial.Serial(port=portnumber, baudrate↩
                =115200,
                                  bytesize=8, timeout=1, parity=serial.↩
                                      PARITY_NONE, stopbits=serial.↩
                                      STOPBITS_ONE)
            #check port
            if self.fluke.isOpen():
                print "Port is open. Start Program."
            else:
                try:
                    self.fluke.open()
                except Exception, e:
                    print "problem while openning the port : " +str(e)
                    exit()
            print "Fluke 289 Digital Multimeter"
```

```
            self.fluke.isOpen()
        except:
            print "Can't find Fluke Multimeter. Please check ↩
                connection"
            sys.exit(0)
    def __del__(self):
        """destructor: closes comunication after class is terminated↩
            """
        try:
            self.fluke.close()
        except:
            print "Connection already terminated."

    def read(self):
        """sends Query Measurement "QM" command and reads the answer ↩
            from Fluke Multimeter"""
        self.fluke.write('QM\r')
        self.fluke.flushInput()
        data=self.fluke.read(18)
        if data=='':
            self.fluke.close()
        else:
            print ""#data
        return data

    def cread(self):
        """reads data from fluke and clears unessessary information ↩
            from it"""
        rdata=self.read()
        rdata=rdata.split()
        try:
            data=rdata[1].split(",")
            data=data[:2]
        except:
            print "Communication Error: check connection"
        return data

if __name__ == "__main__":
    """if top module: reads 20 lines from fluke 0.5 seconds apart """
    Fluke=Fluke()
    for i in range (20):
```

```
        print Fluke.cread()
        time.sleep(0.5)
```

Listing 7.2 Fluke283 Serial Driver

7.1.3 Driver for temperature controller

```
from math import sqrt
import serial, time
import serial.tools.list_ports
import numpy as np
import matplotlib.pyplot as plt
__author__ = 'KOR'
__version__ = 0.32

def frange(x, y, inc):
    while x < y:
        yield x
        x += inc


class PHCD:
    """Class for Peltier heating cooling device"""
    def __init__(self):
        # setup serial communications
        ports = list(serial.tools.list_ports.comports())
        portnumber = 0
        for p in ports:
            print p
            if ("USB Serial Port" in p[1] and "VID_0403+PID_6001+↩
                A600CNMQA" in p[2]) or ("USB-SERIAL CH340" in p[1] and↩
                 "USB VID:PID=1A86:7523" in p[2]):
                print "This is an Arduino!"
                portnumber = int(p[0][3:]) - 1
                print portnumber
        print portnumber
        self.phcd = serial.Serial(port=portnumber, baudrate=38400, ↩
            bytesize=8, timeout=1,
                                  parity=serial.PARITY_NONE, stopbits=↩
                                      serial.STOPBITS_ONE)
        print self.phcd.isOpen()
        # check port
        if self.phcd.isOpen():
```

```
            print "Port " + str(portnumber) + " is open. Start Program."
            self.phcd.write("a")
            time.sleep(0.1)
            print self.phcd.inWaiting()
        else:
            try:
                self.phcd.open()
                self.phcd.write("a")
                print "second trail: ", self.phcd.inWaiting()
            except Exception, e:
                print "problem while openning the port : " + str(e)
                exit()
        print "Peltier Heating Cooling Devise"
        print "_________________________________"
        self.phcd.flushInput()  # discard everything in input buffer
        time.sleep(0.15)
        for i in range(3):
            self.phcd.write("a")
            time.sleep(0.1)
            self.phcd.flushInput()  # discard everything in input buffer
        self.phcd.isOpen()
        time.sleep(2)
        length = self.phcd.inWaiting()
        print self.phcd.read(length)
        self.phcd.flushInput()  # discard everything in input buffer
        for i in range(4):
            time.sleep(0.5)
            length = self.phcd.inWaiting()
            self.phcd.read(length)
        self.phcd.flushInput()  # discard everything in input buffer

    def __del__(self):
        """destructor: turns off PID, sets peltier power to 0 and closes comunication after class is terminated"""
        try:
            self.turnoffPID()
            self.setpercentage(0)
            self.phcd.close()
            print "terminated connection to PCHD"
```

```
        except:
            print "No connection to PCHD found. So it couldn't be terminated"

    def setpercentage(self, p):
        string = "<s,0," + str(p)+">"
        # print string
        self.phcd.write(string)
        print self.getTemp() #reads Temperature
        return

    def recvSerial(self,timeout=0):
        recvInProgress = False
        startMarker = '<'
        endMarker = '>'
        rc = ''
        received = ""
        if (timeout==0):
            waitcounter=50
        elif (timeout==1):
            waitcounter=100
        else:
            waitcounter=400
        while (self.phcd.inWaiting() > 0 or waitcounter > 0):
            rc = self.phcd.read();
            if (recvInProgress == True):
                if (rc != endMarker):
                    received += rc
                else:
                    recvInProgress = False
                    waitcounter=0
            elif (rc == startMarker):
                recvInProgress = True
            waitcounter-=1
        return received


    def read(self):
        """Reads temperature data from PCHD"""
        self.phcd.write("<r>")
        data = self.recvSerial()
```

```
        if data == '':
            pass
            #self.phcd.close()
        else:
            pass
            #print "received: ",data
        return data

    def getTemp(self):
        """reads temperaturedata from PCHD and clears unessessary information from it"""
        rdata = self.read()
        rdata = rdata.split()
        t1=float(rdata[2])
        t2=float(rdata[3])
        return t1,t2

    def sendKs(self, Kp, Ki, Kd, PID=1):
        """changes K values, PID gives the PID for which the values should be changed 1 hot 2 cold"""
        string = "<k,"+ str(PID)+"," + str(Kp) + "," + str(Ki) + "," + str(Kd)+">"
        self.phcd.write(string)
        time.sleep(1)
        print ("sendKs")
        print self.recvSerial()# discard and print serial

    def getPIDdata(self):
        self.phcd.write("<g>")
        time.sleep(0.5)
        data = self.recvSerial()
        l = data.split()
        try:
            rl = [float(l[2]), float(l[3]), float(l[4]), float(l[5]), float(l[6]), float(l[7])]
        except:
            print "ERROR splitting PID from serial data"
            rl = [0, 0, 0, 0, 0, 0]
        return rl

    def setPIDTemp(self,th,tc=20,PID=1):
```

```
        self.phcd.write("<t,"+str(PID)+","+str(th)+","+str(tc)+">")
        time.sleep(0.75)
        print self.recvSerial()# discard and print serial

    def startPID(self,th,tc=20,PID=1):
        """send setpoints for PIDs and starts them (right now only hot side see firmware)"""
        self.setPIDTemp(th,tc,PID)
        self.phcd.write("<p>")
        time.sleep(0.75)
        print "startPID"
        print self.recvSerial()# discard and print serial

    def switchtempgradient(self):
        """changes direction of current in both peltier elements"""
        self.phcd.write("<c>")
        time.sleep(1.2)

    def turnoffPID(self,PID=0):
        """turns off PID, PID=0 both, 1 hot, 2 cold"""
        self.phcd.write("<o,"+str(PID)+">")
        time.sleep(0.2)
        print self.recvSerial()# discard and print serial

    def plotPIDCurve(self, y, sp, fname, sp2=0,sp3=0,steps=200):
        fig = plt.figure()
        ax = fig.add_subplot(1, 1, 1)
        ysp=[]
        x=[]
        ymax=[]
        ymin=[]
        yover=[]
        delta=0.2
        tx=[]
        ty=[]
        for i in range(len(y)):
            x.append(i)
            if i>steps*2:
                ysp.append(sp3)
            elif i>steps:
                ysp.append(sp2)
```

```
            else:
                ysp.append(sp)
            ymax.append(sp+delta)
            ymin.append(sp-delta)
            yover.append(sp+1.3)
            tx.append(75)
            ty.append(i)
        plt.plot(x,y,color="red")
        plt.plot(x,ysp,color="blue")
        ax.set_ylim([30,48])
        ax.set_xlabel('Time [s]', fontsize=9)
        ax.set_ylabel('Temperature [$^\circ$C]', fontsize=9)
        ax.set_title(fname)
        plt.savefig(fname+".png")

    def writeheatingcurve(self, percent, steps):
        print ("writing heating curve for " + str(percent) + "%")
        self.setpercentage(percent)
        data = []
        for i in range(steps):
            to, tt = self.getTemp()
            try:
                line = [percent, i, to, tt]
            except:
                line = [percent, i, 0, 0]
            data.append(str(line))
            if i % (steps / 10) == 0:
                print str(i / (steps / 10) * 10) + "%"
            time.sleep(0.5)
        fname = str(percent) + "pc heating cooling curve " + str(steps↩
            ) + "steps.txt"
        f = open(fname, "w")
        f.writelines(data)
        f.close()

    def writePIDtuningcurve(self, sp, Kp, Ki, Kd, steps):
        print ("Obtaining PID Kurve with Kp " + str(Kp) + " Ki " + str↩
            (Ki) + " Kd " + str(Kd))
        self.sendKs(Kp, Ki, Kd, 1)
        self.startPID(sp)
        data = []
```

```
        y = []
        for i in range(steps):
            l = self.getPIDdata()
            data.append(str(l))
            y.append(l[0])
            if i % (steps / 10) == 0:
                print str(i / (steps / 10) * 10) + "%"
            time.sleep(0.5)
        fname = str(sp) + " PID heating cooling curve " + str(steps) + "steps Kp" + str(Kp) + " Ki" + str(
            Ki) + " Kd" + str(Kd) + ".txt"
        f = open(fname, "w")
        f.writelines(data)
        f.close()
        self.plotPIDCurve(y,sp,fname[:-4])

    def writePIDjumpcurve(self, sp1,sp2,sp3, Kp, Ki, Kd, steps):
        print ("Obtaining PID Kurve with Kp " + str(Kp) + " Ki " + str(Ki) + " Kd " + str(Kd))
        self.sendKs(Kp, Ki, Kd, 1)
        self.startPID(sp1)
        data = []
        y = []
        for i in range(steps):
            l = self.getPIDdata()
            data.append(str(l))
            y.append(l[0])
            if i % (steps / 10) == 0:
                print str(i / (steps / 10) * 10) + "%"
            time.sleep(0.5)
        self.setPIDTemp(sp2,20,1)
        for i in range(steps):
            l = self.getPIDdata()
            data.append(str(l))
            y.append(l[0])
            if i % (steps / 10) == 0:
                print str(i / (steps / 10) * 10) + "%"
            time.sleep(0.5)
        self.setPIDTemp(sp3,20,1)
        for i in range(steps):
            l = self.getPIDdata()
```

```
            data.append(str(l))
            y.append(l[0])
            if i % (steps / 10) == 0:
                print str(i / (steps / 10) * 10) + "%"
            time.sleep(0.5)
        fname = str(sp1) + " " + str(sp2) + " " + str(sp3) + " PID ↩
            jumping curve " + str(steps) + "steps Kp" + str(Kp) + " Ki↩
            " + str(
            Ki) + " Kd" + str(Kd) + ".txt"
        f = open(fname, "w")
        f.writelines(data)
        f.close()
        self.plotPIDCurve(y,sp1,fname[:-4],sp2,sp3)
    def cooldown(self, d=0.75):
        t1, t2 = self.getTemp()
        diff = sqrt((sqrt(t1 ** 2) - sqrt(t2 ** 2)) ** 2)
        while diff > d:
            if diff > 5:
                time.sleep(10)
            elif diff > 2:
                time.sleep(5)
            else:
                time.sleep(2)
            t1, t2 = self.getTemp()
            diff = sqrt((sqrt(t1 ** 2) - sqrt(t2 ** 2)) ** 2)
            print ("cooldown continues diffrence:", diff)
        print("cool down done.")
    def betrag(self, value):
        return (value * value) ** 0.5

if __name__ == "__main__":
    """test PHCD class if this is the top module"""
    PHCD = PHCD()
    #test functions
    for i in range (20):
        print PHCD.getTemp()
    PHCD.cooldown()
    PHCD.setpercentage(0)
    PHCD.turnoffPID()
    #del PHCD
```

Listing 7.3 Driver for Peltier temperature controller

7.1.4 Graphical user interface

```
# -*- coding: utf-8 -*-
# coded by Kevin Bethke
# version: 0.10 beta
# betterserial
# version: 0.09 alpha

#  new in 0.08a:
#  added mw to csvwrite
#  added cooling between directions
#  cleaned up some coments

# new in 0.09
# added acustic signal after measurement is done
# more cleanup: include libraries
# removed autoscale from seebeck graph
# added y achsis labels with scaling units (U scaling wrong)

# new in 0.10
# added files for just the shelve values

#include libraries
import os
import sys
from datetime import datetime
import numpy as np
try:
    from flukecomtreiber10 import *
    from PHCD031 import*
except:
    print "ERROR: Driver for PHCD or Fluke 289 ar missing."
    sys.exit(1)
try:
    from pyqtgraph.Qt import QtGui, QtCore
    import pyqtgraph as pg
except:
    print "ERROR: pyqt or pyqtgraph library is missing."
    sys.exit(1)
```

```
try:
    import csv
except:
    print "ERROR: csv library is missing."
    sys.exit(1)
try:
    from pygame import mixer  # Load the required library
    alarm=1
except:
    alarm=0
    print "WARNING: pygame is not installed sound is disabled."

#load alarm if pygame is installed


__author__ = 'KOR'
__version__ = 0.10


class Graph:
    def __init__(self):
        #initialization
        self.win = pg.LayoutWidget()
        self.win.resize(800, 600)
        self.win.setWindowTitle('Peltier Heating Cooling Device: ↩
            Graphs')
        if alarm == 1:
            mixer.init()
            mixer.music.load('Alarm.mp3')
        # Enable anti aliasing for prettier plots
        pg.setConfigOptions(antialias=True)


        self.graph = pg.PlotWidget(title="deltaT")
        self.graph.setLabel("left", text="Temperature difference", ↩
            units="K")
        #self.graph.setYRange(-13, 13, padding=None, update=True) ↩
                                  # no fixed range for temperature plot
        self.win.addWidget(self.graph, row=0, col=0, colspan=1)
        self.curve = self.graph.plot(pen='r')  # y yellow  b blue
        self.graphf = pg.PlotWidget(title="U [mV]")
```

```
        self.graphf.setLabel("left", text="Voltage (mV)", units=None, unitPrefix=None)
        #self.graphf.setYRange(-200, 200, padding=None, update=True)                # no fixed range for Voltage plot
        self.win.addWidget(self.graphf, row=0, col=1, colspan=1)
        self.curvef = self.graphf.plot(pen='m')
        # self.win.nextRow()
        self.seebeck = pg.PlotWidget(title="Seebeck Potential [microV/K]")
        self.win.addWidget(self.seebeck, row=1, col=0, colspan=1)
        self.curvex = self.seebeck.plot(pen='y')
        self.seebeck.setLabel("left", text="Seebeck Voltage", units="microV/K")
        self.seebeck.setYRange(-30, 520, padding=None, update=True)                # fixed range for Seebeck plot

        self.control = pg.LayoutWidget()
        self.label = QtGui.QLabel("""Control Area """)
        self.startBtn = QtGui.QPushButton('Start Measurement')
        self.testBtn = QtGui.QPushButton('test button')
        self.abordBtn = QtGui.QPushButton('Abord Measurement')
        self.startPIDBtn = QtGui.QPushButton('Start PID controlled Measurement')

        self.control.addWidget(self.label, row=0, col=0, colspan=1)
        self.control.addWidget(self.startPIDBtn, row=1, col=0, colspan=1)
        # self.control.addWidget(self.startBtn, row=2, col=0, colspan=1)
        self.control.addWidget(self.abordBtn, row=3, col=0, colspan=1)
        # self.control.addWidget(self.testBtn, row=3,col=0,colspan=1)

        # self.startBtn.clicked.connect(self.startmeasurement)
        self.abordBtn.clicked.connect(self.abordmeasurement)
        self.startPIDBtn.clicked.connect(self.startPIDmeasurement)
        # self.testBtn.clicked.connect(self.testdia)

        self.win.addWidget(self.control, row=1, col=1, colspan=1)
        # setting up vars
        self.dataf = []                     # data from fluke
```

```
        self.datap = []                     # temperature data from PHCD
        self.datas = []                     # seebeck data
        self.T1 = []                        # data from Temperature Sensor 1
        self.T2 = []                        # data from Temperature Sensor 2
      self.nosampleNwarning="no sample name entered! The output file will only contain date and time!"
        # init vars
        self.measurementcountdown = 0
        self.measurementdir = 0
        self.PIDmeasurement = 0
        self.PIDstep = 0
        self.startPIDstep = 0
        self.PIDcooldown = 0                # don't change steps won't end
        # ---------------------- options -----------------------
        self.PIDshelftime = 30              # time to remain on each tempreture shelf; standard 20
        self.PIDsteadyreach = 10            # how many times set temp has to be reached before shelf countdown starts; standard 10
        self.avgnum = self.PIDshelftime/2.0 # number of values (from last) in a shelve are considered for average
        self.shelftime = self.PIDshelftime
        self.PIDTemps = [27,30,35]          # temperature steps; standard 27 30 35
        self.PIDshelfstoptime = []          # record end of PIDTemp shelf
        self.PIDmaxTempdeviationcd =  0.75  # max Temp diff for stopping cooldown; praktikum 1.5 eigene Messungen 0.75
        self.Kp = 98.0                      # values for PID air cooled Kp 98.0, Ki 51.0, Kd 87.0
        self.Ki = 51.0                      # for watercooled Kp 49.0, Ki 2.0, Kd 20.0
        self.Kd = 87.0
        self.PIDdT = 0.2                    # max temp difference before starting shelve
        # ---------------------- end of options --------------
        self.timer = QtCore.QTimer()
```

```
        self.timer.timeout.connect(self.update)
        self.timer.start(1000)
        self.Fluke = Fluke()                # initializing Fluke ↩
            Multimeter
        self.PHCD = PHCD()                  # initializing PHCD
        self.win.show()                     # display gui

    def __del__(self):
        print "turning power to peltiers off"
        self.PHCD.setpercentage(0)

    def update(self):
        #update graphical user interface
        # ------ get data--------
        dphcd = self.getdataphcd()
        dfluke = self.getdatafluke()
        dsebeck = self.calcseebeck()
        # ------ end get data ---

        # ------ non pid controlled measurements ---------
        # outdated for test purposes kept here
        if self.measurementdir == 1:
            print "reverse"
        if self.measurementcountdown != 0: ↩
                                                #if measurement step ↩
            is in progress
            print "Measurement: "
            print "countdown: ", self.measurementcountdown
            self.measurementcountdown -= 1
            self.PHCD.settemp(30)

            if self.measurementcountdown == 0 and self.measurementdir ↩
                == 0:
                self.measurementcountdown = 40
                self.measurementdir = 1
                self.PHCD.switchtempgradient() ↩
                                                # switch temp ↩
                    gradient
            elif self.measurementcountdown == 0 and self.↩
                measurementdir == 1:
                self.measurementcountdown = 0
```

```
                self.measurementdir = 0
                self.PHCD.setpercentage(0) ↩
                                                         # switch off ↩
                    peltier power
                self.PHCD.switchtempgradient() ↩
                                                     # switch back (↩
                    make a klick to indicate end of measurement)
                self.savecsv()
        # ------ end of non pid controlled measurements --------

        # ------------------------------------------------------
        # ------ PID controlled measurements -------------------
        elif self.PIDmeasurement == 1:
            print "PID controlled measurement"
            if self.startPIDstep >= self.PIDsteadyreach: ↩
                                       # if set point was reached ↩
                PIDsteadyreach (std:10) times
                print "Temperature reached"
                self.shelftime -= 1
                print "T1: ", self.T1[-1], " T2: ", self.T2[-1]
                print "Step countdown: ", self.shelftime
                if self.shelftime == 0 and self.PIDcooldown == 0: ↩
                                  # if end of measurement shelf
                    self.PIDstep += 1
                    self.PIDshelfstoptime.append(len(self.dataf)) ↩
                                      # note end of shelf
                    if self.PIDstep >= len(self.PIDTemps): ↩
                                             # if end of measurements ↩
                        is reached for one direction
                        if self.measurementdir == 0: ↩
                                                           # second ↩
                            direction not done
                            # changing direction
                            self.measurementdir = 1
                            self.PHCD.turnoffPID()
                            # self.PHCD.cooldown(0.75)
                            self.PIDcooldown=1
                            self.PHCD.turnoffPID()
                            self.PIDstep = 0
                            self.PHCD.switchtempgradient()
                            self.shelftime = self.PIDshelftime
```

```

                        else:
                            print "end of measurement"
                            self.PHCD.turnoffPID()
                            self.shelftime = self.PIDshelftime
                            self.PHCD.switchtempgradient()
                            self.savecsv()
                            self.PIDmeasurement = 0
                            self.abordmeasurement()
                    else:
                        # next step
                        self.startPIDstep = 0
                        self.PHCD.startPID(self.PIDTemps[self.PIDstep])

                        self.shelftime = self.PIDshelftime
                elif self.PIDcooldown == 1:                                    # if in cooldown sequence
                    print "T1: ", self.T1[-1], " T2: ", self.T2[-1], " dT: ", self.T1[-1]-self.T2[-1], " max dT: ",self.PIDmaxTempdeviationcd
                    if self.T1[-1]-self.T2[-1] < self.PIDmaxTempdeviationcd:    # if acceptable dt is reached end cooldown
                        self.PHCD.startPID(self.PIDTemps[self.PIDstep])
                        self.startPIDstep = 0
                        self.PIDcooldown = 0
                        self.PIDstep = 0
                        self.shelftime = self.PIDshelftime  # resetting shelftimer

            else:  # wait for temp to settle before measurement starts
                print "T1: ", self.T1[-1], " T2: ", self.T2[-1]
                print "min: ", self.PIDTemps[self.PIDstep]-self.PIDdT, "max: ", self.PIDTemps[self.PIDstep]+self.PIDdT
                print "reached: ", self.startPIDstep
                if self.measurementdir == 0:
                    if self.T1[-1] != 0:
```

```
                        if self.PIDTemps[self.PIDstep]-self.PIDdT <= self.T1[-1] <= self.PIDTemps[self.PIDstep]+self.PIDdT:
                            self.startPIDstep += 1

                else:
                    if self.T2[-1] != 0:
                        if self.PIDTemps[self.PIDstep]-self.PIDdT <= self.T2[-1] <= self.PIDTemps[self.PIDstep]+self.PIDdT:
                            self.startPIDstep += 1
        self.curve.setData(dphcd)
        self.curvef.setData(dfluke)
        self.curvex.setData(dsebeck)

    def calcseebeck(self):
        if self.datap[-1] != 0:
            self.datas.append(self.dataf[-1]/self.datap[-1]*1000)
        else:
            print "devision by zero prevented. seebeck set to 0. Check later!"
            self.datas.append(0)
        print "Seebeck Potential µ[V/K]: ", self.datas[-1]
        return self.datas

    def getdataphcd(self):
        #get temperatures from PHCD
        T1,T2 = self.PHCD.getTemp()
        dT = T2-T1
        self.T1.append(T1)
        self.T2.append(T2)
        # print dT
        # V=V*1000
        self.datap.append(dT)
        return self.datap

    def getdatafluke(self):
        # gets data from Fluke multimeter
        Vl = self.Fluke.cread()
        try:
            V = float(Vl[0])*1000
```

```
        except:
            V = 0
            print "Error receiving data from Fluke"
        print " Fluke U [mV] = ", V
        self.dataf.append(V)
        return self.dataf

    def startmeasurement(self):
        # legacy measurement function
        self.suffix = ""
        suffix, ok = self.asksamplename()
        if ok and suffix != '':
            self.suffix = str(suffix)
            print "output file will be named: YYYY-MM-DD_HH-mm_"+self.↩
                suffix
            start = 1
        elif ok:
            print nosampleNwarning
            start = 1
        else:
            # cancel measurement
            self.measurementcountdown=0
            self.measurementdir=0
            start = 0
        if start == 1:
            self.dataf = []
            self.datap = []
            self.datas = []
            self.T1 = []
            self.T2 = []
            self.measurementcountdown = 30
            self.measurementdir = 0

    def startPIDmeasurement(self):
        # initializes measurement with PID controlled temperature
        self.suffix = ""
        suffix, ok = self.asksamplename()
        if ok and suffix != '':
            self.suffix = str(suffix)
            print "output file will be named: YYYY-MM-DD_HH-mm_" + ↩
                self.suffix
```

```
            start = 1
        elif ok:
            print self.nosampleNwarning
            start = 1
        else:
            # cancel measurement
            self.measurementcountdown = 0
            self.measurementdir = 0
            start = 0
        if start == 1:
            self.dataf = []
            self.datap = []
            self.datas = []
            self.T1 = []
            self.T2 = []
            self.measurementdir = 0
            self.PIDmeasurement = 1
            self.PIDstep = 0
            self.startPIDstep = 0
            self.shelftime = self.PIDshelftime
            self.PIDshelfstoptime = []
            self.PHCD.sendKs(self.Kp, self.Ki, self.Kd, 1)
            print "setpoint: ", self.PIDTemps[self.PIDstep]
            self.PHCD.startPID(self.PIDTemps[self.PIDstep])  # start ↩
                PID at first Temp
            time.sleep(1)

    def abordmeasurement(self):
        """
        Abords measurement turns off heating and cooling and resets ↩
            values
        """
        self.measurementcountdown = 0
        self.measurementdir = 0
        self.PIDmeasurement = 0
        self.PHCD.turnoffPID()  # turn off PID
        self.PHCD.setpercentage(0)  # switch off peltier power

    def getText(self, title, label, default=''):
        #open dialog to get text from user e.g: Sample Name
        (ret, ok) = QtGui.QInputDialog.getText(
```

```
            QtGui.QWidget(), title, label,
            QtGui.QLineEdit.Normal, default)
        if not ok:
            return '',False
        return str(ret),True

    def asksamplename(self):
        """
        Asks the user for the name of the sample
        """
        suffix, ok = self.getText("SampleName","Enter the name of your sample")
        return suffix, ok

    def csv_writer(self,data,path):
        """
        Write data to a CSV file path
        """

        f = open(path, "wb")
        with f as csv_file:
            writer = csv.writer(csv_file, delimiter=';')
            for line in data:
                print line
                writer.writerow(line)
        f.close

    def savecsv(self):
        #save measurement to csv file
        #gives accoustic signal if alarm is enabled
        if alarm == 1:
            mixer.music.play()
        print "lengths: T1:", len(self.T1), " T2: ", len(self.T2), " datap: ", len(self.datap)
        print " dataf: ", len(self.dataf), " datas: ", len(self.datas)
        time.sleep(2)
        data = ["Point,T1°[C],T2°[C],Temperatur Differenz dT[K],Spannung U[mV], Seebeck a µ[V/K], average Seebeck a µ6-30[V/K], average Seebeck a 52-69 µ[V/K] ".split(",")]
        avg1 = 0.0
        s1 = 0.0
```

```
        avg2 = 0.0
        s2 = 0.0
        c1 = 0
        c2 = 0

        for i in range(0, len(self.dataf), 1):
            string = "%3i, %7.2f, %7.2f, %7.2f, %7.3f, %7.3f ,," %
            (i+1, self.T1[i], self.T2[i], self.datap[i], self.dataf[i], self.datas[i])
            data.append(string.split(","))
            if self.PIDmeasurement!=1:
                if i > 4 and i < 32:
                    s1 += self.datas[i]
                    c1 += 1
                elif i > 52 and i < 69:
                    s2 += self.datas[i]
                    c2 += 1
            else:
                # fill with dummy values
                c1=100
                c2=100
                s1=100
                s2=100
        if self.PIDmeasurement==1:
            mwtemps=[]
            mwpot=[]
            mwseebeck=[]
            mwT1=[]
            mwT2=[]
            reltempcurve=[]
            relpotcurve=[]
            relseebeckcurve=[]
            reltemp1=[]
            reltemp2=[]
            self.shelfcurves=[["T1 °[C]","T2 °[C]","U µ[V]","dT [K]","a µ[V/K]"]]
            for ii in range(len(self.PIDTemps)*2):
                print str(ii)+" stop time: "+str(self.PIDshelfstoptime[ii])
                for c in range(self.PIDshelfstoptime[ii]-int(self.avgnum),self.PIDshelfstoptime[ii]):
```

```
                    reltempcurve.append(self.datap[c])
                    relpotcurve.append(self.dataf[c])
                    relseebeckcurve.append(self.datas[c])
                    reltemp1.append(self.T1[c])
                    reltemp2.append(self.T2[c])
                sumt = 0
                sump = 0
                sums = 0
                sumt1 = 0
                sumt2 = 0

                for iii in range(len(reltempcurve)):
                    sumt += reltempcurve[iii]
                    sump += relpotcurve[iii]
                    sums += relseebeckcurve[iii]
                    sumt1 += reltemp1[iii]
                    sumt2 += reltemp1[iii]
                    line=[reltemp1[iii],reltemp2[iii],relpotcurve[iii]*1000,reltempcurve[iii],relseebeckcurve[iii]]
                    self.shelfcurves.append(line)

                mwtemps.append(sumt/self.avgnum)
                mwpot.append(sump/self.avgnum)
                mwseebeck.append(sums/self.avgnum)
                mwT1.append(sumt1/self.avgnum)
                mwT2.append(sumt2/self.avgnum)
                reltempcurve=[]
                relpotcurve=[]
                relseebeckcurve=[]
        avg1 = s1/c1
        string = ",,,,,,"+str(avg1)+","
        data.append(string.split(","))
        avg2 = s2/c2
        string = ",,,,,,,"+str(avg2)
        data.append(string.split(","))
        string = "Average for shelfs,,,,,,,"
        data.append(string.split(","))
        string = "start,stop,MW T1,MW T2,MW dT,MW U,MW S,,,,"
        data.append(string.split(","))
        for c in range(len(mwseebeck)):
```

```
            string = str(self.PIDshelfstoptime[c]-10)+","+str(self.↩
                PIDshelfstoptime[c])+","+str(mwT1[c])+","+str(mwT2[c])↩
                +","+str(mwtemps[c])+","\
                    +str(mwpot[c])+","+str(mwseebeck[c])
            data.append(string.split(","))
        today = datetime.today()
        datestr = datetime.strftime(today, "%Y-%m-%d_%H-%M")
        if self.suffix != '':
            suffix = "_"+self.suffix
        else:
            suffix = ""
        path = os.path.abspath(os.curdir)+"/Auswertung/"+datestr+↩
            suffix+".csv"
        self.csv_writer(data, path)
        self.localize(path)
        #file just containing the shelves
        path = os.path.abspath(os.curdir)+"/Auswertung/"+datestr+↩
            suffix+"_forgraphs.csv"
        self.csv_writer(self.shelfcurves, path)
        self.localize(path)
        if alarm == 1:
            time.sleep(2)
            mixer.music.stop()

    def localize(self,filein):
        #creates a second file with , instead of . as decimal ↩
            delimiter
        f = open(filein,'r')
        filedata = f.read()
        f.close()
        fileout=filein[:-4]+"_forexcel.csv"
        newdata = filedata.replace(".",",")

        f = open(fileout,'w')
        f.write(newdata)
        f.close()

if __name__ == '__main__':
    # start gui
    app = QtGui.QApplication([])

```

```
    graph = Graph()

    if (sys.flags.interactive != 1) or not hasattr(QtCore, '↩
        PYQT_VERSION'):
        QtGui.QApplication.instance().exec_()
```

Listing 7.4 Graphical User interface

7.1.5 Schematic Peltier Temperature Control Shield

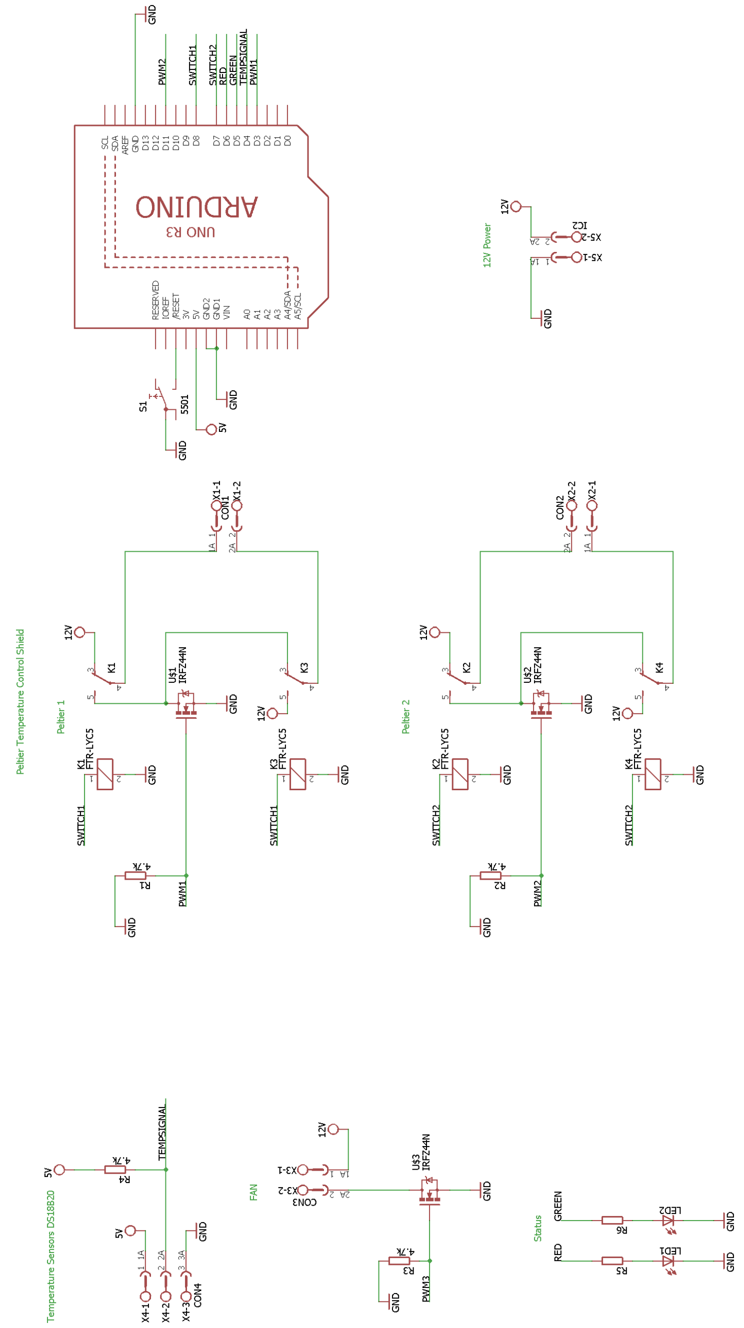

Figure 7.1 Schematic of the Peltier Temperature Control Shield. The image was created with Eagle 7.5.0 Light.

7.1.6 Bill of Materials

Table 7.1 Bill of Materials for Seebeck Measurement Device

Name	quantity	price/pc [€]	source
Multimeter (Fluke 289)	1	765.00[1]	available in lab
Fluke IR189USB	1	58.99[1]	available in lab
Arduino Uno R3	1	2.79[2]	aliexpress.com
MOSFET IRFZ 44N	3	0.43[3]	Reichelt Elektronik
LED 5-10500 RT	1	0.25[3]	Reichelt Elektronik
LED 5-22000 GN	1	0.23[3]	Reichelt Elektronik
Metal oxide resistor 47Ohm	1	0.153[3]	Reichelt Elektronik
Metal oxide resistor 150Ohm	1	0.153[3]	Reichelt Elektronik
Metal oxide resistor 4,7 kOhm	4	0.35[3]	Reichelt Elektronik
screw clamp plug AKL 230-03 3-pole	1	0.84[3]	Reichelt Elektronik
screw clamp plug AKL 249-02 2-pole	4	0.57[3]	Reichelt Elektronik
Box connector AKL 230-02 2-pole	4	0.28[3]	Reichelt Elektronik
Box connector AKL 230-03 3-pole	1	0.41[3]	Reichelt Elektronik
Slim Relay FTR LYCA 005V	4	1.90[3]	Reichelt Elektronik
Header pins SL 1X36G 2,54	2	0.17[3]	Reichelt Elektronik
PCB	10[4]	2.50$[5]	dirtypcbs.com

Table 7.1 contains additional information for the section 3.1.3. The table includes the quantity and price for each necessary item.

---

[1] www.conrad.de (store price 25.01.2018)

[2] www.aliexpress.com (including shipping 25.01.2018)

[3] www.reichelt.de (25.01.2018)

[4] minumum order quantity)

[5] price per piece including shipping(minimum order Quantity is 10 pieces (25$))

7.1.7 Usability

The information displayed here is additional information for the section on the usability of the developed Seebeck measurement device in section 3.1.7 on page 48.

Table 7.2 Statements rated by students who used the device. A rating of ten means, complete agreement. A rating of one means, they do not agree at all. Total participants who filled out the survey: 21. This table is the data used to create the graph: 3.9 on page 50

Statement	Average agreement	Variance
The device is easy to use	9.24	0.75
It took me less than 5 minutes to learn to use the the software	9.38	0.62
The software is intuitive	8.81	1.20
The software is easy to use	9.20	0.82
The graphs displayed are helpful	8.71	1.35
The displayed text is helpful	8.29	1.92
The measurement data is saved with an unique name	9.62	0.43
The measurement data is clearly formatted	9.33	0.70
I was able to use the device and software without assistance after a short introduction	9.62	0.43
The layout of the Software was easy to understand	9.24	1.32

In addition to the questions asked, the students had the opportunity to give suggestions for improvements. Even though the survey was in English, some of the comments were given in German; these have been translated and are marked with [Translated]. All other comments are cited directly. In the following, there is the list of the comments given by the students (marked with S), and comments to put them into context (marked with c):

S „Could be useful to have "END OF OPERATION" or such a text when the measurement is over.“

c There is already a visual and an audible clue to the end of measurement, but this will be even more obvious in future versions

S „Graphs are really nice but the displayed text is repetitive and didn‘t really look at it.“

c The text has to be repetitive since it says, for example, Temperature 1: X.YZ °C Temperature 2: U.VW °C Voltage:...

S „A glass shell or case for the device could be handy to protect it from touch/damage while measuring.“

c A housing is in development.

S „setup for larger samples“

c could be nice but so far there has been no need for a larger setup.

S Would be nice to have a timer. [Translated]

c See previous comments

S „A built-in (estimated) timer would help not to miss the end of measurement. Maybe even a little alarm sound other than that little noise the device makes after the measurement is completed.“

c See previous comments

S There is nothing to improve, since it is already very easy to handle. [Translated]

c nothing to add here.

S „It would be good if the auto-scaling of the graphs could somehow be avoided.“

c Auto-scaling can be turned off but would leave a fixed range for the graphs.

S „Perhaps implement a few more options that one can modify the measurement in a certain way.“

c There are options which can be changed. For now there is no settings menu in graphical user interface, the options can be only changed in the source code.

7.2 Engraving for DIN2409

```
( VHMritzgravur )
G00 G21 G17 G90 G40 G49 G80
G71 G91.1
T1 M06
 (vhm Ritzgravierer)
G00 G43 Z20.000 H1
S0 M03
(Toolpath:- horizontal engraving)
()
G94
X0.000 Y0.000 F800.0
G00 X-10.000 Y-0.500 Z20.000
G1 Z-11.000 F600.0
G1 X10.000 F800.0
G00 Z20.000
G00 X-10.000 Y-1.500
G1 Z-11.000 F600.0
G1 X10.000 F800.0
G00 Z20.000
G00 X-10.000 Y-2.500
G1 Z-11.000 F600.0
G1 X10.000 F800.0
G00 Z20.000
G00 X-10.000 Y0.500
G1 Z-11.000 F600.0
G1 X10.000 F800.0
G00 Z20.000
G00 X-10.000 Y1.500
G1 Z-11.000 F600.0
G1 X10.000 F800.0
G00 Z20.000
G00 X-10.000 Y2.500
G1 Z-11.000 F600.0
G1 X10.000 F800.0
G00 Z20.000
S0M03
(vertical engraving)
```

```
()
G00 X-0.500 Y-10.000 Z20.000
G1 Z-11.000 F600.0
G1 Y10.000 F800.0
G00 Z20.000
G00 X-1.500 Y-10.000
G1 Z-11.000 F600.0
G1 Y10.000 F800.0
G00 Z20.000
G00 X-2.500 Y-10.000
G1 Z-11.000 F600.0
G1 Y10.000 F800.0
G00 Z20.000
G00 X0.500 Y-10.000
G1 Z-11.000 F600.0
G1 Y10.000 F800.0
G00 Z20.000
G00 X1.500 Y-10.000
G1 Z-11.000 F600.0
G1 Y10.000 F800.0
G00 Z20.000
G00 X2.500 Y-10.000
G1 Z-11.000 F600.0
G1 Y10.000 F800.0
G00 Z20.000
G00 Z20.000
G00 X0.000 Y0.000
M09
M30
%
```

Listing 7.5 G-Code used to engrave the 6 horizontal and 6 vertical lines on the sample like it is specified in DIN2409:2013.[154] The full description of the scotch test can be found in section section 3.2.2 on page 55.

7.3 Prediction of the Sputter Pattern

The complete calculation for the prediction of the sputter pattern (see figure 3.14 on page 58). The calculation and plots were performed in Wolfram Mathematica 11.3.

A sample is put 30 mm beneath a sputter target (z direction) and 14 mm off the center point from the plasma source in one direction is sputtered two times with an equal time but is turned around its own z-axis between the two sputtering processes. The sample size is 14 by 14 mm. This should predict the expected sputter pattern:

SetOptions[Plot3D, BaseStyle →

{FontFamily → “Times New Roman“, FontSize → 15}];

$$\mathbf{V1} = \begin{pmatrix} a-14 \\ b \\ 0 \end{pmatrix}; \text{“Dots on sample surface“;}$$

$$\mathbf{V2[n\_]} = \begin{pmatrix} N[10 * \mathrm{Cos}[n * 1\mathrm{Degree}]] \\ N[10 * \mathrm{Sin}[n * 1\mathrm{Degree}]] \\ 30 \end{pmatrix};$$

"Dots on intersection of plasma torus and sputter target (Circle (r=10 mm)) with 30 mm distance from Sample";

V12 = V2[*n*] − V1; “Vector between ring and sample“;

nV12 = Norm[V12]; “magnitude of V“;

$\mathbf{AvgV12} = \left(\sum_{n=1}^{360} \mathrm{nV12}\right) \Big/ 360;$ **“Average length between V1 and V2“;**

ParametricPlot3D[V2[*n*], {*n*, 0, 360}, {*z*, 0, 30},

AxesLabel →

{“x-dimension [mm]“, “y-dimension [mm]“, “z -dimension [mm]“}]

Plot3D[AvgV12, {*a*, −7, 7}, {*b*, −7, 7},

AxesLabel →

{“x-dimension [mm]“, “y-dimension [mm]“, “Average distance [mm]“},

BaseStyle → {FontFamily → “Times New Roman“, FontSize → 15}]

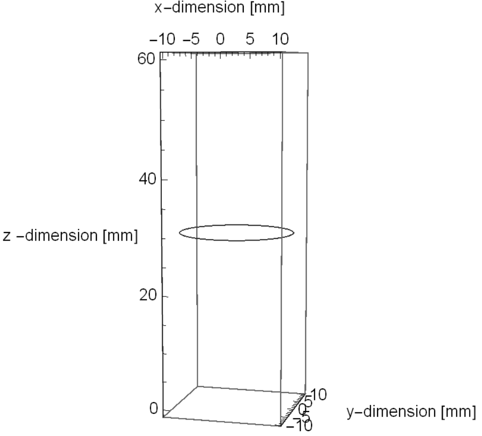

Source of metal atoms sputtered onto the samples

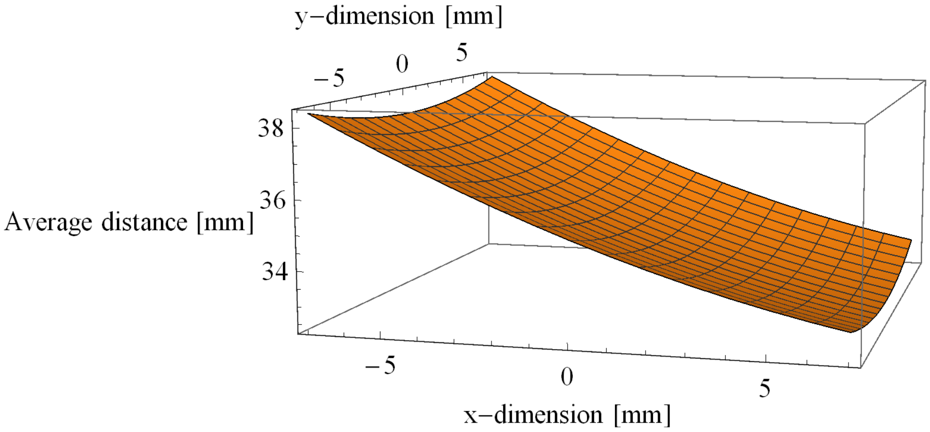

Average distance between each spot on the sample and the sputter source

$$\mathbf{V1t} = \begin{pmatrix} -14 - a \\ -b \\ 0 \end{pmatrix};$$

“Dots on Sample after sample is turned 180 degree around the Z axis“;

V1t2 = V2[*n*] − V1t; “Vector from Zero after sample is turned“;

nV1t2 = Norm[V1t2]; “magnitude of V“;

$$\mathbf{AvgV1t2} = \left(\sum_{n=1}^{360} \mathbf{nV1t2}\right) \Big/ \mathbf{360};$$

```
Plot3D[AvgV1t2, {a, −7, 7}, {b, −7, 7},
AxesLabel →
{“x-dimension [mm]“, “y-dimension [mm]“, “Average distance [mm]“},
BaseStyle → {FontFamily → “Times New Roman“, FontSize → 14}]
```

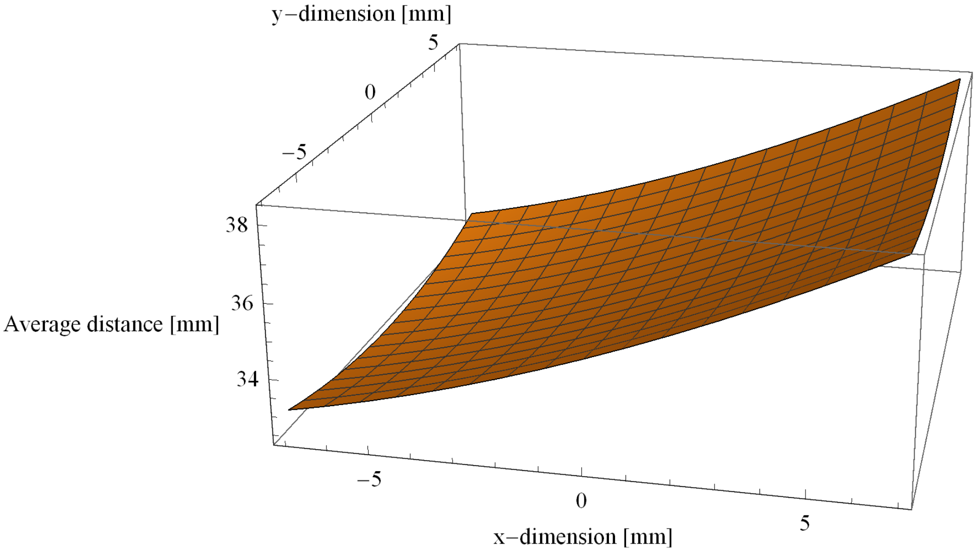

Average distance between each spot on the sample and the sputter source (180 degree turned sample)

```
V12total = (AvgV12 + AvgV1t2)/2;
"Average Distance between plasma source and each point on the sample
when the sample is exposed for half the time in the turned and unturned
position.";
Plot3D[V12total, {a, −7, 7}, {b, −7, 7},
AxesLabel →
{“x-dimension [mm]“, “y-dimension [mm]“, “Average distance [mm]“}]
```

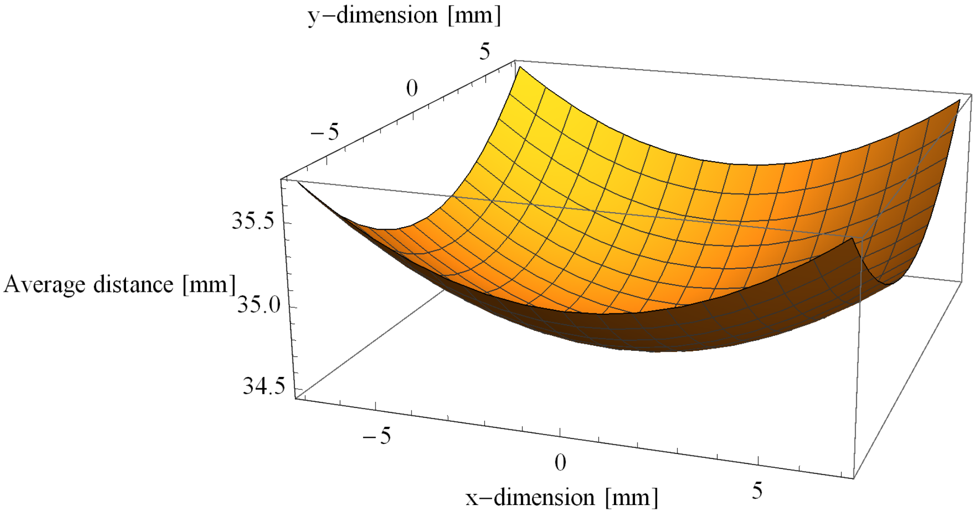

Average distance between each spot on the sample and the sputter source as a time dependent average.

Vm = V2[*n*] − $\begin{pmatrix} -14 \\ 0 \\ 0 \end{pmatrix}$**;**

"Vector between spot right in the middle of the coated sample. This spot should have the smallest distance from V2 in a time dependent average";

nVm = Norm[Vm]; "Length of the Vector";

AvgVm = $\left(\sum_{n=1}^{360} \mathrm{nVm}\right) \Big/ 360$**;**

"Average distance between Vm and V2";

RateV12 = 1/(V12total^2)/(1/(AvgVm^2)) ∗ 100;

"relative sputter rate time dependent average";

Plot3D[RateV12, {*a*, −7, 7}, {*b*, −7, 7},

AxesLabel →

{"x-dimension [mm]", "y-dimension [mm]", "Sputterrate [%]"}]

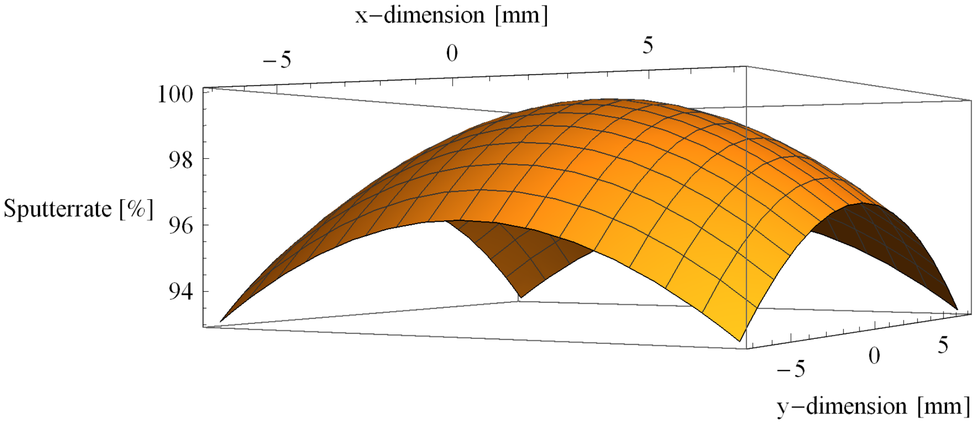

Predicted sputter pattern for the relative film thickness sputtered on to the sample surface.

7.4 Technical Drawings

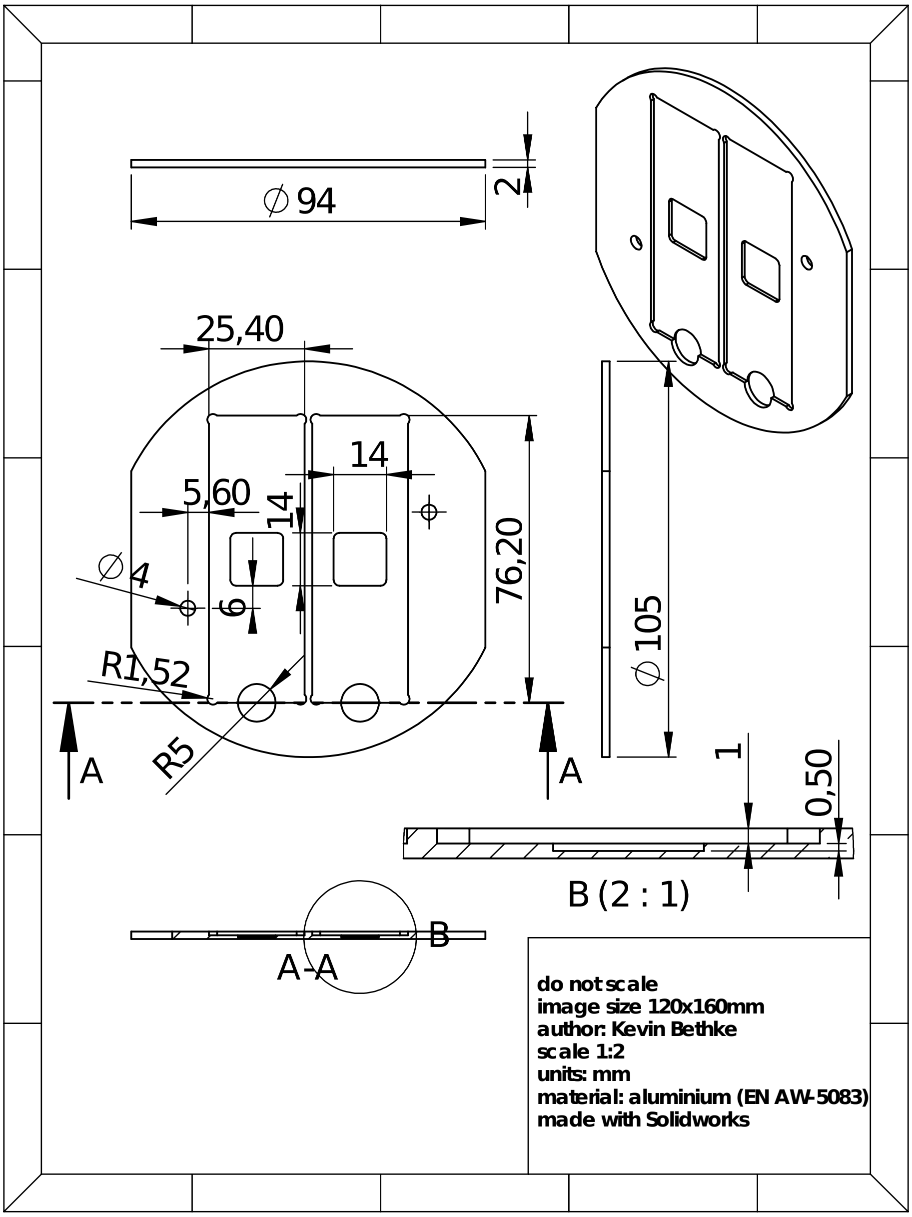

Figure 7.2 Technical drawing of the milled sputter mask for the preparation of thin film samples.

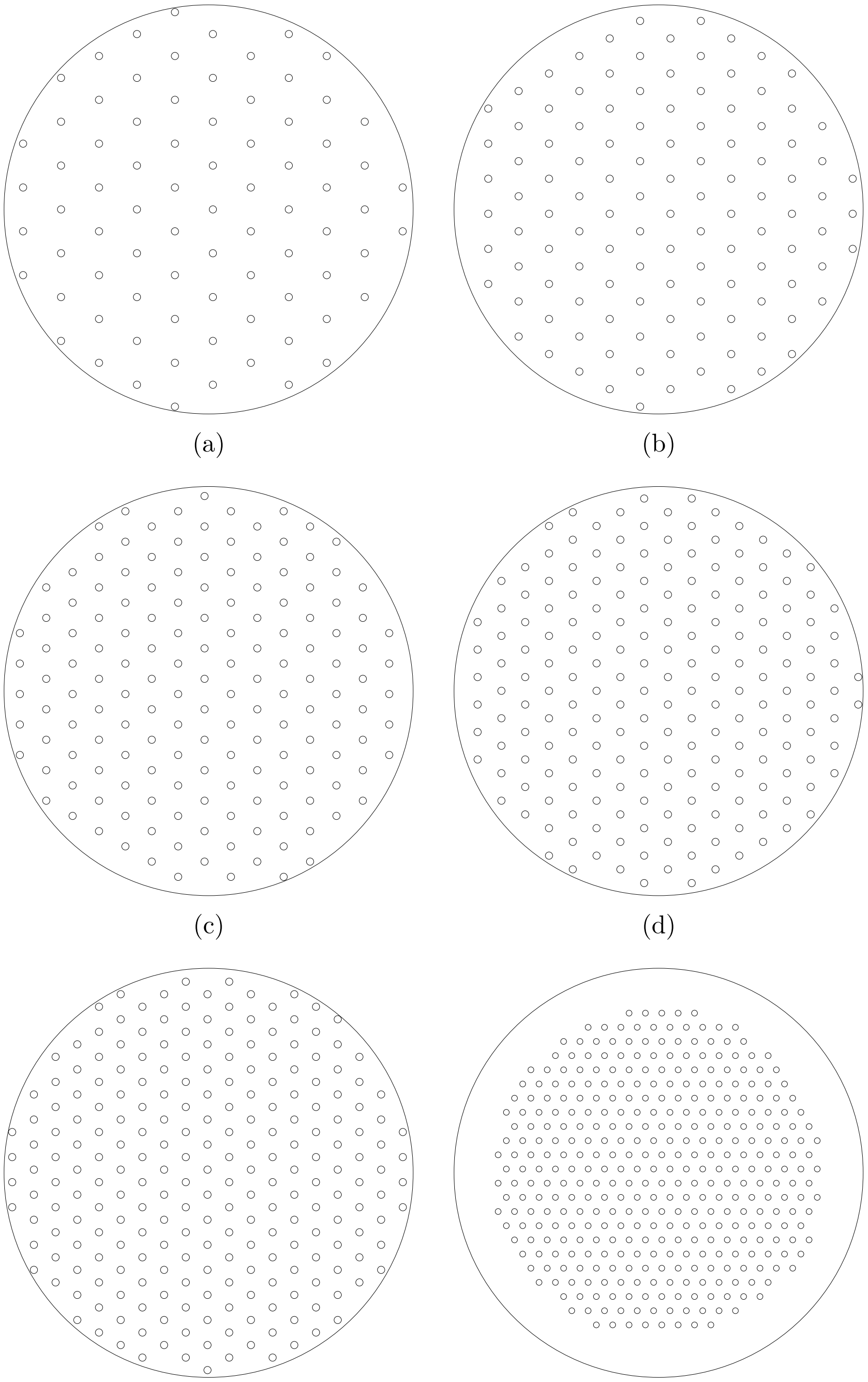
(a) (b)
(c) (d)
(e) (f)

Figure 7.3 Hole patterns of drilled copper targets. The targets expose an area of a second target in a stack to cosputter two materials. Hole area compared to entire target area (rounded): (a) 2.5% (b) 3.75% (c) 5% (d) 6.25% (e) 7.5% (f) 10%.

7.5 Additional Figures

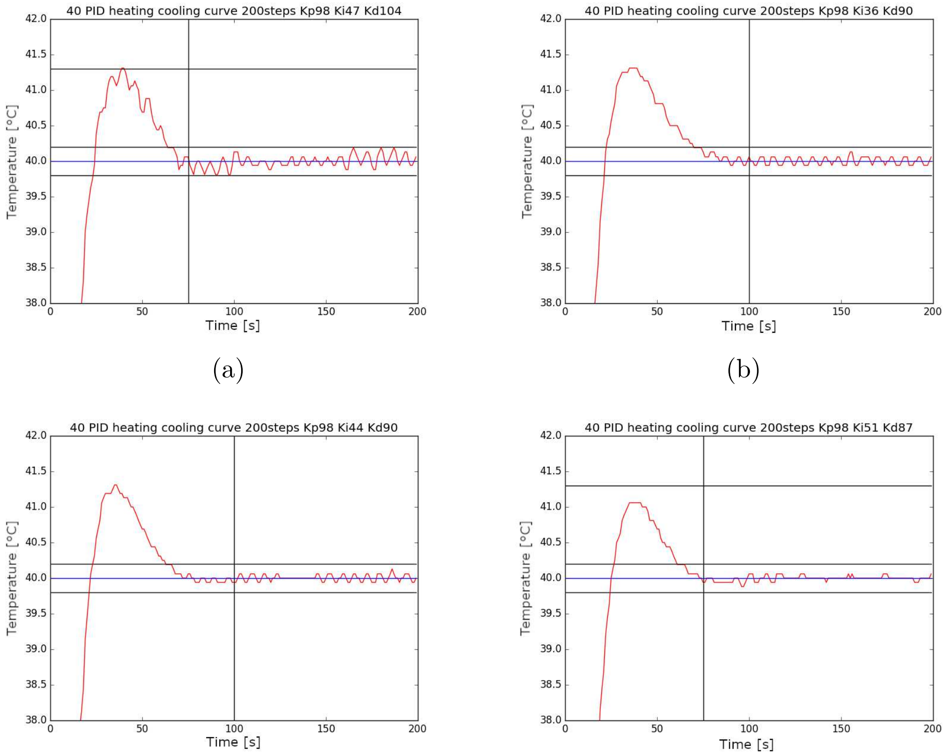

(a) (b)

(c) (d)

Figure 7.4 In this figure, some of the over 1000 curves recorded for the tuning of the PID of the measurement device are shown. This is additional information for section 3.1.5 on page 45. All curves shown here are obtained during the tuning of the air-cooled version. The red curve represents the measured temperature. The blue line represents the setpoint (40 °C), the black horizontal lines around the setpoint represent the maximum allowable oscillation after the initial settling time. The upper black line represents the maximum overshoot; this line was only added in later tuning procedures. Thus, it is missing in (b) and (c). The vertical black line represents the maximum acceptable settling time. All the curves shown here would meet the initial goals represented by the black lines. However, there is a noticeable improvement from the plus-minus 0.2 °C in (a) to the plus-minus 0.02 °C in (d).

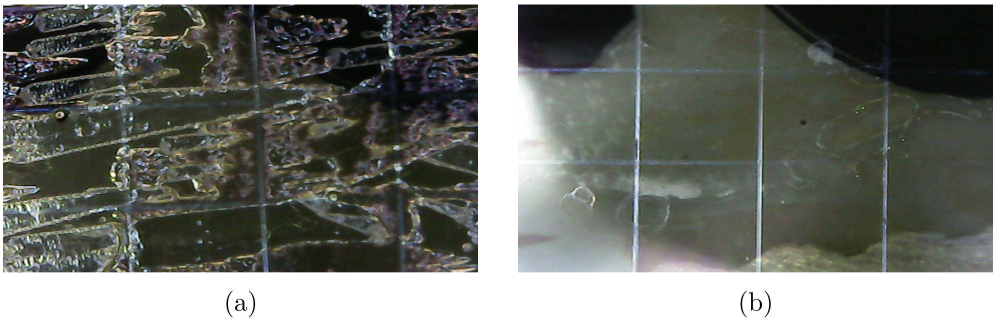

(a) (b)

Figure 7.5 In this image, some samples are shown from the adhesion test (DIN EN ISO 2409:2013). Fig. (a) shows a sample where most of the glue from the sticky tape remained on the sample. Fig. (b) shows the same sample after being washed and gently scrubbed with a soft brush in ethanol. This is additional information for section 3.2.2 on page 55.

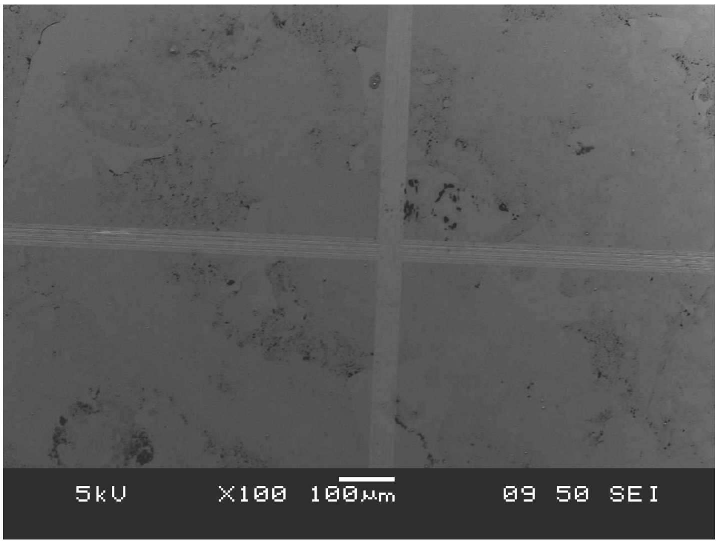

Figure 7.6 Close up SEM image of a sample tested for adhesion with the procedure specified in DIN EN ISO 2409:2013. This image is additional information for section 3.2.2 on page 55.

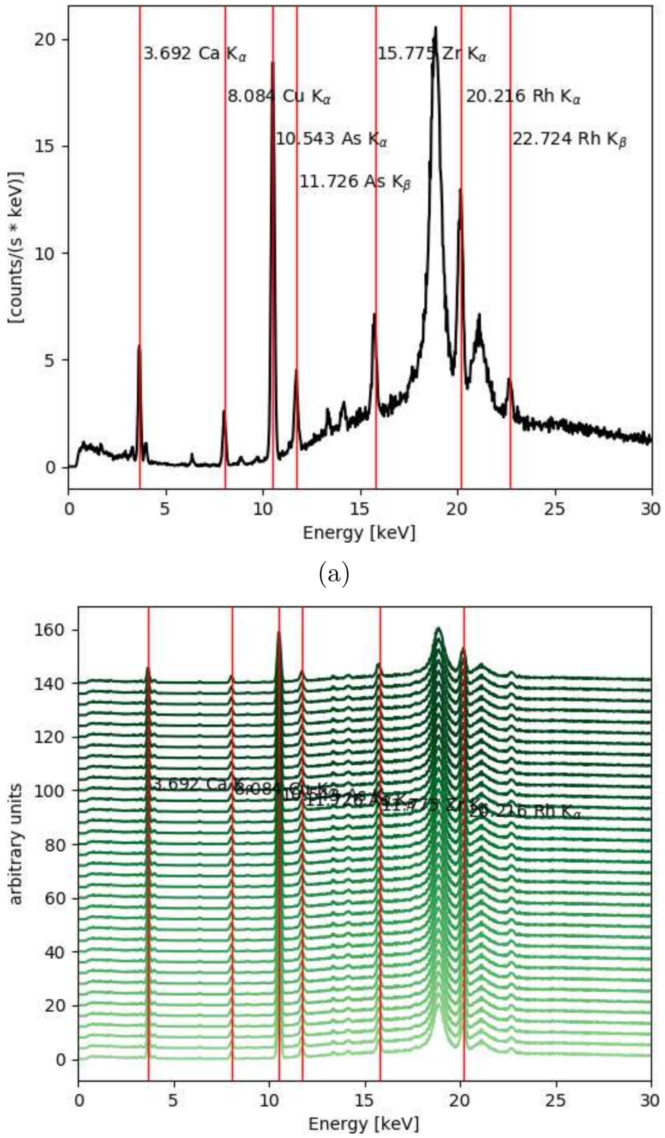

(a)

(b)

Figure 7.7 In (a) one single spectrum of a pure copper sample on soda-lime silicate glass is presented. In (b) all spectra recorded on the central point of sample KB214a (pure copper on soda lime silicate glass) are shown. This is additional information for section 3.2.5 on page 67.

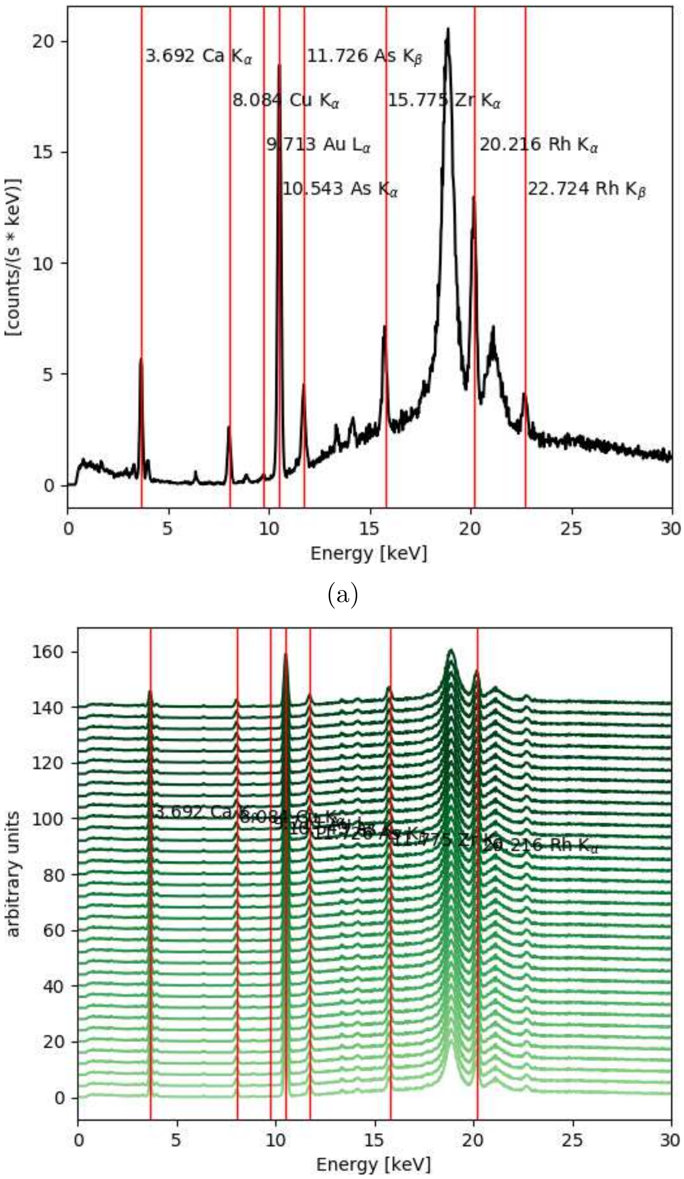

(a)

(b)

Figure 7.8 In (a) one single spectrum of a copper gold sample (3.75% perforated copper target) on soda lime silicate glass is presented. In (b) all spectra recorded on the central point of sample KB208a (pure copper on soda lime silicate glass) are shown. This is additional information for section 3.2.5 on page 67.

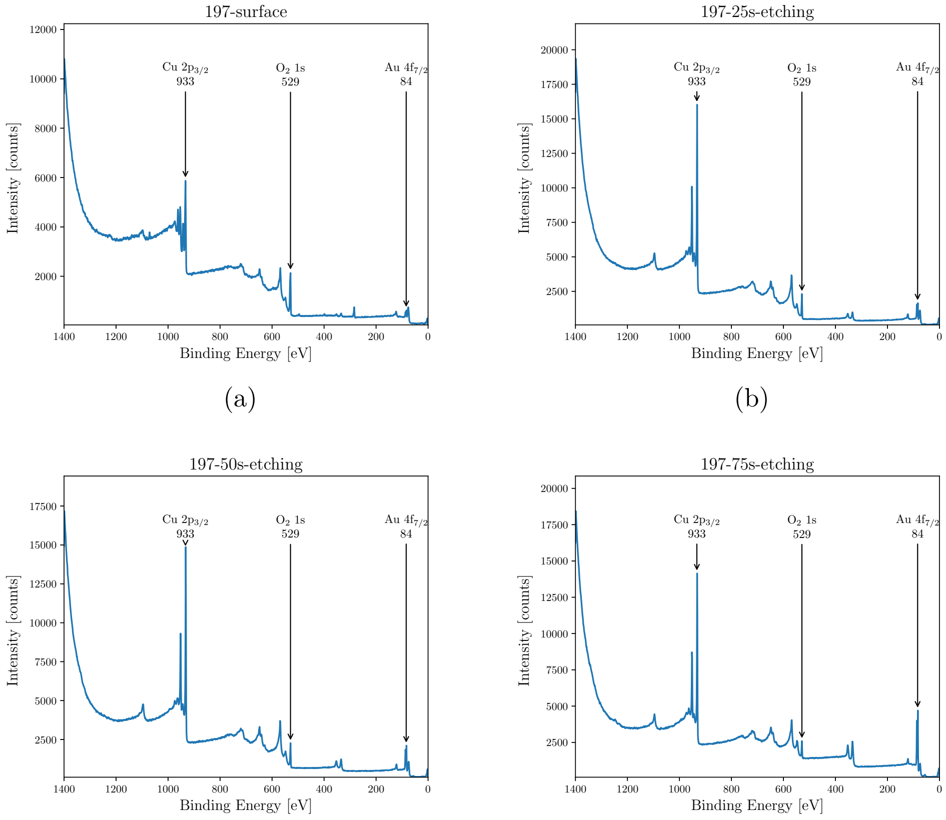

(a) (b)

(c) (d)

Figure 7.9 XPS survey spectra for sample 197a: In (a) an entire energy survey scan is depicted at the sample surface. In (b) the same survey is scanned after 25 s of sputtering. In (c) the surface layer of the sample was removed again by an additional sputtering of 25 s. In (d) the total sputtering time was 75 s. This graph is additional information for section 3.2.8.

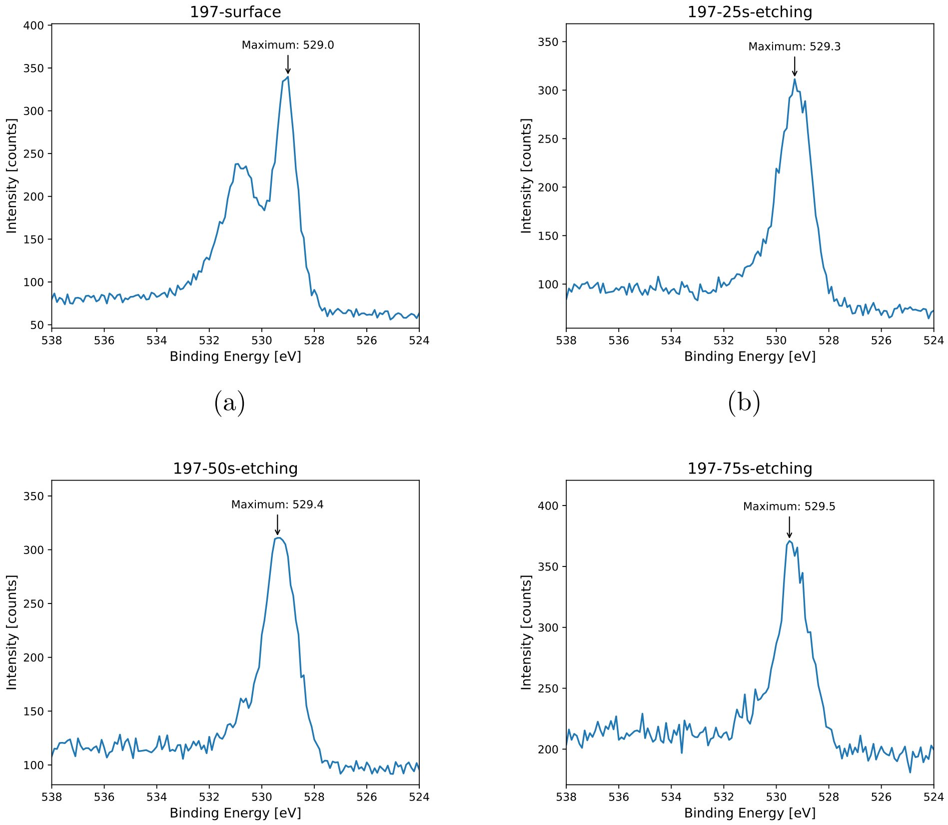

(a) (b)

(c) (d)

Figure 7.10 XPS spectra of the oxygen binding energy region for sample 197a: In (a) the binding energies of oxygen is depicted, at the sample surface. In (b) the same region is depicted after 25 s of sputtering. In (c) the surface layer of the sample was removed again by an additional sputtering of 25 s. In (d) the total sputtering time was 75 s. This graph is additional information for section 3.2.8.

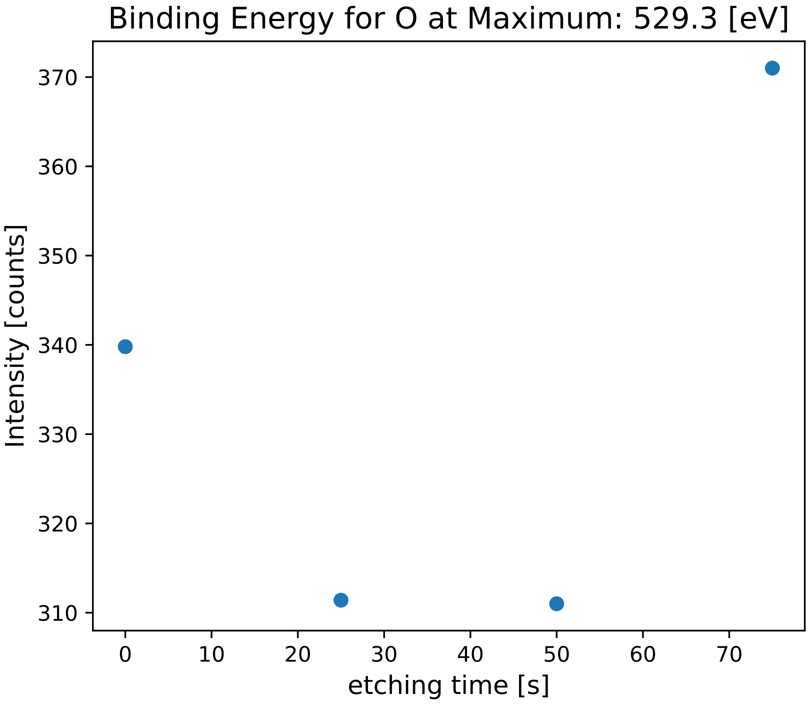

Figure 7.11 The graph displays the maximum counts of the XPS spectra for O_2 at its maxima vs. cumulative etching time. The counts at the maximum have a variation around 340 counts. The oxygen content does not experience a large depth dependent variation. This graph is additional information for section 3.2.8.

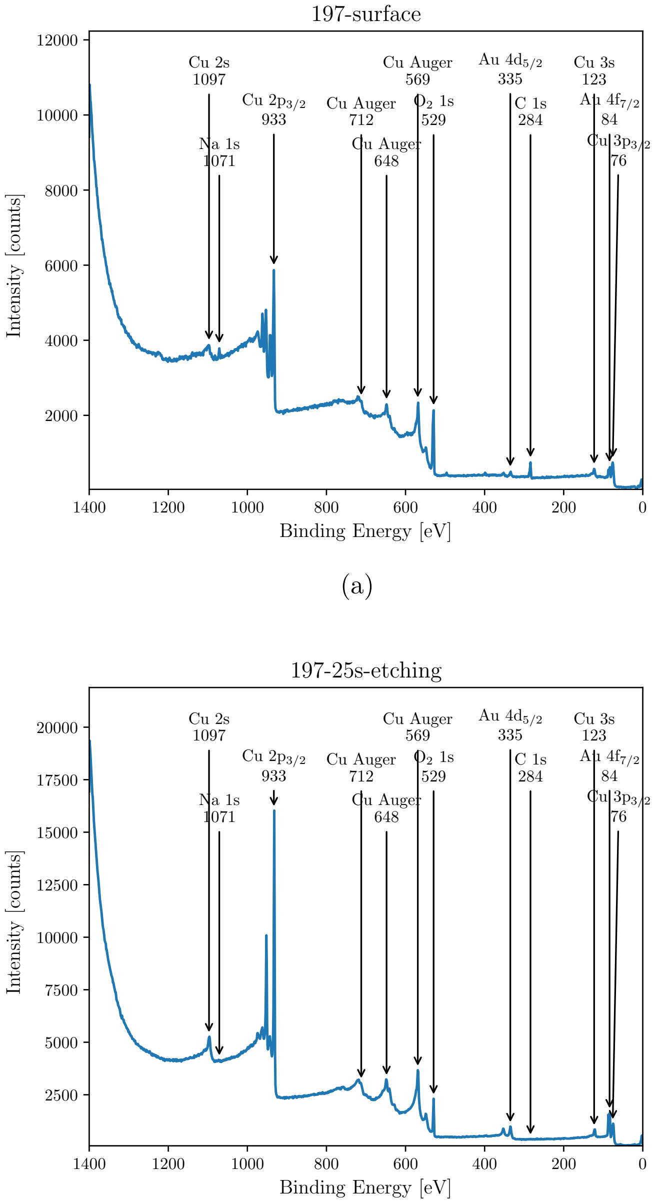

(a)

(b)

Figure 7.12 XPS survey spectra for sample 197a: In (a) an entire energy survey scan is depicted at the sample surface. In (b) the same survey is scanned after 25 s of sputtering. The sodium and carbon contamination at the surface disappears after the etching. This is additional information for section 3.2.8 on pages 86 ff.

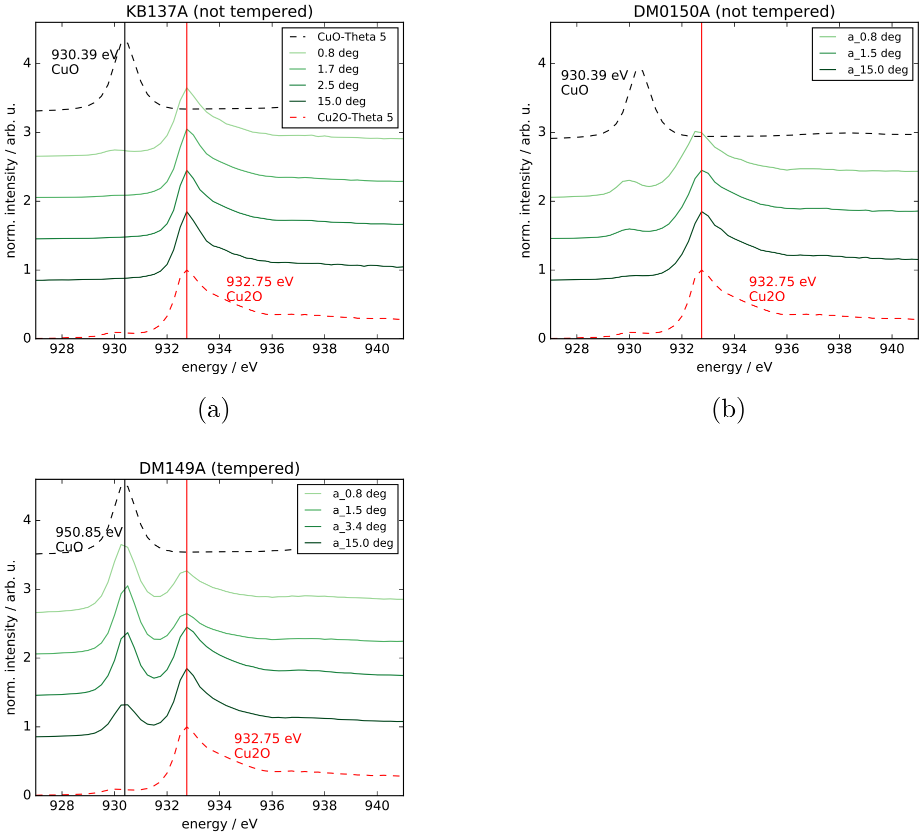

(a)

(b)

(c)

Figure 7.13 Normalized NEXAFS spectra: In the spectra of sample KB-137A and KBDM0150A ((a) and (b)) there is hardly any Cu^{II} species. Only at shallow angles, there is a slight increase in the intensity region of Cu^{II}. In the normalized spectrum of sample DM149A (c) one can see that both Cu^{I} and Cu^{II} are present in the entire depth profile of the sample. The Cu^{II}species are more present in the top layers (shallow angle). With increasing depth, the Cu^{II} content decreases and the Cu^{I} content increases.

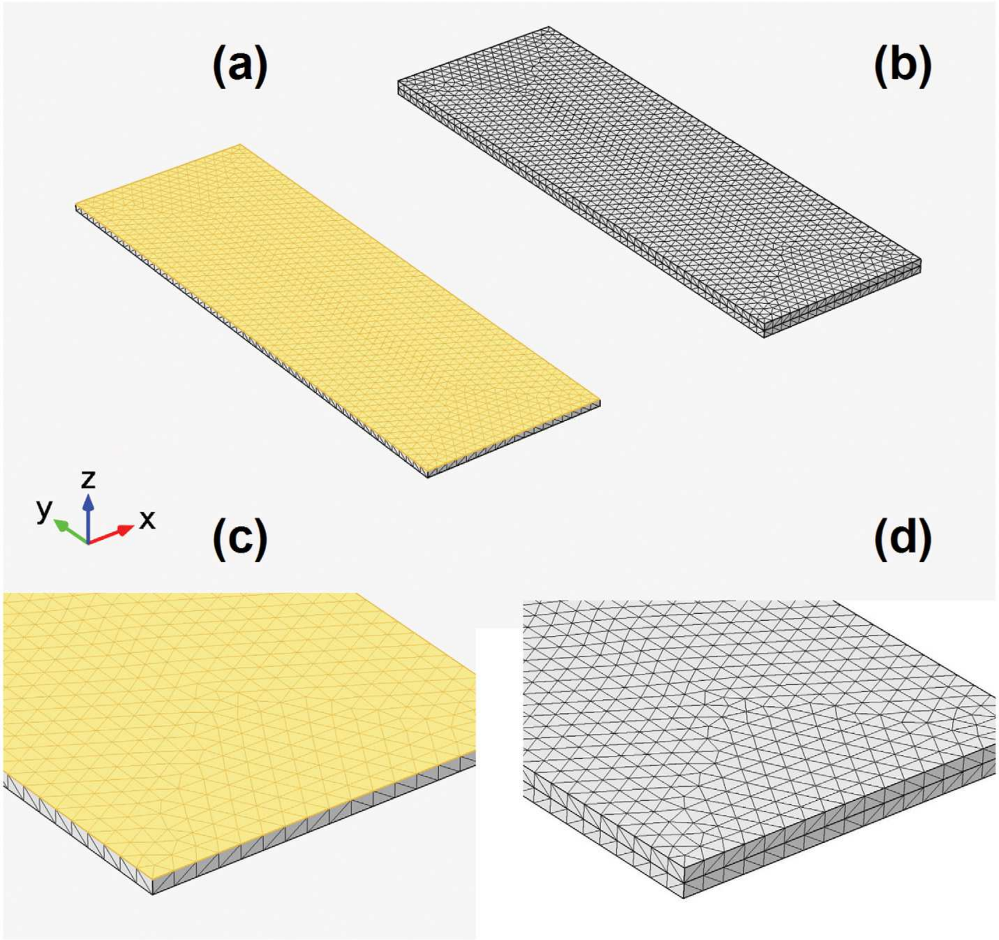

Figure 7.14 This figure visualizes the meshes used for the FEM simulations of the heat transfer in solids. Figure (a) shows the meshes of the 100 nm thin film on the glass support. The film is depicted in yellow. Figure (b) displays the meshes for the 1 mm thick layer on the supporting glass. Magnified views of both cases are given in figure (c) and (d). This figure is additional information for the section "thermal conductivity in thin films" on pages 109 to 134. This image is reproduced from Bethke et al.[145]

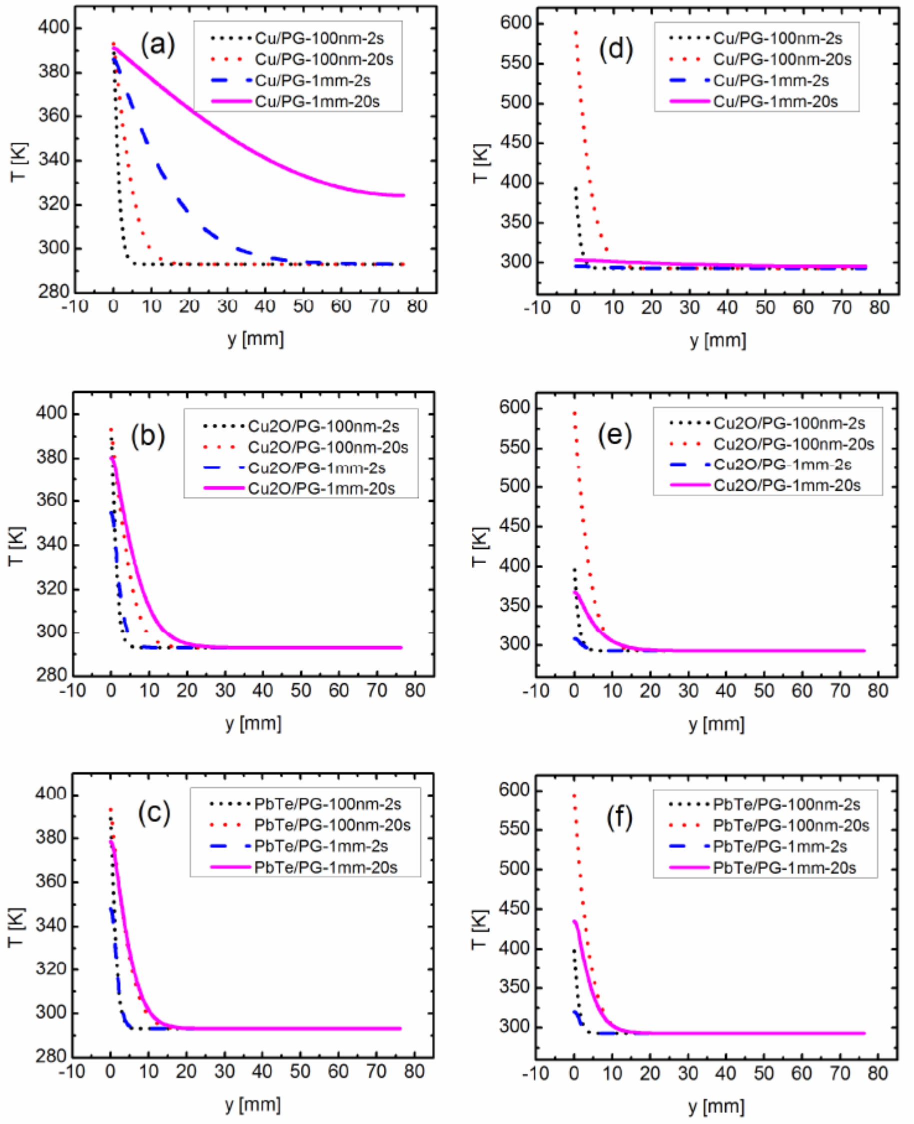

Figure 7.15 Full range of the simulation results of samples heated at the glass face. 1 mm thick films and 100 nm thick films which are supported on a Pyrex glass microscope slide are compared by their temperature distribution along the y-axis. The temperature is kept constant at 393 K at the front face of the glass slide for: (a) Cu, (b) Cu_2O, (c) PbTe. The heat flux of 10^5 Wm^{-2} is applied constantly at the front face of the Pyrex glass for: (d) Cu, (e) Cu_2O, (f) PbTe. This picture is additional information for the graph fig. 3.50 on page 119. This image is reproduced from Bethke et al.[145]

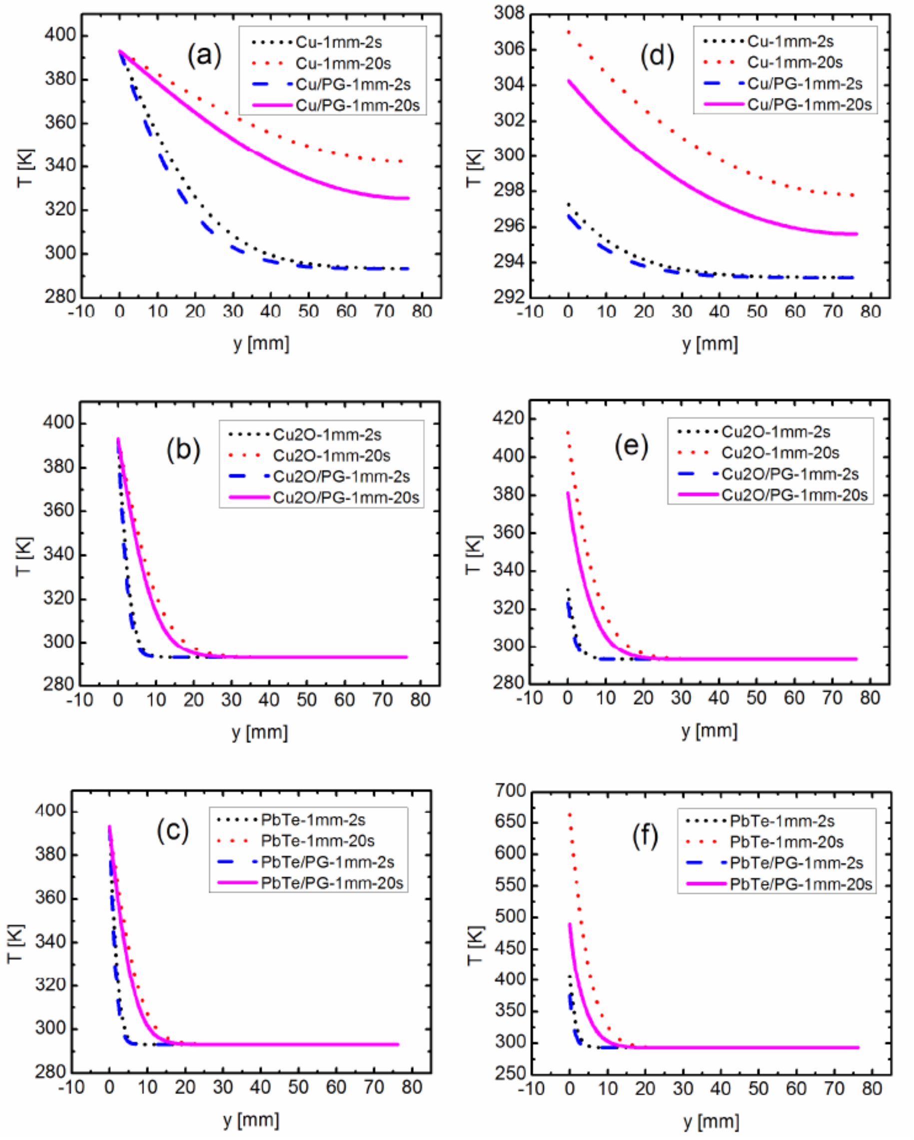

Figure 7.16 Full range of the simulation results of samples heated at the thermoelectric layer front face. Here, 1 mm thick films and 1 mm thick films supported on a Pyrex glass slide are compared by their temperature distribution along the y-axis. The temperature is kept constant at 393 K at the front face of the thermoelectric layer for: (a) Cu, (b) Cu_2O, (c) PbTe. The heat flux of 10^5 Wm^{-2} is applied constantly at the front face of the thermoelectric layer for: (d) Cu, (e) Cu_2O, (f) PbTe.This picture is additional information for the graph fig. 3.52 on page 123. This image is reproduced from Bethke et al.[145]

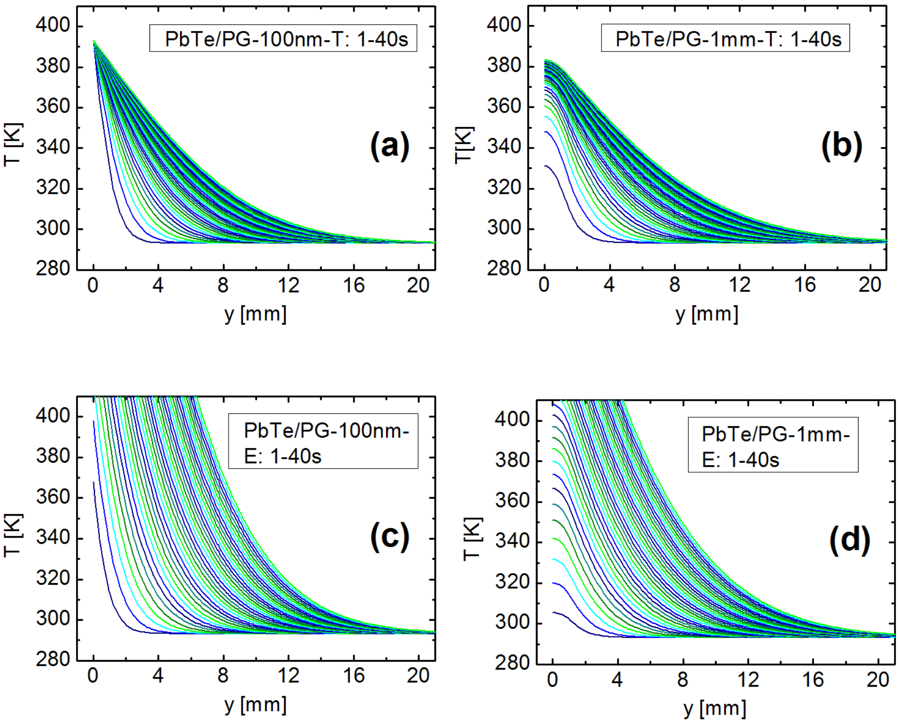

Figure 7.17 Full time range of the time dependent simulations for the temperature distribution in PbTe samples. The temperature distribution is plotted along the y-axis of each sample in the middle of the upper surface (see fig. 3.49 on page 115). The temperature is shown in the range between 1 and 40 s in one second intervals. In (a) and (b) the Pyrex glass face in the xz-plane next to the origin is kept at a constant temperature of 393 K. The heat flux in frames (c) and (d) is maintained constant at the front face of the supporting Pyrex glass. This figure is additional information for the section on thermal conductivity from pages 109 to 109 This image is reproduced from Bethke et al.[145]

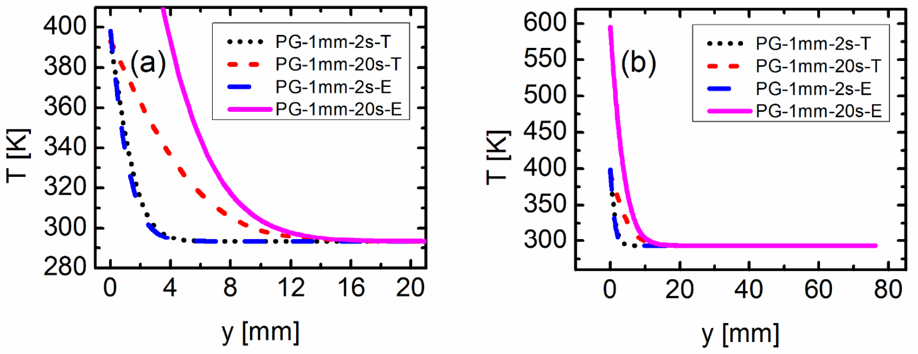

Figure 7.18 The graphs display the temperature distribution profiles in a Pyrex object slide along the y-axis. The Pyrex glass (PG) is heated at the front face y = 0 mm with a constant temperature of 393 K (marked with T in the sample name), or with a constant heat flux of 10^5 Wm^{-2} (marked with E): (a) enlarged and cropped view for better comparison, (b) full range plot. This figure is additional information for the section on thermal conductivity from pages 109 to 134 This image is reproduced from Bethke et al.[145]

Figure 7.19 Nemesis SBA 458, which was used for comparing Seebeck measurement results with the developed measurement device. The measurements where performed by Danny Kojda from the HZB. This picture is additional information for the section Seebeck measurements on pp. 47.

7.6 Additional Tables

Table 7.3 Fitting functions for different properties used for the investigated materials, as taken from Comsol Multiphysics. This table has been reproduced from the manuscript published in PlosONE.[145]

Material	Property	T_{low} [K]	T_{high} [K]	Expression
Pyrex glass	σ^{-1} [Ωm]	293	423	$\mathrm{exp}(144.02-0.7492484\cdot T^1+0.001992116\cdot T^2-2.629179E-6\cdot T^3+1.378133E-9\cdot T^4)$
	κ [W m^{-1} K^{-1}]	90	522	$0.1448239+0.00500369\cdot T^1-6.929144E-6\cdot T^2+3.477568E-9\cdot T^3$
	C_P [J kg^{-1} K^{-1}]	20	700	$-54.4515+3.650568\cdot T^1-0.003602436\cdot T^2+1.22855E-6\cdot T^3$
	ρ [kg m^{-3}]	80	673	$2234.113-0.002096489\cdot T^1-6.441875E-5\cdot T^2+9.703111E-8\cdot T^3-5.572413E-11\cdot T^4$
Cu	σ^{-1} [Ωm]	100	1358	$-3.514582E-9+7.064722E-11\cdot T^1-8.917638E-15\cdot T^2+1.026538E-17\cdot T^3$
	κ [W m^{-1} K^{-1}]	100	300	$831.0-6.986667\cdot T^1+0.04406667\cdot T^2-1.253333E-4\cdot T^3+1.333333E-7\cdot T^4$
		300	1358	$528.9926-1.034752\cdot T^1+0.003059339\cdot T^2-4.399776E-6\cdot T^3+2.929135E-9\cdot T^4-7.326451E-13\cdot T^5$
	C_P [J kg^{-1} K^{-1}]	60	300	$-215.2814+8.236392\cdot T^1-0.04732108\cdot T^2+1.291112E-4\cdot T^3-1.357031E-7\cdot T^4$
		300	1300	$342.764+0.1338348\cdot T^1+5.535252E-5\cdot T^2-1.971221E-7\cdot T^3+1.140747E-10\cdot T^4$
	ρ [kg m^{-3}]	250	800	$9062.242-0.3913962\cdot T^1-8.947644E-5\cdot T^2$
Cu_2O	C_P [J kg^{-1} K^{-1}]	293	1516	$269.8289+0.759696\cdot T^1-7.304674E-4\cdot T^2+2.218871E-7\cdot T^3+4.095487E-11\cdot T^4$
	ρ [kg m^{-3}]	73	1573	$5993.536+0.04921465\cdot T^1-9.434866E-5\cdot T^2+6.27139E-9\cdot T^3$

7.7 List of Publications

- Jonas Baumann, Adrian Jonas, Ruth Reusch, Veronika Szwedowski-Rammert, Malte Spanier, Daniel Grötzsch, Kevin Bethke, Beatrix Pollakowski-Herrmann, Markus Krämer, Thomas Holz, Reiner Dietsch, Ioanna Mantouvalou, and Birgit Kanngießer, "Toroidal multilayer mirrors for laboratory soft X-ray grazing emission X-ray fluorescence", Review of Scientific Instruments, **2020**, 91, 016102, doi: 10.1063/1.5130708

- Sinem Palantöken, Kevin Bethke, Vesna Zivanovic, Gerhard Kalinka, Janina Kneipp, Klaus Rademann, "Cellulose hydrogels physically crosslinked by glycine: Synthesis, characterization, thermal and mechanical properties", J. Appl. Polym. Sci. **2020**,48380, DOI: 10.1002/APP.48380.

- Kim Greis, Kevin Bethke,* Julius B. Stückrath, Tjark T. K. Ingber, Suresh Valiyaveettil, and Klaus Rademann, "One-Pot Synthesis of Xanthate-Functionalized Cellulose for the Detection of Micromolar Copper(II) and Nickel(II) Ions", Clean – Soil, Air, Water, **2019**, 47, 190017, doi: 10.1002/clen.201900179
  * = corresponding author

- Kevin Bethke, Sinem Palantöken, Virgil Andrei, Marcel Roß, Vikram Singh Raghuwanshi, Frieder Kettemann, Kim Greis, Tjark T. K. Ingber, Julius B. Stückrath, Suresh Valiyaveettil, and Klaus Rademann, "Functionalized Cellulose for Water Purification, Antimicrobial Applications, and Sensors", Adv. Func. Mater., **2018**, 1800409-1 - 1800409-14, doi: 10.1002/adfm.201800409.

- Virgil Andrei, Kevin Bethke, Fani Madzharova, Aafke Cecile Bronneberg, Janina Kneipp, Klaus Rademann, "In Situ Complementary Doping, Thermoelectric Improvements, and Strain-Induced Structure within Alternating PEDOT:PSS/PANI Layers", ACS Appl. Mater. Interfaces **2017**, 9, 33308-33316, doi: 10.1021/acsami.7b10106.

- Virgil Andrei, Kevin Bethke, Fani Madzharova, Sebastian Beeg, Axel Knop-Gericke, Janina Kneipp, Klaus Rademann, "Size Dependence of Electrical Conductivity and Thermoelectric Enhancements in Spin-Coated PEDOT:PSS Single and Multiple Layers", Adv. Electron. Mater. **2017**, 1600473-1 - 1600473-8, doi: 10.1002/aelm.201600473.

- K. Bethke, V. Andrei, K. Rademann, "Decreasing the effective thermal conductivity in glass supported thermoelectric layers", Plos One **2016**, 11, e0151708-1 - e0151708-19, doi: 10.1371/journal.pone.0151708.

- V. Andrei, K. Bethke, K. Rademann, "Thermoelectricity in the context of renewable energy sources: joining forces instead of competing", Energy & Environmental Science, **2016**, 9, 1528-1532, doi: 10.1039/c6ee00247a.

  Inside front cover: Energy & Environmental Science, **2016**, 9, 1518.

- V. Andrei, K. Bethke, K. Rademann, "Adjusting the thermoelectric properties of copper(I) oxide–graphite–polymer pastes and the applications of such flexible composites", Physical Chemistry Chemical Physics, **2016**, 18, 10700-10707,
  doi: 10.1039/C5CP06828B.

  Inside back cover: Physical Chemistry Chemical Physics, **2016**, 18, 11560.

- V. Andrei, K. Bethke, K. Rademann, "Copper(I) oxide based thermoelectric powders and pastes with high Seebeck coefficients", Appl. Phys. Lett., **2014**, 105, 233902-1 - 233902-4, doi: 10.1063/1.4903832.
- Chandrasekaran Abinaya, Kevin Bethke, Virgil Andrei, Jonas Baumann, Beatrix Pollakowski-Herrmann, Birgit Kanngießer, Burkhard Beckhoff, G. Cristian Vásquez, Jeyanthinath Mayandi, Terje G. Finstad, Klaus Rademann, "The effect of post-deposition annealing conditions on structural and thermoelectric properties of sputtered Cu films", in submission

Oral Presentations

- International Conference on Energy Materials 2019, MTWU, Kodaikanal, India, „Solar energy and energy storage“, 2019, invited Lecture.
- International Conference on Exploring Nanostructures for Enhanced Power Conversion Efficiency of Solar Cells (ICENES) 2019, Gandhigram University, India, „Solar energy and energy storage“, 2019, invited Lecture.
- International Conference on Advanced Functional Materials for Energy, Environment and Biomedical Applications 2017, „Green Energy“, 2017, invited Lecture.
- Humboldt-University Berlin, 3rd. Workshop on functionalized cellulose, „Potentials of functionalized cellulose“, 2017.
- Madurai Kamaraj University, India „Thermoelectricity“, 2016.
- Madurai Kamaraj University, India „Research opportunities around the world, especially Europe“, 2016.

- Schering Stiftung, "Irreversible Momente", „Der Irreversible Moment aus der Sicht der Chemie“, 2016, invited Lecture.

7.7.1 Poster Presentations

- EMRS 2014: J. Baumann, B. Pollakowski, K. Bethke, D. Eisenhauer, K. Rademann, B. Beckhoff, and B. Kanngießer, „Investigating Embedded Nanosystems with Angle Resolved Fluorescence Spectroscopy“.
- Ringberg Conference 2015: K. Bethke, K. Rademann, „FEM Simulation of Heat Transfer“.
- JCF 2015: V. Andrei, K. Bethke, K. Rademann,„High Seebeck coefficients of copper(I) oxide based thermoelectrics“.
- ICT 2016: K. Bethke, V. Andrei, K. Rademann, „Decreasing the Effective Thermal Conductivity in Glass Supported Thermoelectric Layers“.
- Chip 2016: K. Bethke, V. Andrei, K. Rademann, „Decreasing the Effective Thermal Conductivity in Glass Supported Thermoelectric Layers“.
- ICMAT 2017: K. Greis, J. Stückrath, T. Ingber, K. Bethke, S. Valiyaveettil, K. Rademann, „Cellulose Based Chemicals for Heavy Metal Removal Studied by X-Ray-Fluorescence Spectroscopy (XRF)“.
- ICMAT 2017: T. Ingber, K. Greis, J. Stückrath, M. Rohloff, K. Bethke, S. Valiyaveettil, K. Rademann, „Mercury capture by magnetic iron oxide loaded with silver nano- particles“

- ICT 2017: K. Bethke, V. Andrei, K. Rademann, „Investigation of PEDOT:PSS single and multi-layers“.
- AFMEEB 2017: C. Abinaya, V. Andrei, K.Bethke, K. Rademann, J. Mayandi

7.7.2 Patent

- K. Bethke, M. Roß, K. Rademann, „Thermoelektrisches Komposit“, DE 10 2017 110 949.8, issued.

7.8 Awards, Scholarships and Funding

7.8.1 Awards and Scholarships

- EXIST-Gründerstipendium 2020
- International Max-Planck Research School Scholarship
- ICTS 2016 Student registration waiver

7.8.2 Granted External Funding

- DST-DAAD Scientific exchange program (8000 € + 447195 Rupees) 01.01.2017-31.12.2018
- PI for the NUS HU Profile Partnership (17500 € HU side + 28000S$) 01.09.2018-31.08.2019
- PI for ZIM Project (HU, TU Claustal, Krebs Engineering and 3dk) (140903 € HU) 2018-2020

List of Figures

List of Tables

List of Abbreviations

Acronyms

AFM	Atomic force microscopy
BAM	Bundesanstalt für Materialforschung
BE	Back-scattered electron (signal)
BESSY	Berliner Elektronenspeicherring - Gesellschaft für Synchrotronstrahlung m. b. H.
CNC	Computer numeric control
DMSO	dimethyl sulfoxide
DOF	Degrees of freedom for motion maximum six (three translational three rotational)
EDS	Energy-dispersive X-ray spectroscopy see EDX
EDX	Energy-dispersive X-ray spectroscopy see EDS
FEA	Finite element analysis (equivalent to FEM)
FEM	Finite element method (equivalent to FEA)
GIXRF	Grazing incidence X-ray fluorescence

IMFP	Inelastic mean free path
IO	Input/Output
KMC	„Kristall Monochromator“ beamline
MOSFET	Metal-oxide-semiconductor field-effect transistor
NEXAFS	Near edge X-ray absorption fine structure
PC	Personal computer
pc	Piece
PCB	Printed circuit board
PEDOT:PSS	Poly-(ethylene-3,4-dioxythiophene): Poly(styrenesulfonic acid)
PES	Photoelectron spectroscopy (see XPS)
PGM	Plane-grating monochromator
PID controllers	Proportional integral derivative controllers
PP	Samples prepared from a pure aqueous solution of PEDOT:PSS
PP5D	Samples prepared from an aqueous solution of PEDOT:PSS doped with 5% DMSO
PTB	Physikalisch - Technische Bundesanstalt
PVD	Physical vapor deposition
PWM	Pulse width modulation

RTG	Radioisotope thermoelectric generators
TEC(s)	Thermoelectric cooler(s)
TEG(s)	Thermoelectric generator(s)
UHV	Ultra-high vacuum
USB	Universal serial bus
XPS	X-ray photo emission spectroscopy (sometimes PES)
XRD	X-ray diffraction

Prefixes

μ	micro (10^{-6})
k	kilo (10^{3})
M	Mega (10^{6})
m	milli (10^{-3})
n	nano (10^{-9})

Symbols

α	Seebeck coefficient	μV/K
κ	Thermal conductivity	W/(m · K)
μ	Chemical potential also known as Fermi level E_f	
σ	Electrical conductivity	S/m
E_g	Band gap	eV

U_{Td}	Thermodiffusion potential	V
C_P	Thermal capacity at constant pressure	$J/(kg \cdot K)$
D(E)	Energy dependent density of states function	
G(E)	Energy dependent electron conductance function	
Q	Heat flow	
q	Electric charge $1.6{\cdot}10^{19}C$	
T	Temperature	K
t	Time	s

Units

A	Ampère SI Unit
bar	1 bar = 10^5 Pa = 10^5 $kg/(m \cdot s^2)$
eV	Electron volt $1.6{\cdot}10^{-19}$ J
NM	Nautical mile 1 NM = 1852 m
S	Siemens $S = \Omega^{-1} = \frac{s^3 \cdot A^2}{kg \cdot m^2}$
T	Tesla 1 T = 1 $kg/(A \cdot s^2)$
ton	Metric ton 1,000 kg
W	Watt 1 W = $1\ \frac{J}{s} = 1\ \frac{kg \cdot m^2}{s^3}$

Selbstständigkeitserklärung

Ich erkläre, dass ich, Kevin Oliver Roland Bethke, geboren am 15.09.1986 in Berlin, Deutschland, die vorliegende Arbeit selbstständig und nur unter Verwendung der angegebenen Literatur und Hilfsmittel angefertigt habe.

Berlin den 23.02.2020